

1N-20-CR

182491

91-16

185 P

# Electric Propulsion System Technology

Report — 1990

Biography

Garner

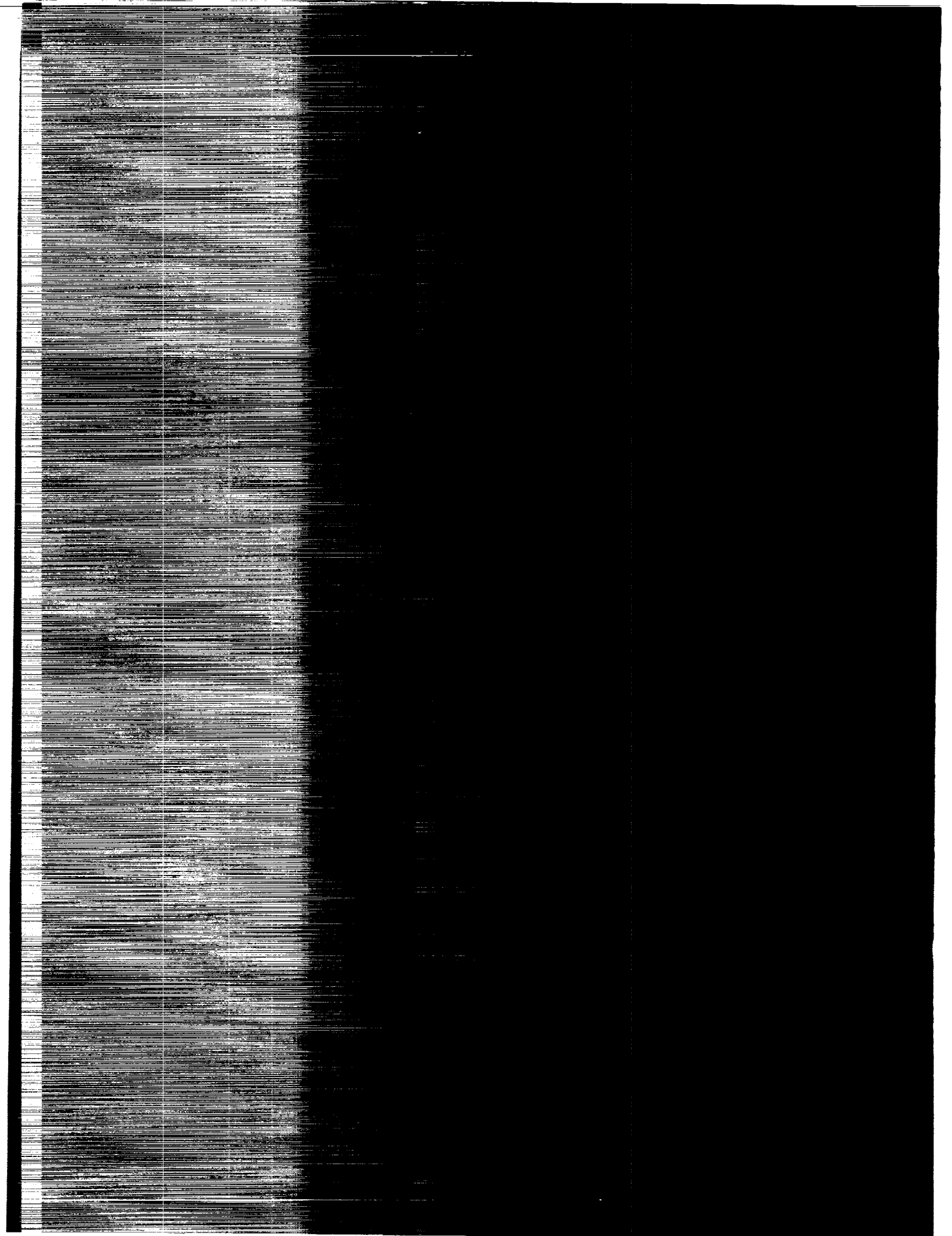
Goodfellow

(NASA-CR-194100) ELECTRIC  
PROPULSION SYSTEM TECHNOLOGY Annual  
Report, 1990 (JPL) 185 p

N94-13055

Unclas

G3/20 0182491



# Electric Propulsion System Technology

Annual Report — 1990

John R. Brophy  
Charles E. Garner  
Keith D. Goodfellow

December 1991



National Aeronautics and  
Space Administration

Jet Propulsion Laboratory  
California Institute of Technology  
Pasadena, California

The research described in this publication was carried out by the Jet Propulsion Laboratory, California Institute of Technology, under a contract with the National Aeronautics and Space Administration.

Reference herein to any specific commercial product, process, or service by trade name, trademark, manufacturer, or otherwise, does not constitute or imply its endorsement by the United States Government or the Jet Propulsion Laboratory, California Institute of Technology.

## ABSTRACT

This report describes the work performed on the Ion Propulsion System Technology Task in FY90. The objectives of this work fall under two broad categories. The first of these deals with issues associated with the application of xenon ion thrusters for primary propulsion of planetary spacecraft, and the second with the investigation of technologies which will facilitate the development of larger, higher power ion thrusters to support more advanced mission applications. Most of the effort was devoted to investigation of the critical issues associated with the use of ion thrusters for planetary spacecraft. These issues may be succinctly referred to as life time, system integration, and throttling. Chief among these is the engine life time. If the engines do not have sufficient life to perform the missions of interest, then the other issues become unimportant.

Ion engine life time was investigated through two experimental programs: an investigation into the reduction of ion engine internal sputter erosion through the addition of small quantities of nitrogen, and a long duration cathode life test. In addition, a literature review and analysis of accelerator grid erosion were performed. The nitrogen addition tests indicated that the addition of between 0.5 and 1.0 percent of nitrogen by mass to the xenon propellant results in a reduction in the sputter erosion of discharge chamber components by a factor of between 20 and 50, with negligible reduction in thruster performance. The long duration test of a 6.35-mm dia. xenon hollow cathode is still in progress, and has accumulated more than 4,000 hours of operation at an emission current of 25 A at the time of this writing.

One of the major system integration issues concerns possible interactions of the ion thruster produced charge exchange plasma with the spacecraft. A computer model originally developed to describe the behavior of mercury ion thruster charge exchange plasmas was resurrected and modified for xenon propellant. This model enables one to calculate the flow direction and local density of the charge exchange plasma, and indicates the degree to which this plasma can flow upstream of the thruster exhaust plane.

A continuing effort to investigate the most desirable throttling technique for noble gas ion thrusters concentrated this year on experimentally determining the fixed flow rate throttling range of a 30-cm dia. thruster with a two-grid accelerator system. These experiments demonstrated a throttling capability which covers a 2.8 to 1 variation in input power. This throttling range is 55% greater than expected, and is due to better accelerator system performance at low net-to-total voltage ratios than indicated in the literature.

To facilitate the development of large, higher power ion thrusters several brief studies were performed. These include the

iii  
INTERNATIONAL BUREAU

PRECEDING PAGE BLANK NOT FILMED

development of a technique which simulates ion thruster operation without beam extraction, the development of an optical technique to measure ion thruster grid distortion due to thermal expansion, tests of a capacitance measurement technique to quantify the accelerator system grid separation, and the development of a segmented thruster geometry which enables near term development of ion thrusters at power levels greater than 100 kW. Finally, a paper detailing the benefits of electric propulsion for the Space Exploration Initiative was written.

## ACKNOWLEDGEMENTS

The authors would like to thank Lew Pless, Alison Owens, William Thogmartin and Robert Toomath for their expert assistance in performing the experimental program described in this report.



# TABLE OF CONTENTS

<u>Section</u>	<u>Page</u>
NOMENCLATURE.....	xiii
1.0 THE EFFECT OF NITROGEN ADDITION ON XENON ION ENGINE EROSION.....	1
2.0 BENEFITS OF ELECTRIC PROPULSION FOR THE SPACE EXPLORATION INITIATIVE.....	2
3.0 SIMULATED ION THRUSTER OPERATION WITHOUT BEAM EXTRACTION.....	3
4.0 AN OPTICAL TECHNIQUE TO MEASURE ION ENGINE GRID DISTORTION DUE TO THERMAL EXPANSION.....	4
5.0 CHARGE EXCHANGE PLUME MODELING.....	10
5.1 Introduction.....	10
5.2 PLASIM Computer Code.....	11
5.2.1 Normalized Number Density Profiles.....	14
5.2.2 Comparison of Mercury and Xenon.....	17
5.3 Spherical Propagation Model.....	18
5.4 Metal Charge-Exchange Ion Model.....	24
5.4.1 Accelerator Grid Erosion Model.....	25
5.4.2 Metal Charge-Exchange Spherical Propagation Model.....	29
5.4.3 Calculation Example.....	30
5.5 Future Recommendations.....	31
6.0 CATHODE LIFE TEST.....	33
6.1 Introduction.....	33
6.2 Apparatus and Procedure.....	34
6.2.1 The Cathode.....	34
6.2.2 Test Facility.....	40
6.2.3 Computer Control System.....	47
6.2.4 Start-Up Procedure.....	47
6.3 Test Results After 4,200 Hours of Operation.....	49
6.4 Model of Cathode Insert Life.....	66
6.5 Summary.....	70
7.0 FIXED FLOW RATE THROTTLING.....	72
7.1 Introduction.....	72
7.2 Throttling With Fixed Beam Current.....	72
7.3 Effect of Fixed Flow Rate Throttling on Mission Performance.....	73
7.4 Experimentally Determined Throttling Range.....	75

## TABLE OF CONTENTS (continued)

<u>Section</u>	<u>Page</u>
8.0 CAPACITANCE MEASUREMENT FOR ACCELERATOR SYSTEM DIAGNOSTICS.....	81
9.0 SEGMENTED ION THRUSTER.....	83
10.0 BAFFLE EROSION STUDIES.....	89
10.1 Introduction.....	89
10.2 Discussion.....	89
11.0 REVIEW OF ACCELERATOR GRID EROSION.....	93
11.1 Implications for Xenon Ion Thruster Accelerator Grid Life.....	101
11.2 Xenon Ion Engine Accelerator Grid Erosion Rate Estimate.....	103
12.0 REFERENCES.....	106
13.0 APPENDICES.....	117
13.1 Appendix A: AIAA Paper No. 90-2591.....	117
13.2 Appendix B: AIAA Paper No. 90-2756.....	131
13.3 Appendix C: AIAA Paper No. 90-2655.....	143
13.4 Appendix D: AIAA Paper No. 90-2650.....	155
13.5 Appendix E: Charge-Exchange Plasma Model.....	162
13.6 Appendix F: Cathode Life Test Software.....	167

## LIST OF FIGURES

<u>Figure</u>	<u>Title</u>	<u>Page</u>
1	Experimental set-up used to measure ion engine grid deflection in situ.....	6
2	Laser positioning technique data.....	6
3	Model geometry for the calculation of charge exchange ion trajectories.....	12
4	Example of calculated charge exchange ion trajectories for a 30-cm dia. xenon ion thruster....	15
5	Example of calculated charge exchange ion number density contours for the ion trajectories given in Fig. 4.....	16
6	Charge exchange ion trajectories calculated using twice the number of ion paths as in Fig. 4.....	19
7	Charge exchange ion number density contours corresponding to the ion trajectories in Fig. 6.....	20
8	Charge exchange ion trajectories calculated using an electron temperature which is 4 times that in Fig. 4.....	21
9	Charge exchange ion number density contours corresponding to the ion trajectories in Fig. 8.....	22
10	Small scale normalized density contours for the spherical propagation model.....	26
11	Large scale normalized density contours for the spherical propagation model.....	27
12	Life test cathode schematic.....	35
13	Cathode orifice plate (2 % thoriated tungsten).....	36
14	SEM photograph of orifice plate welded to cathode tube.....	37
15	Close-up of electron beam weld showing stress crack in the orifice plate.....	38
16	Life test cathode parts.....	39

# LIST OF FIGURES (continued)

<u>Figure</u>	<u>Title</u>	<u>Page</u>
17	Cathode life test facility.....	41
18	Life test xenon feed system.....	42
19	Comparison of MKS flow meter calibrations on nitrogen.....	44
20	MKS flow meter calibration on xenon.....	45
21	Comparison of MKS flow meter calibrations on xenon after 7 months of continuous operation.....	46
22	Life test power supply schematic.....	48
23	Life test cathode in operation.....	51
24	Close-up of cathode orifice during operation at run hour 4046.....	52
25	Discharge current oscillations with Sorenson anode supply -- 2 A per major division vertically, 10 microseconds per major division horizontally.....	53
26	Discharge voltage oscillations with Sorenson anode supply -- 20 V per major division vertically and 10 microseconds per major division horizontally.....	54
27	Discharge current oscillations with Hewlett-Packard anode supply -- 0.5 A per major division vertically, 100 microseconds per major division horizontally....	56
28	Low frequency discharge current oscillations which began after approximately 4000 hours of operation...	57
29	Low frequency discharge voltage oscillations, $\pm 2V$ at 333 Hz.....	58
30	Orifice plate temperature versus cathode run time...	61
31	Comparison of insert and orifice plate brightness temperatures as measured by the optical pyrometer.....	62
32	Measured anode current during life test.....	63
33	Discharge voltage versus cathode run time.....	64

## LIST OF FIGURES (continued)

<u>Figure</u>	<u>Title</u>	<u>Page</u>
34	Temperature of the stainless steel cathode flange versus cathode run time.....	65
35	Xenon flow rate versus cathode run time.....	67
36	Cathode internal pressure versus run time.....	68
37	Starter electrode (keeper) voltage versus cathode life time.....	69
38	Experimentally determined variation in net-to-total voltage ratio for two-grid accelerator system.....	77
39	Thrust variation over input power throttling range with constant beam current of 3.2 A.....	78
40	Efficiency variation over input power throttling range at constant beam current of 3.2 A.....	79
41	Specific impulse variation over input power throttling range at constant beam current of 3.2 A..	80
42	Segmented ion thruster schematic with six 30-cm diameter segments.....	84
43	Power processor configuration for the segmented ion thruster.....	85
44	Ion engine sketch showing cathode plume and the location of the baffle.....	90
45	Plot of baffle erosion as a function of distance from the baffle center.....	92
46	(a) Schematic diagram of the ion engine grids and formation of charge-exchange ions. (b) Plot of ion potential variation.....	98
47	Sputter yield for molybdenum as a function of incident xenon and mercury ion energies.....	102

## LIST OF TABLES

<u>Table</u>	<u>Title</u>	<u>Page</u>
1	Resolution of the Laser Positioning Technique With Engine Discharge Off.....	7
2	Laser Positioning Technique Data.....	8
3	Propellant Property Data.....	18
4	Example Values for Model Input Variables.....	25
5	Cathode Life Test Summary.....	50
6	Comparison of Throttling Strategies.....	74
7	Projected Performance of Segmented Ion Thrusters....	87
8	Summary of References on Ion Engine Life.....	94
9	Accelerator Grid Erosion Data.....	95
10	Grid Mass Loss Ordered by $J_a Y$ .....	99
11	Pit Erosion Rates Ordered by $J_{a,uniform} Y$ .....	99

## NOMENCLATURE

$a$	constant in Eq. (43) (K)
$A$	area ( $m^2$ )
$A_b$	beam area ( $m^2$ )
$A_e$	effective accelerator grid open area ( $m^2$ )
$A_g$	grid area ( $m^2$ )
$B$	constant in Eq. (43) ( $hr^{-1/2}$ )
$C$	constant in Eq. (6)
$C_i$	number of incident ions per second per ampere
$C_1$	constant defined in Eq. (22)
$d$	electrode separation in Eq. (48) (m)
$e$	electron charge (C)
$f_v$	Maxwell-Boltzmann velocity distribution function
$F_a$	grid fractional open area
$F_{\parallel}$	force parallel to charge exchange ion path (N)
$F_{\perp}$	force perpendicular to charge exchange ion path (N)
$g_{io}$	ion-neutral relative velocity (m/s)
$j_{ch}$	Child's law current ( $A/m^2$ )
$J_a$	accelerator grid current (A)
$J_b$	beam current (A)
$k$	Boltzmann constant
$K_C$	Clausing factor
$L$	effective length downstream of the accelerator grid that contains the charge exchange ions which can reach the grid (m)
$L_a$	effective ion acceleration length (m)

# NOMENCLATURE (continued)

$L_d$	ion deceleration distance downstream of the thruster (m)
$L_D$	Debye length
$L_g$	grid gap (m)
$m_o$	propellant atom mass (kg)
$m_i$	ion mass (kg)
$m_{o,m}$	neutral metal atom mass (kg)
$\dot{m}_m$	accelerator grid mass loss rate (kg/s)
$m_L$	total accelerator grid mass loss (kg)
$m_{Mo}$	mass of molybdenum atom (kg)
$n_{CE}$	charge exchange number density ( $m^{-3}$ )
$n_{CE,m}$	number density of metal charge exchange ions ( $m^{-3}$ )
$n_{CE,norm}$	normalized charge exchange ion number density
$n_{CE,90}$	charge exchange number density in the direction normal to the ion beam ( $m^{-3}$ )
$n_{norm}$	normalized charge exchange ion number density
$\dot{n}_{CE}$	local charge-exchange generation rate ( $m^{-3}s^{-1}$ )
$n_{e,ref}$	reference electron number density ( $m^{-3}$ )
$n_i$	ion number density ( $m^{-3}$ )
$n_{ref}$	neutral atom number density at the grids ( $m^{-3}$ )
$n_o$	neutral atom number density ( $m^{-3}$ )
$n_{o,m}$	number density of neutral metal atoms ( $m^{-3}$ )

# NOMENCLATURE (continued)

$n_{m,m}$	number density of neutral metal atoms at the accelerator grid ( $m^{-3}$ )
$N$	number of ion paths
$N_{LD}$	number of debye lengths
$\dot{N}_{CE}$	total production rate of charge exchange ions ( $s^{-1}$ )
$\dot{N}_{CE,m}$	total production rate of metal charge exchange ions ( $s^{-1}$ )
$\dot{N}_{o,m}$	total production rate of metal neutral atoms from accelerator grid sputtering ( $s^{-1}$ )
$\dot{N}_i$	total rate of ions leaving the thruster ( $s^{-1}$ )
$\dot{N}_{tot}$	total neutral atom flow rate into the thruster ( $s^{-1}$ )
$q$	quantity of barium remaining in insert after time $t$
$q_0$	initial quantity of barium in insert
$r_b$	beam radius (m)
$R$	net-to-total voltage ratio
$R_s$	radius for spherical propagation model (m)
$S$	sputter yield (atoms/ion)
$t$	time (hrs)
$T$	insert temperature (K)
$T_e$	electron temperature (K)
$T_e'$	electron temperature (eV)
$T_{e,p}$	electron temperature in charge exchange plasma (K)
$T_o$	neutral atom temperature (K)
$T_o'$	neutral atom temperature (eV)

# NOMENCLATURE (continued)

$T'_{o,m}$	neutral metal atom temperature (eV)
$v_{CE}$	velocity of charge exchange ions (m/s)
$v_i$	ion velocity (m/s)
$v_{90}$	charge exchange ion velocity component 90 degrees to ion beam axis (m/s)
$v_{180}$	charge exchange ion velocity component 180 degrees to ion beam axis (m/s)
$v_{o,m}$	velocity of neutral metal atoms (m/s)
$V_a$	net accelerating voltage (V)
$V_t$	total accelerating voltage (V)
$x$	x-coordinate (m)
$Y$	sputter yield (atoms/ion)
$z$	axial position (m)
$\Delta d_m$	local mean spacing between ion trajectories (m)
$\Delta d_p$	distance to previous point (m)
$\Delta d_s$	ion path spacing (m)
$\Delta v_{\parallel}$	change in parallel velocity component (m/s)
$\Delta v_{\perp}$	change in perpendicular velocity component (m/s)
$\Delta V$	potential difference (V)
$\Delta t$	time step interval (s)
$\epsilon_0$	permittivity constant
$\eta_u$	propellant utilization
$\sigma_{CE}$	charge-exchange collision cross section for propellant atoms (m <sup>2</sup> )

## NOMENCLATURE (continued)

$\sigma_{CE,m}$	charge exchange collision cross section for metal atoms ( $m^2$ )
$\theta$	angle from thruster axis



## 1.0 THE EFFECT OF NITROGEN ADDITION ON XENON ION ENGINE EROSION

Sputter erosion of ion engine discharge chamber components can be reduced by a factor of 20 to 50 through the addition of small amounts of nitrogen to the xenon propellant. Short term test segments (typically 24 hours in duration) were performed using a modified 30-cm diameter J-Series ion engine to identify the optimum quantity of nitrogen per unit mass to be added to the xenon. The optimum nitrogen fraction was found to be in the range of 0.5 to 1.0 %. The addition of nitrogen fractions greater than approximately 1.0 % was not found to significantly reduce the sputter erosion beyond that obtained at the 1.0 % level. Surface analyses revealed the presence of tantalum nitrides on tantalum engine components which were exposed to the discharge chamber plasma when nitrogen was added. Additional surface analyses strongly suggested the presence of molybdenum nitrides on molybdenum engine components as well. It is believed that the observed reduction in sputter erosion through the addition of nitrogen results from the formation of these sputter resistant surface nitrides. Details of this work are given in the AIAA paper titled, "The Effect of Nitrogen on Xenon Ion Engine Erosion," which was presented at the 21st International Electric Propulsion Conference and is reproduced in Appendix A.

## **2.0 BENEFITS OF ELECTRIC PROPULSION FOR THE SPACE EXPLORATION INITIATIVE**

The high performance (i.e., high specific impulse) of electric propulsion systems offers substantial benefits for the Space Exploration Initiative. For Lunar cargo, Mars cargo, and piloted Mars missions these benefits include: substantially reduced initial mass in low Earth orbit, reduced round-trip times for piloted Mars vehicles, availability of large amounts of electrical power en route and at the destination, less sensitivity to launch dates and windows, reusability, and growth potential for human exploration of the entire solar system. These benefits are discussed in detail in the AIAA paper titled, "Benefits of Electric Propulsion for the Space Exploration Initiative," which was presented at the 26th Joint Propulsion Conference and is reproduced in Appendix B.

### 3.0 SIMULATED ION THRUSTER OPERATION WITHOUT BEAM EXTRACTION

The development of high power (hundreds of kilowatts) ion engines may be greatly facilitated through the use of a technique which enables optimization of the discharge chamber to be performed without beam extraction. Ion thruster operation without beam extraction results in an experimentally determined decrease in the accelerator system transparency to ions from approximately 0.8 down to 0.22 for the standard 30-cm dia., J-Series ion optics. The decreased ion transparency translates into a decreased propellant flow rate requirement for operation without beam extraction, enabling testing to be performed in smaller vacuum chambers with lower pumping speeds. In addition, discharge chamber optimization without beam extraction initially decouples the discharge chamber development from the ion accelerator system development, allowing development of these engine components to be performed in parallel to a much greater extent than at present.

Performance curves experimentally determined without beam extraction are shown to agree well with actual performance curves obtained with beam extraction. Screen grid temperatures, however, are shown to be significantly higher without beam extraction due to the decrease in accelerator system transparency to ions. Details of this work are described in the AIAA paper titled, "Simulated Ion Thruster Operation Without Beam Extraction," which was presented at the 21st International Electric Propulsion Conference and is reproduced in Appendix C.

#### 4.0 AN OPTICAL TECHNIQUE TO MEASURE ION ENGINE GRID DISTORTION DUE TO THERMAL EXPANSION

Ion engine accelerator system performance is strongly dependent on the inter-electrode separation. Radial temperature gradients and grid-to-grid temperature differences resulting from normal engine operation can significantly alter the grid separation. Thermally induced changes in the grid separation can become increasingly severe as the engine diameter is increased beyond the current state-of-the-art 30 cm size. Finite element models of the grid thermal/mechanical behavior can greatly facilitate the design of large diameter, high power ion accelerator systems. These models, however, require experimental verification before they can be used with confidence. Accurate grid gap measurements made during engine operation are needed for this verification.

Grid temperatures are known to be different for operation with and without beam extraction (see Appendix C); therefore, it is most desirable to obtain grid deflection measurements with beam extraction. Non-intrusive optical techniques are the best candidates to perform these measurements and several different approaches were examined. A technique which measures grid deflection by imaging laser light reflected from the screen and accelerator grids was selected. Bench tests using this technique with a set of 600 series, 30-cm dia. ion optics showed very promising results. Details of this work are given in the AIAA paper titled, "An Optical Technique To Measure Ion Engine Grid Distortion Due To Thermal Expansion," which was presented at the 21st International Electric Propulsion Conference and is reproduced in Appendix D.

Based on the successful results described in this paper, continuing effort focussed on the measurement of the screen-to-accelerator grid gap on grids mounted to an ion engine operating in a vacuum tank. To measure the gap between the screen and accelerator grids, the mirrors must be glued onto the grids so that the mirrors are perpendicular with respect to the incident laser light. The important difference between the work discussed in Appendix D and the work discussed below is that in the former case, the grids were not attached to the ion engine, but instead were placed on a bench. Therefore the grids and mirrors were easily accessible and it was a simple matter to adjust the mirrors glued to the grids so that they were perpendicular to the incident laser light. However, with the grids attached to the engine, and the engine mounted inside the vacuum tank, positioning the mirrors perpendicular to the laser light became more difficult. It was not possible to correctly align the mirrors within the time and equipment constraints of this task for this fiscal year. Therefore no measurements were made of the gap between the screen and accelerator grids when the ion engine was inside the vacuum tank. However, useful information of the displacement of a single grid

with the ion engine operating in the vacuum tank was obtained using this technique.

The ultimate resolution of this grid displacement measurement technique is limited in part by the distance between the imaging optics which form the images of the laser spot that is reflected from the grids and the grids themselves (see Fig. 1). This distance is called the "optical path". In order to maximize the resolution obtainable with the optical equipment available for these tests, a vacuum facility was prepared which minimizes this optical path. A schematic diagram of the test set-up is shown in Fig. 1.

A 30-cm diameter, divergent field ion engine was operated without beam extraction in this vacuum facility, using argon as the propellant. The ion engine grids were heated by the 700 watt discharge plasma and/or cathode radiation, and the grid displacement was measured using a technique described in Appendix D. Mirrors made from single crystal silicon wafers were glued to the screen and accelerator grids. A 300 mm camera lens was used as lens 1.

Laser light reflected from the screen grid was focussed onto the photo-detector such that the detector output indicated by a digital storage oscilloscope was at a maximum. Any movement of the screen grid results in a decrease in the photo-detector output, because the laser light is no longer focussed onto the detector. The laser light reflected from the screen grid mirror is re-focussed onto the detector by moving the pinhole/aperture assembly. The absolute movement of the screen grid was measured by adjusting the pinhole/aperture assembly with a micrometer stage and reading the amount of movement of the stage from the micrometer barrel.

The shape of the photodetector signal at peak maximum was somewhat irregular, as shown in Fig. 2. Uncertainty in the peak height, due to the irregular peak shape, was typically one to two percent of the signal amplitude. Since a decrease in peak amplitude of five percent was readily discernable over the uncertainty in peak amplitude due to irregular peak shape, uncertainty in grid movement was defined as the distance moved by the micrometer stage such that the peak height was reduced by five percent of the peak maximum.

The resolution of the technique, as implemented with available equipment, was determined by performing tests with the ion engine off. First, the laser light reflected from the screen grid mirror was focussed onto the photo-detector, and the peak amplitude of the signal was measured on the oscilloscope display. Next, the micrometer stage (Fig. 1) was adjusted (rotating the micrometer barrel clockwise) until the signal amplitude decreased by five percent of the peak amplitude, and the micrometer reading was

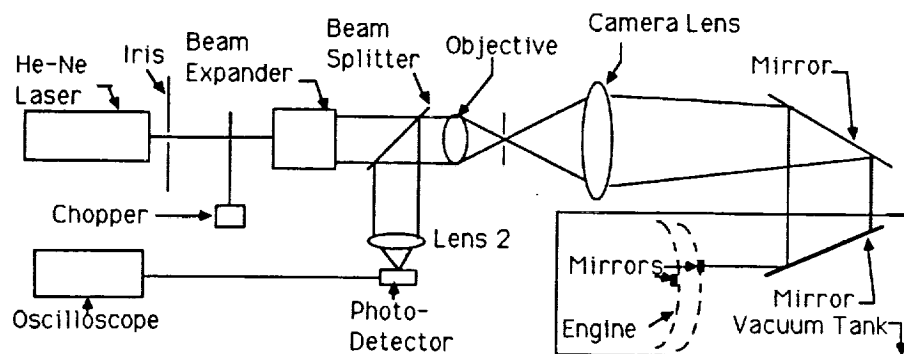


**Figure 1** Experimental set-up used to measure ion engine grid deflection in situ.

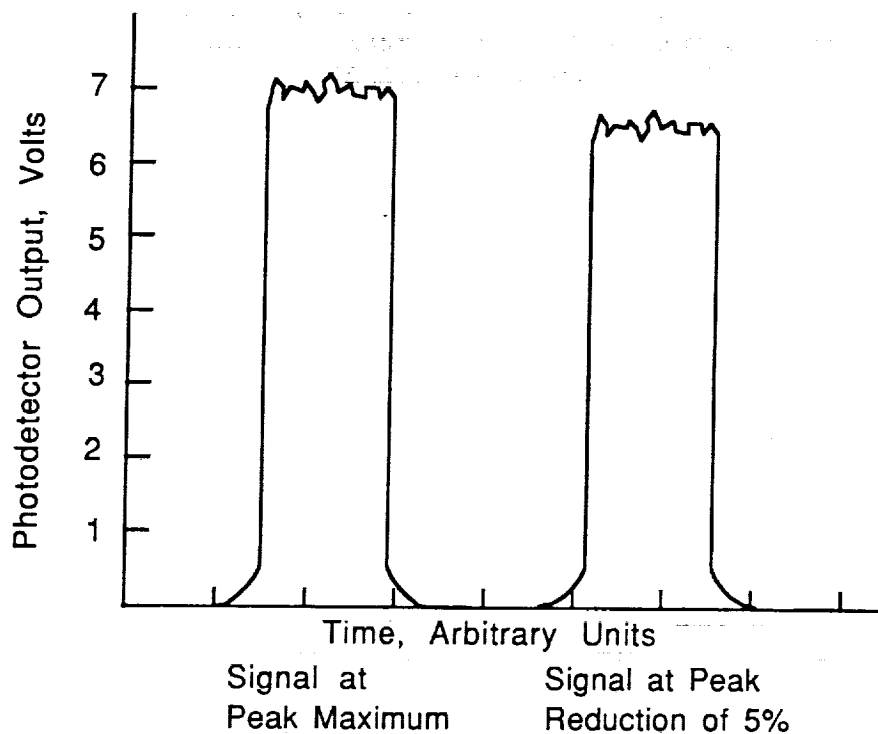


**Figure 2** Laser positioning technique data.

recorded. Finally, the micrometer stage was adjusted (rotating the barrel counter-clockwise) in the opposite direction until the signal amplitude had again decreased by five percent.

**Table 1** Resolution of the Laser Positioning Technique  
With Engine Discharge Off

Micrometer Position for 5 % Decrease in Detector Output, Clockwise Turn (mm)	Micrometer Position for 5 % Decrease in Detector Output, Counter-clockwise Turn (mm)
10.04	9.84
10.04	9.83
10.06	9.83
10.06	9.84
10.05	9.83
10.07	9.82
10.07	9.82
10.06	9.81
10.05	9.82
10.07	9.83
10.06	9.81
10.07	9.81
Average 10.05	Average 9.82

The above procedure was performed several times over a period of several days, again with the ion engine off. Typical values are shown in Table 1. For the data in this table the maximum signal amplitude was obtained at a micrometer position of 9.94 mm.

The resolution of this technique, when defined as the amount of micrometer movement to reduce the signal by five percent, was  $\pm 0.10$  to  $\pm 0.13$  mm. Normal grid separation would be expected to be approximately 0.51 mm. It was found that the resolution of the technique was not affected by vibrations from pumps, valves, and motors required to operate the laser imaging set-up or the vacuum system. Resolution could be improved by using better quality optics to increase the uniformity in the shape of the peak; specific hardware requirements are discussed in a later part of this report.

The next series of experiments were conducted with the cathode tip heater or discharge chamber plasma heating the ion engine grids, for the purpose of measuring both the resolution of the laser positioning technique and the absolute movement of the screen grid. The tip heater consisted of a coil of tantalum wire wrapped around the cathode. The cathode was heated to over 1100 degrees centigrade when a current of several amperes was conducted through the tip heater wire. The radiation from the cathode and tip heater assembly then heated the ion engine screen grid. Resolution and absolute grid movement were both determined using the same procedure described above. Results from these studies are summarized in Table 2. The data under the heading "% Decrease in Signal Amplitude" are discussed below.

**Table 2 Laser Positioning Technique Data**

Engine Status	Absolute Movement (mm)	Resolution (mm)	% Decrease in Signal Amplitude (over 60 s)
Engine Off	0	0.12	< 2.5
Tip Heater On	0.13	0.14	6.8
Discharge On at 25 A	1.23	0.14	12

The screen grid mirror moved 1.23 mm when the engine discharge plasma was turned on. It is not known if this reflects movement of the screen grid alone, or thermal expansion of the entire engine.

The amplitude of the detector signal was very stable when the ion engine was off. However, when the tip heater and/or engine plasma were turned on, the amplitude of the detector signal oscillated by the amount shown in Table 2 under the heading in the fourth column. The approximate period of the oscillation was 75 seconds. The reason for this oscillation is unknown, but it implies that the engine or grids oscillate in position when the engine or grids are heated. This phenomenon was observed when the grids were mounted in the open on an optics bench, but the oscillations were significantly smaller in magnitude. Oscillations in the accelerator system capacitance (with approximately the same time scale) were observed in bench tests using the technique described in Section 8.0 of this report.

The resolution can be increased by using optical components that are superior in quality to those used for these tests. Specific requirements are listed below:

1. Replace the laser used in these experiments.  
The laser used had a guaranteed signal output of  $\pm 5\%$ .  
The signal output of a superior laser would be better than  $\pm 1\%$ .
2. Replace the objective lens.  
The objective lens used in these experiments reflected some of the incident light, which was transmitted through the beam splitter and then focussed onto the photo-detector. Use of an objective lens with a non-reflective coating for the appropriate frequency laser would result in increased resolution.
3. Replace the camera lens (lens 1) with a single, high-quality lens.  
The camera lens employed actually consists of 6 separate lenses; this resulted in multiple spot images at the photo-detector.
4. Replace the optical table used in these tests with a high-quality optical table, to reduce vibration.
5. Replace the beam chopper.  
The home-made beam chopper used in these tests added a slight amount of oscillation to the amplitude of the signal collected at the photo-detector.

## 5.0 CHARGE EXCHANGE PLUME MODELING

As inert gas ion propulsion systems are maturing toward flight applications, integration issues are becoming increasingly important. These issues include: the effect of plasma produced by the ion propulsion system on spacecraft charging and solar array power drain; contamination of critical spacecraft surfaces due to the arrival of propellant atoms or other thruster produced particles; radiated and conducted electromagnetic interference; and direct ion beam impingement on spacecraft surfaces. The first two of these integration issues are either directly or indirectly a result of the ion engine produced charge exchange plasma.

### 5.1 Introduction

During normal ion engine operation a small fraction of the propellant atoms injected into the engine do not become ionized and escape through the accelerator system apertures as neutral atoms. A small fraction of the fast beam ions, which are accelerated through these same apertures, occasionally pass close enough to the relatively slow moving neutral atoms for charge exchange collisions to take place. The end products of these collisions are fast moving neutral atoms and relatively slow ions. Most charge exchange ions are produced in close proximity to the downstream surface of the engine. Electrons from the neutralizer cathode, along with the slow ions, form the charge exchange plasma.

In general, ions produced by the thruster may be conceptually divided into four groups:

1. High velocity beam ions.
2. Charge exchange ions which are formed between the screen and accelerator grids and subsequently escape in straight line paths with angles up to 90 degrees from the thruster axis.
3. Charge exchange ions which are formed just downstream of the accelerator grid. These ions are accelerated back to the accelerator grid and sputter off grid material.
4. Charge exchange ions which are created farther downstream of the accelerator grid and subsequently propagate radially from the ion beam.

The group 4 ions have energies significantly less than both the local electron temperature and the local potential differences in the plasma. Consequently these ions are not limited to line-of-sight trajectories. It is this group of ions, therefore, which may potentially have the greatest interaction with the spacecraft. The purpose of this study is to develop a first order modeling

capability to describe the behavior of these ions.

A considerable number of investigations have been performed on spacecraft charging/contamination and on the nature of the charge exchange plasma. The majority of this work was performed in the middle to late 1970's using mercury propellant (see, for example, Refs. 1-7). In general, the present modeling capability results in predicted values of charge-exchange ion number densities which are in agreement with experimental data to only within an order of magnitude. This is a result of the relatively simple models employed and the difficulty of making accurate experimental measurements due to vacuum facility effects. Recent studies on spacecraft contamination induced by xenon ion thrusters, however, concluded that ion thrusters probably do not pose a significant contamination problem for the ETS-VI spacecraft.<sup>8,9</sup>

Nevertheless, ion engine induced contamination issues are still of major importance for the integration of ion propulsion systems with other commercial and government spacecraft. The objective of the work described herein was to first resurrect the charge exchange plasma propagation code (PLASIM) developed for mercury ion thrusters at Colorado State University (CSU), and subsequently to modify this code as required for xenon propellant. Finally, experiments to test the validity of the computer predictions were to be identified.

## 5.2 PLASIM Computer Code

The PLASIM code developed by CSU simulates the propagation of mercury charge-exchange ions emanating from the exhaust beam of a mercury ion thruster.<sup>1</sup> The trajectories of individual ions are simulated to determine the overall charge exchange plasma propagation characteristics. The model consists of two parts: a simple one-dimensional model for the generation of the charge-exchange ions, and a model which subsequently calculates the trajectories of these ions. The ion generation portion is used as a line source of charge-exchange ions for the trajectory portion. The PLASIM program considers only ions which initially propagate radially from the ion beam, i.e., the group 4 ions described above.

The model for the charge-exchange ion generation within the ion beam is used to establish the initial distribution of the ion paths along the beam (axial direction), as well as the magnitude of the charge-exchange ion densities. This model (from Ref. 1) is briefly reviewed here, and a detailed description of the model is presented in Appendix E. The beam is divided into  $2N$  number of regions for  $N$  ion trajectories (one region on each side of the ion path) as illustrated in Fig. 3. The distribution of the trajectories is established such that an equal number of charge-exchange ions are created within each region. The generation rate for the charge-exchange ions is given by

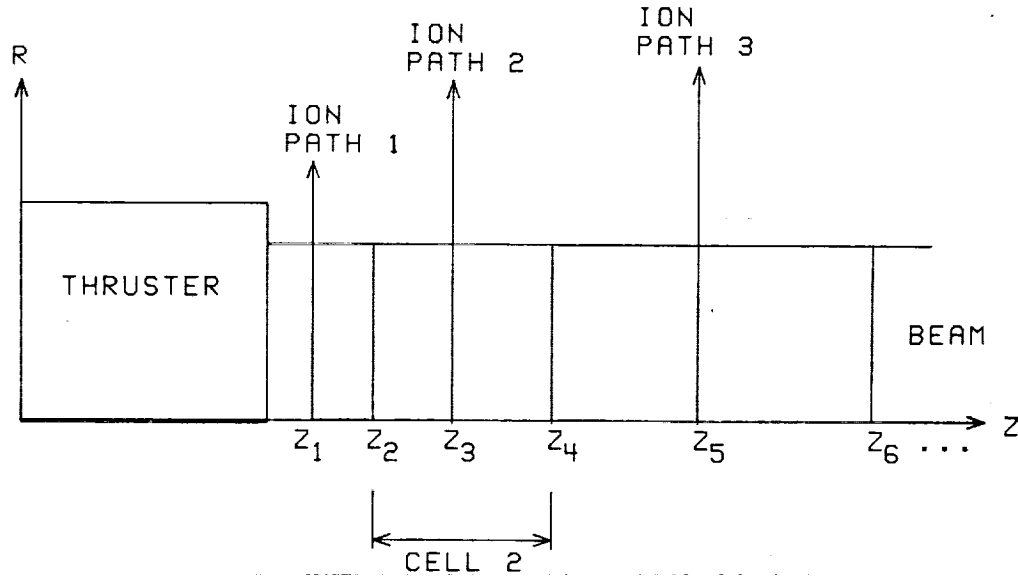


**Figure 3** Model geometry for the calculation of charge exchange ion trajectories.

$$\dot{n}_{CE} = n_0 n_i v_i \sigma_{CE} . \quad (1)$$

Since the neutral number density will decrease with increasing distance from the thruster, the ion trajectories are more closely spaced near the thruster. The neutral number density distribution is given by

$$n_0 = \frac{n_{ref}}{2} \left( 1 - \frac{z}{\sqrt{z^2 + r_b^2}} \right) . \quad (2)$$

The ion current density is assumed to be constant and concentrated on the z-axis. This assumption allows for a closed form solution of the charge-exchange ion generation rate.<sup>1</sup> The ion current density is given by

$$J_b = \pi r_b^2 e n_i v_i , \quad (3)$$

The total number of charge-exchange ions created is determined by integrating the local generation rate, Eq. (1), over the axial range yielding

$$\dot{N}_{CE} = \pi r_b^2 \int_0^\infty n_{CE} dz . \quad (4)$$

The local number density of the charge-exchange ions is calculated as discussed in Appendix F, resulting in the following equation,

$$n_{CE} = \frac{\dot{N}_{CE}}{N} \frac{1}{2\pi X \Delta d_m v_{CE}} = \frac{C}{\sqrt{T_e} X \Delta d_m} , \quad (5)$$

where

$$C = \frac{J_b^2 (1-\eta_u) \sigma_{CE} m_o}{\pi^2 e^2 r_b \eta_u N \sqrt{T_o}} . \quad (6)$$

The paths of the charge-exchange ions are determined by calculating the position of each ion through a series of iterations. At each location a series of calculations are performed to determine the local forces on the ion and its velocity components. The velocity components and the iteration time-step are used to determine the new position of each ion.

The ions are assumed to obey the "barometric equation" relating the number density and electric potential

$$n_e = n_{e,ref} \exp\left(\frac{-eV}{kT_e}\right) . \quad (7)$$

At each location, the potential on the left and the right is calculated from the number density on each side of the ion path. Once the left and right potentials are known, the perpendicular force (with respect to the ion trajectory) on the ion is calculated using

$$F_\perp = \frac{-e \Delta v_\perp}{\Delta d_s} , \quad (8)$$

where  $d_s$  is the smaller of the left and right spacing. (Note: It is reported that this technique is used to help eliminate instabilities at the boundaries and has a negligible effect compared to averaging the left and right spacing.<sup>1)</sup> The parallel force is calculated using

$$F_\parallel = \frac{-e \Delta v_\parallel}{\Delta d_p} , \quad (9)$$

where  $d_p$  is the distance to the previous point. The parallel and

perpendicular velocities are then calculated using

$$\Delta v_{\perp,i} = \frac{F_{\perp,i} \Delta t}{m_o} . \quad (10)$$

The velocities are converted from parallel and perpendicular coordinates to x-z coordinates and then the new position of each ion is determined using

$$x_{new} = x_{old} + v_x \Delta t , \quad (11)$$

and

$$z_{new} = z_{old} + v_z \Delta t . \quad (12)$$

This process is then repeated until either a boundary is reached or the maximum number of iterations (as specified by the operator) is reached. A detailed description of the handling of special conditions and boundaries is provided in Ref. 1.

Typical results are shown in Figs. 4 and 5. Figure 4 shows the charge-exchange ion trajectories and Fig. 5 shows the normalized ion number density contours. The number density values are calculated by the model only along the ion trajectories. The values between the trajectories are calculated by interpolation. The first and last trajectories mark the end points of the density calculations, that is, no extrapolation has been made for densities beyond the simulation region.

**5.2.1 Normalized Number Density Profiles:** It was determined that the charge-exchange ion number density values could be normalized for the PLASIM model. This normalization is suggested from the theory and is discussed in detail in Appendix F. It should be noted that this feature of the model was not discussed in the previous publications.<sup>1,2</sup> The number density values are normalized as follows

$$n_{norm} = \frac{n_{CE} \sqrt{T_e}}{C} , \quad (13)$$

where  $C$  is given in Eq. (6). The variables in this constant include the thruster operating parameters, the beam radius, and the propellant properties. All of the model variables are included in the normalization constant except for the beam electron temperature,  $T_e$ , and the geometry of the thruster and the modeling region. These latter variables can have a significant effect on the ion trajectories and therefore on the shape of the number density contours.

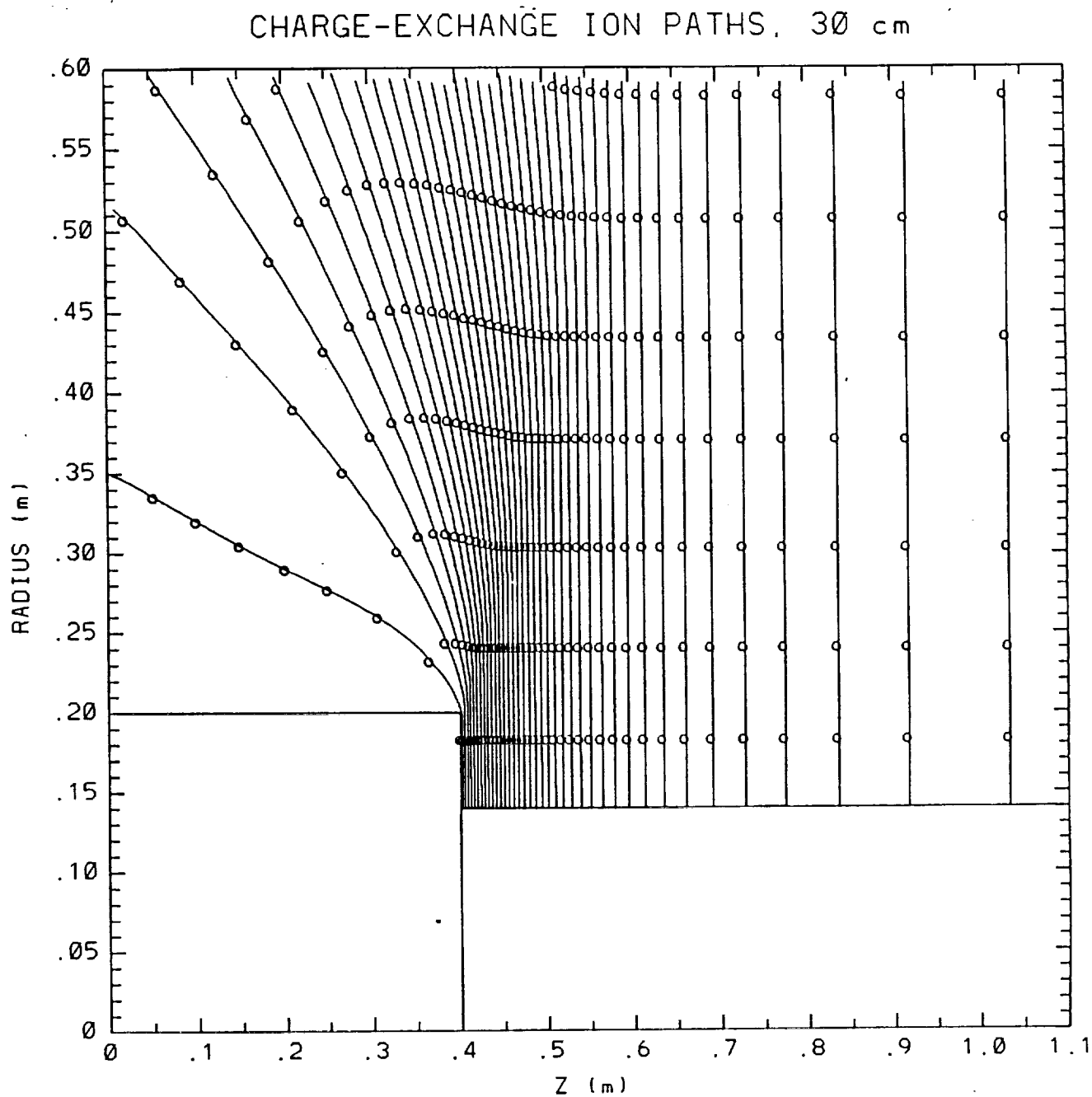


**Figure 4** Example of calculated charge exchange ion trajectories for a 30-cm dia. xenon ion thruster.

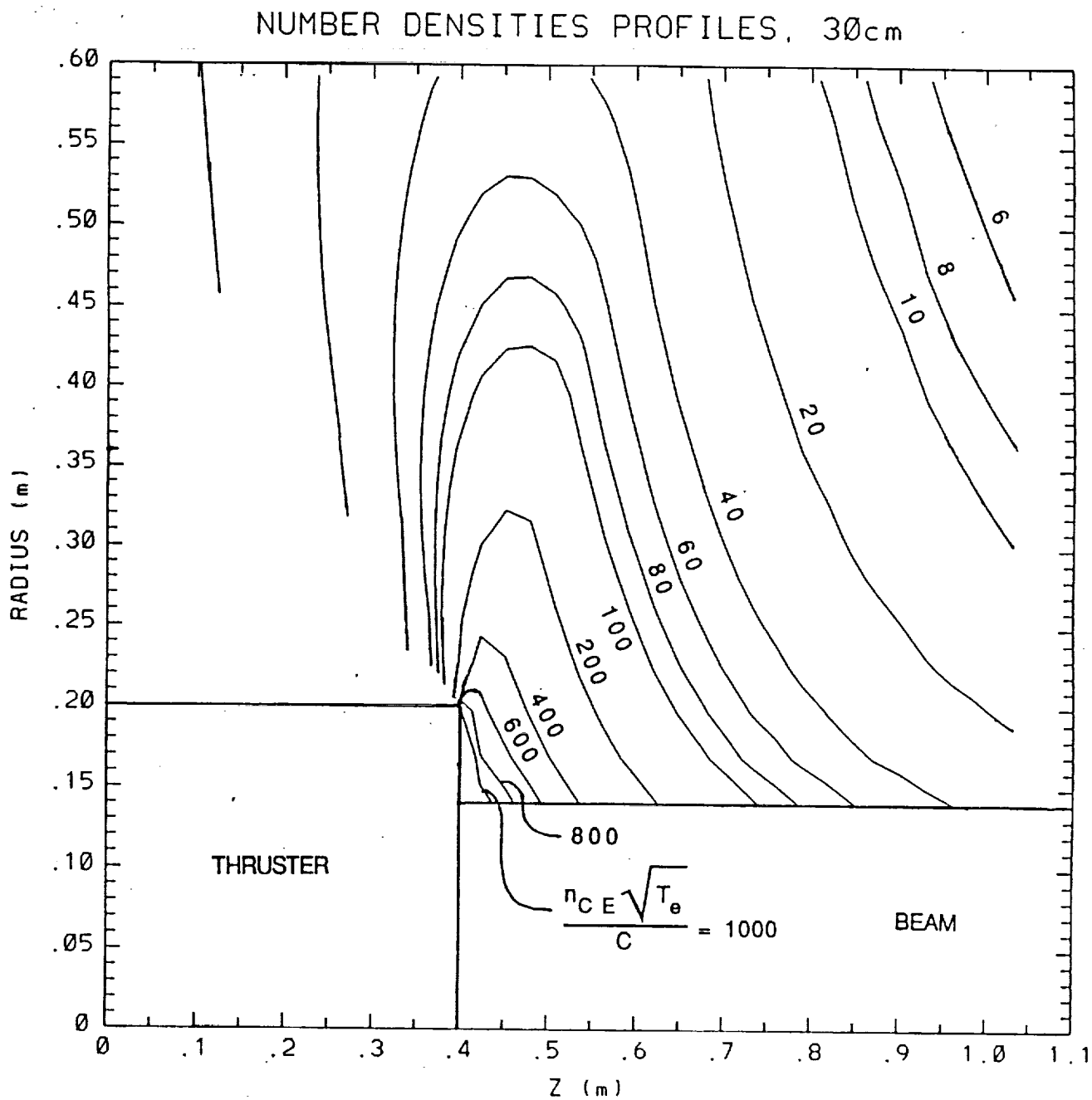


**Figure 5** Example of calculated charge exchange ion number density contours for the ion trajectories given in Fig. 4.

The normalization technique was tested by comparing the normalized density profiles for cases with different input variables. Each variable in the normalization constant was tested by changing its value over a range varying from a factor of two for some variables, to two orders of magnitude for others. All of the resulting ion trajectories and density profiles appeared to be the same. Changing the number of ion paths,  $N$ , changes the ion paths slightly, primarily in the upstream region, as can be seen by comparing Figs. 4 and 6. The number density profiles are, however, very similar as seen by comparing Figs. 5 and 7. The difference in the normalization values in Figs. 5 and 7 is a result of the difference in the number of ion paths used (Fig. 5,  $N=40$  and Fig. 7,  $N=20$ ). However, the values of the number density on the same contour in each figure will be the same for similar input parameters.

The effect that a factor of 4 increase in the beam electron temperature,  $T_e$ , has on the results can be seen in Figs. 8 and 9. A small effect can be seen on the first few ion trajectories (paths near the thruster), by comparing the trajectories in Figs. 4 and 8. Since the effect is small and confined to the upstream region, the same normalized curves can be used for changes in  $T_e$  less than about a factor of 4 or 5. However, the values in the upstream region will be less accurate. If this is the region of interest, then new results should be calculated using the temperature of interest. In the previous cases, Figs. 4 through 7,  $T_e$  equal to 0.35 eV was used.

The effects of changes in the input variables on the number density can quickly be determined using the normalized contours. For example, if the beam current is doubled the magnitude of the number densities will increase by a factor of four, but the contour profile shapes will be unchanged.

**5.2.2 Comparison of Mercury and Xenon:** Since the majority of the published work on ion engine charge-exchange plasmas and on ion engine plume contamination is for mercury propellant, it is desirable to compare the charge-exchange ion trajectories and number density profiles for xenon with a similar computation for mercury. A comparison of the relevant properties of mercury and xenon is shown in Table 3, and the charge-exchange collision cross sections for mercury and xenon as a function of ion energy are determined from Ref. 10. Since xenon has a much lower boiling temperature than mercury, it is expected that xenon condensation on the spacecraft would be less of a problem.

In addition to the PLASIM model developed by CSU and modified herein, two other related models were developed. A spherical propagation model was developed to determine the number densities of both propellant and molybdenum charge exchange ions at distances beyond the capabilities of the PLASIM model, and a first order model for the accelerator grid erosion was developed to provide a

source of metal neutral atoms required as input to the model for spherical propagation of metal charge-exchange ions. These models are described below.

**TABLE 3 Propellant Property Data**

Property	Mercury	Xenon
Molecular Weight (AMU)	200.59	131.3
Atomic Mass (kg)	$3.33 \times 10^{-25}$	$2.18 \times 10^{-25}$
Boiling Temperature (K)	630	165

### 5.3 Spherical Propagation Model

The spherical propagation model estimates the charge-exchange ion number densities at greater distances from the thruster than the PLASIM model. The PLASIM model has a limited geometric range because of its iterative solution technique. The spherical model is capable of a much larger scale but is less accurate; therefore for regions near the thruster the PLASIM model should be used. The spherical model assumes that all of the charge-exchange ions originate at a point source located one beam radius downstream of the thruster as opposed to the line source used for the PLASIM model. For the line source, 56 percent of the charge exchange ions are created within one beam radius of the thruster and 76 percent are created within two beam radii. Therefore, at distances that are large compared to the thruster size, the assumption that the charge-exchange ions originate at a point is reasonable.

The charge-exchange ion production portion of the spherical propagation model is similar to that for the PLASIM model. The total number of charge-exchange ions created is determined by integrating the local generation rate over the appropriate axial range resulting in Eq. (F12) in Appendix F. The charge-exchange ions are assumed to propagate spherically from the point source given in Eq. (F12) which is assumed to be located one beam radius downstream from the thruster. The charge-exchange ion number density is given by

$$n_{CE} = \frac{\dot{N}_{CE}}{4\pi R_s^2 v_{CE}} \quad (14)$$

where

$$v_{CE} = \sqrt{\frac{kT_e}{m_i}} \quad (15)$$

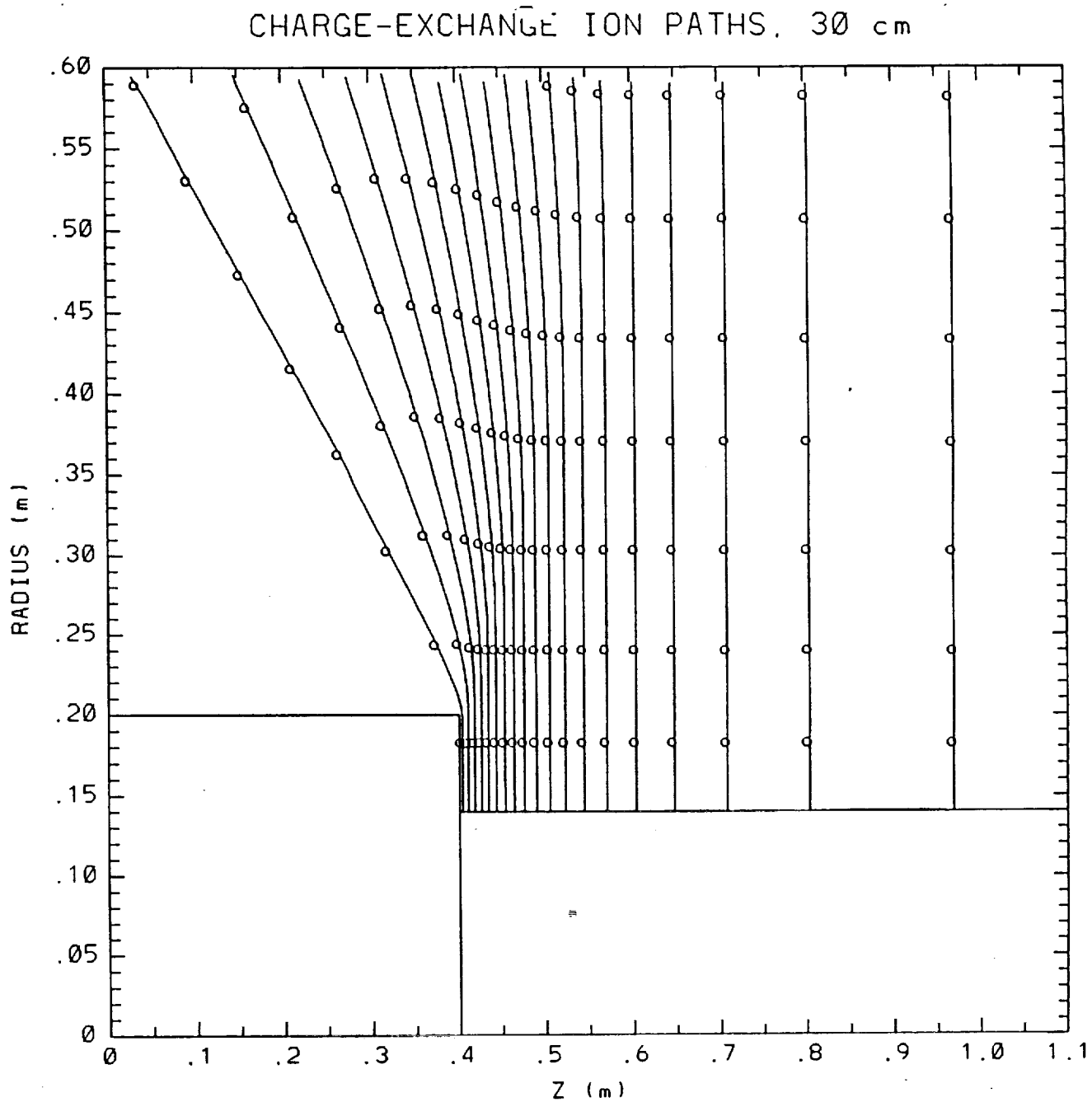


**Figure 6** Charge exchange ion trajectories calculated using twice the number of ion paths as in Fig. 4.

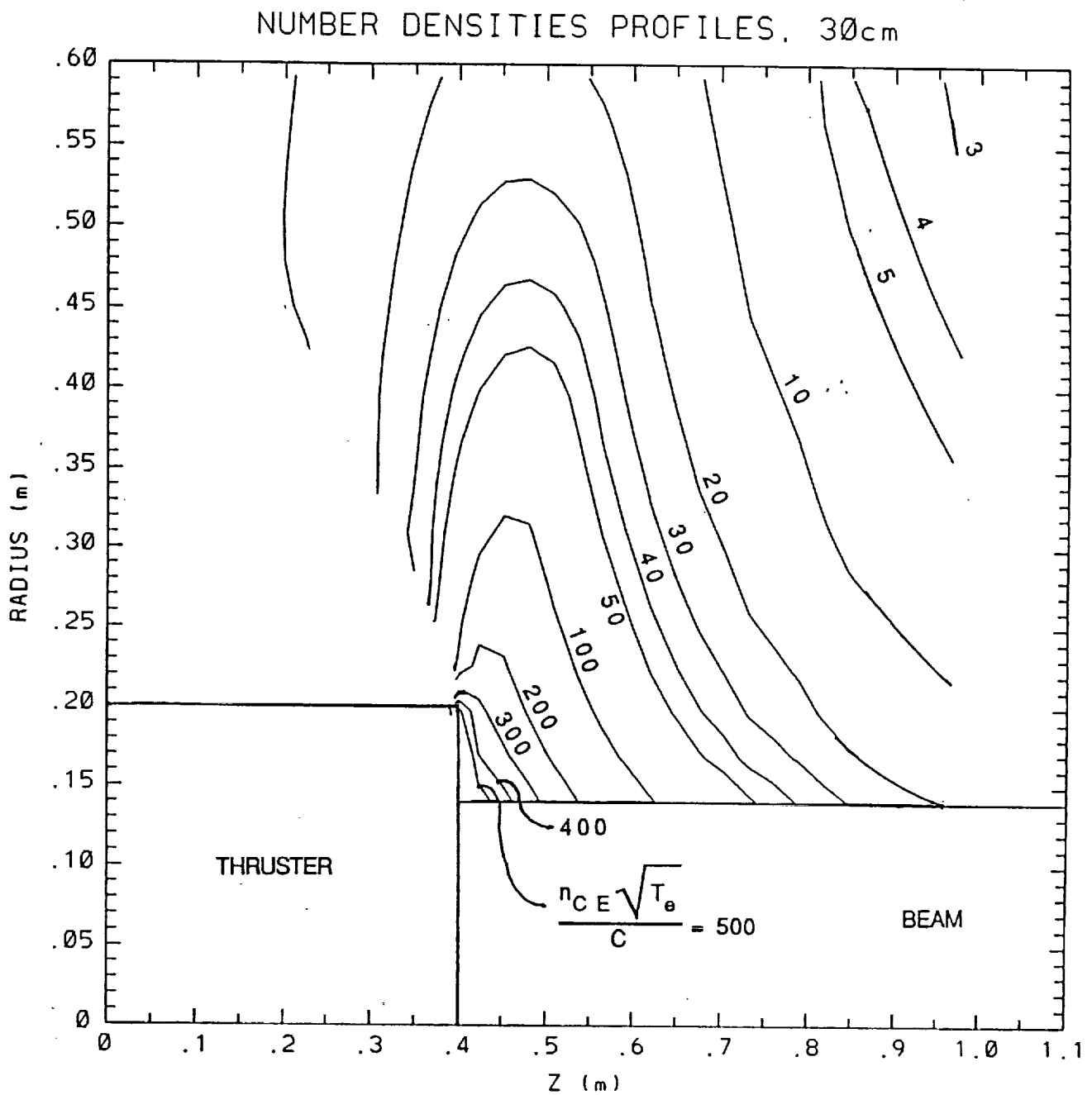


**Figure 7** Charge exchange ion number density contours corresponding to the ion trajectories in Fig. 6.

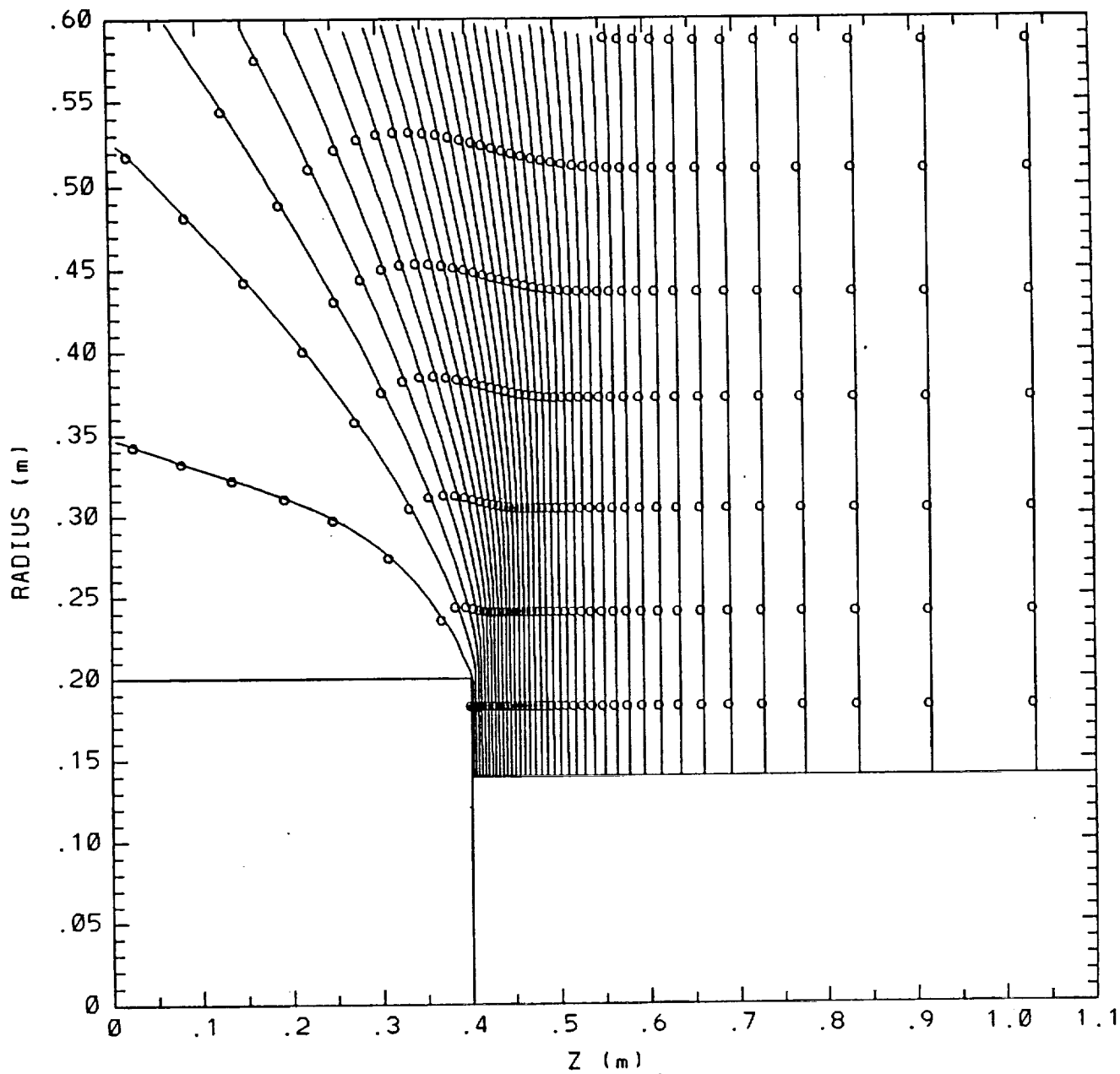


**Figure 8** Charge exchange ion trajectories calculated using an electron temperature which is 4 times that in Fig. 4.

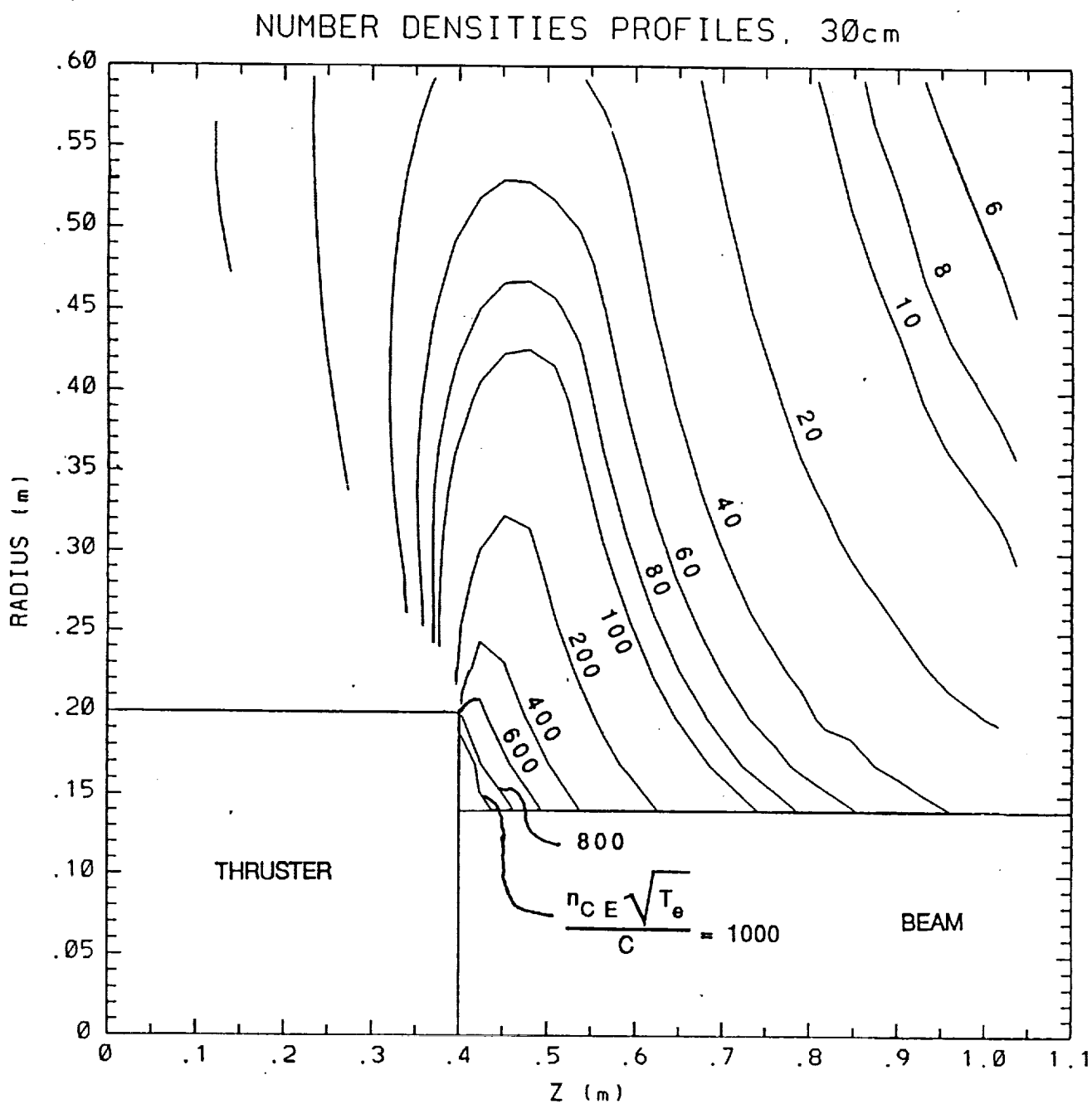


**Figure 9** Charge exchange ion number density contours corresponding to the ion trajectories in Fig. 8.

is the Bohm velocity for the ions. Substituting Eq. (F12) into Eq. (14) yields

$$n_{CE} = \frac{J_b^2 (1 - \eta_u) \sigma_{CE} m_o}{4\pi e^2 \sqrt{2\pi} r_b \eta_u \sqrt{kT_o} \sqrt{kT_e} R_s^2} \frac{1}{R_s^2} \quad (16)$$

Substituting appropriate values for the constants yields

$$n_{CE} = 1.28 \times 10^{28} \frac{J_b^2 (1 - \eta_u) m_o}{r_b \eta_u \sqrt{T_o' T_e'} R_s^2} \quad (17)$$

where  $T_o'$  and  $T_e'$  are in eV.

The ion densities within an angle of 90 degrees from the beam axis are calculated using the isotropic model given in Eq. (17). For angles between 90 and 180 degrees the angular dependence is included.<sup>2,3,8</sup> The ions close to the thruster leave with velocities normal to the beam. Since the equipotentials are also approximately normal to the beam, the ions are deflected upstream of the thruster by the electric field. The minimum ion velocity is used for the initial ion velocity in the 90 degree direction. This velocity is equivalent to the accelerating potential,  $kT_e/2e$ . The potential difference antiparallel to the beam direction is  $V$ . The ratio between the 90 and 180 degree velocity components is

$$\frac{v_{180}^2}{v_{90}^2} = \frac{2e\Delta V}{kT_e} = \cot^2(\theta) \quad (18)$$

The barometric equation may be written as

$$\frac{n_{CE}}{n_{CE,90}} = \exp\left(\frac{-e\Delta V}{kT_{e,p}}\right) \quad (19)$$

The charge-exchange plasma electron temperature is assumed to be half of the beam electron temperature ( $T_{e,p} = T_e / 2$ ).<sup>2,3</sup> Substituting into Eq. (19) yields

$$\frac{n_{CE}}{n_{CE,90}} = \exp[-\cot^2(\theta)] \quad (20)$$

For angles greater than 90 degrees the local ion number density is determined by multiplying Eq. (19) by Eq. (20). Kaufman reports a good comparison between this model and the experimental data.<sup>2</sup> The experimental data and the model results typically agree to within a factor of two or three.

The charge-exchange ion number density values can be normalized in a manner that is similar to that for the PLASIM model; however, the normalization constant is different as a result of the different geometry. The number density values are normalized as follows:

$$n_{CE, norm} = \frac{n_{CE} R_s^2}{C_1}, \quad (21)$$

where

$$C_1 = 1.28 \times 10^{28} \frac{J_b^2 (1 - \eta_u) \sigma_{CE} m_o}{r_b \eta_u \sqrt{T_o T_e}}. \quad (22)$$

The variables in the constant  $C_1$  include the thruster operating parameters, the beam radius, and the propellant properties. All of the model variables are included in the normalization. The effects of changes in the input variables on the number density can quickly be determined using the normalized contours. For example, if the beam current is doubled the magnitude of the number density will increase by a factor of four, but the contour profiles will be unchanged.

Typical results are shown in Figs. 10 and 11. Figure 10 shows a set of small scale normalized charge-exchange ion density contours and Fig. 11 shows a set of large scale density contours. The region near the thruster where the PLASIM model is applicable is shown by the dashed line. The value of the number density may be quickly calculated using this model. For example using the model variables from Table 4 the constant,  $C_1$ , is equal to  $6.658 \times 10^{12}$ . For a normalized constant value,  $n_{CE, NORM}$ , of 0.20 (radius of 2.236 m) the number density is  $1.332 \times 10^{12} \text{ m}^{-3}$ .

#### 5.4 Metal Charge-Exchange Ion Model

The data from the SERT II test revealed that the spacecraft contamination was primarily due to molybdenum originating from the thruster and that the contamination from the mercury propellant was negligible.<sup>6</sup> Even though the molybdenum contamination was confined to line-of-sight trajectories, it is desirable to have a simple model for quickly estimating the metal charge-exchange ion number densities at various distances from the thruster (including non-line-of-sight locations) in order to estimate potential contamination levels at different points on the spacecraft.

The metal charge-exchange ions are formed when sputtered metal atoms from the accelerator grid interact with the high energy propellant ions. The sputtered atoms are a result of propellant charge-exchange ions that form near the grids impacting with the accelerator grid. The metal charge-exchange ions then propagate

away from the thruster. The model is considered in two parts: a grid erosion model, and a spherical ion propagation model.

**Table 4** Example Values for Model Input Variables

Parameter	Symbol	Value
Grid open area fraction	$F_a$	0.23
Beam current (A)	$J_b$	2.0
Clausing factor	$K_c$	0.7545
Grid separation (mm)	$L_g$	0.6
Propellant atomic mass (AMU)	$M_o$	131.3
Grid material atomic mass (AMU)	$M_{o,m}$	95.94
Beam radius (m)	$r_b$	0.14
Sputter yield (atoms/ion)	$S$	0.80
Electron temperature (eV)	$T_e'$	1.0
Electron temperature in charge-exchange plasma (eV)	$T_{e,p}'$	0.5
Propellant atom temperature (eV)	$T_o'$	0.058
Metal atom temperature (eV)	$T_{o,m}'$	0.058
Net accelerating voltage (V)	$V_n$	1100
Total voltage (V)	$V_t$	1400
Propellant utilization	$\eta_u$	0.90
Propellant charge exchange collision cross section ( $m^2$ )	$\sigma_{CE}$	$3.0 \times 10^{-19}$
Metal charge exchange collision cross section ( $m^2$ )	$\sigma_{CE,m}$	$6.0 \times 10^{-20}$

**5.4.1 Accelerator Grid Erosion Model:** Some of the propellant charge-exchange ions are accelerated into the accelerator grid because it is at a lower potential than the charge-exchange plasma. The ions will acquire an energy approximately equal to the accelerator potential (typically 300 volts). When these high energy ions strike the grid, they sputter off neutral metal atoms. The flux rate of ions to the grid is the accelerator grid current,  $J_a$ . The sputter rate is given by

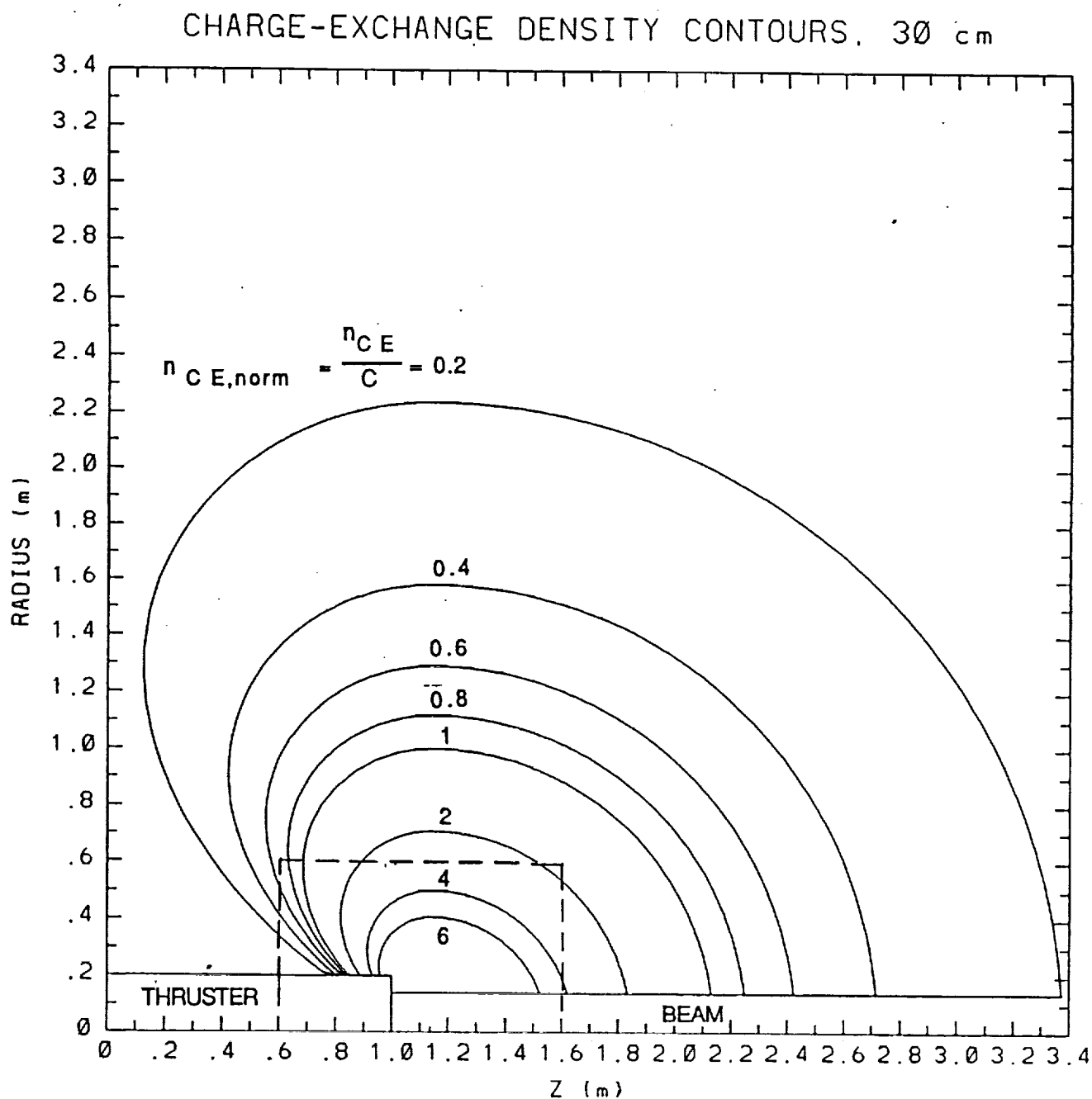


**Figure 10** Small scale normalized density contours for the spherical propagation model. Dashed box indicates the region of applicability of the PLASIM model.

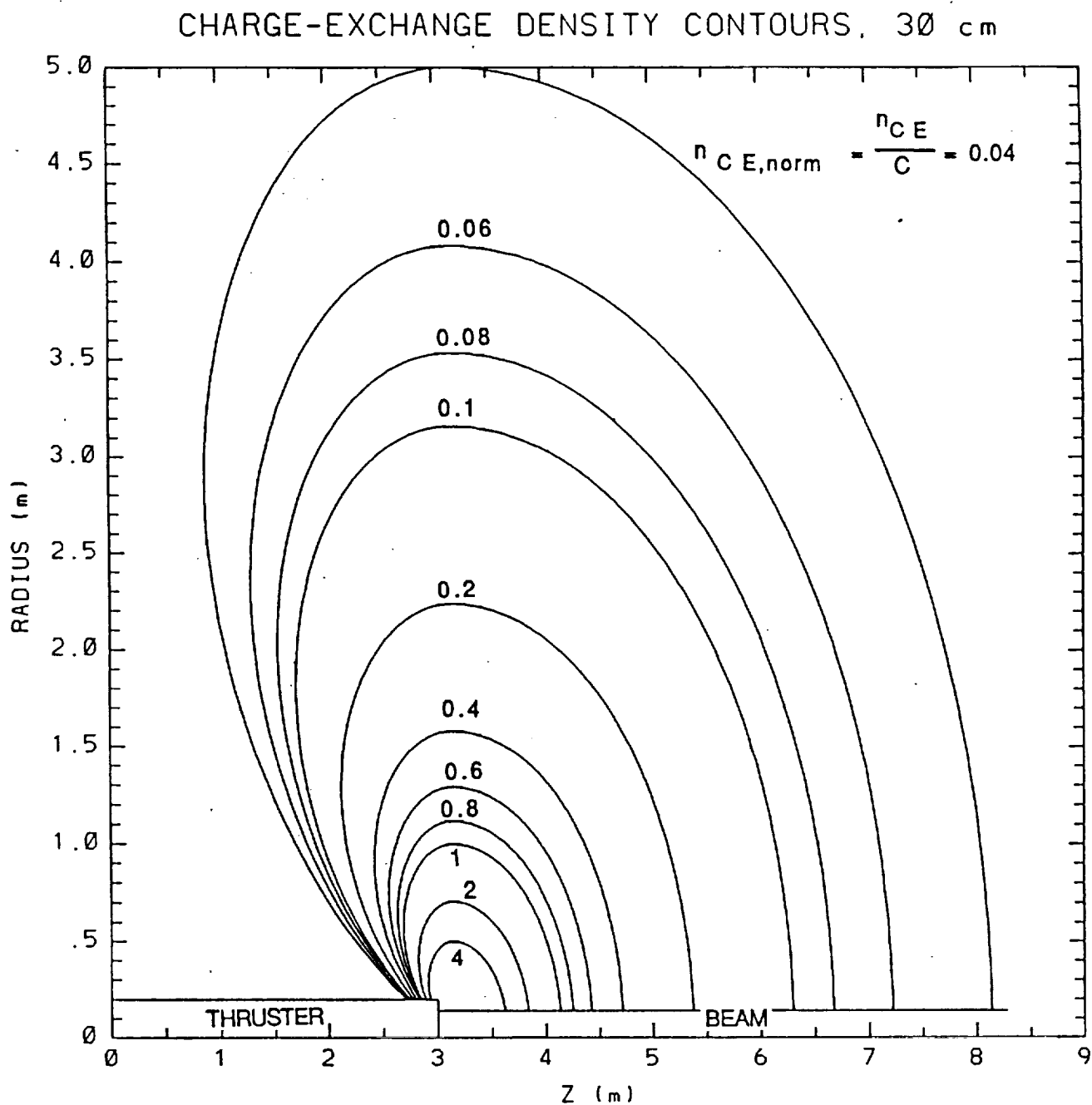


**Figure 11** Large scale normalized density contours for the spherical propagation model.

$$\dot{N}_{o,m} = \frac{J_a S}{e} \quad (23)$$

For xenon ions sputtering molybdenum, the sputter yield ranges from 0.72 to 0.87 for 500 eV ions and increases to 1.60 for 1 keV ions.<sup>11</sup> A value of 0.80 is used here. The accelerator current is given by

$$J_a = \sigma_{CE} n_o J_b L, \quad (24)$$

where  $L$  is the effective length from the grid that contains the charge-exchange ions that may reach it. Equation (24) may also be written as

$$J_a = n_{CE} e L, \quad (25)$$

where  $n_{CE}$  is the local charge-exchange ion production given by Eq. (F11) of Appendix F with  $z=0$  (location at the thruster). Equation (F11) may be written for this case as

$$n_{CE} = \frac{2J_b^2 (1 - \eta_u) \sigma_{CE}}{e^2 \bar{V}_o \eta_u A_b}, \quad (26)$$

where

$$A_b = \pi r_b^2 F_a K_C. \quad (27)$$

Note that in the PLASIM model the neutral flow area was not corrected for the grid open area fraction or the Clausing factor. Substituting Eqs. (26) and (27) into Eq. (25) yields

$$J_a = \frac{4J_b^2 (1 - \eta_u) \sigma_{CE} L}{\pi e \eta_u \bar{V}_o r_b^2 F_a K_C}, \quad (28)$$

and substituting for the constant values yields

$$J_a = 2.53 \times 10^{14} \frac{J_b^2 (1 - \eta_u) \sigma_{CE} L}{\eta_u r_b^2} \sqrt{\frac{m_o}{T_o}}. \quad (29)$$

The effective length,  $L$ , is given by

$$L = L_a + L_d + N_{LD} L_D, \quad (30)$$

where the first term is the effective ion acceleration distance for the accelerator system, the second term is the deceleration distance downstream of the thruster, and the third term is an effective length for the ion source determined by the upstream end of the ion beam plasma. At this location the electric field established by the accelerator grid negative potential falls off

exponentially into the plasma. This form of the third term was suggested by Kaufman<sup>8</sup> to account for ions that reach the grid due to this effect. Kaufman suggests using a thickness of Debye lengths, that is,  $N_{LD} = 5$ . The Debye length is given by

$$L_d = \sqrt{\frac{e_o k T_e}{e^2 n_e}} = 6.21 \times 10^{-4} \sqrt{\frac{T_e'}{J_b} \left(\frac{V_n}{m_i}\right)^{1/4}} r_b . \quad (31)$$

The physical grid separation is frequently used for the effective acceleration distance,  $L_a$ . The deceleration distance,  $L_d$ , is calculated using the following equation<sup>12,13</sup>

$$L_d^2 = (1 + 3\phi^{1/2} - 4\phi^{3/2}) \frac{j_{CH} A_e}{J_b} , \quad (32)$$

where

$$A_e = \pi r_b^2 F_a , \quad (33)$$

and  $j_{CH}$  is the Child current between parallel plates which is given by

$$j_{CH} = \frac{4e_o}{9} \sqrt{\frac{2e}{m_i} \frac{V_t^{3/2}}{L_g^2}} . \quad (34)$$

Substituting for the Child current and the constant values yields

$$L_d^2 = 1.72 \times 10^{-7} \frac{V_t^{3/2} r_b^2}{\sqrt{m_i} J_b} (1 + 3\phi^{1/2} - 4\phi^{3/2}) . \quad (35)$$

All of the parameters for calculating the accelerator grid current from Eq. (24) are now known, and the sputter rate can be calculated using Eq. (23). Using Eq. (23) along with the mass of the metal atoms, the wear rate of the grid can be calculated from

$$\dot{m}_m = \dot{N}_{o,m} m_{o,m} = \frac{J_a S m_{o,m}}{e} . \quad (36)$$

The wear rate can be used to estimate the material loss from the grid over time. This rate provides the average loss over the grid only, and cannot provide local wear rates.

**5.4.2 Metal Charge-Exchange Spherical Propagation Model:** The spherical model previously discussed may also be used for the metal charge-exchange ions. The grid erosion model provides an estimate of the erosion rate of the metal and therefore is used as a source of neutral species for the charge-exchange model. The metal neutral atoms are modeled the same way the propellant neutral atoms

were, and are considered as a Boltzmann gas with a temperature equal to the accelerator grid temperature. The flux of the neutral metal atoms is given by

$$\dot{N}_{o,m} = \frac{1}{4} n_{o,m} v_o A_g , \quad (37)$$

where  $A_g$  is the grid area,

$$A_g = \pi r_b^2 (1 - F_a) . \quad (38)$$

Note that since the metal neutrals originate from the grid material, the fraction of grid area  $(1-F_a)$  is used. For comparison purposes the same density distribution of the propellant neutrals is used for the metal neutrals, namely,

$$n_{o,m} = \frac{n_{o,m}}{2} \left( 1 - \frac{z}{\sqrt{r_b^2 + z^2}} \right) . \quad (39)$$

It may be recalled that the total production rate of the charge-exchange ions is calculated by integrating the local production rate as follows:

$$\dot{N}_{CE,m} = \int_0^\infty \dot{n}_{CE}(z) dz = \frac{J_b \sigma_{CE,m} n_{o,m} r_b}{2e} . \quad (40)$$

Substituting Eqs. (23), (38) and (39) into Eq. (40) yields

$$\dot{N}_{CE,m} = \frac{2 J_a J_b S \sigma_{CE,m}}{\pi e^2 r_b v_{o,m} (1 - F_a)} . \quad (41)$$

For the spherical propagation, the number density is calculated using Eq. (14). Substituting for the constant values and using Eq. (29) for  $J_a$  yields

$$n_{CE,m} = 3.25 \times 10^{33} \frac{J_b^2 (1 - \eta_u) \sigma_{CE} \sigma_{CE,m}}{\eta_u r_b^3 (1 - F_a) F_a K_C} \sqrt{\frac{m_o}{T_o'}} \frac{m_{o,m}}{\sqrt{T_{o,m}' T_e'}} (L_g + L_d + N_{LD} L_D) \quad (42)$$

The density of the metal charge-exchange ions depends upon both the propellant and the metal properties since the propellant charge-exchange ions produce the metal neutral atoms. The metal charge-exchange ion number density can be normalized like the propellant charge-exchange ions as shown in Eq. (21). The contour profiles will be the same for both ion types, since they are both assumed to propagate spherically from a point located one beam radius downstream of the thruster.

**5.4.3 Calculation Example:** Using the values for the model variables presented in Table 4 the following values were calculated

at a radius of 2.236 m from the thruster and  $\theta < 90$  degrees  
( $n_{CE, norm} = 0.20$ ):

$$\begin{aligned}n_{CE} &= 1.332 \times 10^{12} \text{ m}^{-3} \\n_{CE, m} &= 1.772 \times 10^9 \text{ m}^{-3} \\J_a &= 1.558 \text{ mA} \\\text{wear rate} &= 4.463 \text{ mg/hr} \\n_{CE} / n_{CE, m} &= 752\end{aligned}$$

At  $\theta = 120$  degrees

$$\begin{aligned}n_{CE} &= 9.544 \times 10^{11} \text{ m}^{-3} \\n_{CE, m} &= 1.270 \times 10^9 \text{ m}^{-3}\end{aligned}$$

Although the metal charge-exchange ion number density is a factor of 752 lower than the propellant ion number density, the metal ions are more likely to condense on the spacecraft due to their much higher melting point. The metal ions are therefore more likely to be a contamination problem.

### 5.5 Future Recommendations

An experimental investigation of the behavior of mercury charge-exchange ions was performed by Carruth and Brady (Ref. 5, pp. 67-72). This study consisted of using long cylindrical Langmuir probes to determine the local charge-exchange ion number density, flow angle and velocity/energy. An end effect associated with long Langmuir probes enhances the ion current when the probe is aligned with the ion flow direction. Therefore, by rotating the probe, the flow direction can be determined by locating the maximum current. For regions upstream of the thruster exit, the plot of ion current verses probe angle shows a distinct peak. For regions downstream of the exit the peak is not as distinct due to the presence of ions that exit the thruster at "large" angles.

Facility effects have a significant effect on the accuracy of the experimental data. Charge-exchange ions may be produced when neutrals sputtered from the frozen mercury target enter the beam. These ions were observed to flow from the target direction by Carruth and Brady. This effect was investigated by tilting the target to different angles during the testing. The facility ions did not affect the charge-exchange ion flow directions but did have an effect on the number density. Due to the large fraction of facility ions, number density and velocity measurements were made in the upstream region only. A discussion of both modeling and experimental work for estimating the nature of the facility-produced ions is provided in Ref. 5. The types of experiments performed by Carruth and Brady appear to be a reasonable first step to experimentally investigate the behavior of the charge-exchange

plasma produced by xenon thrusters.

Finally, a two-dimensional axisymmetric model of the thruster beam, including density profiles for both the neutrals and the high energy ions, is required for the development of more sophisticated charge exchange plasma flow models. Such a model could, for example, be used to determine the spatial distribution of charge-exchange ions and corresponding accelerator grid erosion patterns, which could then be compared to experimental measurements of accelerator grid erosion.

## 6.0 CATHODE LIFE TEST

### 6.1 Introduction

The power-limited, low thrust nature of ion propulsion results in very long engine burn times being required to accomplish typical missions of interest. Engine burn times of 10,000 to 15,000 hours are generally required for deep space missions. The hollow cathode is a key component of the ion engine, and therefore must be capable of reliable, long term operation. Hollow cathodes have been under development for ion engines since the middle 1960's<sup>14</sup> and have been the subject of numerous studies and endurance tests.<sup>14-50</sup> The vast majority of these investigations performed up until the early 1980's used mercury as the working fluid, although some early studies also looked at cesium. Cathode operation was found to be very reliable with mercury vapor, and a life-time of greater than 25,000 hours was demonstrated<sup>31</sup> with a 6.35-mm diameter hollow cathode operating at a discharge current of 10.5-11.5 A.

More recently ion engine research and development efforts have centered on the use of rare gases (argon, krypton and xenon) rather than mercury. Along with this switch from mercury is the trend to operation at higher powers and thrust levels. These higher power operating regimes require significantly greater cathode emission currents. There is little long term, hollow cathode operating experience with rare gases, especially at emission currents above 15 A. Most notably a 6.35-mm dia. hollow cathode was operated at an emission current of 6.3 A for approximately 4,000 hours, and a similar cathode (but with a larger orifice diameter) was operated for 900 hours at an emission current of approximately 19 A.<sup>48</sup> In both of these tests, which used xenon gas, the cathodes were tested as part of a full-up engine life test. In addition to these tests, a 12.7-mm dia. hollow cathode was operated on argon for 1,000 hrs at an emission current of 100 A.<sup>42</sup> A summary of inert gas hollow cathode testing is given in Ref. 53.

There have been no tests of a rare gas hollow cathode, at an emission current required for a 5 kW xenon ion engine, in which the test duration was a significant fraction of the engine design life time (10,000 hrs<sup>48</sup>). Therefore, the present program was initiated to perform a 5,000 hour test of a 6.35-mm dia. xenon hollow cathode at an emission current of 25 A. The 25 A emission current level was selected to be a more severe test of a cathode similar to that which would be required to operate at an emission current of 19 A in the 5 kW engine under development at NASA Lewis Research Center.<sup>48</sup> The test duration of 5,000 hours was selected to be half of the engine design life, with the expectation that major design deficiencies may be uncovered in this time span. Ultimately, cathode tests of 10,000 hours or longer will be required.

## 6.2 Apparatus and Procedure

**6.2.1 The Cathode:** The cathode used in this test is shown schematically in Fig. 12. The body of this cathode consists of a 6.35-mm diameter by 57.12-mm long molybdenum tube with a nominal wall thickness of 0.635 mm. This tube is electron beam welded to a 2.54-mm thick molybdenum flange at the upstream end, and a 2 % thoriated tungsten orifice plate (shown in Fig. 13) is electron beam welded to the downstream end. The orifice plate is 1.52 mm thick with a minimum orifice diameter of 1.80 mm. A 56 degree half-angle chamfer is machined into the downstream face of the orifice plate. An SEM photograph of the orifice plate welded to the cathode tube is shown in Fig. 14. A close-up of the molybdenum weld-bead is given in Fig. 15, indicating a high quality weld with no cracks in the weld bead itself. Evident also in this photograph, however, is a stress crack in the tungsten orifice plate. Two such stress cracks were found subsequent to the electron beam welding process. Leak tests indicated that these cracks do not go completely through the orifice plate. Previous experience indicates that the formation of such cracks is not unusual, so the decision was made to use this cathode for the life test.

A 12.7-mm diameter by 12.7-mm long cartridge heater assembly is used for the cathode tip heater. This heater assembly consists of a molybdenum wire potted in aluminum oxide. The cartridge heater is friction fitted over the downstream end of the cathode tube. The downstream end of the cartridge heater is positioned approximately 0.25 mm upstream of the end of the cathode. One of the molybdenum heater leads is crimp connected to a copper lead using the crimp portion of a nickel lug. This entire lead assembly is insulated using ceramic beads. The other molybdenum heater lead is connected directly to the stainless steel cathode flange with a stainless steel screw. No radiation shielding is used around the heater assembly. In addition, it is expected that with good thermal contact between the cathode and the cartridge heater, the downstream face of the heater will act as a radiation fin and facilitate cooling of the cathode at high emission currents.

A 3.2-mm diameter stainless steel tube is welded into the stainless steel cathode flange, and a gas passage is machined into this flange as shown in Fig. 12. A gastight seal between the stainless steel and molybdenum flanges is provided by a Grafoil gasket and a knife edge machined in the downstream surface of the stainless steel flange. Leak tests using nitrogen indicate that this configuration is leak-tight to greater than  $2.0 \times 10^5$  Pa (15 psig). These leak tests are performed using a shaped elastomer to plug the cathode orifice and then submerging the entire assembly in water. The internal cathode pressure during operation is on the order of  $2.7 \times 10^3$  Pa (20 torr) so this seal arrangement is leak-tight at a pressure two orders of magnitude higher than required. A photograph of the unassembled cathode is given in Fig. 16.

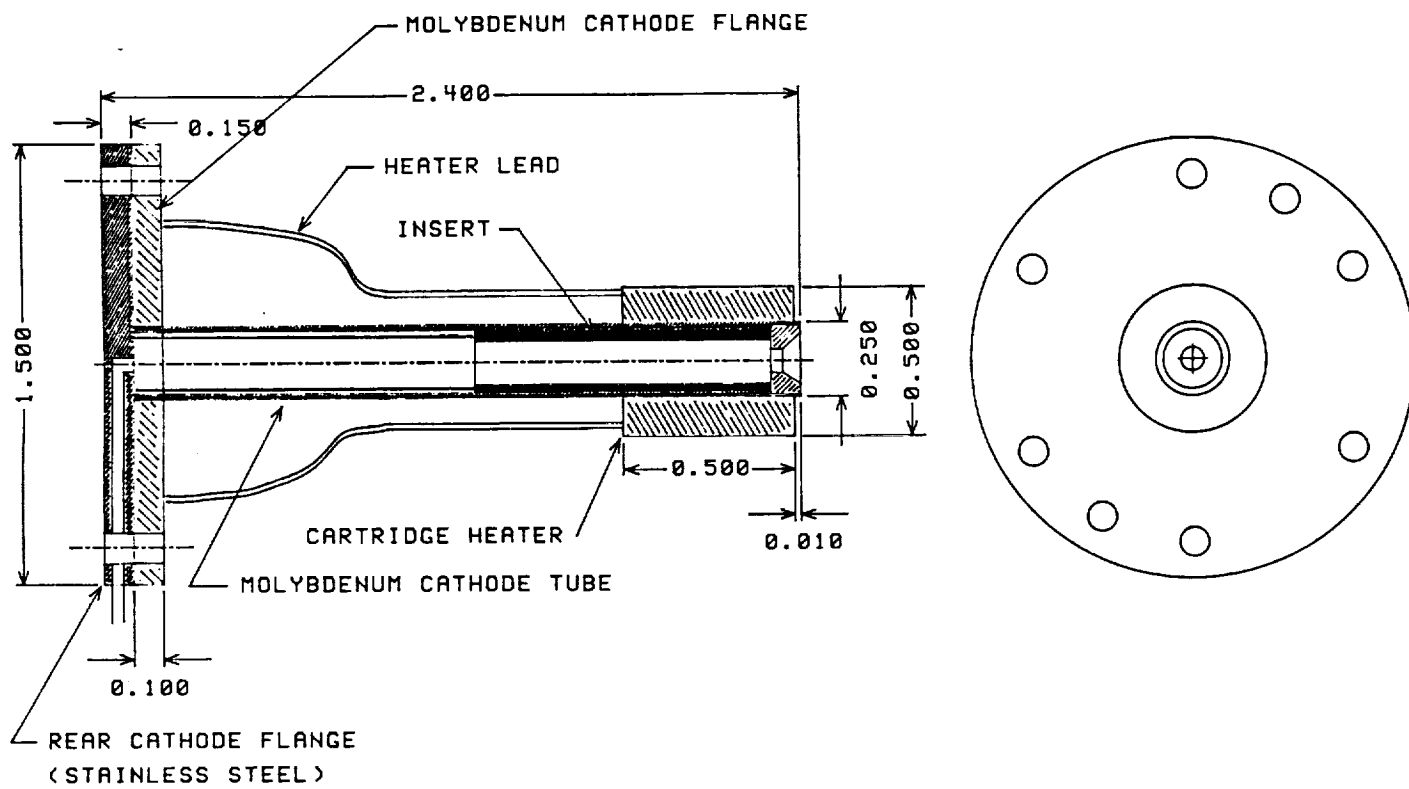


**Figure 12** Life test cathode schematic.

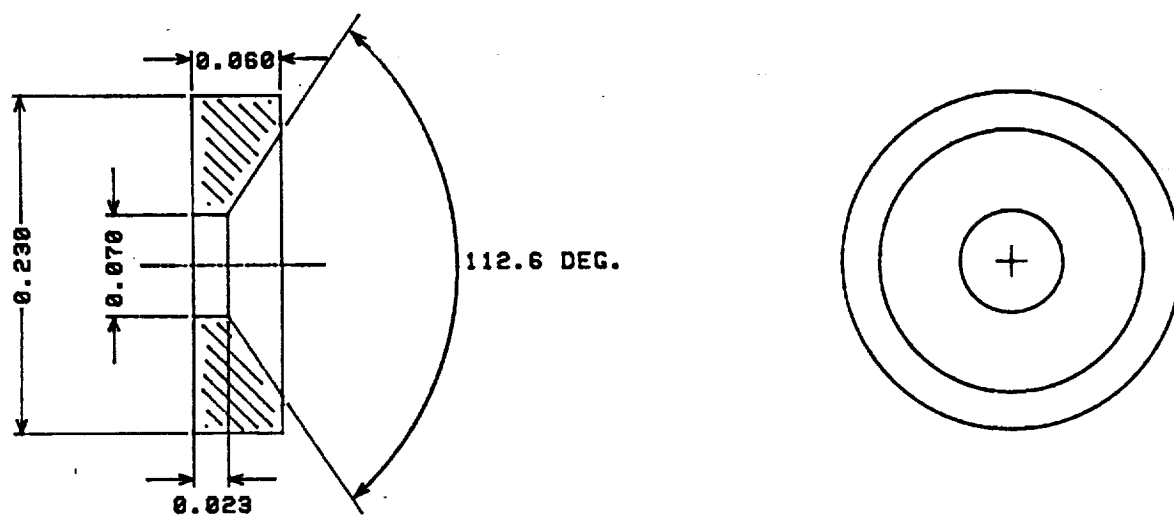


**Figure 13 Cathode orifice plate (2 % thoriated tungsten).**

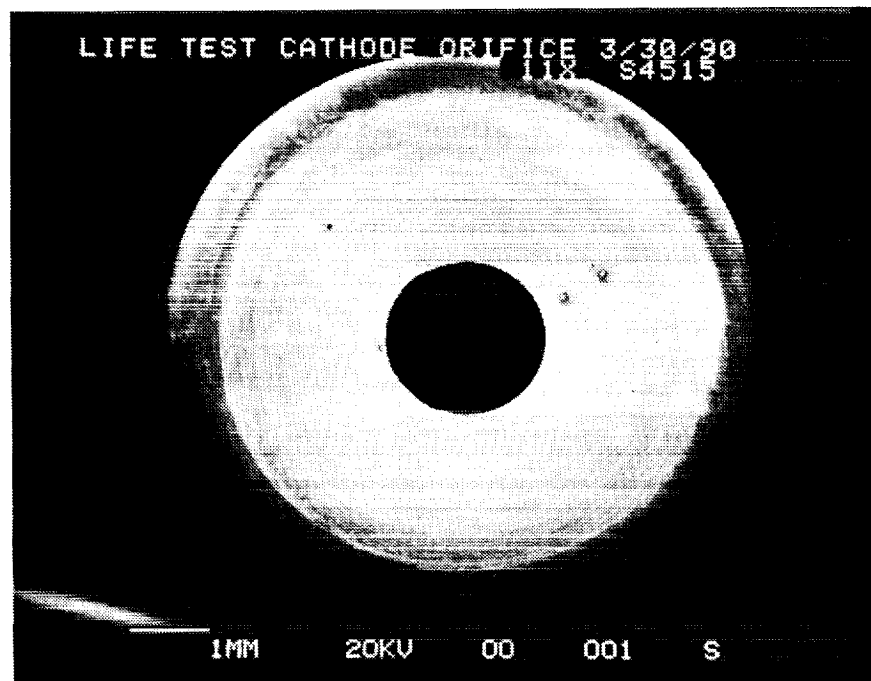


**Figure 14** SEM photograph of orifice plate welded to cathode tube.

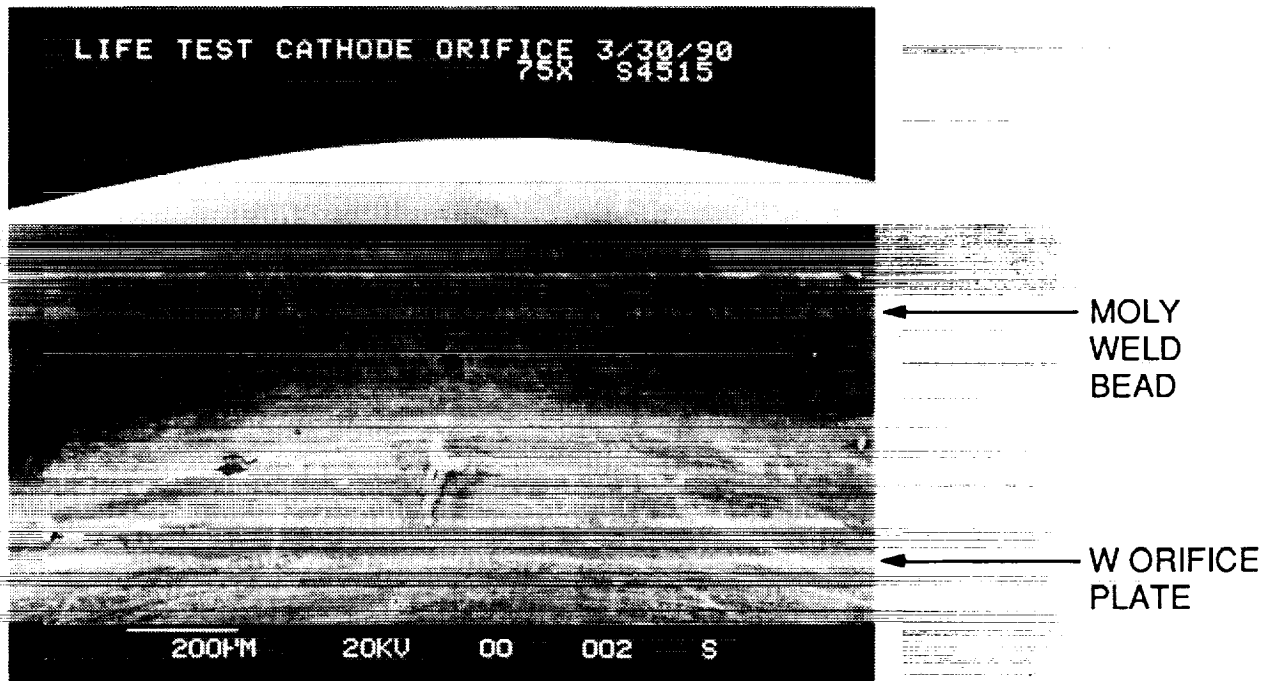
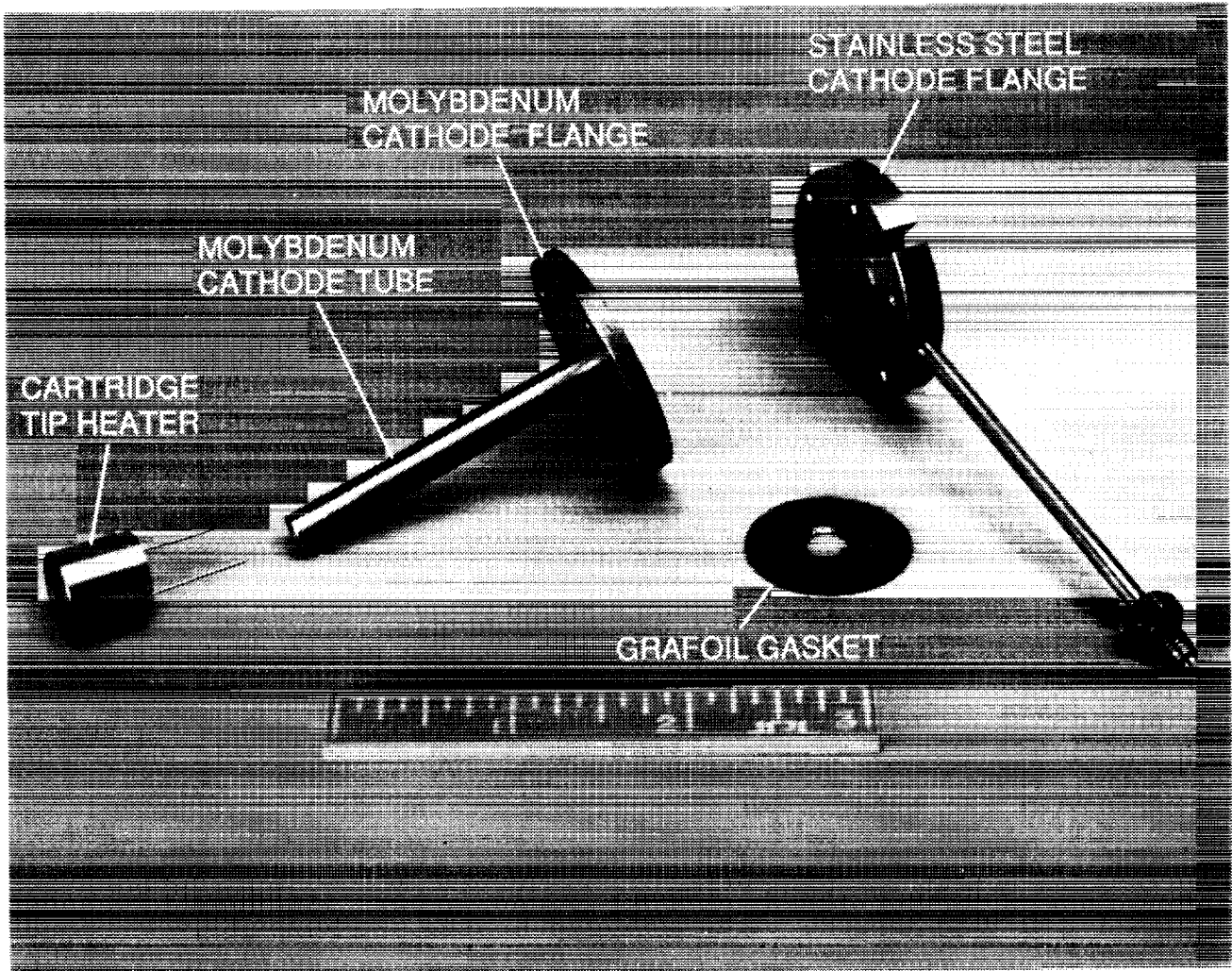


**Figure 15** Close-up of electron beam weld showing stress crack in the orifice plate.



ORIGINAL PAGE  
BLACK AND WHITE PHOTOGRAPH

**Figure 16** Life test cathode parts.

The cathode insert indicated in Fig. 11 consists of an 80 % dense porous tungsten cylinder impregnated with a barium-calcium-aluminate oxide mix with a molar ratio of 4:1:1 and is identical to the inserts used in other recent tests.<sup>48,50</sup> The insert is 25.4-mm long and has a wall thickness of 0.76 mm. A Mo-Re collar is brazed to the upstream end of the insert to provide a transition material from the tungsten insert to the three rhenium leads which are brazed to this collar. The insert is placed into the cathode tube with the downstream end of the insert touching the upstream face of the orifice plate. The insert leads are clipped so that they extend slightly beyond the upstream surface of the molybdenum cathode flange. The assembly process of tightening the bolts which hold the stainless steel and molybdenum flanges together compresses the insert leads and firmly holds the insert against the orifice plate. The cathode tube was cleaned in acetone and then in alcohol prior to the insertion of the cathode insert. During the assembly of the cathode and installation of the cathode into the vacuum test facility, the insert was exposed to air for a total of 2 hours and 15 minutes.

**6.2.2 Test Facility:** The cathode test facility, which is shown in Fig. 17, consists of a 0.91-m diameter by 2.1-m long stainless steel vacuum tank with two 0.25-m diameter oil diffusion pumps. The cathode is mounted in a J-Series ion engine style cathode pole piece assembly with the baffle and baffle support legs removed. The standard J-Series thruster keeper assembly is used for the started electrode. The cathode pole piece assembly is bolted to a stainless steel plate which also supports the disk-shaped anode positioned 130 mm downstream of the cathode. A cylindrical, tantalum foil enclosure attached to the stainless steel plate facilitates pressurization of the region between the cathode and the anode permitting operation at lower cathode flow rates. The anode consists of a SERT II thruster style, flat molybdenum ion extraction grid with tantalum foil spot welded to the side facing the cathode, and is radiation cooled.

Two W-5%Re/W-26%Re thermocouples were attached to the downstream face of the cartridge tip heater. These thermocouples were attached by first spot-welding tantalum foil to the molybdenum heater surface. The thermocouples were then spot-welded to the tantalum. A second layer of tantalum foil was spot-welded over the thermocouples to secure them in place. In addition, a disappearing-filament type optical pyrometer is used to measure the temperature of the cathode as indicated in Fig. 17. The optical pyrometer was calibrated by placing a standard lamp with a 2 % thoriated tungsten filament in the vacuum system at the location of the cathode. The calibration was accomplished by viewing the lamp through the vacuum tank window over the same optical path used in the life test.

The xenon feed system consists of approximately 1.8 m of 6.35-mm diameter stainless steel tubing and is shown in Fig. 18. All tubing pieces and fittings were cleaned in acetone and rinsed in

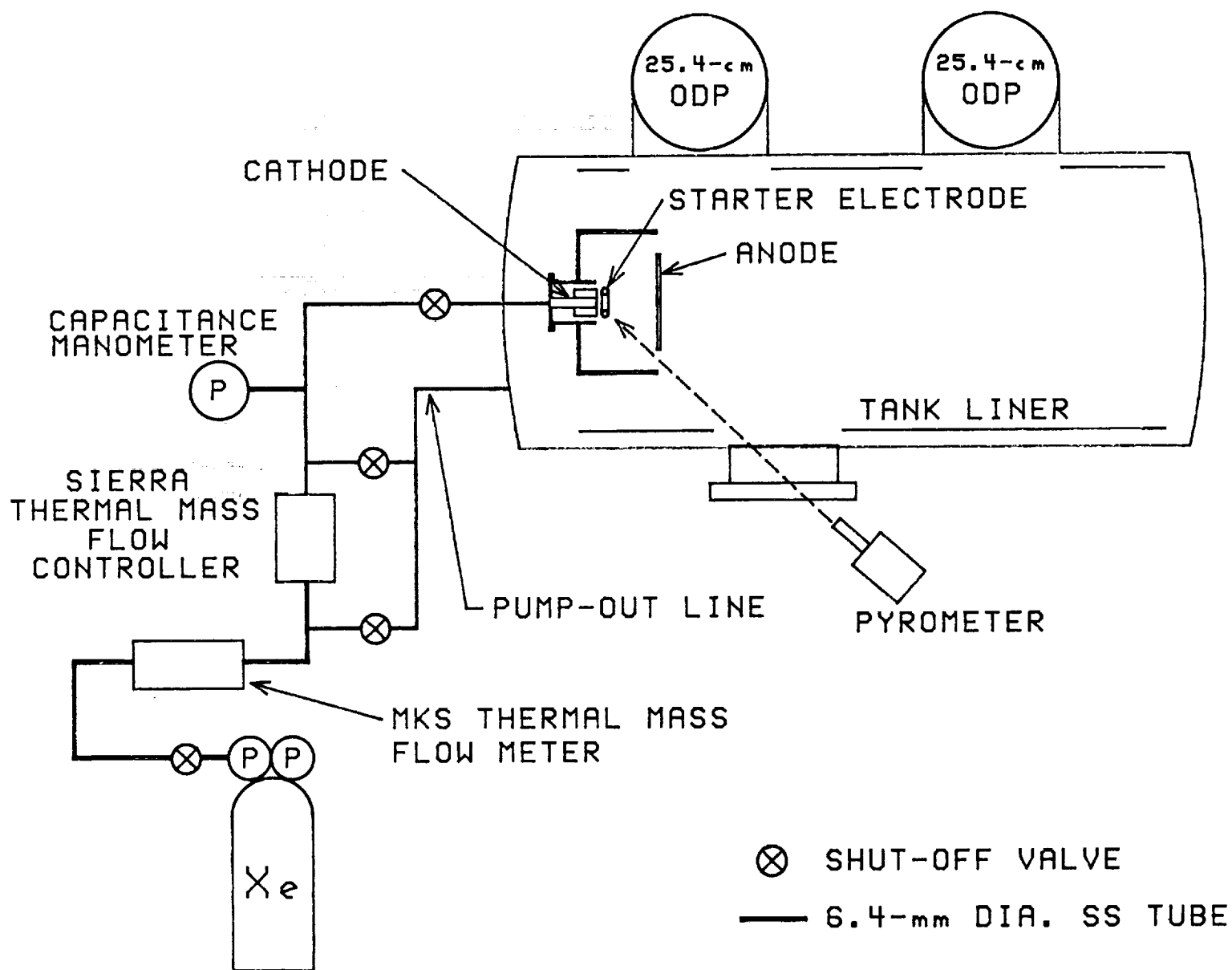
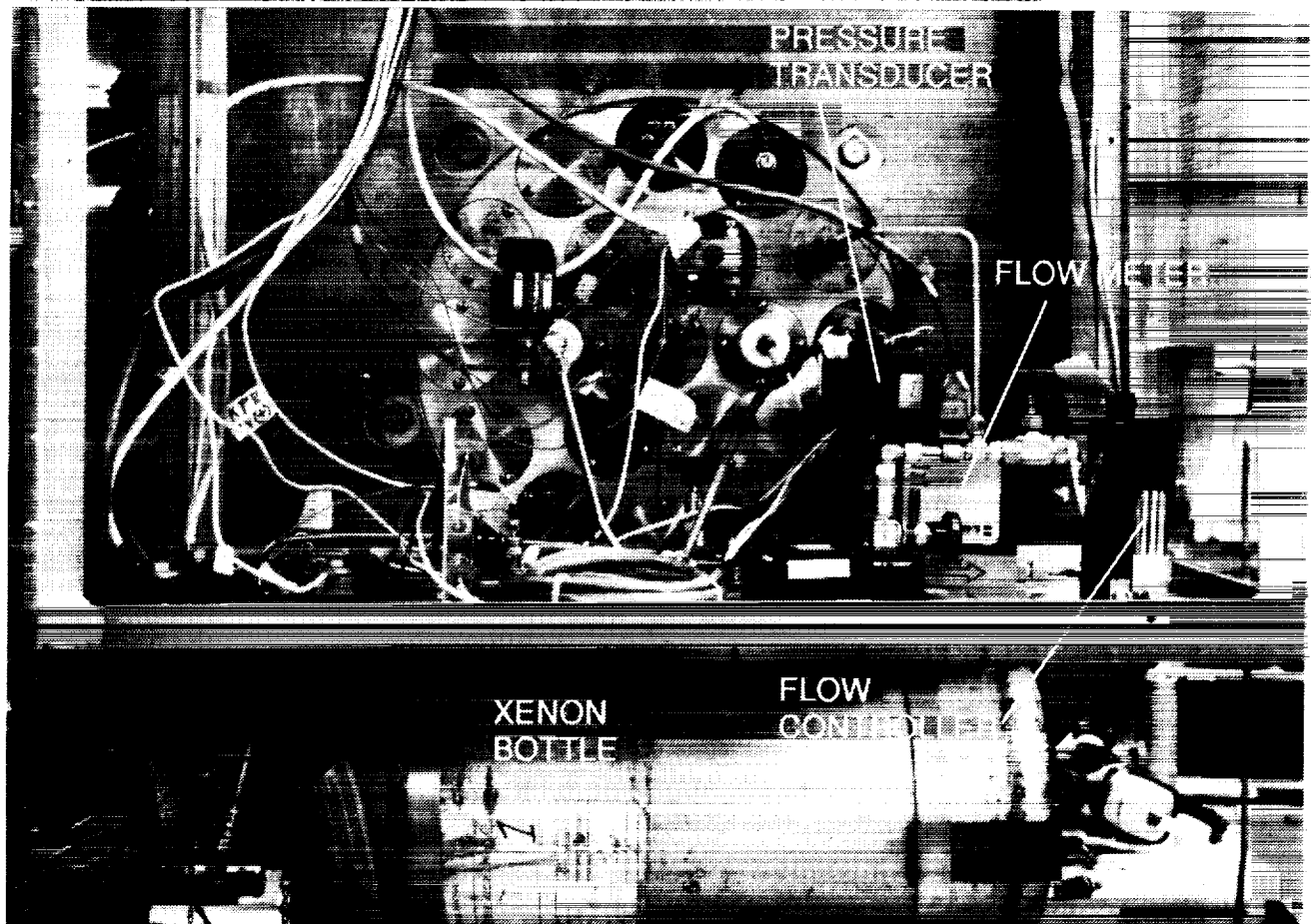


Figure 17 Cathode life test facility.

ORIGINAL PAGE  
BLACK AND WHITE PHOTOGRAPH



**Figure 18** Life test xenon feed system.

alcohol prior to assembly. A new MKS, Inc., 0-20 sccm, thermal mass flow meter is used to measure the xenon flow rate into the cathode. Downstream of this flow meter, a thermal mass flow controller from Sierra Instruments is used to control the xenon flow rate. This arrangement permits measurement of the flow rate independent of the action of the flow controller. It also eliminates possible thermal feed-back effects from the solenoid valve in the flow controller from affecting the flow sensor. Furthermore, this arrangement always results in the same pressure downstream of the MKS flow meter, regardless of the pressure to which the flow controller is exhausting. A capacitance manometer positioned downstream of the flow controller is used to measure the cathode internal pressure during operation. The capacitance manometer was calibrated immediately prior to installation in the gas feed system.

A separate pump-out line is included in the feed system to facilitate removal of contaminant gases from the feed lines. This pump-out line is connected to both sides of the flow controller to provide a large diameter path for the gas. Four shut-off valves are included in the feed system to permit isolation of different feed system components. The entire feed system was subjected to two series of leak tests. In the first, the two pump-out line shut-off valves were closed along with the shut-off valve to the cathode. The feed lines were then pressurized to  $2.45 \times 10^5$  Pa (35 psig) and carefully checked for leaks using a soap-like bubble solution. No leaks of xenon gas out of the system were detected. The second set of leak tests were designed to look for air leaks into the feed system for those components which would be operated at pressures less than atmospheric pressure during normal operation. In this case the feed system was pumped out to high vacuum for several days, then all of the shut-off valves were closed and the pressure increase indicated by the capacitance manometer over another period of several days was recorded. From these data a maximum leak rate into the propellant feed system was estimated to be  $2 \times 10^{-7}$  standard  $\text{cm}^3/\text{s}$ .

Both the flow controller and the flow meter were carefully calibrated prior to the initiation of the life test. The new MKS thermal mass flow meter was calibrated at the manufacturer's facility on the east coast of the United States using nitrogen and a secondary calibration standard. The flow meter was then shipped to JPL where it was subsequently taken to the manufacturer's facility on the west coast and recalibrated on both nitrogen and xenon using a primary volumetric calibration standard. Next, the flow meter was calibrated in-house at JPL on nitrogen and xenon using a secondary volumetric calibration standard (i.e., a "bubble" volume calibration kit from the Hastings corporation).

The results of these calibrations are shown in Figs. 19-21. The comparison between the calibrations performed with the MKS primary calibration standard and the Hastings calibration kit is

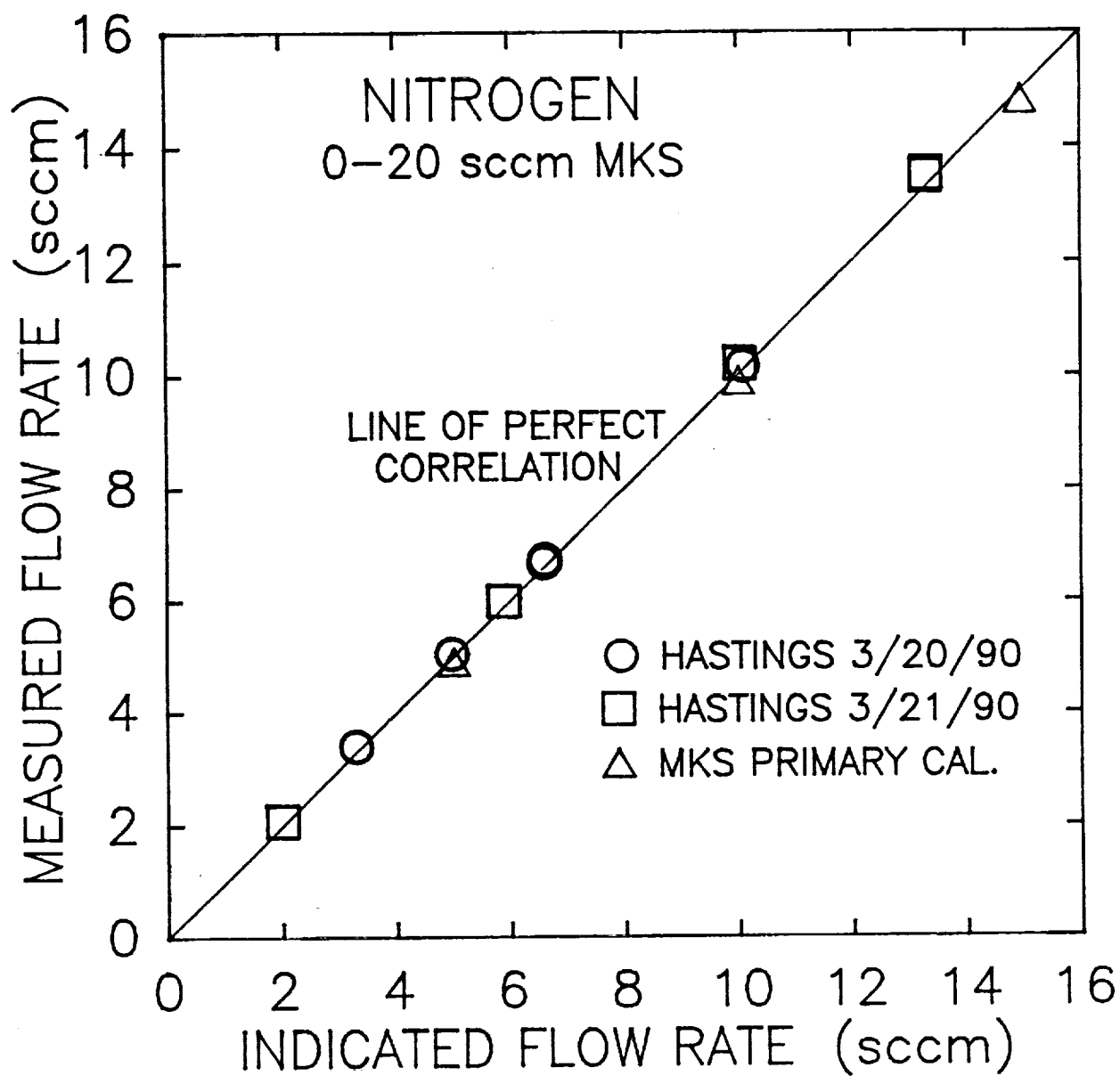


Figure 19 Comparison of MKS flow meter calibrations on nitrogen.

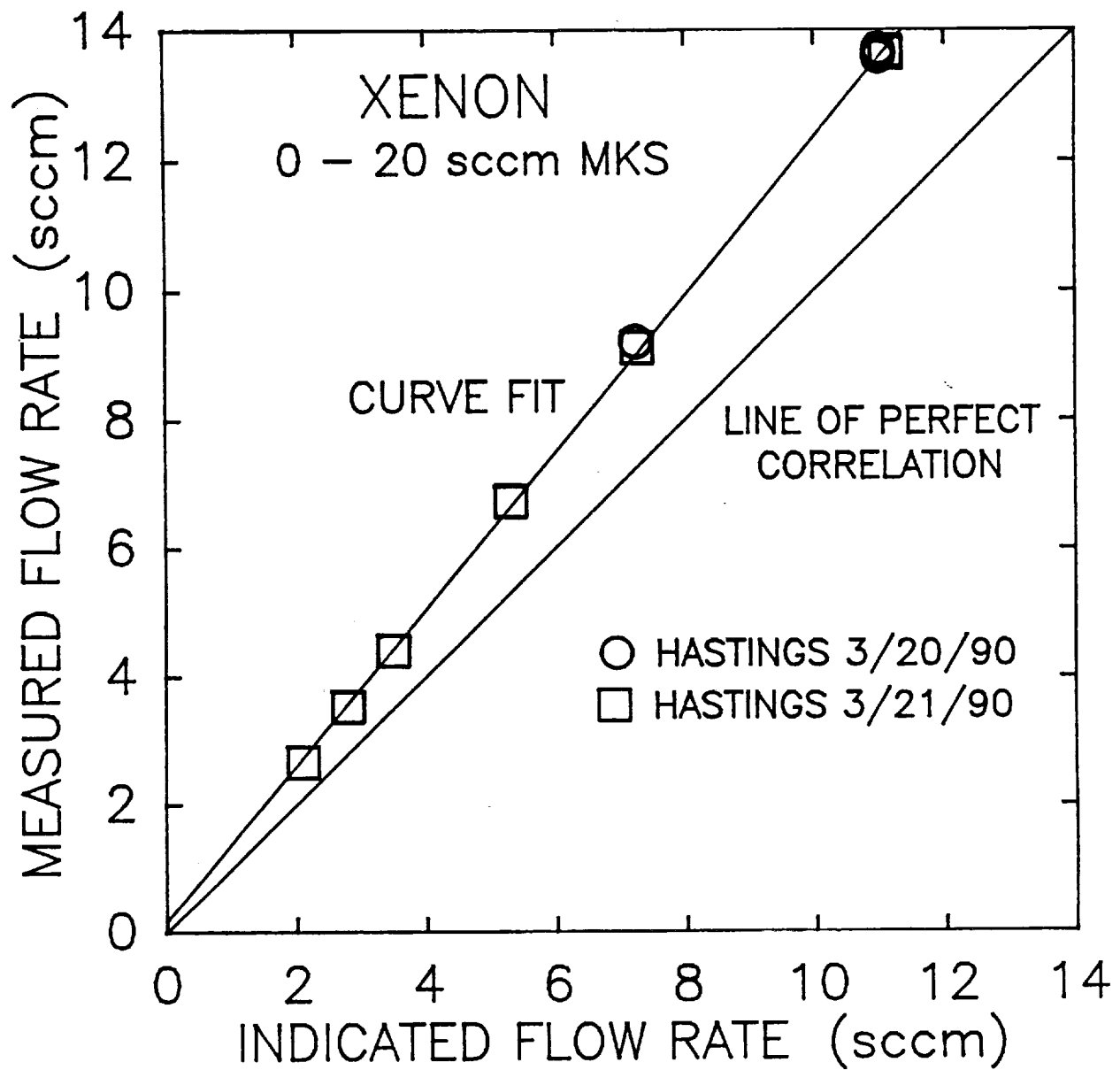
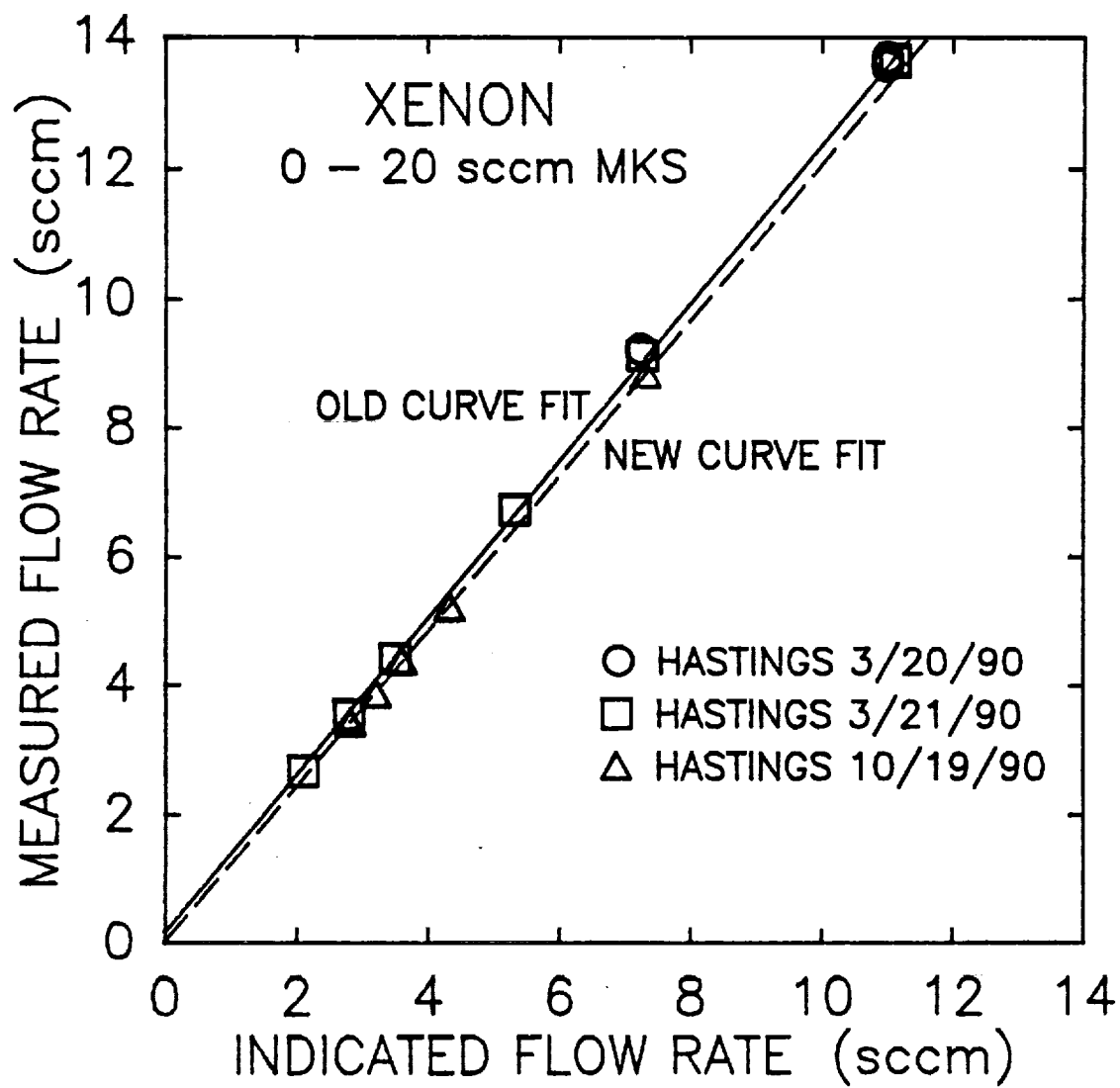


Figure 20 MKS flow meter calibration on xenon.



**Figure 21** Comparison of MKS flow meter calibrations on xenon after 7 months of continuous operation.

given in Fig. 19 for nitrogen. These data indicate that the Hastings calibration kit agrees well with the primary standard calibration. The calibrations with the Hastings kit were performed on two separate days with no difference in the results. In addition, the calibration on nitrogen at the MKS facility indicated that the flow meter's calibration had not changed (within the manufacturer's tolerance of 0.8 % of full scale) as a result of being shipped from the east coast to the west coast.

The data in Fig. 20 indicate the flow meter's response to xenon gas instead of nitrogen over the range of flow rates of interest. A straight line curve fit to these data indicates a slope of 1.22 and an intercept of 0.171. The slope of 1.22 differs from the manufacturer's recommended correction factor for xenon of 1.32 by a significant amount. Finally, after seven months and more than 4,000 hours of operation, the flow meter was recalibrated on xenon using the Hastings calibration kit. The results of the new calibration are compared to those of the old one in Fig. 21. A curve fit to the new calibration data indicates a slope of 1.20 and an intercept of 0.029. The new calibration data indicate a shift in the flow meter response after seven months of continuous operation that amounts to approximately 5 % of the flow rate. The shift is such that the actual flow rate is 5 % less than the indicated flow rate.

The electrical schematic for the cathode life test is given in Fig. 22. There are three power supplies, a tip heater supply, a starter supply, and the anode supply, all of which are 60 Hz laboratory supplies. The starter supply is actually a parallel combination of two separate supplies. One is a high voltage supply capable of 900 V at 100 mA, and the other is a 35 V, 10 A supply with current regulation. Both the tip heater and starter supplies are only used to start the cathode. During normal operation only the current regulated anode supply is used. A calibrated 100 mV, 30 A current shunt is used to measure the discharge current.

Commercial heater elements were installed on the vacuum tank liner in order to heat the liner prior to initiation of the life test. These heaters were used to bake the tank liner out at  $>100^{\circ}\text{C}$  for 30 hours prior to the beginning of the test. This bake-out procedure resulted in an ultimate tank pressure of  $9.3 \times 10^{-5}$  Pa ( $7 \times 10^{-7}$  torr). After 4000 hours of nearly continuous high vacuum operation the no-flow tank pressure had decreased to approximately  $6.7 \times 10^{-5}$  Pa ( $5 \times 10^{-7}$  torr).

**6.2.3 Computer Control System:** A computer data acquisition and control system is used to run the life test and enables long duration, unattended operation. A detailed description of this system is given in Appendix F.

**6.2.4 Start-Up Procedure:** The following procedure is used to condition the insert and start the cathode. The insert

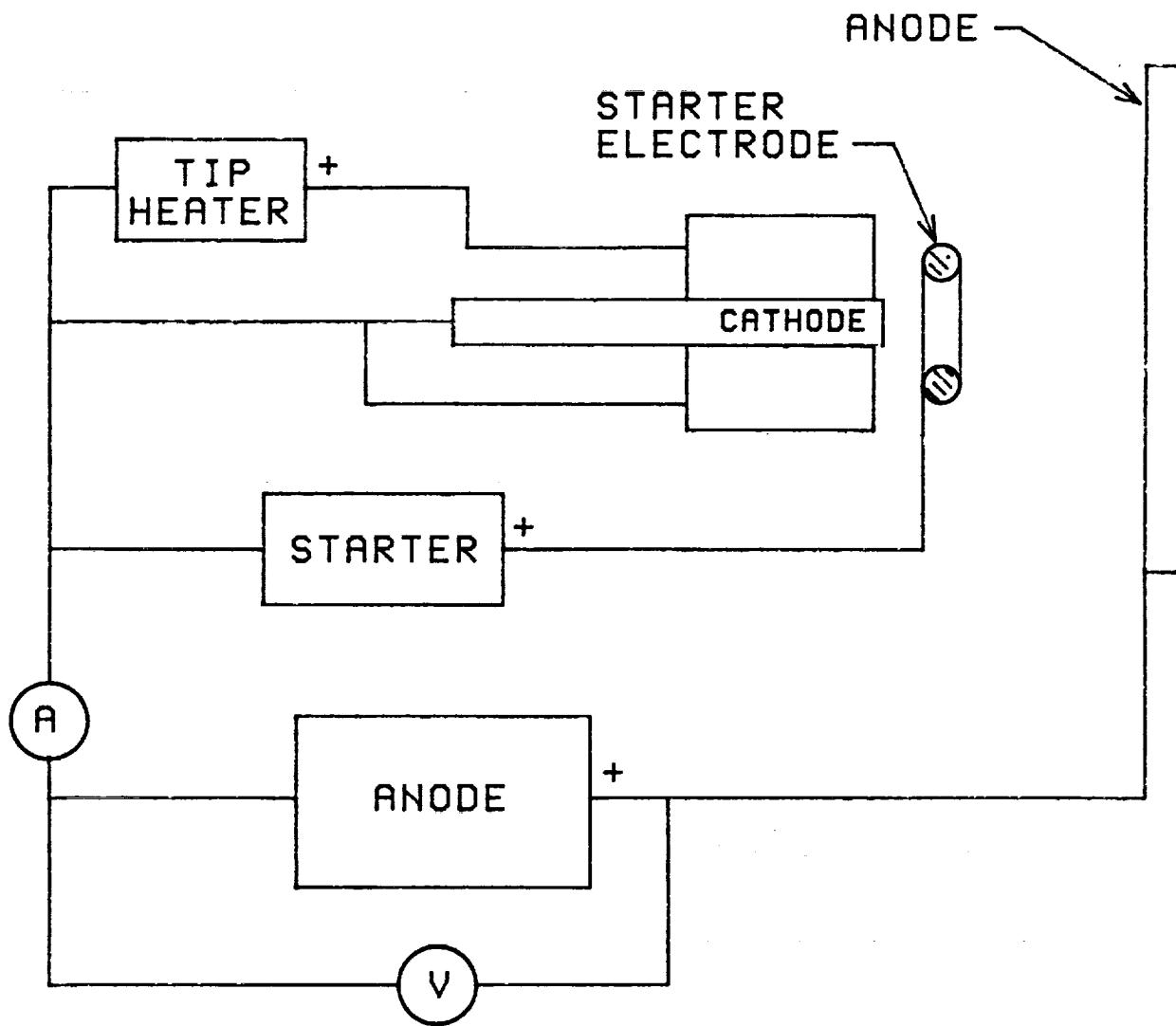


**Figure 22** Life test power supply schematic.

conditioning is accomplished by first setting the xenon flow rate to the normal run condition (4.0 sccm). The tip heater current is then set to 4.0 A and the cathode is heated to approximately 500°C (as indicated at the orifice plate) for 3 hours. After 3 hours the heater power is removed and the cathode is allowed to cool for 30 minutes. The cathode heater current is then set to 7.0 A and the cathode is heated to > 1050°C for 1 hour. After 1 hour the cathode is again allowed to cool for 30 minutes after which the tip heater current is set to 7.5 A to heat the cathode to > 1100°C. The cathode is heated under these conditions for 30 minutes before attempting to initiate the discharge.

### 6.3 Test Results After 4,200 Hours of Operation

A photograph of the cathode in operation is shown in Fig. 23 and a close-up of the cathode orifice plate is shown in Fig. 24. The photograph in Fig. 24 was taken after 4,046 hours of operation and indicates the view of the cathode which the test operator sees through the optical pyrometer. The orifice plate is clearly visible through the aperture in the starter electrode. Orifice plate temperatures are normally taken at a radial location corresponding to the midpoint of the visible portion of the orifice plate. Temperature measurements indicate a significant radial temperature gradient along the orifice plate. The optical pyrometer was also used to measure the temperature of the insert itself. The emitting surface of the insert can be clearly seen through the cathode orifice as indicated in this photograph. Furthermore, the insert surface appears considerably brighter than the orifice plate. This photograph also indicates that after 4,046 hours of operation, the starter electrode does not appear to be significantly eroded. Finally, no material deposits on the interior diameter of the cathode orifice are evident.

A summary of the cathode life test operating history is given in Table 5. The first five shutdowns indicated in this table were ultimately traced to a faulty anode power supply. The faulty power supply was an SCR regulated Sorenson supply which resulted in rather noisy operation of the cathode as indicated in Figs. 25 and 26. Current oscillations, as indicated in Fig. 25, were typically +2.0 and -3.5 A around a nominal value of 25.1 A, with a frequency of approximately 80 kHz. The corresponding voltage oscillations are shown in Fig. 26 where the average voltage is 19 V with spikes to greater than 65 V. These data were taken with a xenon flow rate of 4.0 sccm. After 123 hours of operation, the faulty Sorenson power supply was replaced with a transistor regulated Hewlett-Packard supply.

**Table 5 Cathode Life Test Summary**

Shutdown #	Run Time (hrs)	Test Segment Duration (hrs)	Explanation	Restart	Conditions
				Orifice Plate Temperature (°C)	Start Voltage Required (V)
1	40	40	Low anode voltage detected by the computer. Faulty anode power supply.	1143	25
2	62	22	Faulty anode power supply.	1047	22
3	114	52	Faulty anode power supply.	1047	18
4	121	7	Faulty anode power supply.	1047	35
5	122	1	Faulty anode power supply.	1024	35
6	123	1	Manual shutdown to change anode power supply.	1029	35
7	295	172	Lightning strike closed hi-vac. valves. Computer shut down cathode.	1041	35
8	558	263	Data acquisition system failure. Computer shut down cathode.	1052	50
9	581	23	Failure of primary and back-up printers. Computer shut down cathode.	1048	50
10	697	116	Data acquisition system failure. Computer shut down cathode.	1041	80
11	743	46	Data acquisition system failure. Computer shut down cathode.	1047	80
12	1289	546	Mechanical pump belt broke. Operator error led to computer shutdown of cathode.	1153	900
13	1649	360	Lightning strike. Computer shut down cathode.	1085	900
14	2704	1055	Operator error led to computer shutdown of cathode.	1050	300
15	3020	316	Xenon bottle changed. Gas pulse required to restart (200 torr).	1050	> 900
16	3069	49	Flow controller failure. Computer shut down cathode. Cathode exposed to air for approximately 5 minutes. Gas pulse required to restart (200 torr).	1050	> 900
17	4221	1152	Xenon bottle changed. Gas pulse required to restart (200 torr).	1050	> 900

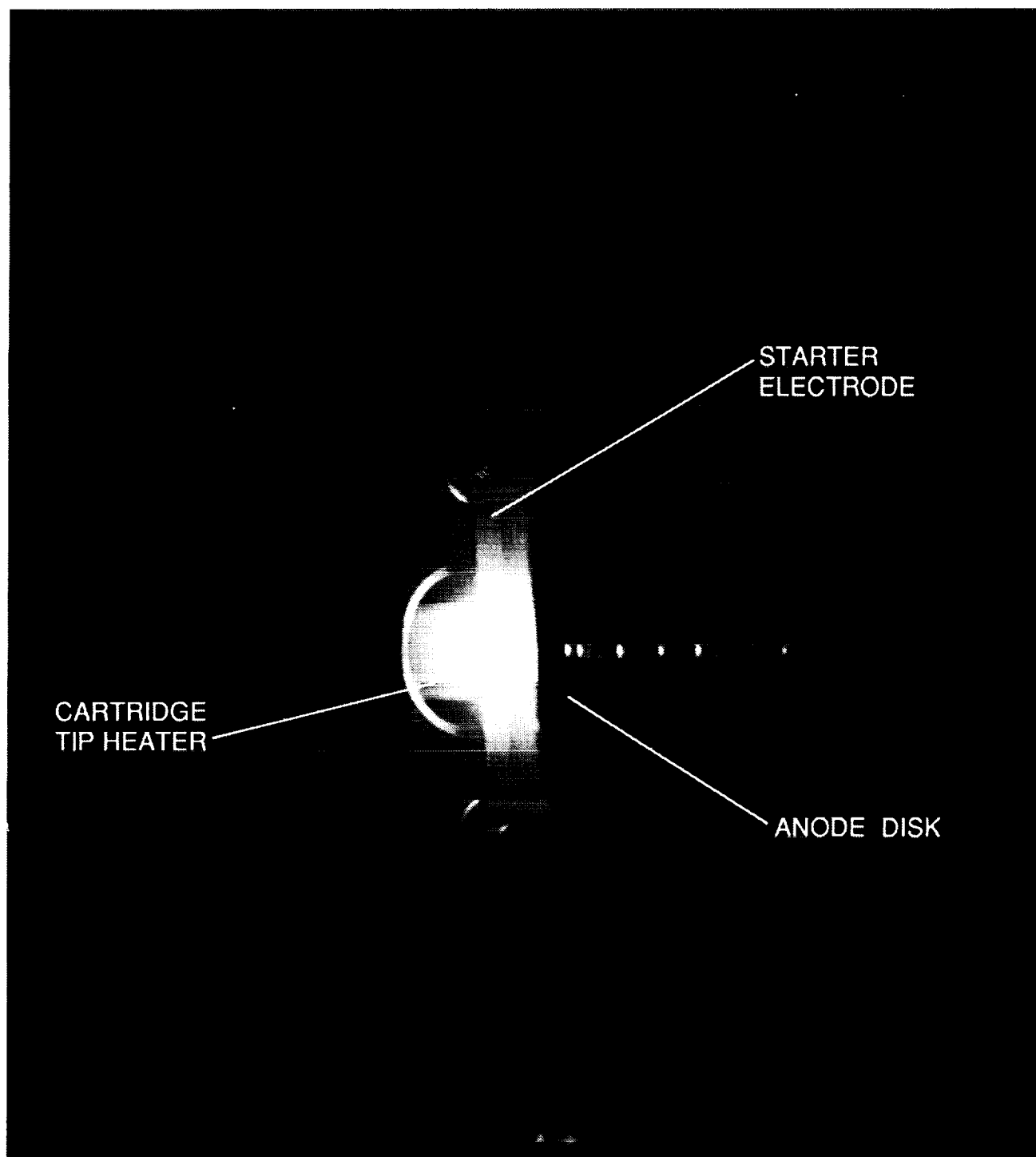


**Figure 23** Life test cathode in operation.

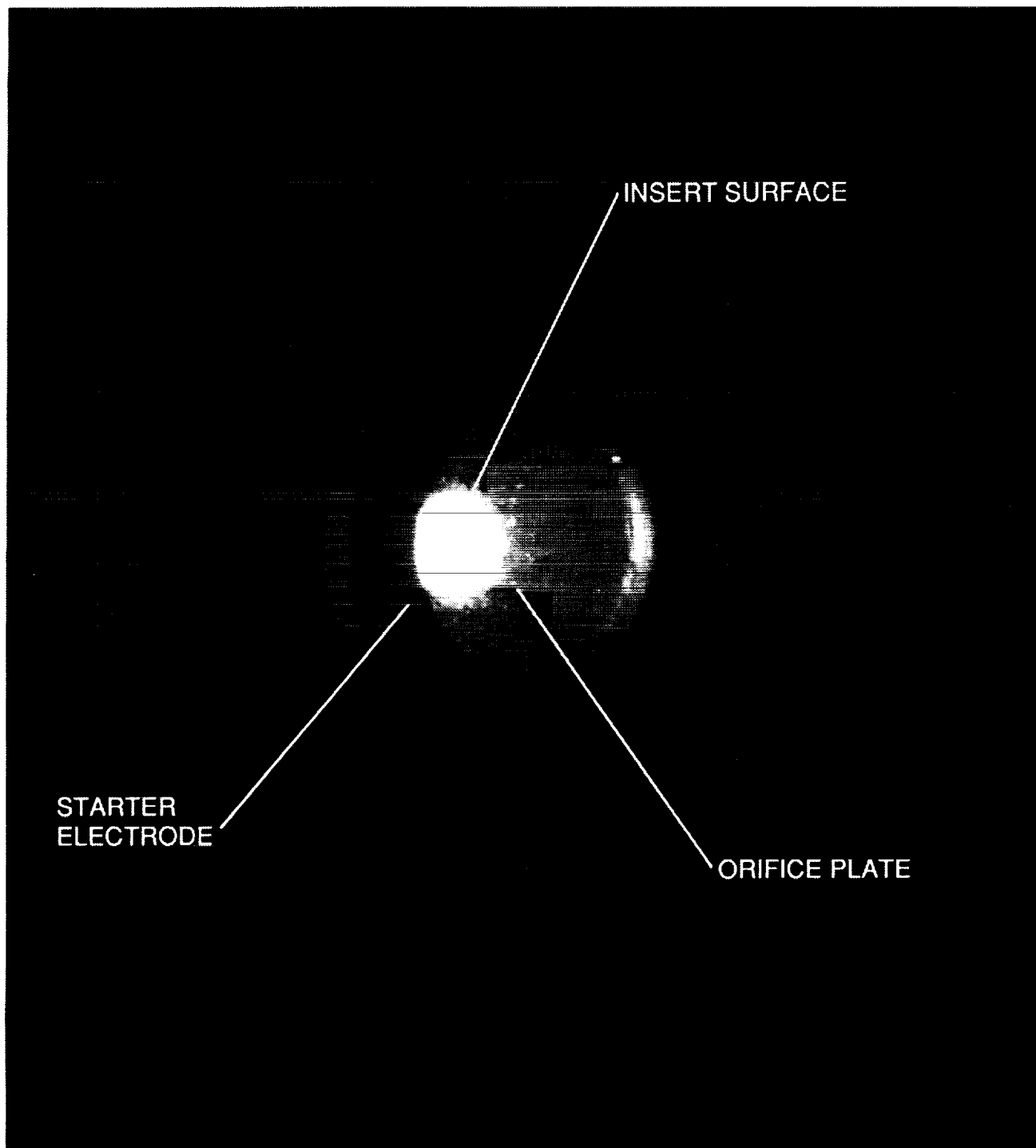


**Figure 24** Close-up of cathode orifice during operation at run hour 4046.

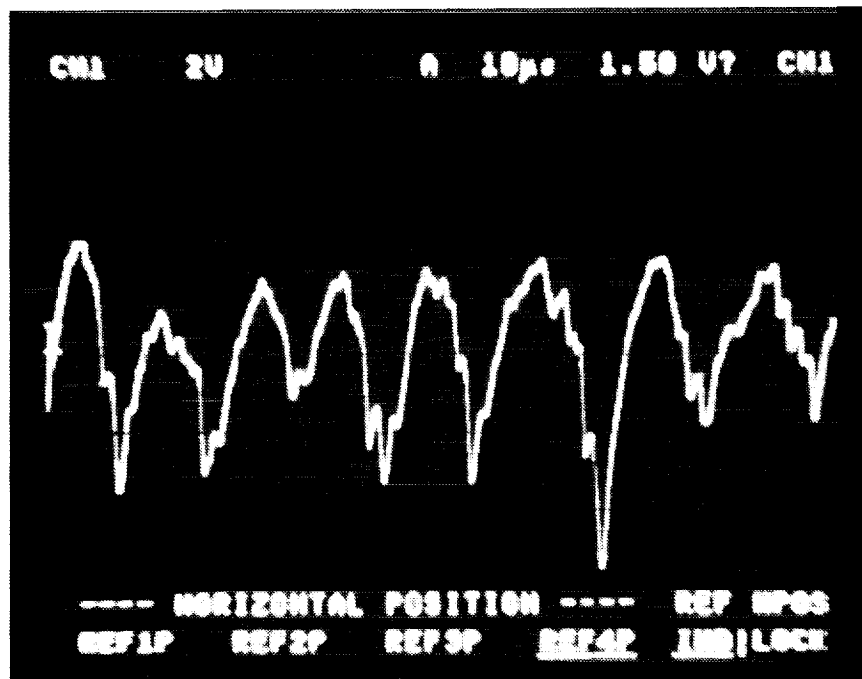


**Figure 25** Discharge current oscillations with Sorenson anode supply -- 2 A per major division vertically, 10 microseconds per major division horizontally.

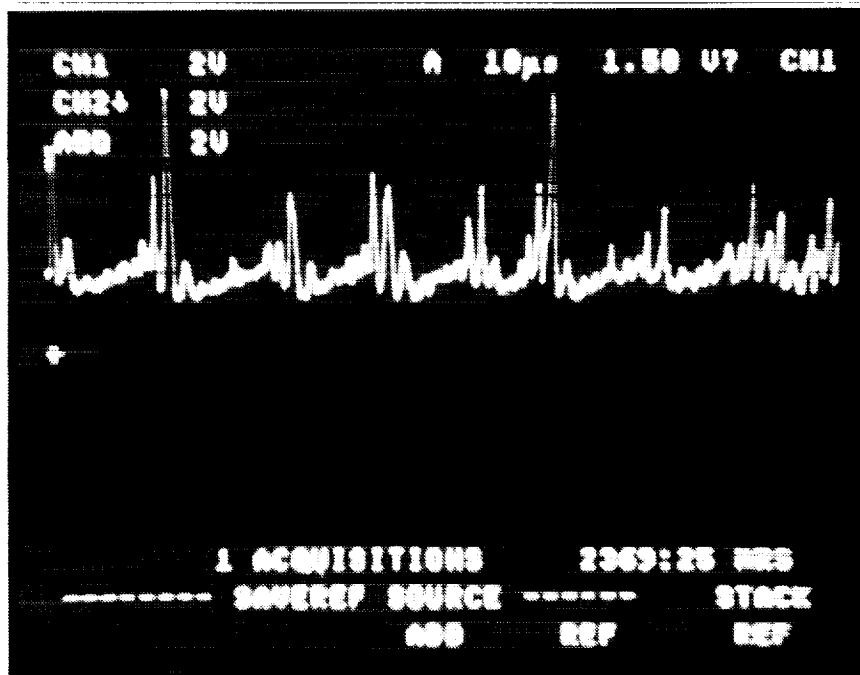


**Figure 26** Discharge voltage oscillations with Sorenson anode supply -- 20 V per major division vertically and 10 microseconds per major division horizontally.

Operation on the Hewlett-Packard power supply was significantly less noisy than with the Sorenson supply as indicated in Fig. 27. This figure shows a discharge current oscillation of  $\pm 0.75$  A with a frequency of 5 kHz. A higher frequency oscillation (approximately 100 kHz) superimposed on this 5 kHz oscillation is also evident from this oscilloscope trace. Discharge voltage spikes, with occasional peaks to +30 V, were also detected at this frequency. The switch from the Sorenson to the Hewlett-Packard power supply also resulted in a decrease in orifice temperature of approximately 50°C.

With the exception of the first 123 hours, the entire test was conducted with the Hewlett-Packard supply, and the discharge current oscillations shown in Fig. 27 remained unchanged until approximately 4,000 hours of operation. At this time a low frequency oscillation (330 Hz) appeared. The magnitude of this oscillation was  $\pm 4$  A for the current and  $\pm 2$  V for the discharge voltage as indicated in Figs. 28 and 29. The very high frequency (100 kHz) oscillations were still present at this time, but the 5 kHz oscillations had disappeared. By increasing the xenon flow rate from 4.0 sccm to 5.0 sccm the low frequency oscillations were eliminated. Operation at the higher flow rate, however, resulted in an anode voltage of only 12 V. It is planned that the last 700 hours of the test will be conducted at the higher flow rate.

Shutdown number 7 resulted from a nearby lightning strike which momentarily removed power from the diffusion pump high vacuum valves causing them to close. The computer detected the resulting increase in tank pressure and shut down the cathode. Shutdown number 9 occurred when both the primary and the backup printers failed and the computer responded by turning off the cathode. Shutdowns 8, 10 and 11 resulted from failures in the data acquisition hardware, which, when detected by the computer, caused the computer to shut down the test. A software change to increase the tolerance to data acquisition system errors eliminated these shutdowns.

Of the 17 shutdowns which have occurred in the 4,200 hours of operation to date, 11 occurred in the first 750 hours. Shutdown number 12 occurred as a result of a broken belt in one of the two mechanical pumps backing the diffusion pumps. The broken belt itself did not result in the shutdown since the system can operate on a single mechanical pump. The problem occurred when the pump was brought back on line following replacement of the belt. Bringing the pump back on line created a momentary surge in the foreline pressure which the computer detected and interpreted as serious pumping system failure causing it to shut down the cathode. This shutdown could have been avoided by disabling the computer shutdown authority.

Shutdown number 13 resulted from another lightning strike which again momentarily removed power from the laboratory. The

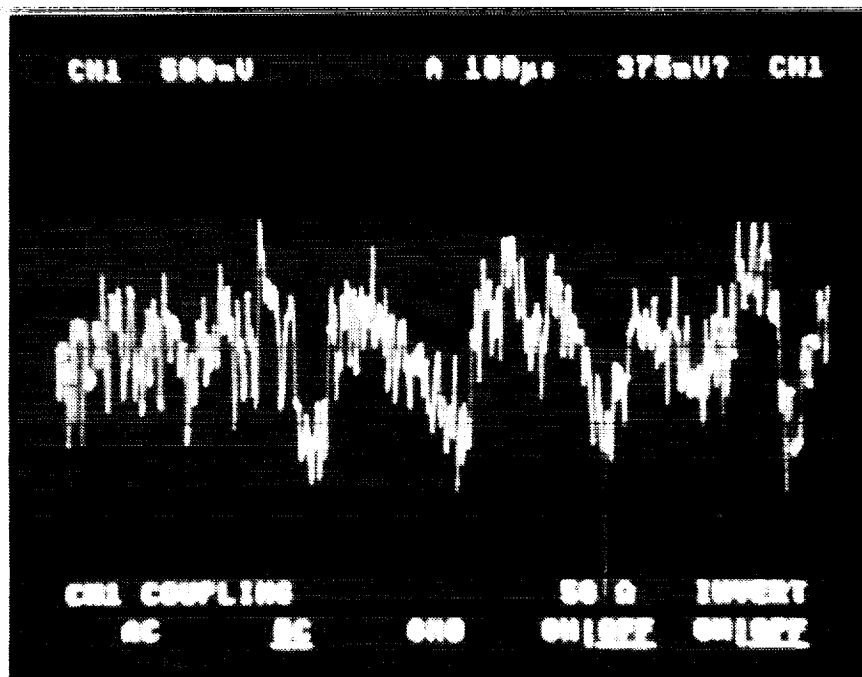


**Figure 27** Discharge current oscillations with Hewlett-Packard anode supply -- 0.5 A per major division vertically, 100 microseconds per major division horizontally.

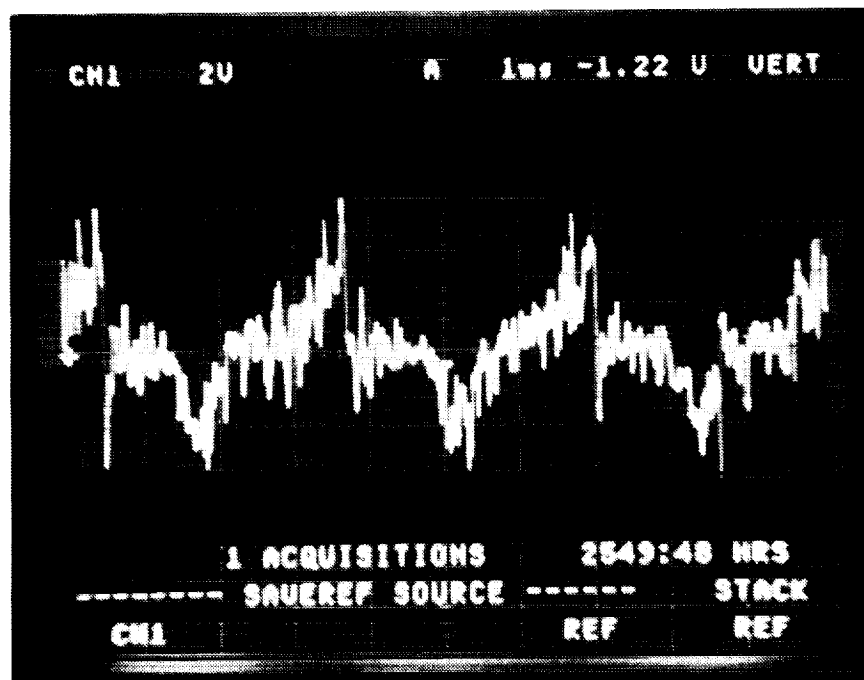


**Figure 28** Low frequency discharge current oscillations which began after approximately 4000 hours of operation. Oscillations are  $\pm 4$  A at 333 Hz.

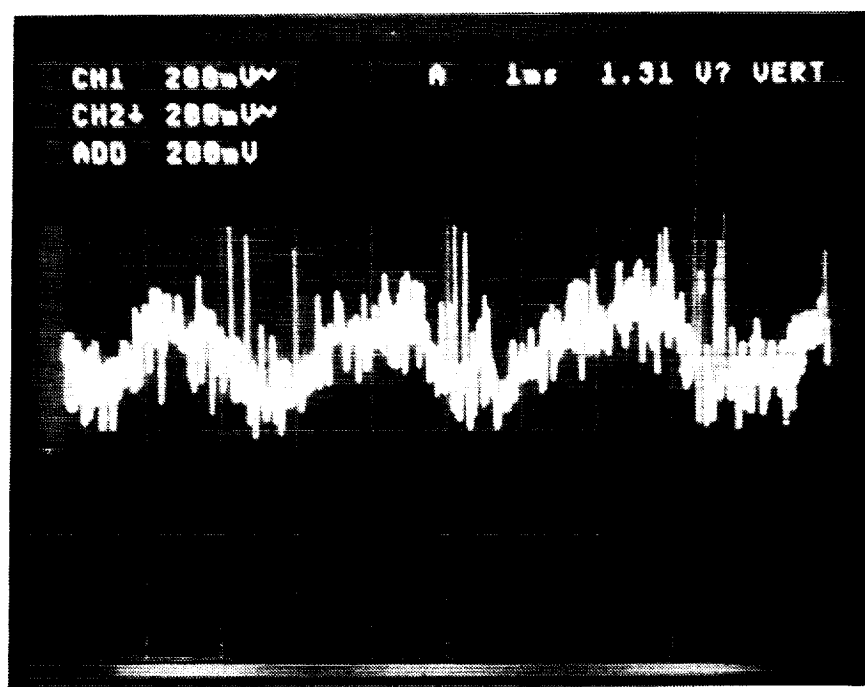


**Figure 29** Low frequency discharge voltage oscillations,  $\pm 2V$  at 333 Hz.

14th shutdown was a result of operator error. This error occurred near the depletion of the 1000 liter bottle of xenon used in the test. The high pressure side of the regulator indicated zero pressure, but the low pressure side still indicated 35 psig. In an attempt to determine the remaining bottle pressure, the regulated pressure setting was increased until it reached a maximum. The flow controller, however, could not respond adequately to the change in upstream pressure, resulting in a momentary decrease in the flow rate to the cathode. This decrease in flow rate resulted in a discharge voltage which exceeded the maximum allowable voltage level set in the computer, causing the computer to shut down the cathode.

The 15th and 17th shutdowns were manual shutdowns required to change xenon bottles. Finally, shutdown number 16 was caused by failure of the Sierra thermal mass flow controller. The flow controller failure was such that it slowly decreased the xenon flow rate over a period of several hours. As the flow rate decreased, the discharge voltage increased. When the discharge voltage exceeded the maximum allowable voltage level, the computer shut down the cathode.

Also evident in the data in Table 5 are the conditions required to restart the cathode following a shutdown. The first 11 times the cathode was restarted, covering a period of 743 hours of operation, the cathode started very easily, and with relatively low voltages applied to the starter electrodes. All of these restarts were performed with the normal 4.0 sccm xenon flow rate through the cathode. No conditioning procedure was used prior to these restarts since the cathode was maintained at high vacuum with continuous xenon flow throughout each shutdown. The lightning strikes which caused shutdowns 7 and 13 occurred during normal working hours and high vacuum operation was restored within minutes. The 12th restart required 900 V applied to the starter electrode to ignite the cathode.

Clearly evident in these data is the trend toward increasing restart difficulty with operating time. The only exception is restart number 14 which required 300 V applied to the keeper. This restart, however, was accomplished within minutes of the cathode shutdown, and the cathode did not cool off significantly before the restart. All other restarts were performed beginning with a cold (i.e., room temperature) cathode. The last three cathode restarts required a 200 torr gas pulse to force the transition from the low current high voltage glow discharge mode to the high current arc mode. In this case, applying 900 V to the keeper electrode would result in a 900 V, 10 mA glow discharge which would not transition to the arc mode. To force this transition, the starter supply was turned off and the shut-off valve leading to the cathode was closed until the pressure indicated by the capacitance manometer indicated 200 torr. At this time the shut-off valve was opened rapidly and the starter supply was turned on to 900 V. This procedure caused

an immediate establishment of a 2.0 A arc discharge to the starter electrode which was then easily transferred to the anode electrode.

The variation in the orifice plate temperature as a function of cathode run time is given in Fig. 30. The decrease in orifice plate temperature resulting from the change in power supplies at run hour 123 is clearly evident in this figure. Also evident is that subsequent to the change in power anode supplies, the orifice plate temperature remained essentially constant at approximately 1125°C until run hour 1,000. From this point on, the orifice plate exhibits a gradual increase in temperature with time. These data indicate an occasional significant decrease in orifice plate temperature. These decreases are accompanied by decreases in the temperatures of the cathode flange and cathode support plate as indicated by the thermocouples located there, as well as by changes in the discharge voltage.

Beginning after run hour 2950 measurements of the insert brightness temperature were made using the optical pyrometer looking at the insert surface through the cathode orifice. Comparisons of the insert and orifice plate brightness temperatures are given in Fig. 31 covering the time period from 2950 to 4000 hours of cathode operation. The insert and orifice plate temperatures appear to be relatively well correlated as one would expect. The unexpected feature of these data, however, is the high brightness temperature of the insert. Models of the insert barium depletion rate (as discussed in the next section) predict a very short life time for insert operation at the temperatures indicated in this figure.

The temperature of the stainless steel cathode flange as a function of run time is given in Fig. 32. The large spikes appearing in this figure correspond to cathode shutdowns. In general, the cathode flange temperature shows a slight, gradual increase with time. The anode current and voltage over this same time period are given in Figs. 33 and 34. The anode power supply is operated in the current regulating mode so that a constant 25 A anode current is maintained. The large spikes in the anode current correspond to cathode re-starts in which the cathode was operated at less than 25 A for a short time. On the compressed time scale of Fig. 33 these short time intervals appear as spikes. The corresponding discharge voltage versus time is shown in Fig. 34. At the beginning of the life test the discharge voltage was between 19 to 21 volts. After approximately 900 hrs the discharge voltage dropped to 18 V and remained there for 500 hrs. At approximately run hour 1400 the discharge voltage decreased to between 15 and 16 volts. This discharge voltage level was maintained for the next 1400 hrs, after which the discharge voltage began a gradual increase back to approximately 18 V. The discharge voltage spike at run hour 3069 corresponds to the flow controller failure.

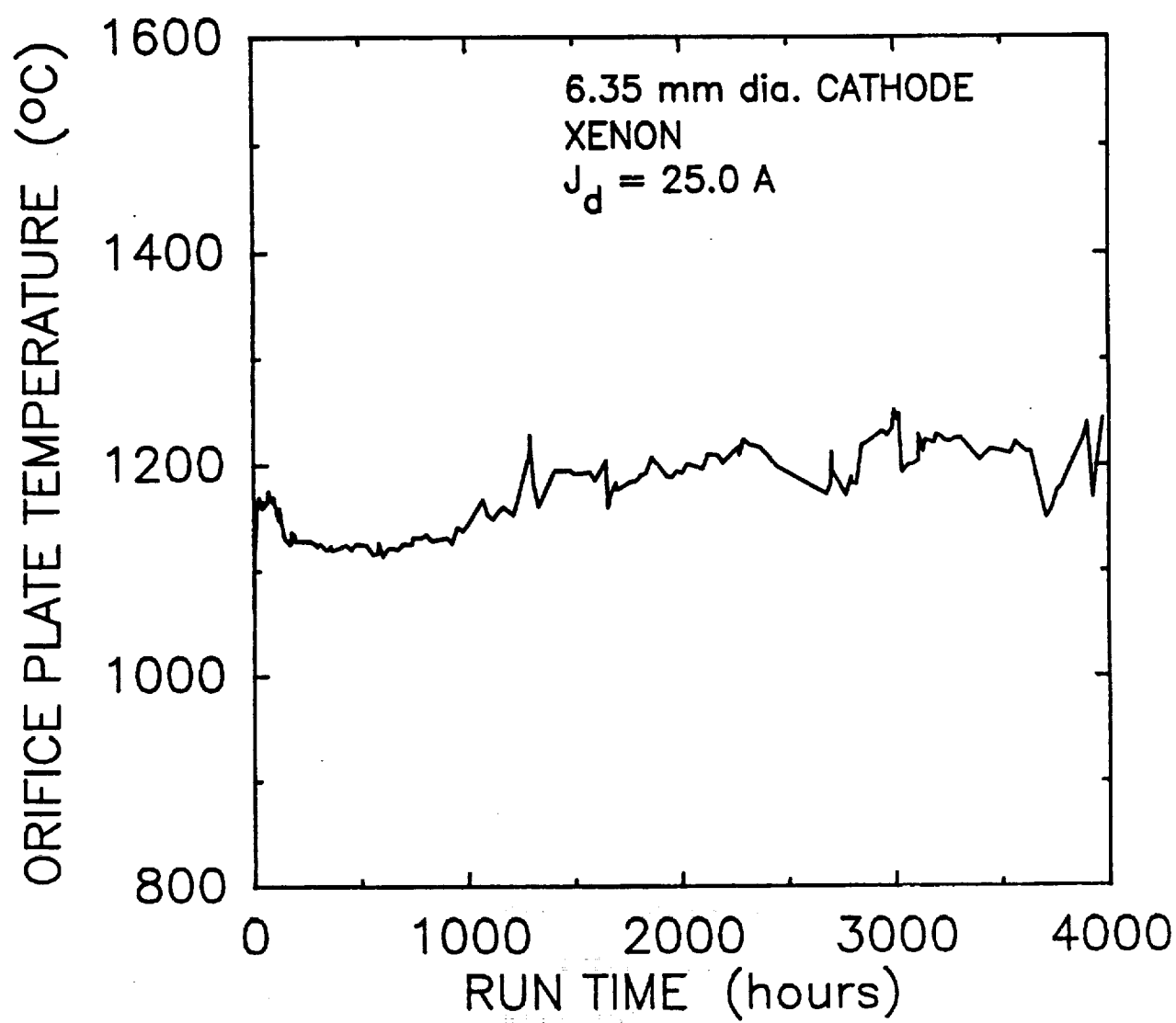


**Figure 30** Orifice plate temperature versus cathode run time.

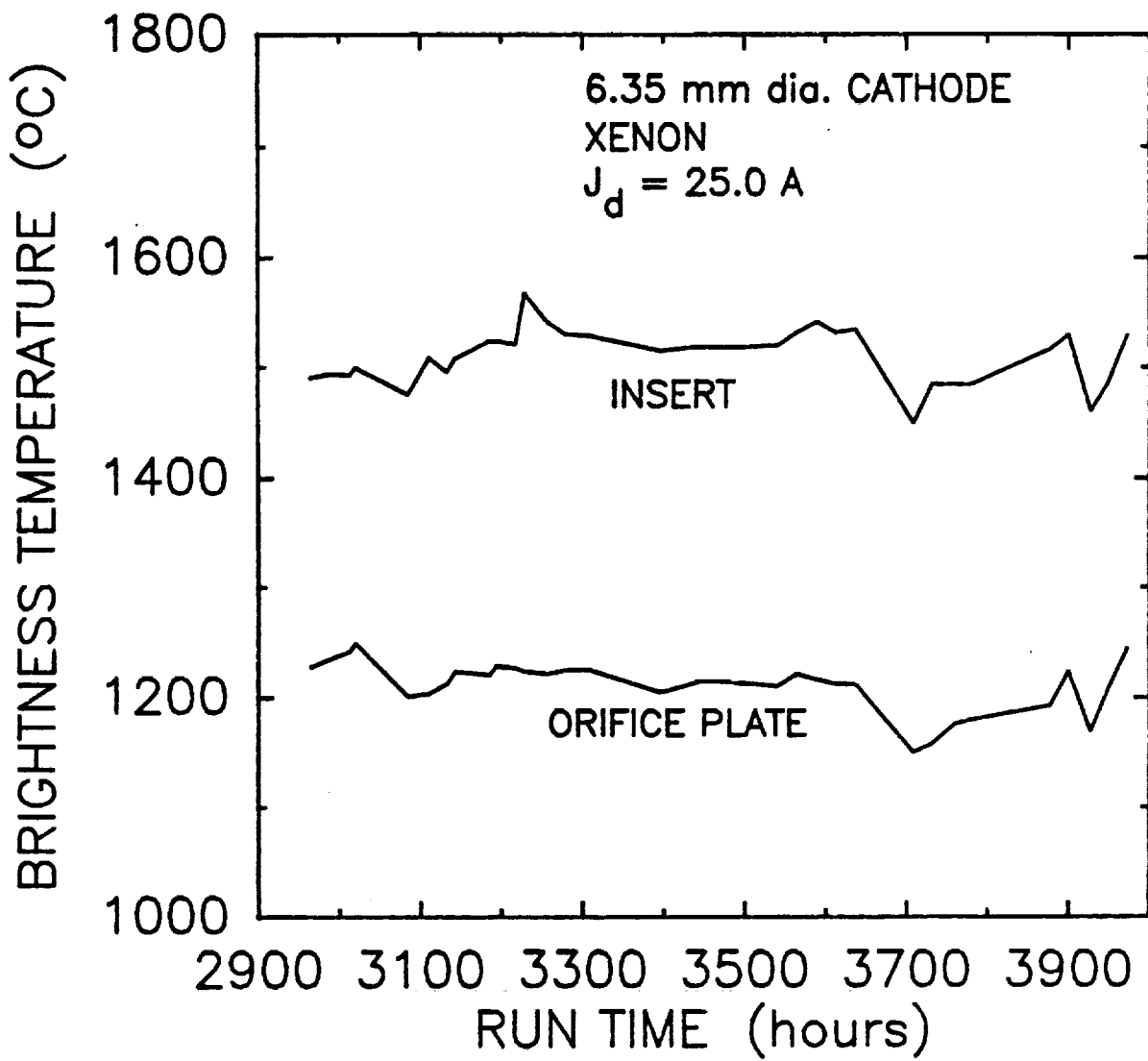


**Figure 31** Comparison of insert and orifice plate brightness temperatures as measured by the optical pyrometer.

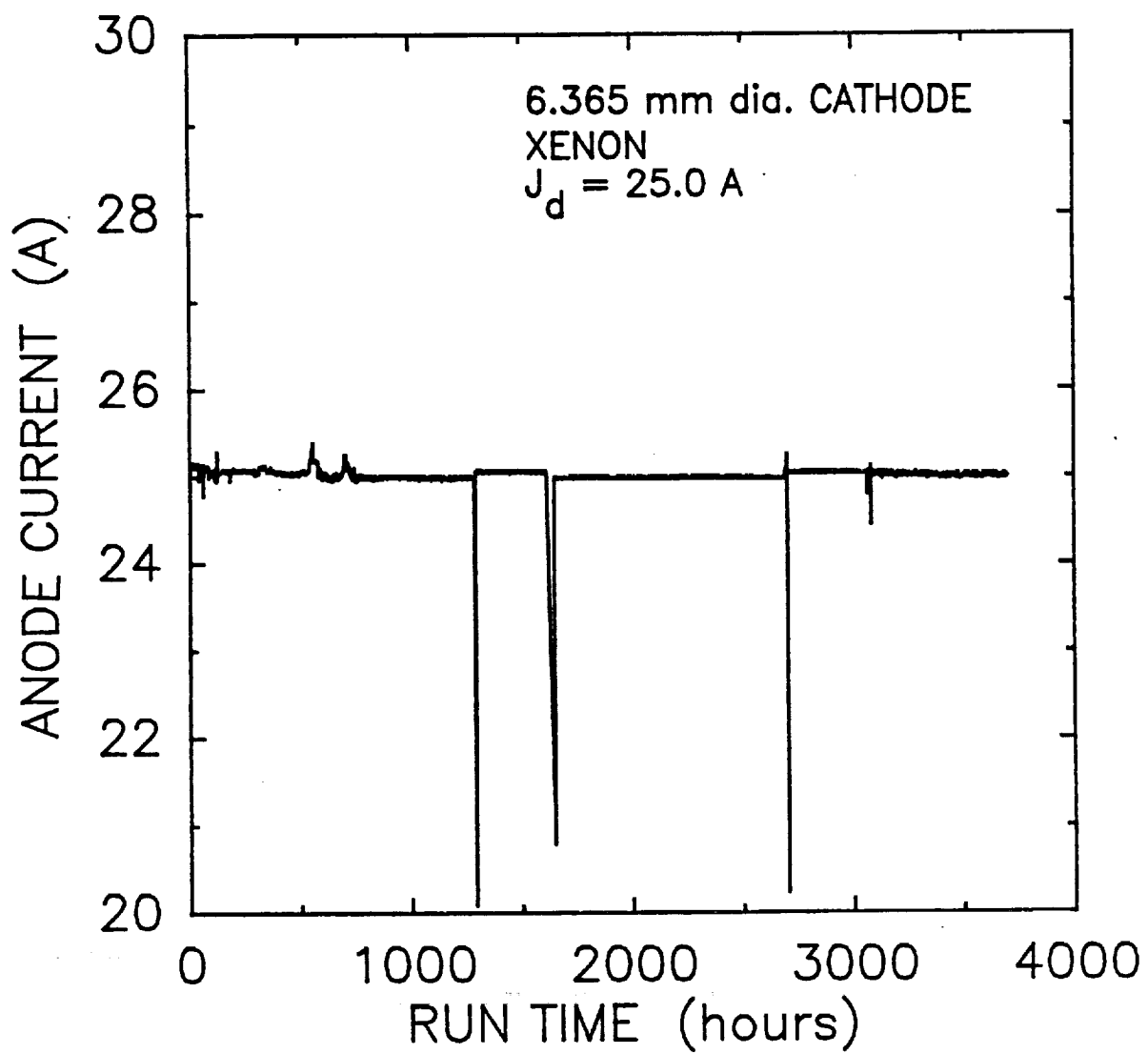


**Figure 32** Measured anode current during life test.

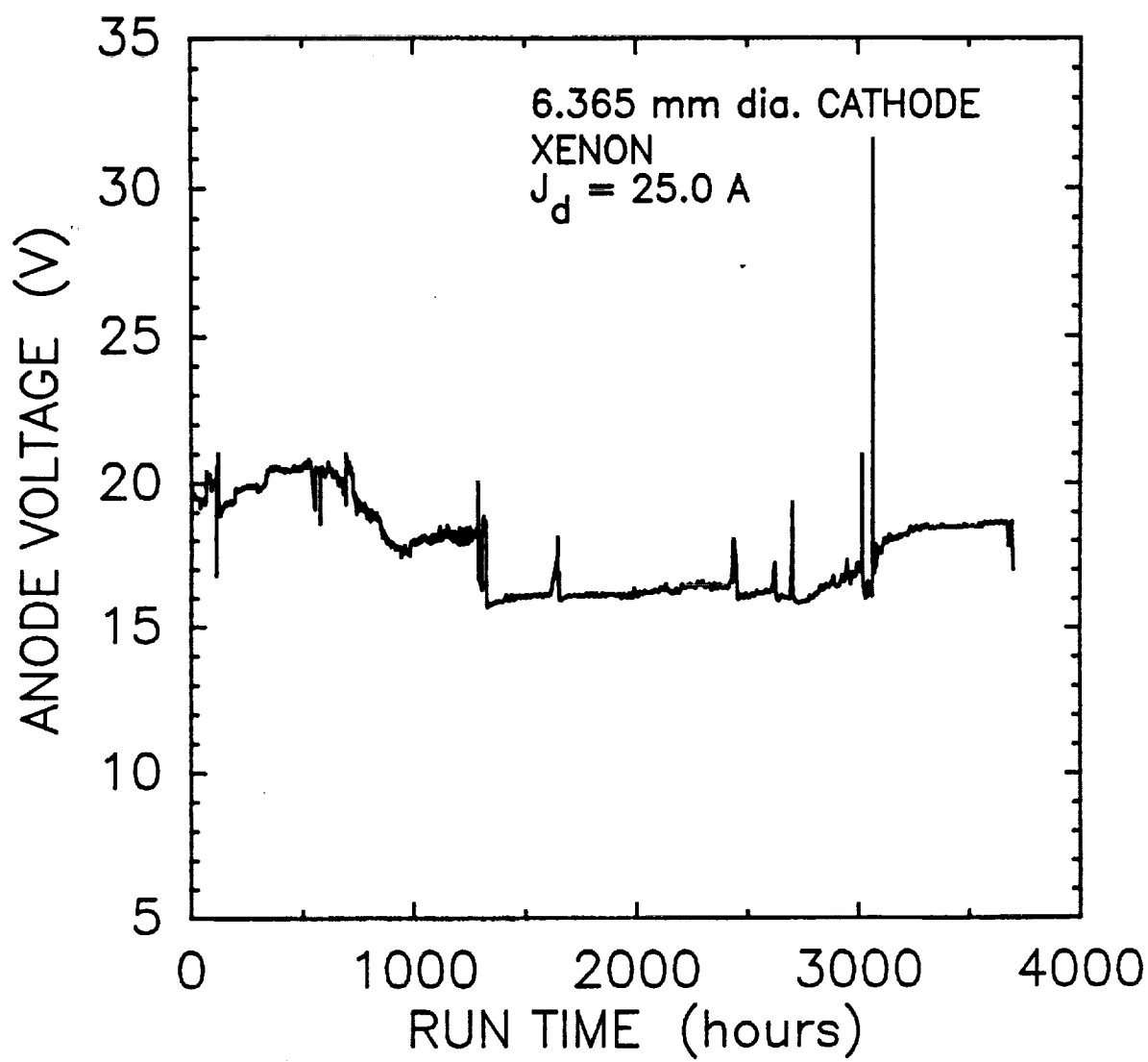


**Figure 33** Discharge voltage versus cathode run time.

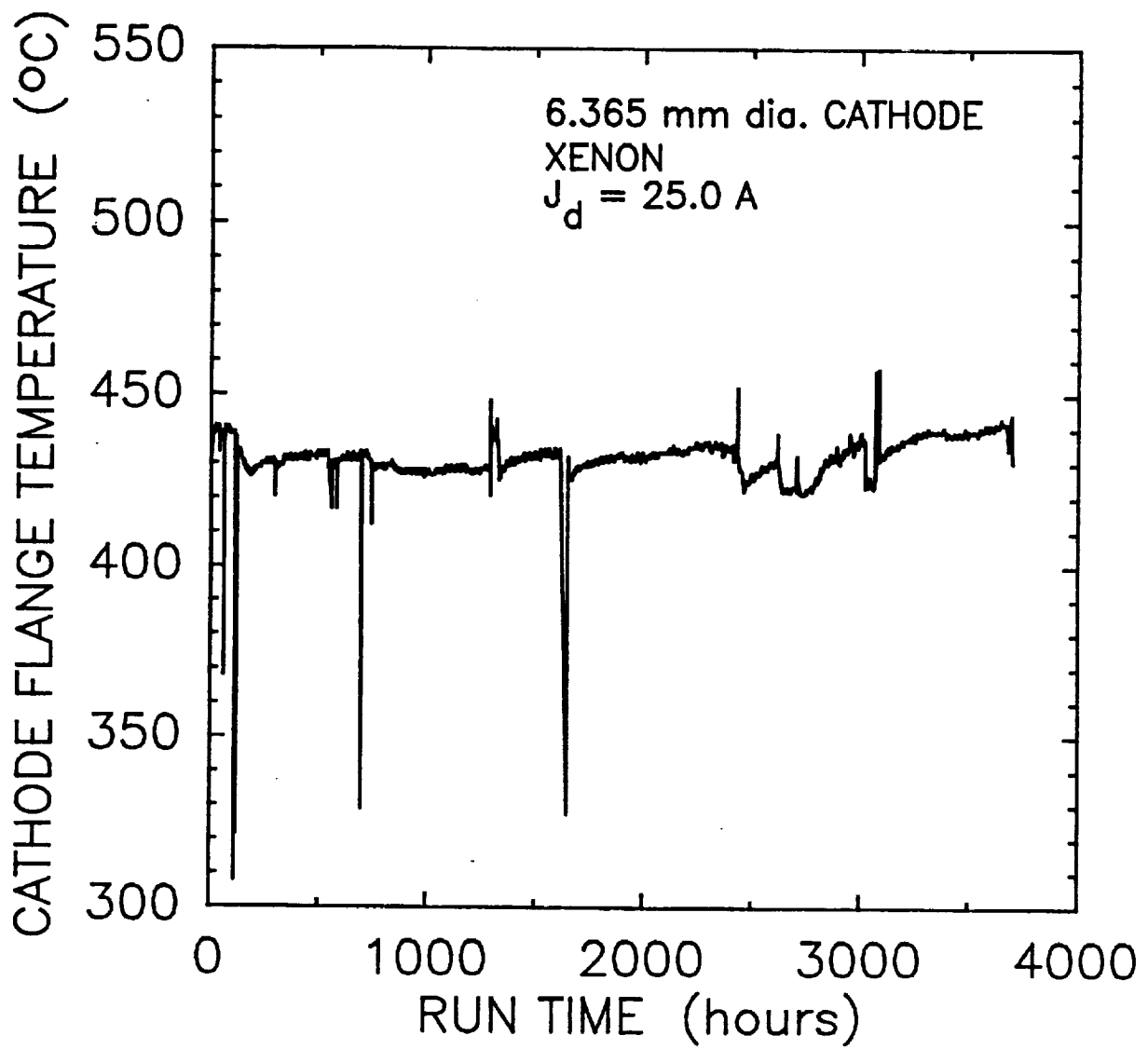


**Figure 34** Temperature of the stainless steel cathode flange versus cathode run time.

The xenon flow rate, as measured by the MKS thermal mass flow meter, and the interior cathode pressure are given in Figs. 35 and 36 over the first 3700 hours of cathode operation. The xenon flow rate is maintained approximately constant by the Sierra flow controller. Again, the spikes in the data represent short duration operation at other flow rate settings. The cathode pressure data indicate a slight, gradual increase in the interior pressure. This pressure increase is most likely a result of the increase in cathode operating temperature, since no obstructions to the xenon gas flow can be seen in Fig. 24. Finally, the keeper voltage versus run time is given in Fig. 37.

#### 6.4 Model of Cathode Insert Life

A cathode life time model, developed in Ref. 34, gives the fraction of barium lost from the insert as a function of insert temperature and operating time according to the equation

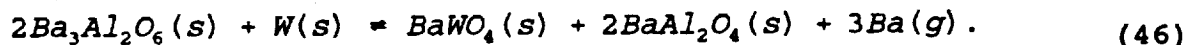
$$\frac{q}{q_0} = B e^{-a/T} t^{1/2}, \quad (43)$$

where  $a$  and  $B$  are constants with the values<sup>32</sup>

$$a = 1.61 \times 10^4 \text{ [K]} \quad (44)$$

$$B = 400 \text{ [hr}^{-1/2}\text{]}. \quad (45)$$

In general the chemical reaction for the production of barium on a hot tungsten surface is given by<sup>25</sup>



If this is the only reaction producing free barium, then only half of the initial barium can be used. The other half becomes locked-up in  $\text{BaWO}_4$  and  $\text{BaAl}_2\text{O}_4$ . However, because of other possible reactions that may take place inserts made of impregnated porous tungsten may be capable of dispensing between 1/3 and 2/3 of the total impregnated barium.<sup>23</sup> Thus, the most optimistic life time prediction would be obtained from Eq. (43) by assuming that 2/3 of the initial barium is available to lower the surface work function.

Assuming that the insert is at the brightness temperature of 1500°C as indicated in Fig. 31 and assuming that this temperature controls the insert life, then Eq. (43) predicts an insert life of only 321 hours to deplete 2/3 of the total barium ( $q/q_0 = 0.5$ ). Since the cathode has been operating for more than 4,000 hours, there is clearly a flaw in the reasoning. Equation (46) implicitly assumes that all of the barium that is evaporated from the surface is immediately lost from the cathode. However, as stated in Ref. 25, if the barium can be prevented from permanently condensing on non-emitting cathode surfaces, then a greatly increased insert life should result. This can be accomplished if these other cathode

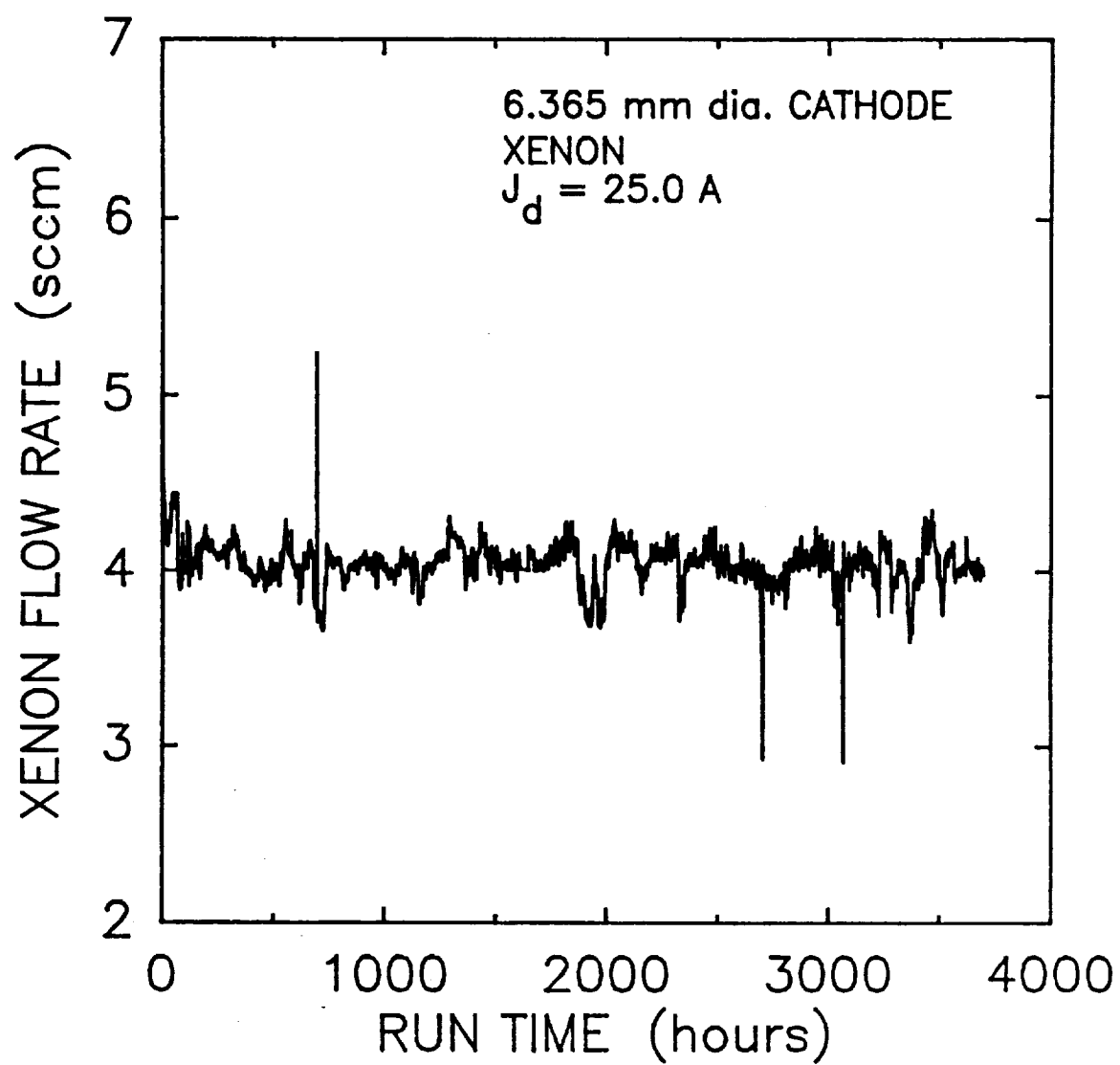


**Figure 35** Xenon flow rate versus cathode run time.

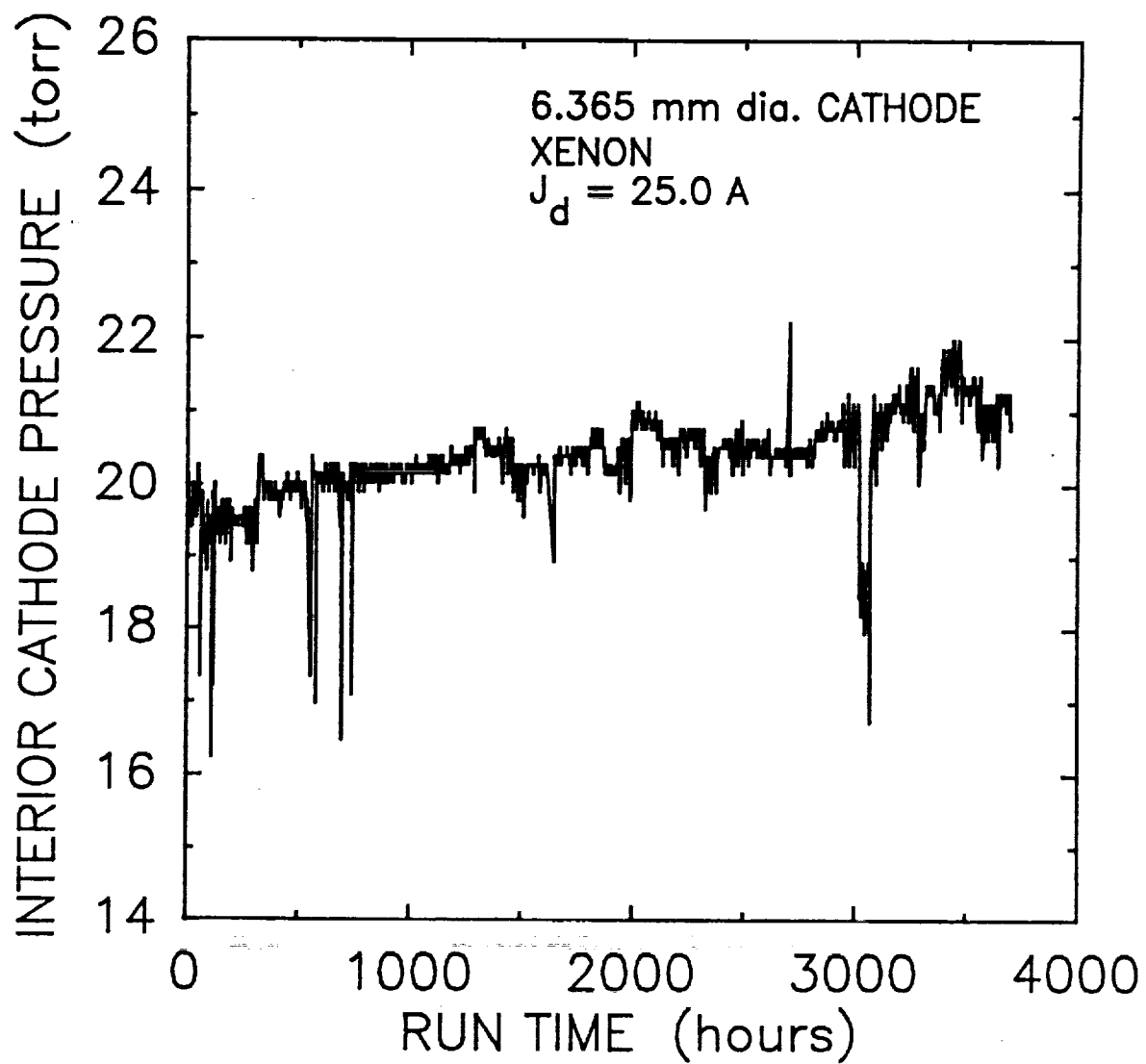


**Figure 36** Cathode internal pressure versus run time.

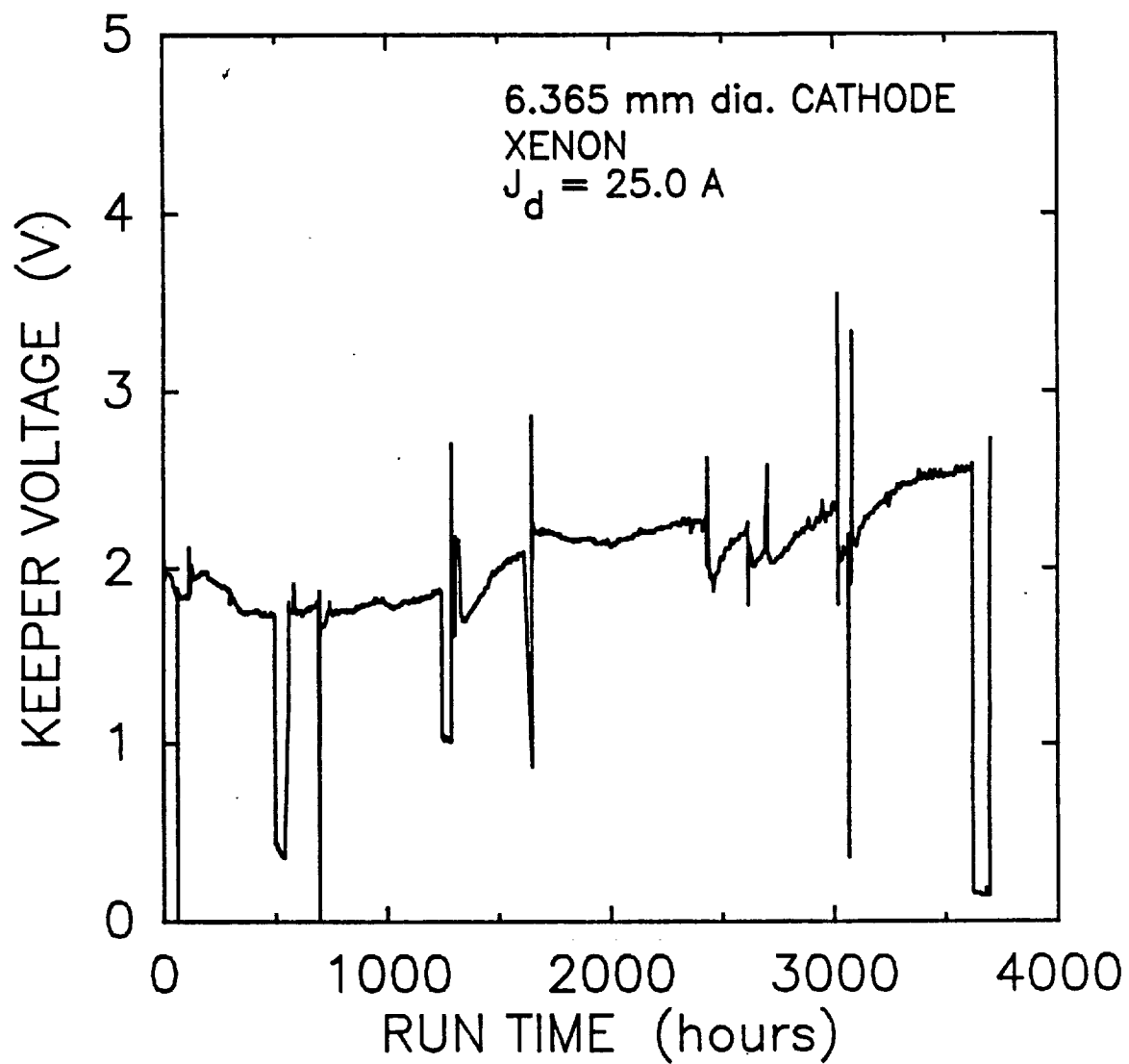


**Figure 37** Starter electrode (keeper) voltage versus cathode life time.

surfaces are maintained at or above 300°C, and preferably above 400°C.<sup>23</sup> In the present life test cathode, the temperature of the stainless steel flange at the back of the cathode is typically 430°C or greater, as indicated in Fig. 32, suggesting that the cathode life could be considerably greater than that predicted by Eq. (47). In this case, the barium that is evaporated from the insert may migrate to other cathode surfaces, but the temperature of these surfaces is such that the barium is prevented from condensing. Eventually, the barium may return to the insert surface. Under these circumstances, barium is lost from the cathode only through the cathode orifice.

It is unlikely, however, that this non-condensing feature of the life test cathode is sufficient to account for the difference in predicted and demonstrated cathode life times by itself. Other possibilities include:

1. A strong axial temperature gradient along the 25.4 mm insert length, resulting in an average insert life which is considerably greater than that determined by the temperature at the downstream end.
2. A true insert temperature which is significantly less than the brightness temperature indicated by the optical pyrometer. If the temperature of the orifice plate (approximately 1200°C) is used in Eq. (46), it is calculated that 4850 hours would be required to deplete half of the initial barium.
3. Barium reaction and evaporation rates at high temperatures that are significantly different than those represented by the constants in Eqs. (47) and (48). The life time predictions from Eq. (46) are very sensitive to the value of the constant which appears in the exponential function.

Clearly there is a need for increased understanding of barium impregnated, hollow cathode operation at high temperatures.

## 6.5 Summary

A hollow cathode life test is currently in progress to investigate the long term operating characteristics of xenon hollow cathodes operated at emission currents greater than 20 A. At the time of this writing a 6.35-mm diameter, molybdenum body, hollow cathode with a barium oxide impregnated porous tungsten insert has accumulated more than 4,000 hours of operation at an emission current of 25 A. Visual observations of the cathode orifice plate and starter electrode suggest that very little erosion of these components has occurred over this time period. Furthermore, no material deposits in the interior diameter of the cathode orifice can be seen. Variations in discharge voltage of several volts at

constant current and flow rate have been observed over the course of the life test. A gradual increase in the orifice plate temperature with time has been recorded. In addition to this gradual increase, changes in orifice plate temperature of  $\pm 50^{\circ}\text{C}$  have been observed over time periods of a few hundred hours. Restarting the cathode has become progressively more difficult over the course of the life test. Finally, optical pyrometer measurements of the insert brightness temperature indicate an insert temperature which is far too high to be consistent with a cathode life time of several thousand hours according to existing models.

## 7.0 FIXED FLOW RATE THROTTLING

### 7.1 Introduction

It has generally been accepted that ion engine throttling for outbound solar electric propulsion missions would be accomplished through a reduction in both beam current (i.e., propellant flow rate) and beam voltage. This throttling technique permits the largest variation in input power. The J-Series mercury ion engines were throttled in this manner, and were capable of operating over a 3.8 to 1 variation in input power.<sup>51</sup> Modification of these engines to run on xenon at higher power levels led to an engine which could be throttled over an 8 to 1 power range by varying both the beam current and the beam voltage.<sup>52</sup>

### 7.2 Throttling With Fixed Beam Current

The overall propulsion system for inert gas ion engines, however, could be greatly simplified if the engines could be throttled over a large variation in input power at constant beam current. In this case, power throttling would be accomplished by changes in the beam voltage alone. The simplifications made possible through constant beam current operation include the following considerations. Constant beam current implies engine operation with fixed propellant flow rates which, in turn, eliminate the need for active propellant flow controllers. In this case the fixed propellant flow rate is determined through the use of a pressure regulator and a flow restrictor. Constant beam current operation also implies operation at a single discharge current, thus eliminating the need for complex software which is currently required to control and throttle the engines.<sup>53</sup> Finally, life testing is significantly simplified since there is only a single discharge chamber operating point at which the engine must be tested. Long duration testing at fixed flow rate was first demonstrated in tests by Beattie et al.<sup>54</sup> in which a 25-cm diameter thruster was operated for more than 4,000 hours on xenon at a constant power level.

Operation at constant flow rate and constant beam current requires that engine throttling be accomplished through variations in beam voltage alone. Consequently, the allowable variation in beam voltage at constant beam current determines the throttling range. For the beam current to remain constant as the beam voltage is varied, the total voltage between the screen and accelerator grids must be constant. The total voltage is the sum of the magnitudes of the beam voltage and the accelerator grid voltage. As the beam voltage is decreased, the accelerator grid voltage must be increased in order for the sum to remain fixed. The allowable range of beam voltages for a fixed total voltage is determined by the ratio of the beam voltage, also referred to as the net voltage, to the total voltage as indicated in Eq. (47):

$$R = \frac{V_b}{V_t} \quad (47)$$

The maximum value of the net-to-total voltage ratio,  $R_{max}$ , occurs when the magnitude of the accelerator grid voltage is a minimum. The lower limit on the magnitude of the accelerator grid voltage is determined by the electron backstreaming limit. If there is insufficient negative voltage on the accelerator grid, then electrons from the neutralizer cathode will be accelerated into the engine by the positive high voltage. The result is a large power drain and very inefficient engine operation. Therefore, a certain magnitude of negative voltage must be applied to the accelerator grid to prevent this electron backing phenomena. In general, for a two-grid accelerator system, the maximum net-to-total voltage ratio is in the range 0.85 to 0.90.

The minimum value of the net-to-total voltage ratio occurs when the magnitude of the accelerator grid voltage is a maximum. The maximum accelerator grid voltage is determined by defocussing effects of the individual ion beamlets for each pair of screen and accelerator grid apertures. At low net-to-total voltage ratios the ions are accelerated through the full total voltage and then decelerated through the accelerator grid voltage, so that in the end the ions leave the thruster with an energy equivalent to only the net, or beam, voltage. The deceleration process defocuses the ion beamlets, and the greater the deceleration, the more the beamlets are defocused. The minimum net-to-total voltage ratio occurs when the beamlets are defocused to the point where they begin to impinge directly on the accelerator grid webbing. Data<sup>55,56</sup> obtained with mercury propellant indicated that the minimum net-to-total voltage ratio for a two-grid accelerator system was in the range 0.4 to 0.55. Three-grid accelerator systems have been successfully operated at net-to-total voltage ratios as low as 0.21.<sup>56,57</sup>

### 7.3 Effect of Fixed Flow Rate Throttling on Mission Performance

The effect of constant beam current throttling on mission performance for outbound solar electric propulsion missions is detailed in Refs. 58, 59, and 60, and is briefly summarized here. Performance comparisons between constant beam current and variable beam current throttling systems were made for a comet nucleus sample return (CNSR) mission to comet Kopff. A solar electric propulsion system was assumed to be used for the first leg of this mission. Specifically, the mission assumed an indirect rendezvous trajectory to Kopff launched in the year 2000 by a Titan IV-Centaur in which the electric propulsion system is used to deliver a payload of between 2000 and 3000 kg to the comet. A beginning-of-life solar array power level of 25 kW was assumed and this power level was derated by 10 % to allow for system and environmental

degradation. In addition, a constant housekeeping power of 400 W was assumed.

Mission performance calculations were performed for several propulsion system configurations and operating modes. For a fixed beam current of 4.0 A per thruster, system operating modes included a maximum of 3, 4, 5 or 6 simultaneously operating thrusters. Other calculations assumed a fixed beam current of 3.0 A per thruster and included cases with a maximum of 4 or 5 operating thrusters. Only one case was investigated for the variable flow rate throttling approach; a maximum of 4 operating thrusters was assumed. In each case, the number of operating thrusters was continuously varied during the mission in order to produce the best mission performance. The results of these calculations, which were made using a modified version of the trajectory optimization program EPITOP<sup>59</sup>, are given in Table 6.

**Table 6 Comparison of Throttling Strategies**

Throttling Strategy	Beam Current (A)	Maximum Operating Thrusters	Launch Energy $C_3$	Initial Vehicle Mass (kg)	Propellant Consumed (kg)	Final Vehicle Mass (kg)	Total Thruster Days
Constant Beam Current	4	3	17.7	5243	1364	3879	2607
	4	4	16.4	5357	1452	3905	2775
	4	5	15.9	5401	1490	3911	2849
	4	6	15.6	5421	1509	3911	2885
	3	4	17.5	5258	1279	3979	3258
	3	5	16.6	5335	1338	3997	3410
Variable Beam Current	1-4	4	17.0	5299	1246	4053	3444

Several interesting things are evident from the data in Table 6. First of all, the propellant expenditure is slightly higher and the total delivered mass is slightly lower for the constant beam current throttling cases than for the variable beam current case. It is expected that this comparison would be true for other types of SEP missions.<sup>59</sup> These mass differences are not considered to be significant, so that the constant beam current throttling appears not to affect the mission performance in a significantly adverse manner.

The second significant item is the total number of thruster-days required for the mission. A thruster-day represents one thruster operated for one day. This operating time can be used together with the number of thrusters in the system to calculate the required thruster life time. For example, the variable beam

current case required a total of 3444 thruster days. Multiplying this number by 24 hours/day and assuming that the propulsion system included 5 thrusters results in an engine life time requirement of 16,530 hours. For a 6 engine propulsion system the engine life time requirement is reduced to 13,780 hours.

It is evident from Table 6 that all of the constant beam current throttling cases require fewer total thruster-days than the variable beam current case. In some cases, significantly fewer thruster-days are required. For the 4.0 A constant beam current throttling case with a maximum of three thrusters operating, the number of thruster-days required is only 2607. If this propulsion system is comprised of 6 thrusters, then a useful thruster life time of only 10,400 hours is required. This is a 24% reduction in required thruster life compared to the 6-engine, variable beam current case, and a 37% reduction with respect to the 5-engine, variable beam current system.

The reduction in total number of thruster-days for the constant beam current throttling cases results from the engines being operated on average at higher thrust-to-power ratios than are typical for the variable beam current case. Thus, at each power level, the engines throttled at constant beam current are producing more thrust than would be produced at the same power level with variable beam current. Since the propulsion system is producing more thrust, the total thrusting time is shorter to produce the same total impulse. Clearly, the propulsion system configuration and throttling technique, in addition to the mission itself, have a substantial impact on the required engine technology, i.e., thruster lifetime and performance characteristics.

#### **7.4 Experimentally Determined Throttling Range**

Experiments were performed to determine the constant beam current throttling characteristics of a 30-cm diameter, two-grid accelerator system. These experiments were performed using a modified J-Series<sup>61</sup> divergent-field thruster. Modifications to the standard J-Series configuration included removal of the isolator and vaporizer heaters, replacement of the mercury high voltage propellant isolators with isolators designed for improved performance with inert gas propellants, replacement of the perforated ground screen with a solid ground screen, and replacement of all of the Teflon-coated, kapton wire with ceramic bead insulated wire. In addition, the standard J-Series thruster main cathode was replaced with a 6.35-mm diameter, molybdenum body, hollow cathode with a 2 % thoriated tungsten orifice plate. A tantalum-sheathed, tantalum heater wire was used for the cathode tip heater. Finally, the J-Series, tantalum-clad, iron baffle was replaced with a smaller (25.4-mm diameter) molybdenum baffle. All tests were performed using the standard J-Series, two-grid accelerator system.

Laboratory power supplies were used for the main and neutralizer cathode tip heater and keeper functions, as well as for the accelerator grid power supply. A parallel combination of two FMPPU main discharge supplies was used for the anode supply.<sup>61</sup> A custom high voltage power supply fabricated by the Spellman Corporation was used for the screen supply and could provide voltage regulated power at up to 4.0 A and 2.0 kV. The negative high voltage accelerator grid power supply was also voltage-regulated and provided up to 100 mA at -2.0 kV.

All throttling tests were performed with a beam current of 3.2 A. This beam current level is the same as that used in the recent endurance test of a 30-cm diameter ring cusp thruster<sup>48</sup> and was selected for that reason. The allowable variation in net-to-total voltage ratio at this beam current is given in Fig. 38 for a total voltage of 1840 V and a discharge voltage of 28.5 V. These data indicate a minimum value for the net-to-total voltage ratio of 0.29. At values of  $R$  less than this, beamlet defocussing results in direct ion impingement on the accelerator grid, resulting in a sharp increase in the accelerator grid current  $J_a$ . This lower limit on  $R$  is considerably less than the 0.40 to 0.55 values reported in the literature for two-grid accelerator systems; however, similar results have been recently obtained at NASA Lewis Research Center which support this new lower limit.<sup>62</sup>

This lower limit for the net-to-total voltage ratio enables a significant power throttling capability at constant beam current with two-grid accelerator systems. It was previously believed that it would be necessary to use a three grid system in order to obtain a sufficiently large power variation. The throttling characteristics for a constant beam current of 3.2 A are given in Figs. 39-41 where the thrust, specific impulse and total engine efficiency are given as functions of the engine input power. These data indicate a maximum to minimum power variation of almost 3 to 1.

Finally, it should be noted that although constant beam current throttling has many advantages over the more conventional variable beam current approach, there is one potentially very serious disadvantage. That is, operation at very low net-to-total voltage ratios implies the use of relatively large negative accelerator grid voltages. These large negative voltages may aggravate an already severe accelerator grid erosion problem.

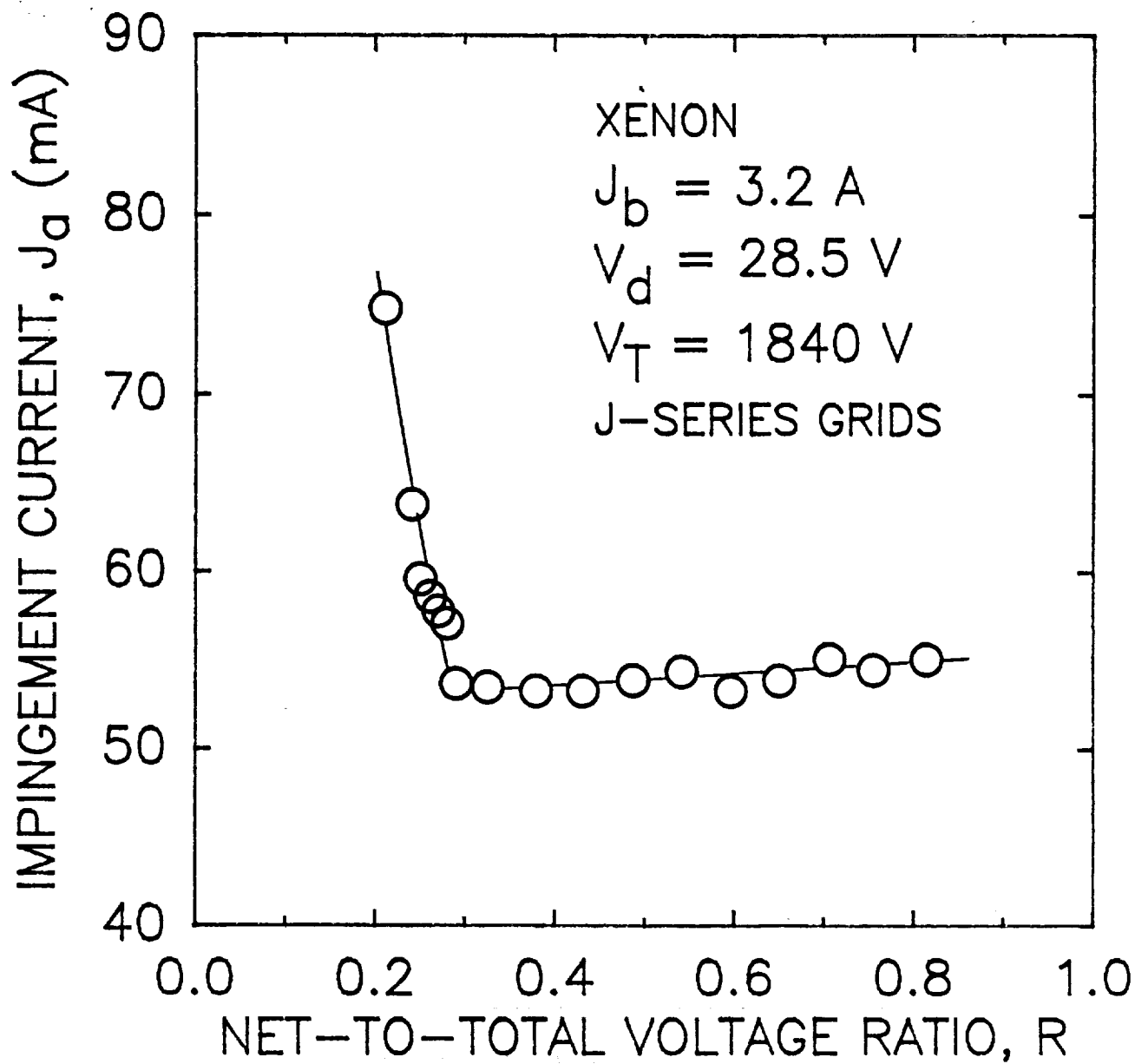


**Figure 38** Experimentally determined variation in net-to-total voltage ratio for two-grid accelerator system.

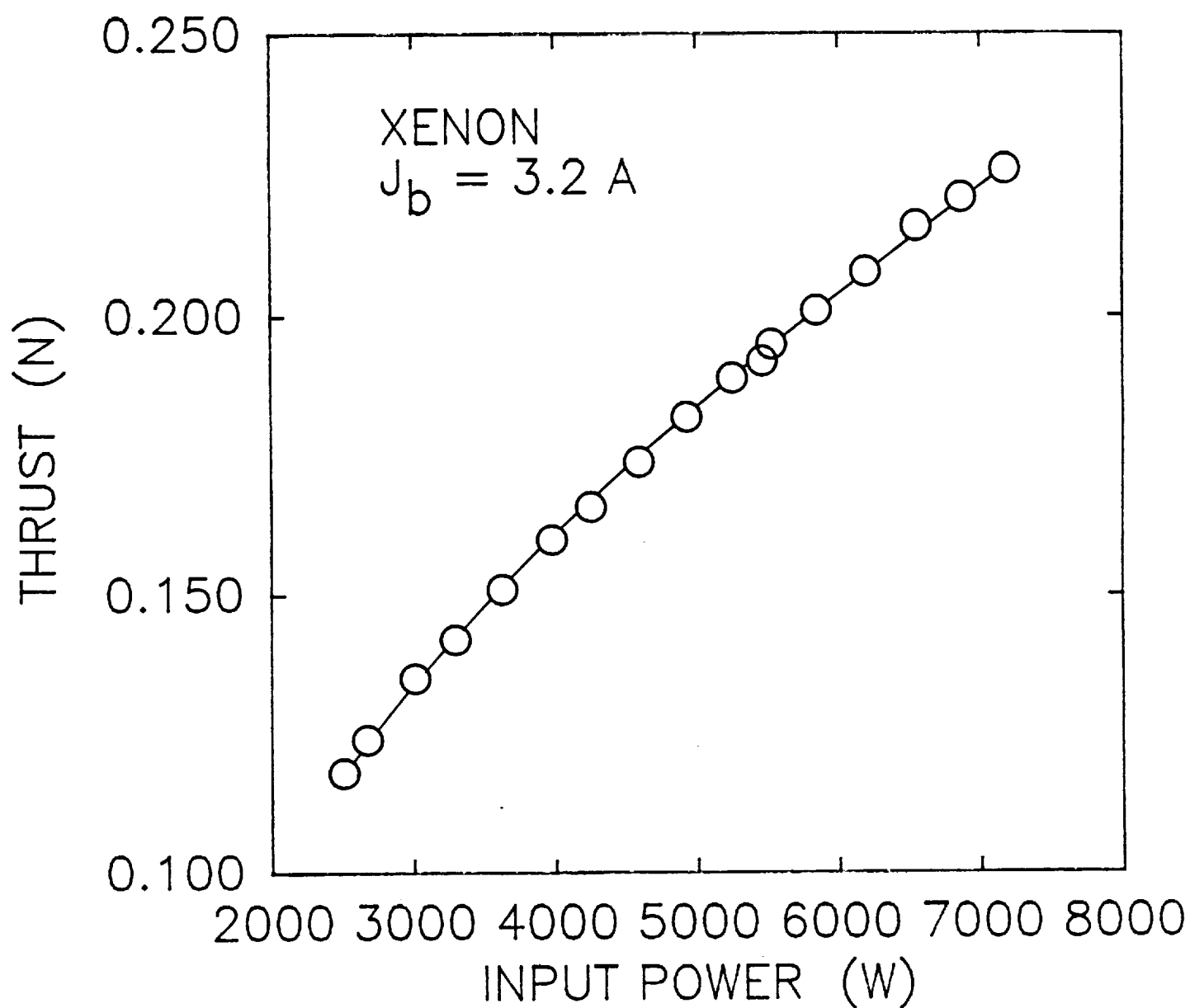


**Figure 39** Thrust variation over input power throttling range with constant beam current of 3.2 A.

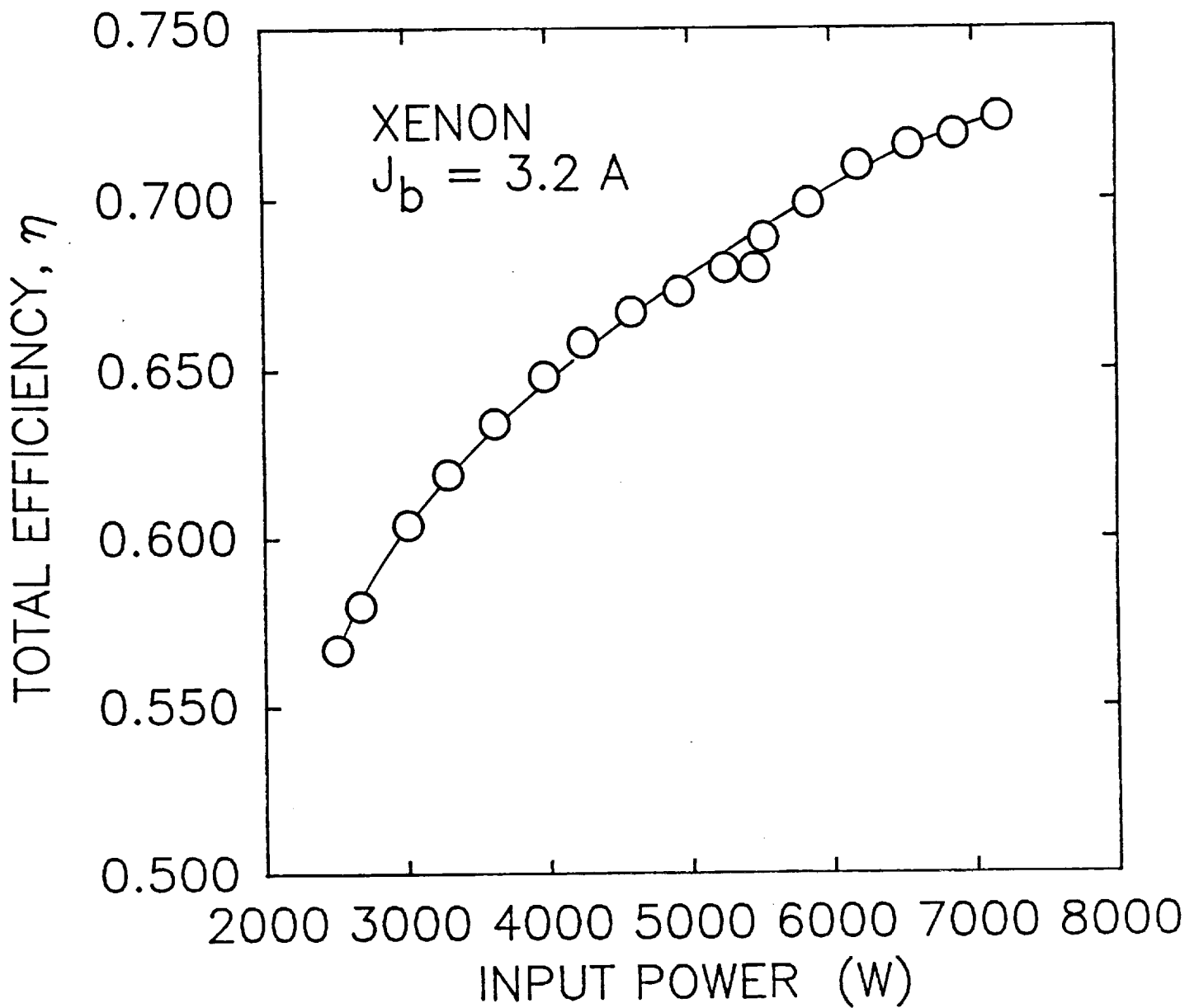


**Figure 40** Efficiency variation over input power throttling range at constant beam current of 3.2 A.

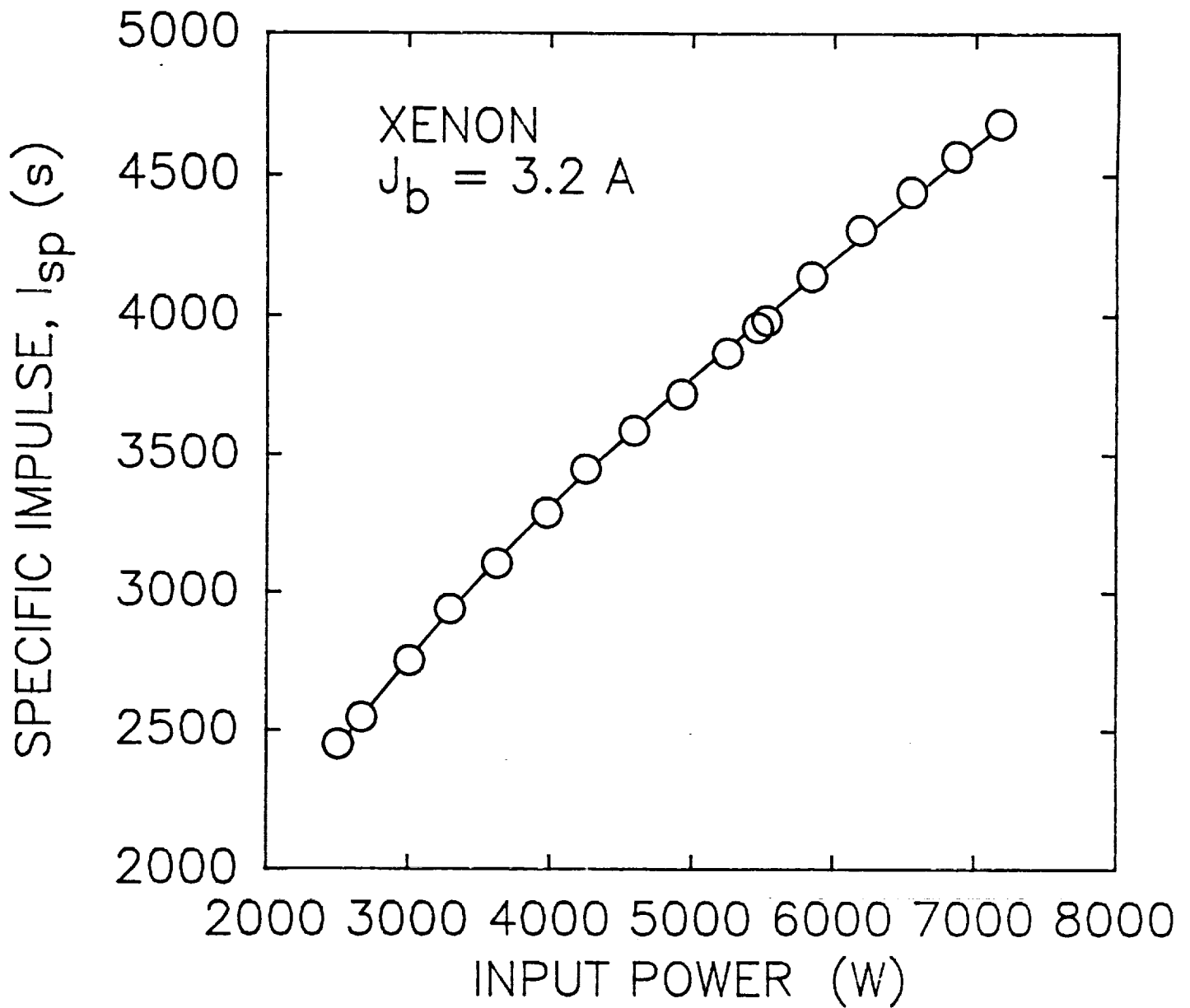


**Figure 41** Specific impulse variation over input power throttling range at constant beam current of 3.2 A.

## 8.0 CAPACITANCE MEASUREMENT FOR ACCELERATOR SYSTEM DIAGNOSTICS

Ion engine accelerator systems typically consist of two closely spaced, perforated electrodes. The performance of the accelerator system is strongly dependent on the electrode spacing. Both normal and abnormal handling of the accelerator system can alter the grid spacing when the electrodes are at room temperature. Furthermore, radial and grid-to-grid temperature differences occurring during normal engine operation result in thermal expansion effects which can alter the hot grid spacing.

Conventional techniques to measure the room temperature grid separation include the use of feeler gauges and optical refocusing techniques. Both of these techniques provide grid separation information at discrete locations, but are tedious to implement and require considerable handling of the accelerator system. Several approaches to measuring the grid separation at normal operating temperatures (typically 300 to 500°C) have also been investigated. These approaches include: the use of dial indicator gauges in direct contact with the grids<sup>63</sup>, the use of calibrated pins attached to the screen grid and extending through the accelerator grid apertures<sup>64</sup>, and various optical techniques. Each of these techniques provides grid separation information at discrete locations with varying degrees of resolution.

The capacitance measurement technique makes use of the relationship between the capacitance of two parallel plate electrodes and their separation, which is given by the equation

$$C = \frac{\epsilon_0 A}{d} \quad (48)$$

Measurement of the total capacitance of the accelerator system due to the juxtaposition of the perforated electrodes results in a number which is proportional to the average electrode separation. Any change in total capacitance is an indication of a change in the average grid separation. This technique is very easy to apply, is non-intrusive, and can be used to provide such critical information as the repeatability of the cold grid separation after thermal cycling or handling operations.

In addition, the technique can be used to indicate the change in average grid separation due to thermal effects generated by normal engine operation. In this case, the engine would be operated until the accelerator system reached thermal equilibrium, at which point the engine would be shut down completely, and the screen grid and accelerator grid leads would be switched into the capacitance measuring circuit. The accelerator system capacitance versus time would be recorded as the grids cooled down.

Preliminary bench tests have been performed with two sets of

30-cm diameter J-Series grids. The first grid set has a nominal grid separation of 0.64 mm (0.025 in). This accelerator system has a total capacitance at room temperature of 1089 pF (including the insulator shadow shields) as measured using a Hewlett-Packard 4280A 1 MHz C Meter. The second grid set has a nominal grid separation of 0.38 mm (0.015 in.). The smaller grid separation for this accelerator system resulted in a measured capacitance of 1515 pF, which is nearly 40% greater than that for the larger grid separation. Preliminary bench tests performed using a heat lamp to heat the accelerator system from the screen grid side indicated that thermal effects can induce changes on the order of 10 % in the total capacitance. In addition, these tests indicated that after cooling back down to room temperature the total measured capacitance returned to its original value (within approximately 0.1%).

A second, related application of the capacitance measurement technique is based on the use of very small pairs of flat plate electrodes which are attached to, but electrically isolated from, the accelerator system grids at discrete locations of interest. The capacitance of each pair of electrodes is proportional to the local grid separation. This technique is more difficult to implement than the global capacitance measurement discussed above, but provides more detailed information.

## 9.0 SEGMENTED ION THRUSTER

The use of ion propulsion in support of the Space Exploration Initiative will require the development of individual ion engines which can process input powers in the range of 100 kW to greater than 1,000 kW at specific impulses in the range of 7000 to 10,000 s. Space charge effects in the accelerator system of ion engines place an upper limit on the thrust density (and hence power density) which ion engines can achieve at a given specific impulse. Therefore, to increase the power and thrust capabilities of an ion engine it is necessary to increase the area of the ion accelerator system while maintaining a constant thrust density. The most straightforward approach to increasing the accelerator grid area is to simply increase the engine diameter. To maintain a constant thrust density, as the engine diameter is increased, requires that the grid-to-grid separation remain constant.

This requirement results in increasing values of the grid span-to-gap ratio, i.e., the ratio of the accelerator system diameter to the grid separation. The current state-of-the-art, 30-cm diameter, ion accelerator system has a span-to-gap ratio of approximately 500. The span-to-gap ratio is limited by mechanical constraints imposed by fabrication and handling procedures, as well as by thermal effects which serve to alter the grid separation during normal engine operation.

Near-term development of > 100 kW argon ion engines may be achieved through the use of the innovative Segmented Ion Thruster (SIT) design approach. This approach uses six distinct ion source chambers (or segments) along with six discrete accelerator systems as suggested in Fig. 42. The six individual ion source segments are configured to operate as a single ion engine from a single power processor unit as suggested in Fig. 43. This single power processor unit consists of six individual anode power supplies (one for each ion source segment), a single positive high voltage screen supply, a single negative high voltage accelerator supply, a neutralizer tip heater supply and a neutralizer keeper supply. The use of multiple anode supplies is probably the easiest way to assure equal current sharing between the cathodes. Multiple anode supplies with multiple cathodes were used successfully in 1.5-m diameter ion thruster tests for operation at power levels up to 130 kW.<sup>65</sup>

The switches in the dashed box labeled "SW1" are used to enable the anode power supplies to heat the main discharge chamber cathodes for engine start-up. Once the cathodes have been heated, the anode power supplies are switched to the anode electrodes for cathode ignition and normal operation. The switches in the dashed boxes "SW2" and "SW3" are used to isolate individual ion source segments from the high voltage power supplies. This feature is not essential, but enables failed segments to be removed from the

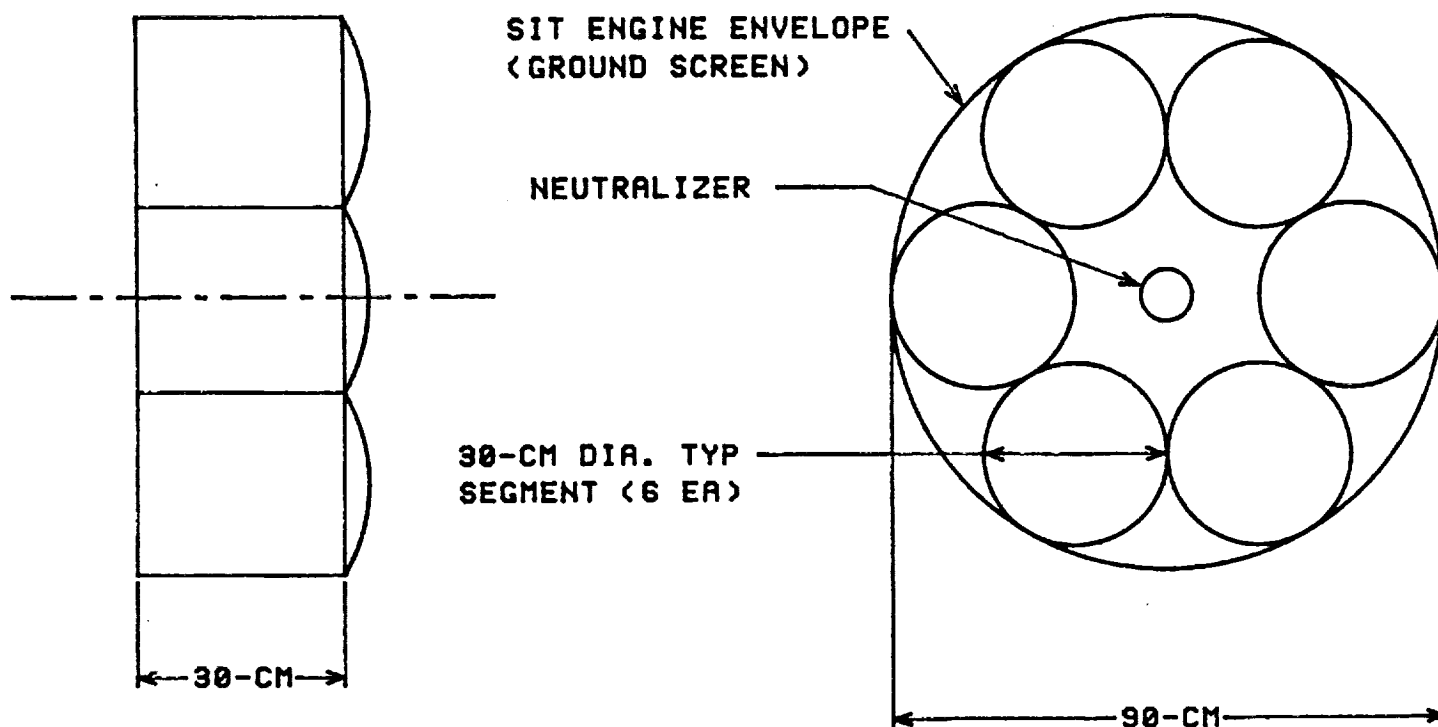


**Figure 42** Segmented ion thruster schematic with six 30-cm diameter segments.

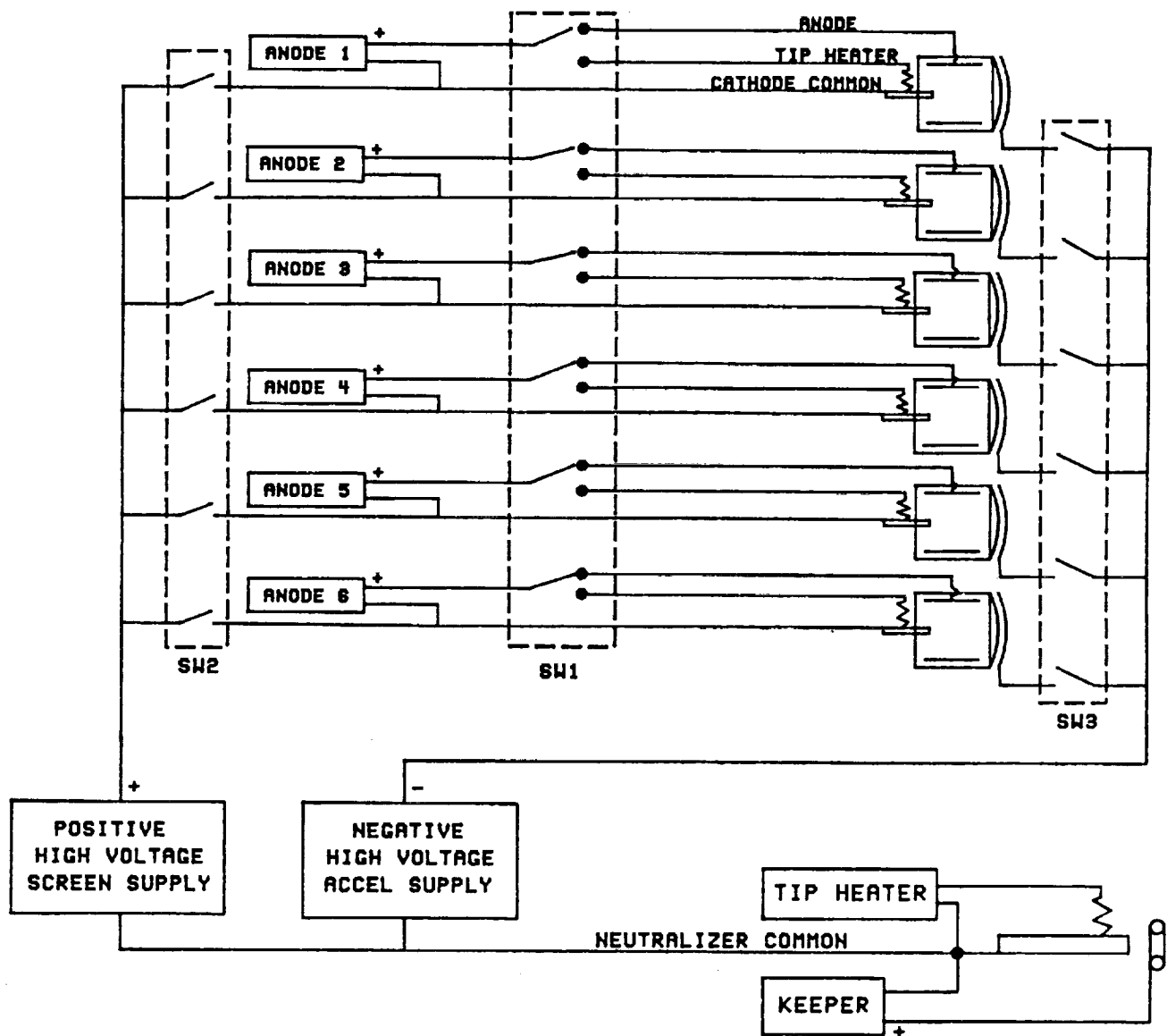


**Figure 43** Power processor configuration for the segmented ion thruster.

system, allowing the segmented ion thruster to continue to function at reduced thrust.

The total accelerator system area for the segmented ion thruster is six times the area of each individual ion source segment. This approach enables large total accelerator system areas to be achieved through the use of smaller, more manageable individual ion source diameters. The use of relatively small ion chamber diameters solves the span-to-gap problem central to the development of large area, high power ion engines. Furthermore, each segment has its own hollow cathode which operates at one sixth the total engine discharge current. This decreased discharge current requirement, together with the use of one cathode per chamber, minimizes the cathode-jet problem of high-current hollow cathodes, solves the plasma uniformity problem characteristic of large diameter engines, and eliminates the starting problems associated with the use of multiple cathodes in a single discharge chamber.

The SIT engine also has the advantage of failing gracefully. Failure of one chamber results in the loss of only one sixth of the total engine thrust, not in complete engine failure. This feature can also be taken advantage of to throttle the engine. Engine throttling can be accomplished by turning off individual segments, thus enabling a minimum 6-to-1 thrust and power throttling range (for a six-chamber SIT configuration). The SIT approach is applicable to any individual chamber size. Projected SIT engine performance values are given in Table 7 for individual segment diameters of 30, 50 and 90 cm. Each SIT engine in this table is comprised of 6 segments and is assumed to use argon as the propellant. The power levels at the top of each column refer to the input power to the power processor unit (which is assumed to be 93 % efficient).

The 100 kW SIT column in Table 7 refers to relatively conservative engine performance which could be achieved using six 30-cm diameter chambers. This SIT thruster has a total grid area equivalent to a conventional 70 cm diameter circular engine, which is significantly beyond the current state-of-the-art, yet the performance requirements for each individual segment are well within current capabilities. The 130 kW SIT column refers to the same SIT engine design as for the 100 kW SIT engine with the exception that somewhat more optimistic segment operating parameters are assumed. The data in this column indicate that with the SIT design approach, a 130 kW argon ion engine operating at a specific impulse of 10,000 s could be fabricated while requiring almost no advancements to the state-of-the-art of engine components.

The third column in this table indicates the performance made possible by the SIT design approach using the 50-cm diameter ion source under development at NASA Lewis Research Center.<sup>66</sup> In this

**Table 7 Projected Performance of Segmented Ion Thrusters**

	100 kW SIT	130 kW SIT	400 kW SIT	1000 kW SIT
Number of Segments	6	6	6	6
Segment Diameter (cm)	30	30	50	90
Specific Impulse (s)	10,000	10,000	10,000	10,000
Power into Power Processor Unit (kW)	100	130	400	1,000
Engine Efficiency	0.71	0.71	0.71	0.71
Thrust (N)	1.36	1.83	5.44	13.6
Total Grid Area (m <sup>2</sup> )	0.383	0.383	1.11	3.69
Equivalent Diameter (m)	0.70	0.70	1.19	2.17
Engine Mass (kg)	60	60	140	300
Each Segment				
- Input power (kW)	15.5	21.0	62.2	156
- Beam Current (A)	4.75	6.42	19.1	47.7
- Discharge Current (A)	33.9	45.8	136	426
- Grid Gap (mm)	1.11	1.11	1.11	1.29
- Beam Voltage (V)	2990	2990	2990	2990
- Total Voltage (V)	3225	3225	3225	3860
- Span-to-Gap Ratio	257	257	438	700
- Screen Hole Dia. (mm)	3.69	3.69	3.69	4.29

case each 50-cm diameter segment would be required to process 62 kW, with a beam current of 19.1 A and a discharge current of 136 A. Achieving these performance values will require modest advancements to the state-of-the-art. It should be noted, however, that argon hollow cathodes have been operated at discharge currents of up to 150 A for as long as 24 hours, and at 100 A for over 1,000 hours.<sup>42</sup> In addition, the accelerator system span-to-gap ratio required for this design is only 438, which is less than the current state-of-the-art. This results from the higher voltage and corresponding large grid separation characteristic of operation at a specific impulse of 10,000 s. The total grid area for this engine is equivalent to a 110 cm diameter circular thruster. The data in this column suggest that a 400 kW argon ion engine based on the SIT design approach could be developed relatively easily.

Finally, the last column in Table 7 indicates the projected performance level for a 1 MW SIT engine and the attendant performance requirements for each individual segment. In this case, each segment is required to be 90 cm in diameter, with an accelerator system span-to-gap ratio of 700 and individual discharge currents of over 400 A. These requirements are beyond the current state-of-the-art, but are not so far beyond it as to be unreasonable.

## 10.0 BAFFLE EROSION STUDIES

### 10.1 Introduction

During the 1970s the 30-cm mercury ion engine, culminating with the J-series ion engine, was developed to technology readiness level 6. The operating life of the J-series ion engine at the 2.7 kW power level was limited by spalling of metal films which were eroded from the baffle, a component placed just downstream of the cathode (Fig. 44). These film flakes could become trapped between the screen and accelerator grids and short them out.

For several reasons, inert gases have replaced mercury as the propellant of choice for interplanetary and earth-orbital ion propulsion systems. Erosion rates within the ion engine discharge chamber, however, are greater with inert gas propellants than the corresponding rates with mercury. This is due to the higher sputter yields of the inert gases as compared to mercury, and to the fact that inert gas ion engines are often operated at discharge currents greater than those used on the J-series mercury ion engine.

Data on erosion and wear rates within the discharge chamber of ion engines operated on inert gases are limited. During the 5 kW, xenon ring-cusp thruster wear test recently conducted at the NASA Lewis Research Center (LeRC), the cathode starter electrode eroded completely away within 890 hours. The neutralizer and engine cathode orifice plates were also heavily eroded. In high current hollow cathode testing conducted at JPL, significant erosion of the pole piece, baffle, and other components was observed in the vicinity of the hollow cathode operated on argon at 100 amperes, in spite of the low discharge voltage (less than 24 volts) which was used in the test.

Data presented in the following paragraphs summarize the results of a three year investigation conducted at JPL on cathode side baffle erosion and its relationship to cathode current density. A more in-depth discussion of discharge chamber erosion is presented in Appendix A.

### 10.2 Discussion

In 1987-1989, J-series ion thruster erosion testing with xenon propellant at JPL revealed unexpectedly high erosion rates and highly peaked erosion profiles on the cathode side of the baffle.<sup>67,68,69</sup> In tests subsequently conducted at LeRC<sup>70</sup>, the erosion rates of the cathode side of the baffle were measured to be between 40-90 times the erosion rate observed on the Mission Profile Life Tests (MPLT) conducted on the 2.7 kW J-series ion engine operated on mercury propellant in 1979-1981. The mechanism responsible for these severe erosion rates was not understood.

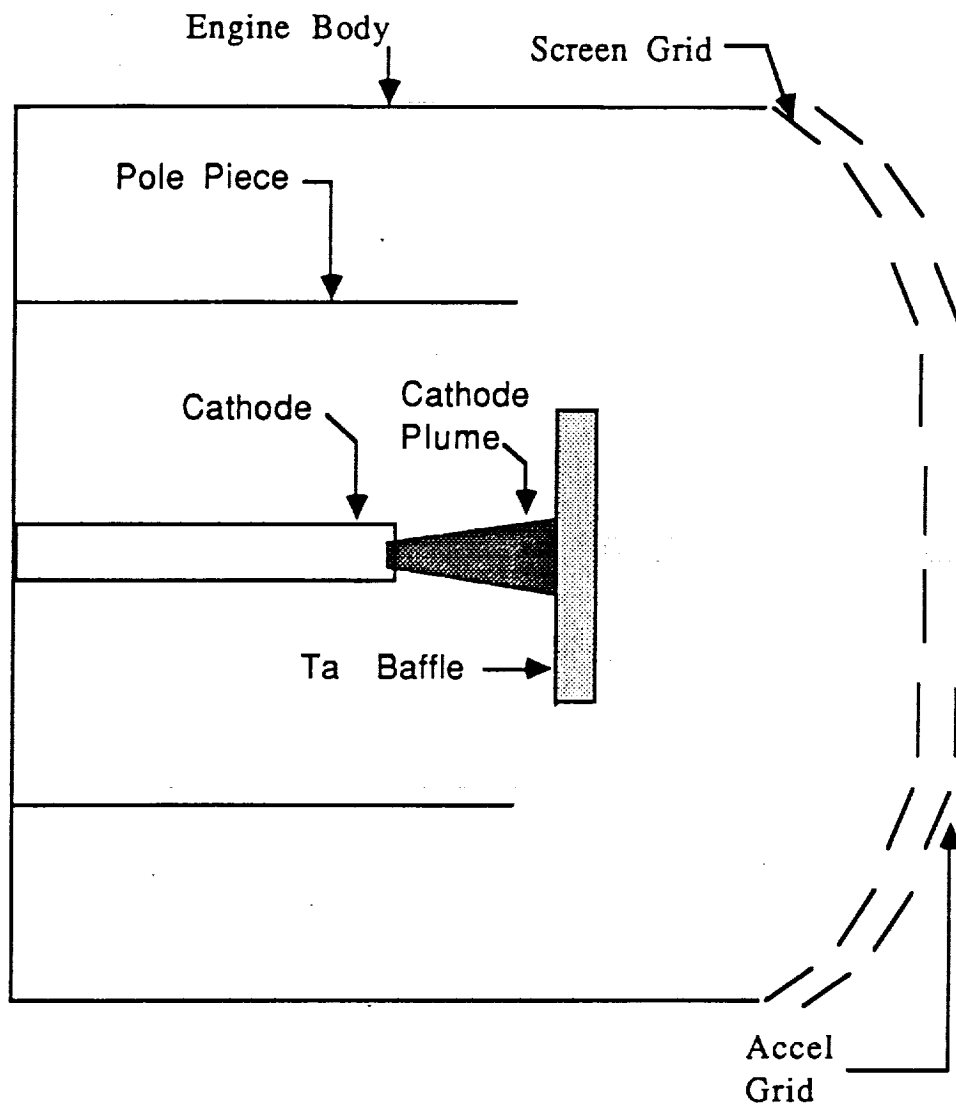


**Figure 44** Ion engine sketch showing cathode plume and the location of the baffle.

It has also been observed in tests at JPL that during the first 160 hours of operation of a new cathode, the erosion rates at the baffle were extreme, approaching 20,000 angstroms per hour. Baffle erosion rates appear to drop significantly afterwards. Thus preliminary indications are that the baffle erosion decreases as the cathode ages, until a steady-state value is reached.

During testing conducted in 1988 on a high current hollow cathode<sup>71</sup> it was observed that a well-defined and collimated plume was produced by the cathode when it was operated at a high emission current. A section of the anode face plate 15 cm downstream of the cathode was eroded, even though this face plate was at anode potential. As a result of this testing it was suggested that a cathode jet having ion energies of tens of electron volts might be the mechanism responsible for the high erosion rates observed at the cathode side of the baffle.<sup>71</sup>

It was hypothesized that the formation of the cathode jet was related to the current density through the cathode orifice. Thus, for a fixed cathode emission current, increasing the cathode orifice will reduce current densities at the cathode orifice, and consequently minimize the effects of the cathode jet. In 1990 some experimental data to support this conjecture were obtained at JPL and are shown in Fig. 45. In this figure, the cathode side baffle erosion rates from three experiments are plotted as a function of the distance from the baffle center. In these experiments the cathode emission currents (discharge currents) were almost identical; the discharge voltage in all tests was 32 volts. However, there are two significant differences in the characteristics of the three sets of data. First, the erosion rates for the test set which used the smaller cathode orifice are greater than for those using the cathodes with the larger orifices. Second, the cathode-side baffle erosion profiles are more peaked for the test set which used the cathode with the smaller orifice. In the case where a 1.78 mm (0.070") diameter cathode orifice and 12.7 A discharge current were used, the erosion profile is flat and the erosion rates are lower than in the case with an 11.8 A discharge.

Data on the ion velocity and number density in the cathode plume were obtained at Colorado State University (CSU) and presented to the 21st International Electric Propulsion Conference (IEPC) in July 1990 (Ref. 72). These data show that the ion energies could exceed 65 eV despite a plasma potential that was on the order of 15 V. In addition these data indicate that ion energy increased with increasing cathode emission current. The data presented in Fig. 45 and Ref. 72 suggest that very significant reductions in baffle erosion can be obtained by increasing cathode orifice diameter.

# Legend:

	Test Date	% N2 Added to Xenon	Cathode Orifice Dia cm
○	1989	0	0.07
△	1990	0	0.11
●	1989	2	0.07
▲	1990	2	0.11
■	1990	0	0.18

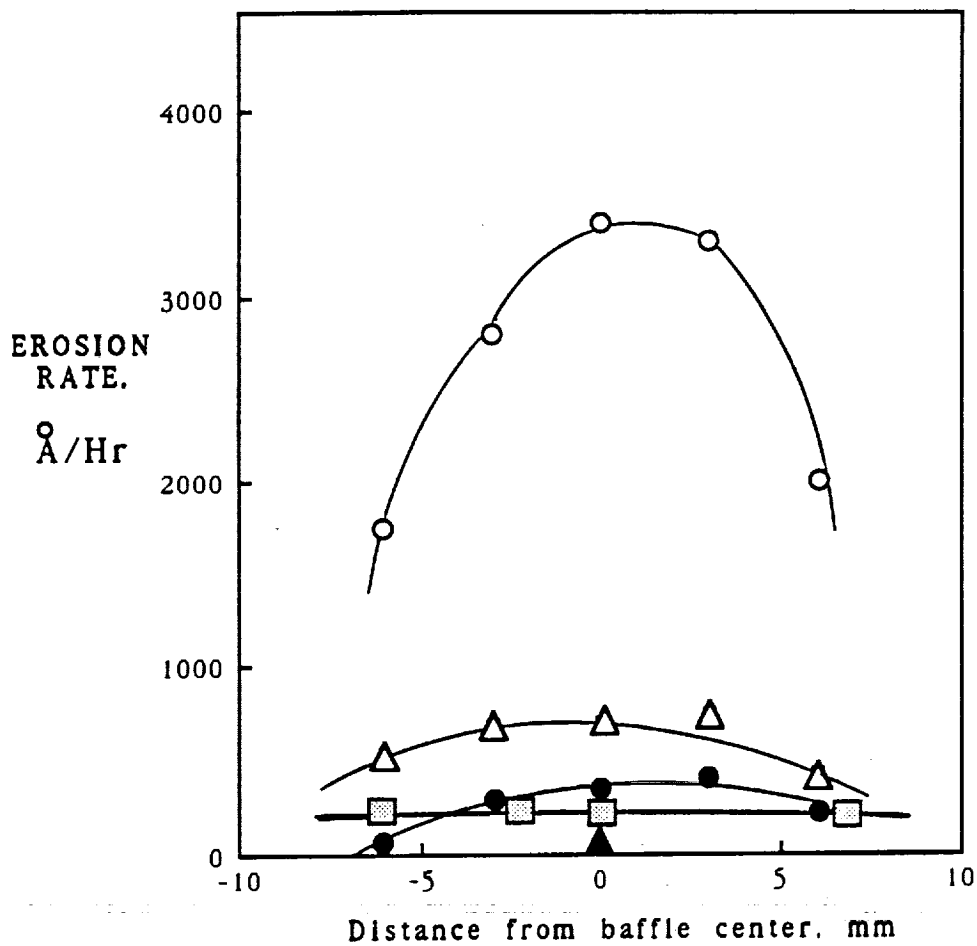


**Figure 45** Plot of baffle erosion as a function of distance from the baffle center.

## 11.0 REVIEW OF ACCELERATOR GRID EROSION

Erosion of the downstream face of the accelerator grid is a potential life-limiting mechanism in moderate or high power inert gas ion engines. Accelerator grid erosion occurs when ions downstream of the accelerator grid bombard the accelerator grid surface with an energy of 200-500 eV and erode the surface in a form of microscopic sand-blasting. During the SERT II flight tests thruster operation was terminated by high-voltage grid shorts.<sup>73-77</sup> Analysis of data and comparison with ground tests indicated that the shorts were due to an eroded web of the accelerator grid which was lodged between the grids. Ground test data indicated that the placement of the neutralizer resulted in a large quantity of slow ions in the vicinity of the accelerator grid which eroded the grid until a grid fragment loosened, cantilevered toward the screen grid, and shorted out the screen and accelerator grids on both thrusters on board SERT II. In subsequent engine designs the neutralizer was repositioned to eliminate the neutralizer as a source of slow ions in the vicinity of the accelerator grid.

Most of the ions extracted from the discharge chamber of an ion engine exit the accelerator grid at high velocity, and are subsequently neutralized approximately 0.5 mm downstream of the accelerator grid by electrons emitted from the neutralizer cathode. However, a fraction of these beam ions collide with neutral propellant atoms drifting slowly out of the engine through the accelerator system apertures and undergo charge-exchange collisions. When charge-exchange occurs, the positive charge of the fast ion is transferred to the slow neutral atom, resulting in a fast neutral and a slow ion. The slow positive ion is attracted to the negative accelerator grid and strikes it with an energy equal to the accelerator grid voltage, causing sputter erosion.

The erosion pattern typically consists of shallow grooves eroded between each hole, and pits located at positions equidistant between a set of three holes, where the charge-exchange impingement current density is greatest. Charge-exchange erosion is highly localized, being maximum at the pits, less at the grooves, and virtually non-existent at other locations on the accelerator grid surface.

Data from recent tests of inert gas ion engines performed at background pressures in the  $10^{-3}$  Pa ( $10^{-5}$  torr) range indicate that accelerator grid erosion from charge-exchange ions is severe at these tank pressures. Pits were eroded completely through the 0.36 mm thick molybdenum grid used for discharge chamber erosion studies described in Appendix A, as well as in the 890 hour endurance test of a 5 kW ring-cusp xenon ion engine discussed in Ref. 157.

Because of the observed severity of the accelerator grid erosion, a literature survey and assessment of accelerator grid erosion were performed. Over 200 references on ion propulsion were

examined, mostly on mercury ion engines that were tested extensively in the 1960s through the 1970s, and a far smaller number on cesium or inert gas ion engines. From this literature survey there were 93 references that addressed engine lifetime, for which accelerator grid erosion is an important consideration. These references<sup>73-165</sup> are grouped into 6 categories as indicated in Table 8.

**Table 8 Summary of References on Ion Engine Life**

CATEGORY	NUMBER OF REFERENCES
1. SERT II flight test descriptions.	5
2. Accelerator grid erosion not addressed.	38
3. Accelerator grid erosion predictions, estimates and/or wear mechanisms discussed.	12
4. Anecdotal descriptions that characterize accelerator grid erosion as being minimal or non-existent.	15
5. Accelerator grid erosion data compromised by experimental difficulties.	10
6. Well-documented accelerator grid erosion data.	13

Despite the extensive testing history and advanced level of mercury ion thruster technology, there is surprisingly little actual data on accelerator grid erosion. From this list of 93 references dealing with engine life, 65 do not mention accelerator grid erosion at all, provide only estimates for accelerator grid erosion, or provide anecdotal information on accelerator grid erosion. Included in this category are all of the Mission Profile Life Test (MPLT) descriptions on the J-series ion engine. It is clear from the discussions in these references that accelerator grid erosion was not perceived to be a significant life-limiting mechanism in mercury ion engines.

Twenty-three references with accelerator grid erosion data were surveyed. Of these, 10 were found to have experimental difficulties that precluded an assessment of accelerator grid erosion, leaving only 13 references that have accelerator grid erosion data not compromised by experimental difficulties. These references are listed in Table 9. In this table, "pit erosion" refers to the holes etched into the accelerator grid at locations in the grid webbing equidistant from 3 holes, "grid mass loss (exp)" refers to the experimentally observed mass loss from charge-exchange erosion or direct impingement current, "grid mass loss (cal)" refers to the grid mass loss that is calculated using

TABLE 9. ACCELERATOR GRID EROSION DATA

REFERENCE NUMBER	PROP	GRID DIA CM	TEST TIME HRS	SPUTTER YIELD Y	Jb A	Ja/Jb	PIT EROSION OBSERVED 10 <sup>-5</sup> mm/hr	GROOVE ERSN OBSERVED 10 <sup>-5</sup> mm/hr	GRID MASS LOSS (EXP) g	GRID MASS LOSS (CAL) g	UNIFORM CURRENT DENSITY 10 <sup>-3</sup> mA/cm <sup>2</sup>
159	Xe	30	895	.51	3.20	.006	40.0	8.5	17.8	28.5	36
160	Xe	14	1000	.70	.47	.003	4.1	-	2.0	4.0	20
155*	Hg	30	1300	.4-.55	2.10	.003	apx 0	-	-	-	20
141+	Hg	30	4263	.27	2.00	.004	apx 0	-	-	-	15
158?	Hg	20	4009	?	.59	.005	16.0	-	-	-	14
156	Hg	10	1050	.55	.16	.003	9.5	-	.2	.97	14
162	Hg	8	15040	.55	.07	.003	3.4	-	3.8	5.90	9
164	Hg	8	1150	.27	.07	.003	-	-	.6	.22	8
163*	Hg	30	10000	.55	1.40	.003	3.4	1.5	-	-	7
161	Hg	5	1367	.55	.03	.001	apx 0	-	-	-	3
157	Hg	30	1552	.55	2.25	.003	.7	-	-	-	1.7
165	Hg	8	7057	.27	.07	.005	3.7	-	-	-	#
166	Hg	5	409	.63	.02	.005	-	-	.04	.15	#
167	Hg	5	1373	?	.03	.005	-	-	.20	?	#

\* Test performed at several different beam currents; for analysis of the data, the thruster operating parameters were averaged.

+ 30-cm J-series MPLT

? Accel. grid voltage not available

# Accel. grid open area unknown

- No data available

a method described in a later section, and "Uniform Current Density" refers to the total accelerator grid impingement current divided by the total accelerator grid surface area.

Included in Table 9 are data from the MPLT.<sup>139</sup> It was reported in this reference that after 4263 hours of operating time at a beam current of 2.0 A and an accelerator grid impingement current of 7.2 mA that, "All components external to the discharge chamber...were examined and no quantifiable wear identified". It is surprising that no grid mass loss or erosion data are presented in the MPLT papers available in the literature. In addition, the experimental result that there was no "quantifiable erosion" is surprising in view of the results of other long duration tests.<sup>160,161</sup> In these tests<sup>160,161</sup>, the erosion rate of pits formed in the central region of the accelerator system was  $3.4 \times 10^{-5}$  mm/hr for an accelerator grid voltage which corresponds to a molybdenum grid sputter yield by mercury ions of 0.55. In Ref. 161 the pits eroded almost completely through the grid, and in Ref. 160 the pits were eroded completely through the 0.51 mm thick grid.

The MPLT life-tests were performed with lower accelerator grid voltages than the tests<sup>160,161</sup> discussed above, resulting in a sputter yield for mercury on molybdenum which was only 0.27, or approximately a factor of two less than earlier long duration tests. However, the total impingement current in the MPLT was almost double that used in the 10,000 hour test of a 30-cm mercury ion engine (Ref. 161), because of the greater beam current. If the accelerator grid used in the MPLT test of thruster J1 had eroded in a pattern similar to that observed in Ref. 161, then it is estimated that there should have been approximately 0.1 mm (0.004") of erosion on the J1 thruster accelerator grid, an amount which should have been easily quantifiable on a grid which is only 0.38 mm (0.015") thick.

Comparisons of accelerator grid erosion data obtained in tests performed on thrusters in different test facilities are valid only if the grids erode in the same way on all the tests. It is uncertain if this is the case for several reasons including, for example, the fact that the MPLT thrusters used small hole accelerator grid (SHAG) optics as opposed to the large hole accelerator grid optics used in the 10,000 hour test.<sup>161</sup> However, it should be noted that the SHAG optics used in the acceptance testing of thruster J10 showed visible accelerator pit and groove erosion after only approximately 20 hours of operating time. It seems surprising that accelerator grid erosion was not quantified in the MPLT test series conducted on the J-series Hg ion engine.

Another method used to assess grid erosion observed in different tests reported in the literature was to calculate the mass loss of the accelerator grid using published sputter yields and to compare the mass loss prediction with experimental data. In calculating the grid mass loss, it was assumed that all of the

accelerator grid impingement current was charge exchange current that eroded grooves or pits into the accelerator grids with ion energies equal to the applied accelerator grid voltage (which is normally in the range of 200-800 volts). This assumption neglects several important effects including the ion focusing which creates the pits and groove patterns, as well as the emission of secondary electrons from the accelerator grid. Secondary electrons resulting from the ion bombardment of the grid surface add to the measured accelerator grid "impingement" current. In addition, in Fig. 46 it is shown that charge-exchange ion energies are a function of where the ions are formed. Since sputter yield, and hence the erosion rate, is a strong function of the ion energy, the assumption that all accelerator grid impingement current strikes the accelerator grid at the full accelerator grid voltage and the neglect of secondary electron emission should result in mass loss predictions which are too high. The mass loss of the grids is calculated using the following expression:

$$m_L = J_a C_i Y m_{Mo} t_L. \quad (49)$$

As can be seen in Table 9, the largest grid mass loss value was obtained during the recent 895 hour ring-cusp, xenon thruster life test<sup>157</sup>, followed by the value obtained during the 10,000 hour life test of a 30-cm Hg ion thruster.<sup>161</sup>

The ratios of calculated grid mass loss to the corresponding experimentally observed values vary from 0.4 to 4.9, with most ratios between 1.6 - 4.9. Those ratios that are greater than 1 are probably due to actual grid erosion rates that are reduced due to facility effects such as oxidation, surface nitriding of the molybdenum grid, back-sputtering of beam target material onto the grid, or to uncertainties in the incident ion energies. In Ref. 164, where the ratio of calculated to experimentally observed grid mass loss is 0.4, the most likely explanation is that there was significant erosion of the grid due to direct ion impingement. These ions would have energies far higher than those assumed for the mass loss calculation, because these ions strike the accelerator grid with the full potential difference between the accelerator grid and the screen grid.

The uniform current density of charge exchange ions at the grid surface is calculated with the assumption that all accelerator grid impingement current is charge exchange current. This impingement current is divided by the total grid surface area (total grid area minus the grid hole area) to obtain the uniform charge-exchange impingement current density in mA/cm<sup>2</sup>. Values for this parameter are listed in Table 9, in which the test data are ordered according to the uniform charge exchange current density.

The product of the uniform charge exchange current density and the sputter yield corresponding to the applied accelerator grid voltage is calculated and compared to the actual grid mass loss and

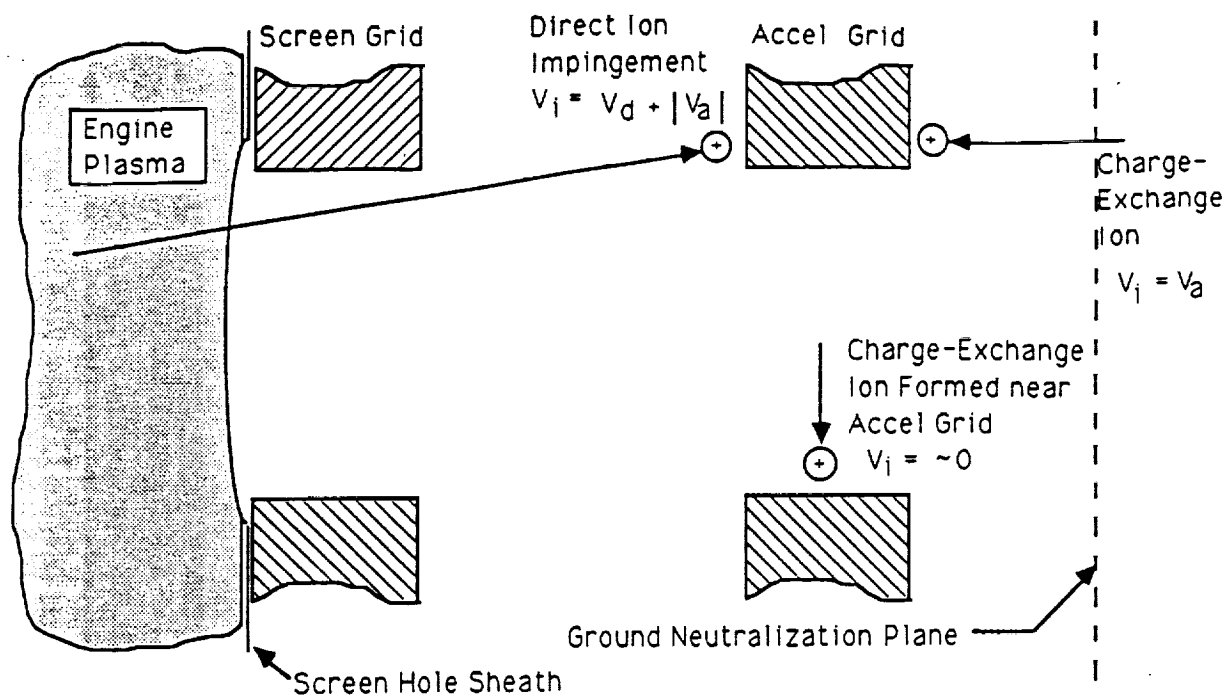


**Figure 46(a).** Schematic diagram of the ion engine grids and formation of charge-exchange ions. Ion potential  $V_i$  is relative to accelerator grid.

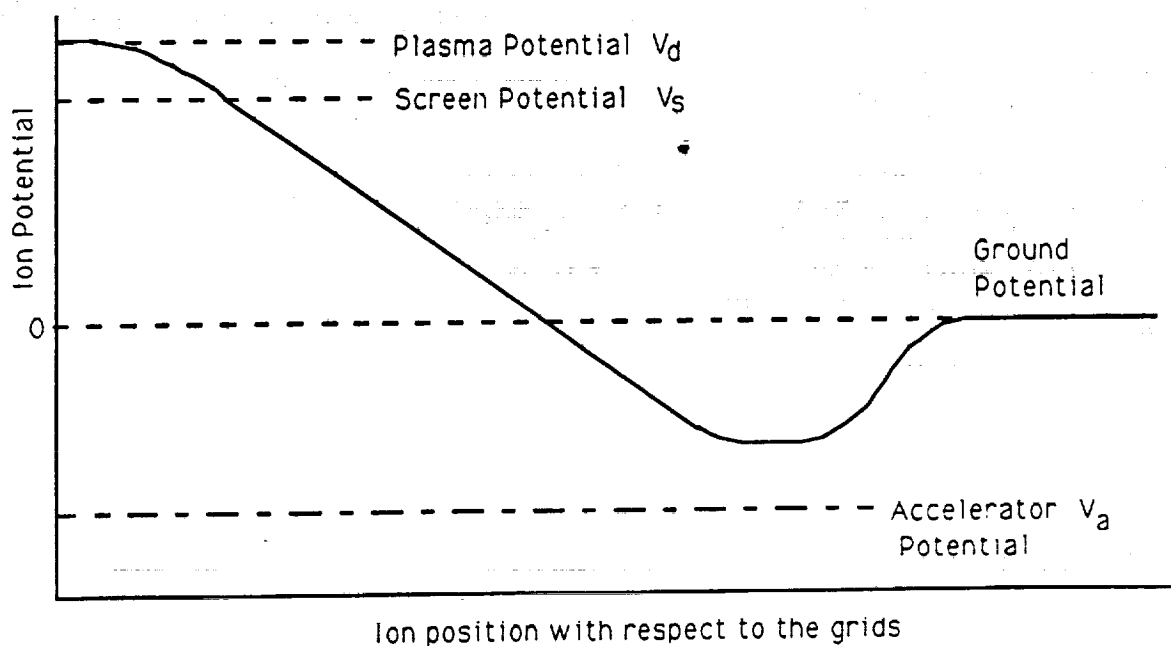


**Figure 46(b).** Plot of ion potential variation.

pit erosion rates, shown in Tables 10 and 11. There is generally poor agreement between these calculations and the measured grid mass losses, but there is generally very good agreement between these calculations and pit erosion rates. There are no grid erosion data for the J-series MPLT; however, the calculated value of uniform current density multiplied by sputter yield for the thruster J1<sup>139</sup> is equal to the value calculated for the 10,000 hour 30-cm Hg thruster test.<sup>161</sup> It is of interest to note that the uniform charge-exchange current density and pit erosion rates for both Ref. 160 and Ref. 161 are almost identical.

**Table 10** Grid Mass Loss Ordered by  $J_a Y$

Reference #	Grid Mass Loss (g)	$J_a Y$ (mA/cm <sup>2</sup> )
157	17.8	18.4
158	2.0	14.0
154	0.2	7.7
163	3.7	5.0
162	0.6	2.2

**Table 11** Pit Erosion Rates Ordered by  $J_{a,uniform} Y$

Reference #	Pit Erosion Rate (mm/hr)	$J_{a,uniform} Y$ (mA/cm <sup>2</sup> )
157	40.0	18.4
158	4.1	14.0
154	9.5	7.7
160	3.4	5.0
161	3.4	3.9
159	0	1.7
155	0.7	0.9

Examination of the erosion pattern on the downstream face of the accelerator grid used during the 895 hour ring-cusp engine life test<sup>157</sup>, as well as on the accelerator grid used in the discharge chamber erosion studies described in Appendix A, shows that pits eroded into the grids contribute approximately 33% of the total volume removed from the grid, with the rest coming from material etched from both the upstream side of the pit and from grooves eroded into the downstream face of the grid. Unfortunately, erosion rate data at these sites are virtually non-existent.

Using measured pit erosion rates and known grid sputter yields, the current density at the pit locations can be calculated. There is some uncertainty in this calculation due to the characteristics of ion sputtering. As a pit begins to form, the pit walls present a surface which is at an angle to the incident ion. Material sputter yields are a function of the ion angle of incidence, and achieve a maximum at approximately 40 degrees to normal. Consequently, the sputter yield of the inclined surface may be up to 50% greater than the nominal sputter yield. Alternatively, material sputtered from the pit walls may be redeposited onto the bottom of the pit, thus reducing the effective sputter yield. The net effect of these competing processes is unknown. It is speculated that the effective sputter yield of the molybdenum grid is somewhat higher due to the dependence of sputter yield on the angle of incidence, and that material eroded from the pit bottom probably deposits onto the pit sidewalls, creating the deep pits seen in severely eroded grids.

The current density calculated at the pits, divided by the current density calculated assuming a uniform distribution of the charge exchange ions, results in fractions ranging from 2.0 to 6.3 for the data in Table 9, with most values in the range of 4.0-6.0. The one exception is for the data from Ref. 160, in which a fraction of 0.38 was calculated. It is unknown why the pit erosion rate for this test was so low.

The results of this study on accelerator grid erosion data are summarized as follows:

1. Actual experimental data on accelerator grid erosion are limited.
2. It was generally perceived in the 1970's and early 1980's that accelerator grid erosion was not a life-limiting mechanism for 2.7 kW Hg ion thrusters with a design operating life of 15,000 hours.
3. There are no published accelerator grid erosion data for the J-series MPLT thruster tests.
4. Significant accelerator grid erosion was observed in long duration tests of low power (< 2 kW) Hg ion thrusters.
5. There is a reasonably good correlation between observed pit erosion rates and the product of the uniform charge exchange current density times the grid sputter yield.
6. The correlation between calculated grid mass loss and experimental data reported in the references is generally poor.
7.  $J_a/J_b$  was generally 0.003-0.006.

### 11.1 Implications for Xenon Ion Thruster Accelerator Grid Life

Accelerator grid erosion in xenon ion thrusters is expected to be greater than in mercury ion thrusters. This is due primarily to increased molybdenum sputter yields (Fig. 47) when using xenon, and to the fact that, because xenon is a lighter atom than mercury, beam voltage is less and hence beam current is greater (for a fixed  $I_p$  and beam power). Greater beam current implies that more charge-exchange ions will be created and available to erode the downstream face of the accelerator grid.

Screen grid life was historically defined<sup>86</sup> as the time required to erode the grid to one-half of its original thickness. However, it has been implied in Refs. 138, 146 and 157 that the formation of pits in the accelerator grid, even if they pierce the entire grid thickness (through-pits), is not a life limiting phenomenon. In Ref. 146 a cesium ion engine was operated with through-pits etched into the accelerator grid with no apparent deleterious effects. In other references<sup>123,156,157</sup> it has been suggested that a suitable definition for accelerator grid operating life is the time required to erode completely through the grooves etched into the grids. Under this definition, the accelerator grid is considered to be a functioning engine component until it begins to disintegrate. No other definitions for accelerator grid life were found in the literature.

Long duration ion engine tests, however, suggest that the end of the useful accelerator grid life will occur before the grooves erode completely through the accelerator grid webbing. Both engines used on the SERT II flight test were rendered temporarily or permanently inoperable when small sections of the accelerator grid, weakened by severe accelerator grid erosion, appear to have cantilevered toward the screen grid, creating a screen to accelerator grid short.<sup>74</sup> In Ref. 144, charge-exchange ions travelling upstream through pits that were eroded completely through the accelerator grid were reflected by the screen grid potential back to the accelerator grid. Material eroded from the upstream surface of the accelerator grid by these ions formed deposits onto the downstream face of the screen grid, which, in post-test handling, flaked off and lodged between the screen and accelerator grids. In Refs. 64 and 20, high rates of grid arcs and recycles were believed to be due to these screen grid deposits. In Ref. 161, high recycle rates were attributed to flaking or loss of electrode structural stability due to excessive grid wear. In Ref. 157, whiskers from charge-exchange and graphite target erosion may have caused a high rate of recycles which frequently extinguished the discharge.

In addition to the difficulties cited above in operating the ion engines until the grooves erode completely through the grids, ion engine performance may degrade significantly. The pits erode through the accelerator grid far sooner than do the grooves. As

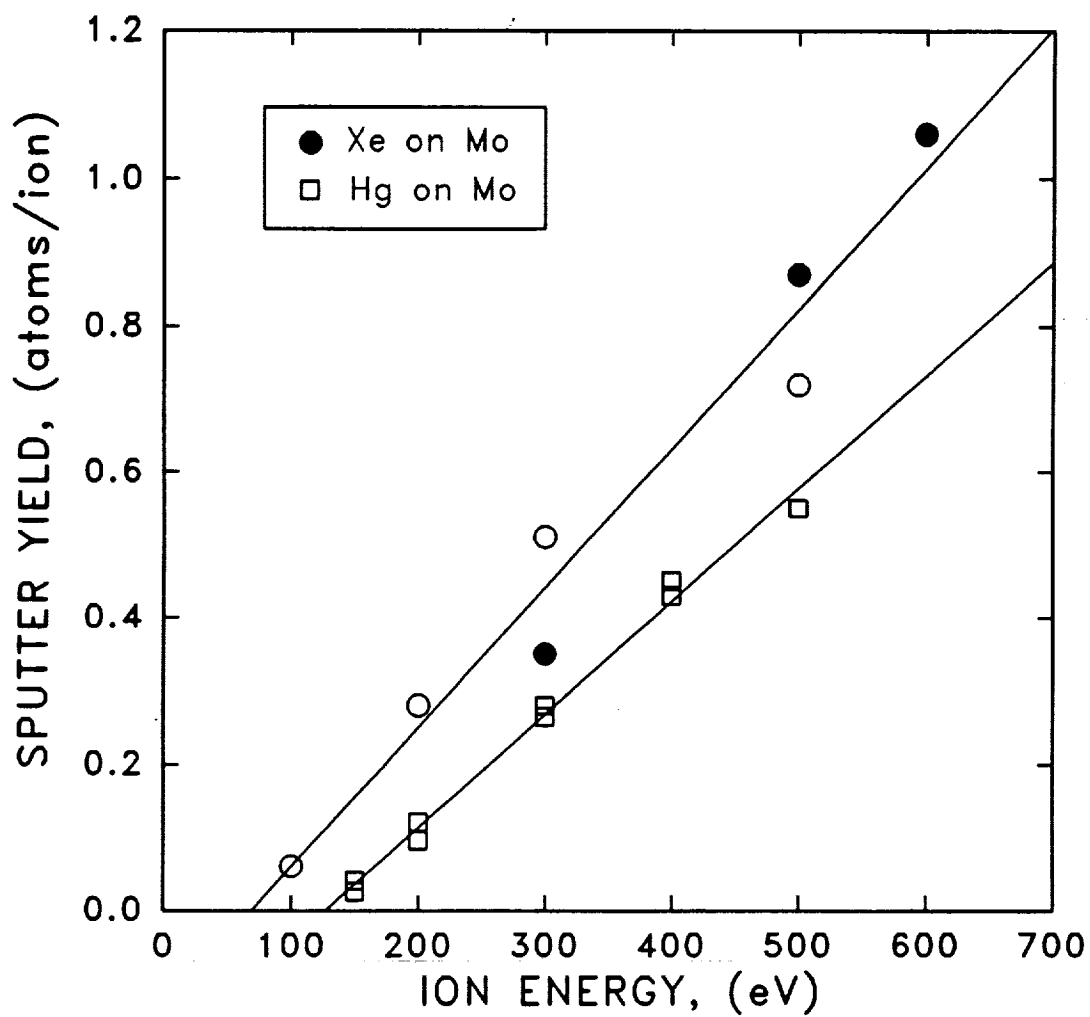


**Figure 47** Sputter yield for molybdenum as a function of incident xenon and mercury ion energies.

they enlarge, the grid open area increases, allowing more neutral atoms to escape the discharge chamber. The increased loss rate of neutral gas atoms increases the production of charge exchange ions, which will increase the erosion rate of both the pits and the grooves. The possibility exists that the pits will enlarge to such a degree that, due to the decrease in discharge chamber pressure, the rate of ion production will be reduced in the discharge chamber. This scenario also illustrates the difficulty of trying to predict ion engine grid life based on short duration tests.

The results of the experimental data listed above and the SERT II flight test experience suggest that a reasonable definition for the end of accelerator grid life may be the time required to erode pits completely through the face of the accelerator grid. Termination of ion engine operation when through-pits are created will prevent the formation of sputter deposits on the downstream face of the screen grid and thus eliminate the excessive high-voltage arcing events caused by these deposits. Termination of ion engine operation prior to excessive groove erosion will prevent the loss of structural integrity of the grids.

#### **11.2 Xenon Ion Engine Accelerator Grid Erosion Rate Estimate**

The best data for xenon ion engine accelerator grid erosion were obtained in the recent life test<sup>157</sup> performed on a ring-cusp ion engine operated at 5 kW. In this test, grooves 0.076 mm deep were eroded into the downstream face of the accelerator grid in 906 hours of operating time; pits were eroded completely through the accelerator grid in less than 895 hours. The ultimate accelerator grid life was estimated to be 11,500 hours. This estimate was based on the following assumptions and data:

1. Accelerator grid life is defined as the time required to erode completely through the grooves formed in the middle portion of the grid, where erosion rates are highest.
2. Grid thickness is 0.36 mm.
3. The groove erosion rate is  $8.4 \times 10^{-5}$  mm/hr, resulting in a grid life of 4200 hours for the conditions under which the test was performed.
4. Of the 17.5 mA of charge-exchange current, 64% are "facility effect" ions, created due to the high background pressure in the vacuum tank which was used for the life test. It was assumed that in space-like conditions, the charge-exchange current would be only 6.2 mA.

Using these assumptions, the accelerator grid life due to groove erosion is 4200 hours; in space conditions this life is increased

by a factor of 2.8 due to the decrease in accelerator charge exchange current:

$$(17.5 \text{ mA}) / (6.2 \text{ mA}) \times (4,200 \text{ hrs}) = 11,854 \text{ hrs.}$$

In reality, a useful grid life time of this value may be difficult to achieve.

1. First, it may not be possible, as discussed above, to operate the engine until grooves are eroded completely through the grid.
2. Second, the groove erosion rate may not remain as low as  $8.5 \times 10^{-5}$  mm/hr, due to increased pit erosion and increased charge-exchange ion production as the accelerator grid erodes.
3. Finally, the ratio  $J_a/J_b$  in space may not be as low as 0.0019. Historical data from Table 9 suggest that typical values for this ratio will be 0.003-0.006.

If the historical value of 0.003 is used for  $J_a/J_b$ , then grid life is calculated to be

$$(0.002/0.003) \times (11,854 \text{ hrs}) = 7,902 \text{ hrs}$$

Grid life, defined as the time required to erode pits through the accelerator grid, can be calculated using the following assumptions:

1. The uniform charge exchange current density is 0.036 mA/cm<sup>2</sup>.
2. The charge exchange current density at pit locations is in the range of 1 to 6 times the uniform current density.
3. The erosion rate, assuming a uniform current density, is  $6.4 \times 10^{-5}$  mm/hr.

The time required to erode through-pits into the 0.36 mm thick grid would be calculated as follows:

Minimum

$$\text{Pit Erosion} \quad (0.36 \text{ mm}) / (6.4 \times 10^{-5} \text{ mm/hr}) \times 1 = 5,625 \text{ hrs}$$

Maximum

$$\text{Pit Erosion} \quad (0.36 \text{ mm}) / (6.4 \times 10^{-5} \text{ mm/hr}) \times 6 = 937 \text{ hrs.}$$

Another way to estimate the accelerator grid life is to assume that the pits appeared after 906 hours of operating time, and that in space the charge-exchange current can be reduced by a factor of

2.8. Then the expected grid life would be

$$(906 \text{ hrs}) \times (2.8) = 2,537 \text{ hrs.}$$

These grid life estimates are all substantially less than that made in Ref. 159 because a different set of assumptions were used. Additional testing is required to accurately determine xenon ion engine accelerator grid life, but preliminary analyses indicate that accelerator grid erosion is a severe problem in xenon ion engines.

## 12.0 REFERENCES

1. Robinson, R.S., Deininger, W.D., Winder, D.R., and Kaufman, H.R., "PLASIM: A Computer Code for Simulating Charge-Exchange Plasma Propagation," CSU Report 955322 JPL, Jan., 1982.
2. Kaufman, H.R., "Charge Exchange Plasma Generated by an Ion Thruster," CSU Report NASA CR-134844, June 1975.
3. Kaufman, H.R., "Charge Exchange Plasma Generated by an Ion Thruster," CSU Report NASA CR-134318, Dec. 1977.
4. Kaufman, H.R., "Plasma Physics Analysis of SERT II Operation," CSU Report NASA CR-159814, Jan. 1980.
5. Carruth, M.R., editor, "Experimental and Analytical Evaluation of Ion Thruster/Spacecraft Interactions," JPL Publication 80-92, Jan. 1981.
6. Staskus, J.V., and Burns, R.J., "Deposition of Ion Thruster Effluents on SERT II Spacecraft Surfaces," NASA TM X-52860, Sept. 1970.
7. Deininger, W.D., "Electric Propulsion Produced Environments and Interactions with SP-100," JPL D-934 (internal document), Aug. 1983.
8. Kaufman, H.R., "Calculations of Charge-exchange Plasma," for Ford Aerospace and Communications Corporation Subcontract SC-995141-AN, August 7, 1987.
9. Shimada, S., Takegahara, H., Gotoh, Y., Satoh, K., Kitamura, S., and Kajiwara, K., "Ion Thruster Contamination Evaluation," AIAA 89-2269, July 1989.
10. Rapp, D., and Francis, W.E., "Charge Exchange between Gaseous Ions and Atoms," *Journal of Chemical Physics*, Vol. 37, No. 11, Dec. 1962, pp. 2631-2645.
11. Vossen, J.L., and Kern, W., *Thin Film Processes*, Academic Press Inc., New York, 1978, pp. 16-17.
12. Kaufman, H.R., "Technology of Electron-Bombardment Ion Thrusters," *Advances in Electronics and Electron Physics*, Vol. 36, Academic Press, Inc., New York, 1974, pp. 329-336.
13. Fay, C.E., Samual, A.L., and Shockley, W., "On the Theory of Space Charge Between Parallel Plane Electrodes," *Bell System Technical Journal*, 17, 1938, p. 76.
14. Kemp, R. F., and Sellen, J. M., Jr., "Investigation of Cesium

- and Mercury Discharge Neutralizers," in "Research on Ion Beam Diagnostics," J. M. Sellen, Jr. and R. F. Kemp, eds., NASA CR-54692, 1966.
15. Rawlin, V. K., and Kerslake, W. R., "Durability of the SERT II Hollow Cathode and Future Applications of Hollow Cathodes," NASA TM X-52532, 1969.
  16. Csiky, G. A., "Investigation of a Hollow Cathode Discharge Plasma," AIAA Paper No. 69-258, March 1969.
  17. Philip, C. M., "A Study of Hollow Cathode Discharge Characteristics," AIAA Paper No. 70-1087, 1970.
  18. Goldstein, R., Pawlik, E. V., and Wen, L., "Preliminary Investigations of Ion Thrusters Cathodes," JPL Technical Report 32-1536, August 1971.
  19. Weigand, A., and Nakanishi, S., "A Survey of Kaufman Thruster Cathodes," NASA TM X-67918, October 1971.
  20. Hudson, W. R., and Weigand, A. J., "Hollow Cathodes with BaO Impregnated Porous Tungsten Insert and Tips," AIAA Paper No. 73-1142, 1973.
  21. Mirtich, M. J., "Investigation of Hollow Cathode Performance for 30-cm Thrusters," AIAA Paper No. 73-1138, October 1973.
  22. Wintucky, E. G., "A 20,000 hr Endurance Test of a Structurally and Thermally Integrated 5-cm Diameter Ion Thruster Main Cathode," AIAA Paper No. 75-368, 1975.
  23. Mirtich, M. J., and Kerslake, W. R., "Long Lifetime Hollow Cathodes for 30-cm Mercury Ion Thrusters," AIAA Paper No. 76-985, 1976.
  24. Collett, C. R., et al., "Thruster Endurance Test," NASA CR-135011, May 1976.
  25. Collett, C. R., and Bechtel, R. T., "An Endurance Test of a 900 Series 30-cm Engineering Model Ion Thruster," AIAA Paper No. 76-1020, November 1976.
  26. Nakanishi, S., "A 15,000-Hour Cyclic Endurance Test of an 8-cm Diameter Mercury Bombardment Ion Thruster," AIAA Paper No. 76-1022, November 1976.
  27. Sovey, J. S., "Characteristics of a 30-cm Diameter Argon Ion Source," AIAA Paper No. 76-1017, 1976.
  28. Mantenicks, M. A., and Wintucky, E. G., "5200 Cycle Test of an 8-cm Diameter Hg Ion Thruster," NASA TM-78860, April 1978.

29. Fearn, D. G., "Cyclic Life-Test of an Ion Thruster Hollow Cathode," *J. Spacecraft*, Vol. 15, No. 3, June 1978.
30. Rehn, L., and Kaufman, H. R., "Correlation of Inert Gas Hollow Cathode Performance," AIAA Paper No. 78-707, April 1978.
31. Mantenicks, M. A., "Mercury Ion Thruster Component Testing," AIAA Paper No. 79-2116, 1979.
32. Poeschel, R. L., and Beattie, J. R., "Primary Electric Propulsion Technology Study," NASA CR-159688, November 1979.
33. Siegfried, D. E., "A Phenomenological Model of Orified Hollow Cathodes," NASA CR-168026, December 1982.
34. Stillwell, R. P., Robinson, R. S., Kaufman, H. R., and Cupp, R. K., "Experimental Investigation of an Argon Hollow Cathode," AIAA Paper No. 82-1890, November 1982.
35. Bechtel, R. T., Trump, G. E., and James, E. J., "Results of the Mission Profile Life Test," AIAA Paper No. 82-1905, November 1982.
36. Beattie, J. R., "Extended Performance Technology Study: 30-cm Thruster," NASA CR-168259, June 1983.
37. Kudo, I., Machida, K., and Toda, Y., "10,000-Hours Neutralizer Hollow Cathode Endurance Test," IEPC 84-38, presented at the International Electric Propulsion Conference, Tokyo, Japan, May 1984.
38. Ninoo, H., "Gas Pressure and Electron Density in the Active Zone Level of Hollow Cathode Arc Discharges," NASA TM-77468, April 1984.
39. Schatz, M. F., "Heaterless Ignition of Inert Gas Ion Thruster Hollow Cathodes," AIAA Paper No. 85-2008, Sept. 1985.
40. Kudo, I., Murakami, H., Toda, Y., and Machida, K., "Recycle Test of an Ion Thruster Main Cathode," 15th International Symposium on Space Technology and Science, Tokyo, Japan, May 1986, Proceedings Volume 1.
41. Rawlin, V. K., et al., "High Current Hollow Cathodes for Ion Thrusters," AIAA Paper No. 87-1072, May 1987 (viewgraphs only).
42. Brophy, J. R., and Garner, C. E., "Tests of High Current Hollow Cathodes for Ion Engines," AIAA Paper No. 88-2913, July 1988.
43. Rawlin, V. K., "Internal Erosion Rates of a 10-kW Xenon Ion

Thruster," NASA TM 100954, July 1988.

44. Gair, S. A., and Harris, P. T., "A Review of the Cathode Construction for the RAE 10/25 mN Thruster," IEPC-88-078, October 1988.
45. Maslyany, N. V., Pridantzev, V. F., Prisnyakov, V. F., and Khitko, A. V., "Parametric Investigations of the Hollow Cathodes for Ion Thrusters," IAF-88-260, 39th Congress of the International Astronautical Federation, October 1988.
46. Beattie, J. R., Matossian, J. N., and Robson, R. R., "Status of Xenon Ion Propulsion Technology," *J. Propulsion*, Vol. 6, No. 2, March-April 1990, pp. 145-150.
47. Friedly, V. J., "Hollow Cathode Operation at High Discharge Currents," NASA CR-185238, April 1990.
48. Patterson, M. J., and Verhey, T. R., "5kW Xenon Ion Thruster Lifetest," AIAA Paper No. 90-2543, July 1990.
49. Fearn, D. G., Singfield, A., Wallace, N. C., Gair, S. A., and Harris, P. T., "The Operation of Ion Thruster Hollow Cathodes Using Rare Gas Propellants," AIAA Paper No. 90-2584, July 1990.
50. Verhey, T. R., and MacRae, G. S., "Requirements for Long-life Operation of Inert Gas Hollow Cathodes -- Preliminary Results," AIAA Paper No. 90-2586, July 1990.
51. Bechtel, R. T., "The 30-cm J-Series Mercury Bombardment Thruster," AIAA Paper No. 81-0714, 1981.
52. Aston, G., Brophy, J. R., Garner, C. E., Pless, L. C., Owens, A. G., and Toomath, R. L., "Operating Characteristics of a 10 kW Xenon Ion Propulsion Module," AIAA Paper No. 87-1006, 1987.
53. Brophy, J. R., "Computer-Controlled Operation of a Two-Engine Xenon Ion Propulsion System," AIAA Paper No. 87-1007, 1987.
54. Beattie, J. R., Matossian, J. N., and Robson, R. R., "Status of Xenon Ion Propulsion Technology," AIAA Paper No. 87-1003, May 1987.
55. Rawlin, V. K., "Sensitivity of 30-cm Mercury Bombardment Ion Thruster Characteristics to Accelerator Grid Design," NASA TM-78861, April 1978.
56. Rawlin, V. K., and Hawkins, C. E., "Increased Capabilities of the 30-cm Diameter Hg Ion Thruster," NASA TM-79142, May 1979.
57. Aston, G., and Kaufman, H. R., "Ion Beam Divergence

- Characteristics of Three-Grid Accelerator Systems," *AIAA Journal*, Vol. 17, No. 1, Jan. 1979, pp. 64-70.
58. Brophy, J. R., "Simplified Xenon Ion Engine Throttling Strategy for SEP Missions," IOM 353EP-87-099, June 1987, internal JPL document.
  59. Sauer, C. G., "Xenon Thruster Throttling with Constant Beam Current," IOM 312/88.3-4160, April 1988, internal JPL document.
  60. Garner, C. E., Brophy, J. R., and Pless, L. C., "Ion Propulsion System Design and Throttling Strategies for Planetary Missions," AIAA Paper No. 88-2910, July 1988.
  61. Aston, G., Brophy, J. R., Garner, C. E., and Pless, L. C., "A Xenon Ion Propulsion Module for Enhanced Spacecraft Capability," AIAA Paper No. 86-1393, June 1986.
  62. Personal communication with M. J. Patterson at NASA LeRC, August 1990.
  63. Brophy, J. R., and Aston, G., "Thermal/Mechanical Analyses of Large Diameter Ion Accelerator Systems," AIAA Paper No. 89-2718, July 1989.
  64. Ramsey, W. D., "12-cm Multi-Cusp Ion Thruster Inert Gas Performance (Research on Inert Gas Thrusters)," NASA CR-168208, January 1983.
  65. Nakanishi, S., and Pawlik, E. V., "Experimental Investigation of a 1.5-m-diam Kaufman Thruster," *J. Spacecraft*, Vol. 5, No. 7, July 1968.
  66. Patterson, M. J., and Rawlin, V. K., "Performance of 10-kW Class Xenon Ion Thrusters," AIAA Paper No. 88-2914, July 1988.
  67. Brophy, J. R., and Garner, C. E., "Tests of High Current Hollow Cathodes for Ion Engines," AIAA Paper No. 88-2913, July 1988.
  68. Garner, C. E., et al., "The Effects of Gas Mixtures on Ion Engine Erosion and Performance", AIAA-87-1080 (1987).
  69. Garner, C. E., et al., "Techniques for Reduced Spalling and Increased Operating Life in Xenon Ion Engines", AIAA-89-2714 (1989).
  70. Rawlin, V. K., "Internal Erosion Rates of a 10 kW Xenon Ion Thruster", AIAA-88-2912 (1988).
  71. Brophy, J. R., and Garner, C. E., "Tests of High-Current

- Hollow Cathodes for Ion Engines," AIAA-88-2913 (1988).
72. Friedly, V., and Wilbur, P. J., "High Current Hollow Cathode Phenomena", AIAA-90-2587 (1990).
  73. Kerslake, W. R., et al., "Sert II: Mission, Thruster, Performance, and In-Flight Thrust Measurements", *Journal Spacecraft & Rockets*, 8(3), 213 (1971).
  74. Kerslake, W. R., and Ignaczak, L. R., "Status of Sert II Spacecraft and Ion Thrusters - 1978", AIAA-78-622 (1978).
  75. Kerslake, W. R., "Status of Sert II Thrusters and Spacecraft 1976", AIAA-76-1601 (1976).
  76. Kerslake, W. R., and Finke, R. C., "Sert II Thruster Space Restart - 1974", AIAA-75-365 (1975).
  77. Byers, D. C., and Staggs, J. F., "Sert II: Thruster System Ground Testing", *Journal of Spacecraft & Rockets*, 7(1), 7 (1970).
  78. Martin, A. R., et al., "A UK Large Diameter Ion Thruster for Primary Propulsion", AIAA-87-1031 (1987).
  79. Fearn, D. G., et al., "The Development Status of the UK-10 and UK-25 Ion Thruster Systems", IAF-87-293 (1987).
  80. Groh, K. W., and Loeb, H. W., "State of the Art of Radio Frequency Ion Thruster", AIAA-89-2381 (1989).
  81. Rawlin, V. K., "Operation of the J-Series Thruster Using Inert Gas", AIAA-82-1929 (1982).
  82. Martin, A. R., et al., "Performance Assessment of a UK Rare Gas Ion Thruster", *Journal of British Interplanetary Society*, 41, 183 (1988).
  83. Byers, D. C., "Critical Elements of E-Bombardment Propulsion for Large Space Systems", *Journal of Spacecraft and Rockets*, 14(11), 648 (1977).
  84. Kitamura, S., et al., "ETS-III Ion Engine Flight Operations in the Extended Mission Period", AIAA-85-2010 (1985).
  85. Rawlin, V. K., and Hawkins, C. E., "Increased Capabilities of the 30 cm Dia Hg Ion Thruster", NASA TM-79142 (1979).
  86. Rawlin, V. K., "Sensitivity of 30-cm Hg Bombardment Ion Thruster Characteristics to Accelerator Grid Design", NASA TM-78861 (1978).

87. Mantele, M. A., "Hg Ion Thruster Component Testing", AIAA-79-2116 (1979).
88. Pye, J. W., "Component Development for a 10 cm Hg Ion Thruster", AIAA-72-487 (1972).
89. Kruehle, G., and Zeyfang, E., "Recent Tests Performed for the Design Verification of RIT-10 Engineering Models", AIAA-79-2102 (1979).
90. Pinks, W., and Kruehle, G., "Performance Mapping and Lifetime Investigations of Thruster Components with Reference to the Development of a RIT-10 Flight Prototype", AIAA-79-2115 (1979).
91. Williamson, W. S., et al., "8-cm Engineering Model Thruster Technology: A Review of Recent Developments", AIAA-79-2103 (1979).
92. Kerslake, W. R., and Ignaczak, L. R., "Sert II 1980 Extended Flight Thruster Tests", AIAA-81-0665 (1981).
93. Mantele, M. A., "Hg Ion Thruster Component Testing," AIAA-79-2116 (1979).
94. Masek, T. D., "Solar EP Thrust Sub-System Development", JPL Technical Report 32-1579 (1973).
95. King, H. S., and Poeschel, R. L., "An Ion Thruster Module for Primary Propulsion Systems", *Journal of the British Interplanetary Society*, 26, 203 (1973).
96. Nakanishi, S., and Finke, R. C., "A 9700 Hour Durability Test of a 5 cm Dia Ion Thruster", AIAA-73-1111 (1973).
97. Lathem, W., "1000 Hour Test of a Dual Grid, Electrostatic Beam Deflection Accelerator", NASA TMS-67907 (1967).
98. Fearn, D. G., "Thruster Component Life Testing Under Cyclic and Steady-State Conditions", AIAA-76-987 (1976).
99. Masek, T., "Solar Electric Propulsion Thrust Subsystem Development", JPL Technical Report 32-1579 (1973).
100. Kerslake, W. R., and Pawlik, E. V., "Additional Studies of Screen and Accelerator Grids for E-Bombardment Ion Thrusters", NASA TN-D-1411 (1963).
101. Page, J. K. R., and Stewart, D., "Life Testing of the UK T4A Thruster", 3rd Proc. Eur. E. P. C. 181 (1974).
102. King, H. J., and Poeschel, R. L., "A 30 cm Hg Ion Thruster

- Module", *Journal of Spacecraft and Rockets*, 8(4), 420 (1971).
103. Eilenberg, S. L., et al., "Evaluation of Electrode Shapes for Ion Engines", AIAA J-3(5), 866 (1965).
  104. Ignaczak, L. R., et al., "Performance of the Sert 2 Spacecraft After 4 1/2 Years in Space", NASA TMS-71632 (1974).
  105. Mantenieks, M. A., and Rawlin, V. K., "Sputtering Phenomena in Discharge Chamber Components in a 30 cm Dia Hg Ion Thruster", AIAA-76-988 (1976).
  106. Bechtel, R. T., "30 cm J-Series Hg Bombardment Thruster", AIAA-81-0714 (1981).
  107. Collett, C. R., and Bechtel, R. T., "An Endurance Test of a 900 Series 30 cm Engineering Model Ion Thruster", AIAA-76-1020 (1976).
  108. Collett, C. R., and Poeschel, R. L., "A 10,000 Hour Endurance Test of a 700 Series 30 cm Engineering Model Thruster", AIAA-76-1019 (1976).
  109. Kami, S., et al., "Status of the J-Series Hg Ion Thruster", AIAA-82-1904 (1982).
  110. Mantenieks, M. A., and Rawlin, V. K., "Sputtering in Hg Ion Thrusters", NASA-TM-79266 (1979).
  111. Mantenieks, M. A., "Sputtering Phenomena of Discharge Chamber Components in a 30 cm Dia Hg Ion Thruster", NASA TMX-73532 and 73533 (1976).
  112. Beattie, J. R., "Endurance Test of a 30 cm Dia Engineering Model Ion Thruster", NASA CR-168132 (1983).
  113. Poeschel, R. L., "215 kW Advanced Technology Ion Thruster", NASA CR-134687 (1974).
  114. Mantenieks, M. A., "Performance Capabilities of the 8 cm Hg Ion Thruster", AIAA-81-0754 (1981).
  115. Rawlin, V. K., "Operation of the J-Series Thruster Using Inert Gas", AIAA-82-1929 (1982).
  116. Fearn, D. G., "An Assessment of the Durability of the UK-25 Ion Thruster", Working Paper SP(89) WP23 (June 1989).
  117. Smith, P., "Design and Development of the UK-10 Ion Propulsion System", AIAA-88-2911 (1988).
  118. Rawlin, V. K., and Mantenieks, M. A., "A Multiple Thruster

- Array for 30 cm Thrusters", AIAA-75-402 (1975).
119. Berkopce, F.D., et al., "Flight and Ground Performance of the Sert II Thruster", AIAA-70-1125 (1970).
  120. Fearn, D. G., et al., "The UK 10 cm Hg Ion Thruster Development Program", AIAA-75-389 (1975).
  121. Groh, K., et al., "Development Status of the RIT Ion Engines", AIAA-90-2671 (1990).
  122. Kerslake, W. R., "Charge-Exchange Effects of the Accelerator Impingement of an E-Bombardment Ion Rocket", NASA-TN-D-1657 (1963).
  123. Poeschel, R. L., and Beattie, J. R., "Primary Electric Propulsion Technology Study", NASA CR-159688 (1979).
  124. Reader, P. D., "Investigation of a 10 cm Dia E-Bombardment Ion Rocket", NASA TN-D-1163 (1962).
  125. Fearn, D. G., "Factors Influencing the Integration of the UK-10 Ion Thruster System with a Spacecraft", AIAA-87-1004 (1987).
  126. Stone, J. R., "Recent Advances in Low-Thrust Propulsion Technology", AIAA 88-3283 (1988).
  127. Masek, J. D., "Evolution and Status of the 30 cm Engineering Model Thruster", AIAA-76-1006 (1976).
  128. Rawlin, V. K., "Performance of 30 cm Ion Thruster with Dished Accel Grids", AIAA-73-1053 (1973).
  129. Collett, C. R., "A 7700 Hour Endurance Test of a 30 cm Kaufman Thruster", AIAA-75-366 (1975).
  130. Bechtel, R., "Component Testing of a 30 cm Dia E-Bombardment Thruster", AIAA-70-1100 (1970).
  131. Lathem, W. C., "Grid Translation Beam Deflection System for 5 cm and 30 cm Dia Kaufman Thrusters", AIAA-72-485 (1972).
  132. Weigand, A. J., "5 cm Dia Ion Thruster Development Summary Program", NASA TMX-68110 (1972).
  133. James, E. L., and Bechtel, R. T., "Results of the MPLT 1st Test Segment: Thruster J1", AIAA-81-0716 (1981).
  134. Collett, C. R., "Endurance Test of a 30 cm Kaufman Thruster", AIAA-73-1085 (1973).

135. Rawlin, V. K., et al., "Design, Fabrication, and Operation of Dished Accelerator Grids on a 30 cm Ion Thruster", AIAA-72-486 (1972).
136. Nakanishi, S., "Durability Tests of a 5 cm Dia Ion Thruster System", AIAA-72-1151 (1972).
137. Nakanishi, S., and Finke, R. C., "A 2000 Hour Durability Test of a 5 cm Dia Hg Bombardment Ion Thruster", AIAA-73-1111 (1973).
138. Lathem, W. C., "5000 Hour Test of a Grid Translation Beam Deflection System for a 5 cm Dia Kaufman Thruster", NASA TMX-68185 (1973).
139. Bechtel, R. T., "Results of the MPLT", AIAA-82-1905 (1982).
140. Bechtel, R. T., and James, E.L., "Preliminary Results of the MPLT of a 30 cm Hg Bombardment Thruster", AIAA-79-2078 (1979).
141. Kerslake, W. R., "Accel Grid Tests of an E-Bombardment Ion Rocket", NASA TNB-1168 (1962).
142. Beattie, J. R., et al., "Status of Xenon Ion Propulsion Technology", AIAA-87-1003 (1987).
143. Nakamura, Y., et al., "Electric Propulsion Work in Japan", IAF-86-171 (1986).
144. Dulgeroff, C., et al., "IAPS (8 cm) Ion Thruster Cyclic Endurance Test", IEPC-84-37 (1987).
145. Nakanishi, S., et al., "9700 Hg Durability Test of a 5 cm Dia Ion Thruster", *Journal of Spacecraft & Rockets*, 11(8), 560 (1974).
146. Fosnight, V. V., et al., "Cesium Ion Engine System Life Test Results", *Journal of Spacecraft & Rockets*, 5(4), 465 (1968).
147. Hyman, J. R., "Performance Optimized, Small Structurally Integrated Ion Thruster System", NASA CR-121183 (1973).
148. Reid, G.C., et al., "Cesium E-Bombardment Ion Engines", *Journal of Spacecraft & Rockets*, 3(7), 1093 (1966).
149. Mantenieks, M. A., and Wintucky, E. G., "5200 Cycle Test of a 8 cm Dia Hg Ion Thruster", AIAA-78-649 (1978).
150. Rawlin, V. K., "Internal Erosion Rates of a 10 kW Xenon Ion Thruster", AIAA-88-2912 (1988).

151. Mantiņieks, M. A., and Rawlin, V. K., "Studies of Internal Sputtering in a 30 cm Ion Thruster", AIAA-75-400 (1975).
152. Mantiņieks, M. A., and Wintucky, E. G., "5200 Cycle Test of an 8 cm Dia Hg Ion Thruster", NASA TMX-78860 (1970).
153. Rawlin, V. K., et al., "Dished Accel Grids on a 30 cm Ion Thruster", *Journal of Spacecraft & Rockets*, 10(1), 29 (1973).
154. Stewart, P., "Life Testing of the UK T4A Thruster", AIAA-76-1023 (1976).
155. Rawlin, V. K., "Studies of Dished Accel Grips for 30 cm Ion Thruster", AIAA-73-1086 (1973).
156. Eckerdt, W. O., et al., "E-Bombardment Thrusters Using Liquid Hg Cathodes", *Journal of Spacecraft & Rockets*, 4(5), 599 (1967).
157. Patterson, M. J., "5 kW Xenon Ion Thruster Lifetest", AIAA-90-2543 (1990).
158. Kitamura, S., et al., "1000 Hour Test of a 14 cm Dia Ring-Cup Xenon Ion Thruster", AIAA-90-2542 (1990).
159. Lathem, W. C., "A Single Axis Electrostatic Beam Deflection System For a 5 cm Dia Ion Thruster", NASA TMX-68133 (1973).
160. Nakanishi, S., "A 15000 Hour Cyclic Endurance Test of an 8 cm Dia Hg Bombardment Ion Thruster", AIAA-76-1022 (1976).
161. Collett, C. R., "Thruster Endurance Test", NASA CR-135011 (1976).
162. Banks, B.A., "8 cm Hg Ion Thruster System Technology", AIAA-74-1116 (1974).
163. Francisco, D. R., "Successful Completion of a Cyclic Ground Test of a Hg Ion Auxiliary Propulsion System," IEPC-88-035 (1988).
164. Power, J. L., "Sputter Erosion and Deposition in the Discharge of a Small Hg Ion Thruster", AIAA-73-1109 (1973).
165. Nakamura, Y., et al., "Long Time Operation Test of Engineering Model of ETS-III Ion Thruster", IEPC-84-36 (1984).

**13.0 APPENDICES**  
**13.1 Appendix A**

**AIAA 90-2591**  
**The Effect of Nitrogen on**  
**Xenon Ion Engine Erosion**  
C. E. Garner, J.R. Brophy,  
L.C. Pless, and J. W. Barnett,  
Jet Propulsion Laboratory  
Pasadena, CA

# THE EFFECT OF NITROGEN ON XENON ION ENGINE EROSION

Charles E. Garner\*, John R. Brophy\*, L.C. Pless+, and John W. Barnett\*\*  
*Jet Propulsion Laboratory*  
*California Institute of Technology*  
*Pasadena, Ca 91109*

## ABSTRACT

Erosion studies were performed on a 30-cm diameter J-series ion engine modified for operation on xenon propellant. The erosion rates of molybdenum and tantalum badges placed at different locations within the discharge chamber were measured as a function of the percentage of nitrogen (by mass) added to the xenon propellant. Reductions in the erosion rates of these badges of a factor of 8 to 50 were observed at nitrogen addition fractions between 0.5 to 2.0 percent. Reductions in cathode-side baffle erosion were achieved by adding nitrogen to the xenon propellant or by increasing the cathode orifice diameter. Analyses show that no significant degradation in ion engine performance should be expected at these nitrogen mass fractions. XRD, XPS and Auger analyses indicate the existence of nitrogen and nitrides in the surfaces of some but not all of the badges used in the tests where nitrogen was added to the xenon. Difficulty in identifying surface nitrides in the samples may be due to the existence of surface oxides and contaminants, or to the small thicknesses of the nitride layers.

## INTRODUCTION

Ion engine operating life is limited, in-part, by ion sputter erosion of surfaces in the discharge chamber which are at or near cathode potential. Internal engine components subject to ion sputtering include the screen grid, the cathode starter electrode (keeper), and in the J-series ion engine, the baffle and pole piece assembly. For several reasons, inert gases have replaced mercury as the propellant of choice for interplanetary and earth-orbital ion propulsion systems. Erosion rates within the ion engine discharge chamber, however, are expected to be greater with inert gas propellants than the corresponding rates with mercury. This is due primarily to the higher sputter yields of the inert gases as compared to mercury.

\* Member of the Technical Staff, Electric Propulsion and Plasma Technology Group. Member AIAA.

+ Member of the Technical Staff, Electric Power Systems Section.

\*\* Supervisor, Electric Propulsion and Plasma Technology Group. Member AIAA.

Data on erosion and wear rates within the discharge chamber of ion engines operated on inert gases are limited. During the 5 kW, xenon ring-cusp thruster wear test recently conducted at the NASA Lewis Research Center (LeRC), the cathode starter electrode eroded completely away within 890 hours.<sup>1</sup> In high current hollow cathode testing conducted at JPL, significant erosion of the pole piece and other components was observed in the vicinity of the hollow cathode operated on argon at 100 amperes,<sup>2</sup> in spite of the low discharge voltage (less than 24 volts) which was used in the test. In 1988 a screen grid life of 7000 hours<sup>3</sup> was inferred from a 10 kW xenon thruster life evaluation test; however, there was a good deal of uncertainty in the screen grid life estimate.

In 1987, J-series ion thruster erosion testing<sup>4</sup> revealed unexpectedly high erosion rates and highly peaked erosion profiles on the cathode side of the baffle, a result substantiated by later tests<sup>3</sup>. During testing of a high current hollow cathode<sup>2</sup> it was observed that a well-defined and collimated plume was produced by the cathode when it was operated at a high emission current. A section of the anode face plate 15 cm downstream of the cathode was eroded, even though this face plate was at anode potential. As a result of this testing it was suggested that a cathode jet having ion energies of tens of eV might be the mechanism responsible for the high erosion rates observed at the cathode side of the baffle<sup>2</sup>. At sufficiently high discharge currents this cathode jet might result in increased screen grid erosion.

Techniques which could be used to reduce discharge chamber erosion include reducing the discharge voltage, which reduces the energy of the sputtering ions, and reducing the propellant utilization efficiency (propellant utilization efficiency is defined as the fraction of the neutral propellant flow which is ionized and extracted as beam ions), which reduces the fraction of multiply charged ions. However, it may be desirable to operate ion engines at the highest possible discharge voltage and propellant utilization to reduce the number of neutrals escaping from the discharge chamber. These neutrals are responsible for the creation of charge-exchange ions which can erode the accelerator grid at unacceptably high rates.<sup>1</sup> Thus, internal component erosion may be traded against accelerator grid erosion.

Previous testing of J-series mercury ion engines indicated that the presence of certain facility background

gases reduced molybdenum screen grid erosion.<sup>5-7</sup> Subsequently it was proposed<sup>8</sup> that small quantities of nitrogen added to the mercury propellant could reduce discharge chamber component erosion and extend the useful life of the engine. Preliminary data<sup>4,9</sup> have suggested that the addition of small quantities of nitrogen to the xenon propellant reduces erosion within the discharge chamber of xenon ion engines. It was proposed<sup>6</sup> that the mechanism responsible for the reduced erosion rates observed when nitrogen or other facility gases are present within the discharge chamber is the formation of sputter-resistant oxides or nitrides that have lower ion sputter erosion rates than the native metal. However, there have been no analyses to verify the formation of these sputter-resistant compounds.

This paper presents the results of a continuing investigation of the effects of the addition of small quantities of nitrogen on discharge chamber erosion within xenon ion engines. The erosion rates for erosion badges placed at the cathode side of the baffle, the discharge side of the baffle, near the screen grid, and at the cathode pole piece are presented as a function of the percentage of nitrogen added to the xenon propellant. Erosion of the cathode side of the baffle and its relationship to cathode current density are discussed. Finally, the results of various techniques used to analyze the surface of the erosion badges will be reviewed.

## EXPERIMENTAL PROCEDURE

Erosion tests were performed using a J-series 30 cm ion engine modified for use with xenon propellant. J-series ion thrusters, developed approximately 10 years ago at LeRC, employ an axially diverging magnetic field in the discharge chamber to increase engine efficiency. The engine was operated in a stainless steel vacuum chamber 2.3 meters in diameter and 4.6 meters in length, and pumped by silicone-based oil diffusion pumps. A liquid nitrogen cryo-liner, which consisted of a stainless steel cylindrical shroud 2.1 meters in diameter and 3.1 meters in length, was used to cold-trap facility gases such as water vapor during testing. Vacuum tank pressure was measured using a calibrated ionization gauge tube and controller. After chilling the cryo-liner the no-load tank pressure prior to flowing xenon into the tank was  $1.5 \times 10^{-7}$  torr or less. Tank pressure during thruster operation was typically  $2.9 \times 10^{-5}$  torr.

Erosion badges, polished to a mirror-like finish, were placed in the discharge chamber at the locations shown in Fig. 1. The erosion badges were polished to the specifications shown in Table 1. The screen grid erosion badges were hung by a 0.254 mm diameter tungsten wire on the centerline of the thruster, approximately 10 mm from the screen grid. Each end of the tungsten wire was

wrapped around an Alnico magnet retainer and tightly stretched to minimize sag. Because the tungsten wires were tied to the magnet retainers, the screen grid erosion badge was at screen potential. Tantalum erosion badges were mounted to the inner diameter of the cathode pole piece using stainless steel screws. The tantalum baffle and all the tantalum erosion badges used in the experiments were machined from a single sheet of electron-beam melted tantalum. Similarly, all of the molybdenum erosion monitors used in the tests were machined from a single sheet of electron-beam melted, low carbon molybdenum.

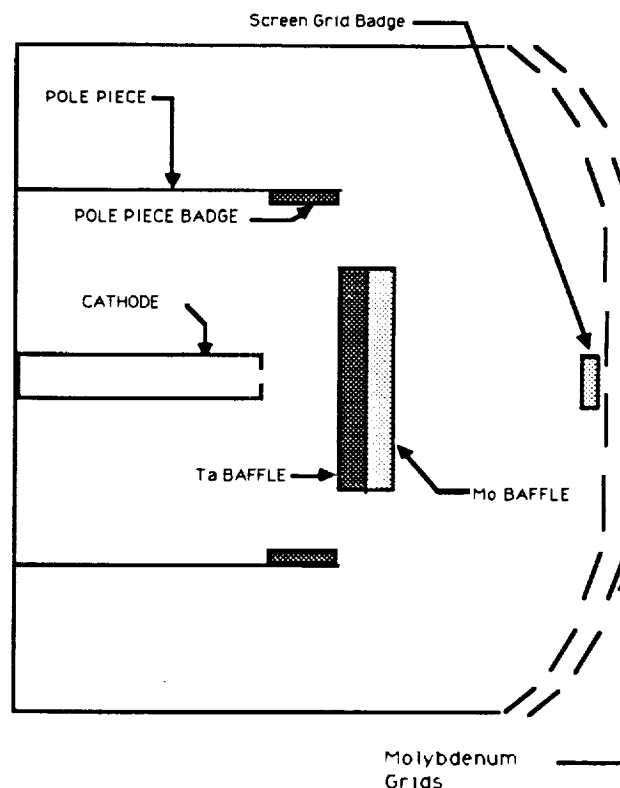


Fig. 1. Schematic diagram of the ion engine discharge chamber showing the locations of the erosion badges.

TABLE I. Erosion Badge Polishing Specifications

Badge Material	Surface Roughness (Angstroms)	Surface Flatness (Angstroms)
Molybdenum	$\pm 75$	$\pm 75$
Tantalum	$\pm 200$	$\pm 75$
304 Stainless	$\pm 50$	$\pm 50$

The polished erosion badges were masked using either 0.005" thick tantalum or 0.001" thick tungsten

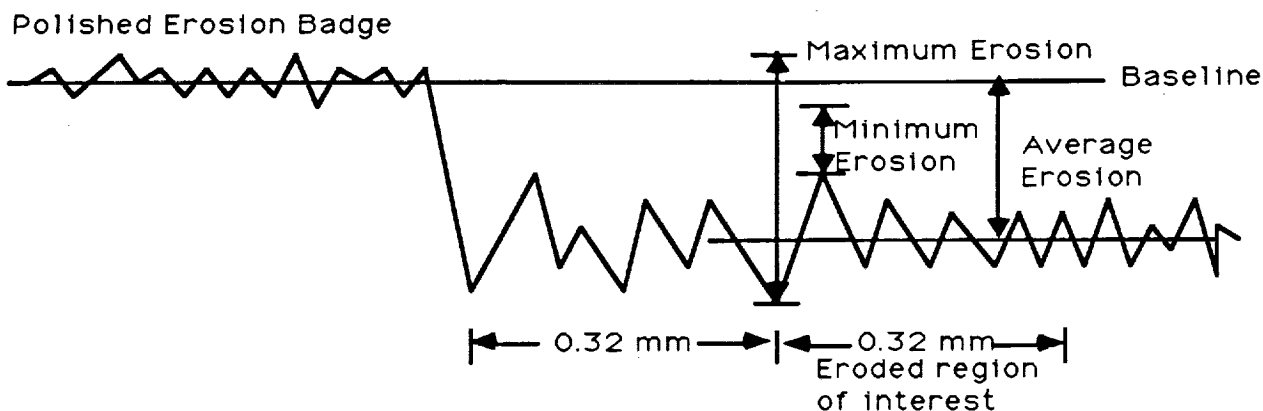


Fig. 2. Simulated profilometer trace used to determine the depth of the trench eroded into the erosion badge by discharge chamber ions.

foils. Electric Discharge Machining (EDM) was used to pattern the tungsten masks, and the tantalum masks were cut and patterned manually. Discharge chamber component erosion rates were determined by measuring the trench depth eroded into the unmasked portions of the erosion badges by discharge chamber plasma ions. A profilometer capable of resolving surface features as low as 20 angstroms was used to measure trench depths.

Trench depths from the profilometer traces were determined as follows. The uneroded surface height (baseline height) of the sample was determined as an average of peaks and trough heights in the uneroded region of the sample (Fig. 2). The same procedure was used for the etched regions, with only a 0.32 mm long region considered for purposes of determining the trench depth of the sample. This 0.32 mm region is 12.5 mask thicknesses away from the mask edge; previous experimental data<sup>4</sup> suggest that this is a suitable distance to minimize mask effects on the etch rates of the erosion badges. Furthermore, it is far enough away from the sample edge such that there is no spurious data due to roll-off at the badge edges. The average erosion rate was determined subjectively by estimating an average surface location between the peaks and troughs in the eroded region, and then calculating the difference in heights between this subjective guess and the baseline.

Uncertainties in the erosion depth measurements were determined by adding the peaks in the baseline to the troughs in the eroded region to determine the maximum erosion rate, and troughs in the baseline to peaks in the eroded region to determine the minimum erosion rate. The uncertainties in the erosion rate measurements were due primarily to the formation of deep valleys and high peaks in the portions of the badges exposed to the discharge plasma ions (Fig. 2). Because the engine was operated for only 24 hours during each test, and because of the formation of peaks and valleys in the eroded region, there is a significant amount of uncertainty in some of the erosion data. 24-hour test periods were selected to allow

many experimental conditions to be investigated. This technique could be used with longer duration tests to greatly reduce the measurement uncertainties. Long-duration discharge chamber erosion studies were beyond the scope of this work and are a topic for future investigations.

A schematic diagram of the propellant system used to operate the ion engines and to introduce nitrogen into the xenon is given in Fig. 3. The flow rate of xenon and nitrogen into the ion engine (exclusive of facility back-flow) was measured using the flow meters labelled "Xenon" and "Nitrogen" respectively. As indicated in Fig. 3, there is a micrometer valve located downstream of the flow meter used to measure the total xenon flow rate into the engine. The pressure drop developed across the micrometer valve served to minimize the diffusion of nitrogen upstream to the xenon flow meter, a feature which is essential to the accurate determination of the xenon flow rate for those tests performed with nitrogen addition. The propellant system was made leak-tight by closing hand-valves HV-1 through HV-3, pressurizing the propellant lines to the pressure used during erosion testing ( $2.52 \times 10^5$  Pa), measuring the leak rate, and eliminating any leaks found, down to the resolution of the flow meters (0.1 sccm). Leaks downstream of the hand valves were checked by plugging connections leading into the ion engine or by plugging the cathode orifice.

The xenon and nitrogen thermal mass flow meters labelled "Xenon" and "Nitrogen" were calibrated at the manufacturer's calibration facility using a primary calibration standard. Calibration of the flow meter on nitrogen showed that the flow meters have a very linear response on nitrogen. The calibration on xenon, however, revealed that the correction factor for xenon (required when a flow meter is used for measuring the flow rate of one gas but was calibrated on a different gas) to nitrogen varied with flow rate. The results of this calibration are shown in Table II.

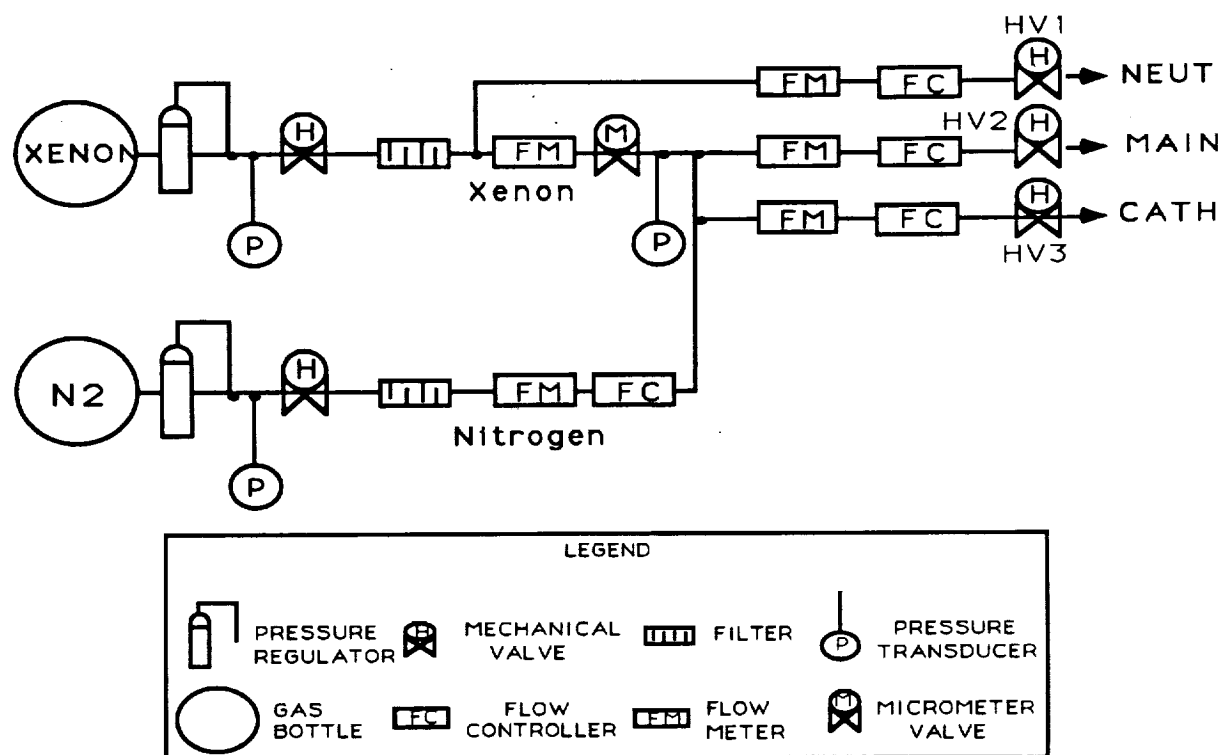


Fig. 3. Schematic diagram of the propellant system used for the erosion tests.

TABLE II. Calibration of the Xenon Mass Flow Meter

Calibrated Xenon Flow (sccm)	Indicated Nitrogen Flow (sccm)	Correction Factor
5.05	6.86	1.36
10.0	13.14	1.31
20.0	25.40	1.27
25.3	31.92	1.26
50.0	65.63	1.31
75.0	119.40	1.59
100.0	199.60	2.00

The correction factor is seen to vary as a function of flow rate, with a minimum at approximately 25.25 sccm true xenon flow. It is likely that the correction factors for thermal mass flow meters are a function of the design of the particular mass flow meter. Since accurate measurement of the xenon flow rate was critical for these tests, careful flow rate calibrations at the mass flow rates of interest were conducted.

After the propellant system was assembled, the mass flow meters were recalibrated in-house using a bubble volumeter. Analysis of the bubble volumeter calibrations showed that these calibrations were within 1.5% of the calibration values from the primary standard.

A fourth-order polynomial curve fit was used to interpolate between the calibration points. The nitrogen flow meter was calibrated in a similar manner, and the erosion tests were conducted at calibrated nitrogen mass flow rates to eliminate uncertainties in interpolating between calibrated data points. An analysis of the calibration data showed that all data points for both the xenon and nitrogen calibrations fit within two standard deviations and met the Chauvenet criterion<sup>10</sup> for acceptable data.

Backflow of xenon or nitrogen into the ion engine was calculated using the method developed by Wilbur et. al.<sup>11</sup> The largest source of error in the uncertainty analysis of the xenon engine flow was the backflow calculation. This was due to uncertain knowledge of the local tank wall or liquid nitrogen liner temperatures, which affect the rate at which facility gases backflow into the thruster. Tank wall and cryo-liner temperatures were measured with thermocouples at three locations during testing. The backflow of nitrogen and xenon, both a function of tank pressure, were calculated and added to the values of xenon or nitrogen injected into the engine through the propellant system. The total xenon flow, the sum of the flow through the xenon meter and the backflow, was kept constant.

In most tests a computer data acquisition and control system monitored and controlled the engine discharge voltage, cathode xenon flow rate, and total engine xenon flow rate. Control of the discharge voltage

was maintained to within  $\pm 0.5\%$  by varying the cathode flow. The total flow of xenon into the ion engine was fixed at 32.9 sccm, which was the sum of the "XENON" flow meter flow and the computed backflow into the engine. The propellant utilization efficiency of 0.91 was corrected for facility backflow but not for doubly charged ions. Under computer control, the backflow was continuously calculated and the main flow adjusted such that the total engine flow remained constant. The discharge current was fixed at 11.8 amperes.

The erosion tests were conducted in the following manner. Erosion badges were placed in the discharge chamber, with the polished face of the screen grid badge facing the cathode side of the discharge chamber. The cathode side baffle erosion badge was placed such that the polished tantalum surface faced the cathode. The main discharge side baffle erosion badge was placed with the polished molybdenum surface facing the screen grid. The vacuum tank was then pumped to  $5 \times 10^{-7}$  torr with the propellant lines open to vacuum up to the xenon and nitrogen bottle valves. Next the liquid nitrogen cold trap was cooled until the no-load tank pressure was at  $1.5 \times 10^{-7}$  or less. Nitrogen at the desired flow rate was flowed into the vacuum tank and the tank pressure was noted. The backflow of nitrogen into the ion engine was calculated using Eq. (1),

$$N_2 \text{ Backflow} = K (\text{Tank Pressure} - 0.25 \times (\text{No load Tank Pressure})) \quad (1)$$

where K is a constant determined by the vacuum tank wall temperature, tank pressure, and grid geometry.<sup>11</sup> (Previous residual gas analyses<sup>9</sup> indicated that 75% of the vacuum constituent species at the no-load tank pressure after the cold trap has been chilled was nitrogen). The propellant lines were then pumped out to high vacuum. The propellant lines were re-pressurized to  $2.52 \times 10^5$  Pa with the nitrogen flow controller off and hand valves HV-1 to HV-3 closed. After at least 30 minutes the flow meter values were checked for any indications of zero shift.

Engine start-up was accomplished by flowing xenon through the engine and neutralizer cathodes and gradually increasing the cathode tip heater power over a period of approximately one hour. For those tests conducted with nitrogen addition to the xenon, the nitrogen was mixed with the xenon propellant at the start of the tip heat cycle. After one hour the ion engine discharge was started and was run with a discharge current and voltage of 11.8 amps and 32 volts, respectively, for approximately five minutes. Beam extraction was then initiated, with an additional five minutes required to achieve the correct engine operating conditions. When these conditions were achieved, the run time clock was set to zero hours and the erosion test was started. The engine operating conditions used for the tests are shown in Table III.

Table III. Ion Engine Operating Conditions Used for Erosion Testing

Beam Current	(A) :	2.0
Beam Voltage	(V) :	1100
Discharge Current	(A) :	11.8
Discharge Voltage	(V) :	32.0
Cathode Flow Rate	(sccm) :	2.5 - 4.0
Total Xenon Flow Rate	(sccm) :	32.9
eV/ion	:	211
Prop. Util.	:	0.91

The tests were run for a period of 24 hours. After a minimum cool-down period of 3.5 hours, the vacuum tank was vented to atmosphere and the erosion badges were removed from the engine and replaced with a new set of erosion badges. The position of the screen grid erosion badge was noted before and after each test to insure that this badge had not moved during tank opening or closure. The cathode orifice diameter was measured before and after each test. The cathode orifice diameter decreased from a diameter of 1.20 mm at the start of run #1 to 1.10 mm at the end of run #9. The decrease was due to a small quantity of deposit of unknown origin which partially closed the cathode orifice.

The first and last tests conducted were baseline tests to measure the erosion rates of discharge chamber components when no nitrogen was added to the xenon. In between the baseline tests, nitrogen in varying quantities was added to the xenon and component erosion rates were measured. Three tests were conducted at a concentration of approximately 0.5% nitrogen by mass added to the xenon for the purposes of checking repeatability of the results.

## RESULTS AND DISCUSSION

Table IV describes the tests in the order in which they were conducted.

Table IV. Ion Engine Discharge Chamber Erosion Testing

Test #	Test Duration (Hrs)	%N <sub>2</sub> Added To Xenon	Comments
1	24.0	0	Baseline test
2	24.0	1.19	
3	24.0	0.51	
4	24.0	0.51	
5	24.0	0.51	
6	24.0	0.26	
7	24.0	2.06	
8	24.0	0	Last baseline test
9	24.0		LN2 liner not cold-trapped

It is useful to compare ion engine erosion data obtained both with and without cold-trapping water vapor and other volatiles in the vacuum tank, so that comparisons of component erosion rates between the two cases can be made. In test #9, the vacuum tank cryo-liner was not chilled with liquid nitrogen, and water vapor outgassing from the tank walls was not cold-trapped, resulting in increased backflow of oxygen into the ion engine. The nitrogen and water vapor partial pressures in the vacuum tank were not measured in these tests; estimates of the nitrogen and water vapor partial pressures were made, based on a tank pressure measurement that was taken while no xenon was flowing into the vacuum tank. Backflow rates for nitrogen and oxygen were then calculated. It is important to note that, in test #9, water vapor was probably the majority constituent in the vacuum tank background. Data from these tests are included in figures which plot erosion rate as a function of the percentage of nitrogen added to the xenon, and are denoted by grey circles.

The effects on component erosion rates of adding small quantities of nitrogen to the xenon propellant are depicted graphically in Figs. 4-8. There is significant uncertainty in some of the data due to the surface profiles created by ion bombardment of the erosion badges during engine operation. In general, however, there is a direct correlation between the percentage of nitrogen added to the xenon and the reduction in component erosion rate. Erosion rates of all samples tested decreased as the percentage of nitrogen added to the xenon increased. The erosion rates of all materials tested dropped rapidly up to a nitrogen concentration of 0.5%; thereafter the erosion rates continued to decrease with increasing nitrogen concentrations, but at a far reduced rate. The results of tests #4 through #6, and baseline tests #1 and #8, show that the data are repeatable.

A possible explanation of the observed phenomena is that the presence of nitrogen results in the formation of a sputter-resistant nitride. As the concentration of nitrogen increases, nitride surface coverage increases until it is complete and the addition of more nitrogen has little or no effect on the erosion rate of the erosion badge.

#### SCREEN GRID EROSION

The side of the screen grid facing the cathode is eroded by discharge chamber plasma ions with energies at or near plasma potential. Grid life time is typically defined as the time required for one-half of the grid thickness to be eroded. For the J-series mercury ion engine operating at 2.6 kW and a discharge voltage of 32 volts, the screen grid erosion rate during the Mission Profile Life Test (MPLT) was determined to be 64 angstroms per hour at the center.<sup>12</sup> In this test, conducted at 2.7 kW and a discharge voltage of 32 volts,

the baseline (no nitrogen added to the xenon) erosion rate of the molybdenum screen grid erosion badge placed at the center of the screen grid was approximately 255 angstroms per hour, a factor of almost four greater than that obtained during the MPLT.

It is difficult to make an exact comparison of the two erosion rates, however, because the plasma uniformity and doubly charged ion content of the J-series ion engine operating on xenon have not been sufficiently characterized. It is reasonable to expect, however, that the screen grid erosion rate of the ion engine used for this test would be greater than the corresponding rate obtained with mercury because of increased discharge chamber currents and xenon sputter yields. Figure 4 shows that the addition of 0.5% nitrogen to xenon reduces screen grid badge erosion by a factor of 5. The addition of nitrogen at a rate of approximately 2.06% reduced screen grid badge erosion by a factor of 19.6, to a total of 13 angstroms per hour. Typical grids are approximately 0.381 mm thick; thus, for the thruster geometry and operating conditions used, the screen grid could theoretically be operated for over 146,500 hours before half of its thickness would be eroded. However, if no nitrogen were added to the xenon, the useful operating life would be under 7500 hours based on these data. The addition of nitrogen to the propellant may be a significant life-enhancing technique in developing high power (> 10 kW) inert gas thrusters.

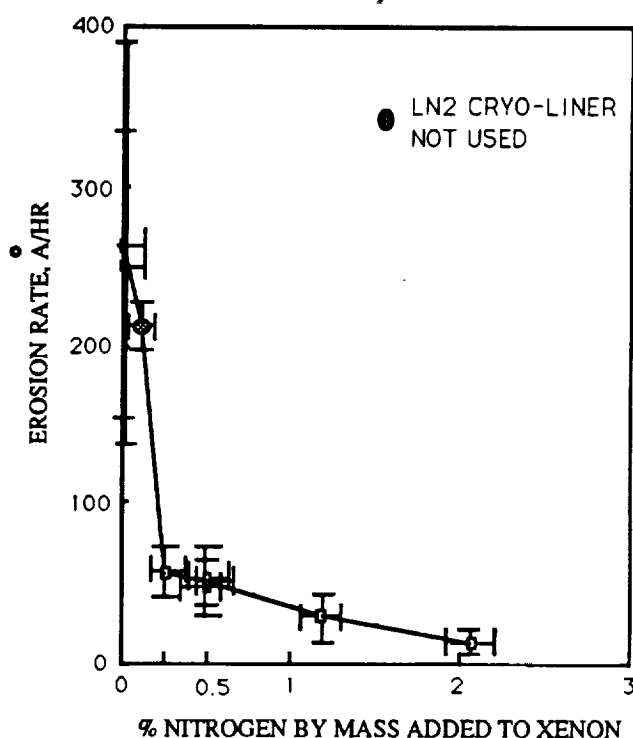


Fig. 4. Plot of the erosion rate of the molybdenum screen badge vs the percentage by mass of nitrogen added to the xenon propellant.

## BAFFLE EROSION: DISCHARGE SIDE

The 38.1 mm diameter molybdenum baffle facing the screen grid was masked by a 0.001" thick tungsten foil. The unmasked portion of the baffle consisted of a cross-shaped pattern 20 mm in diameter. Spatially uniform erosion rates at all locations exposed to the discharge chamber plasma were observed in all tests, including when nitrogen was added to the xenon (Fig. 5).

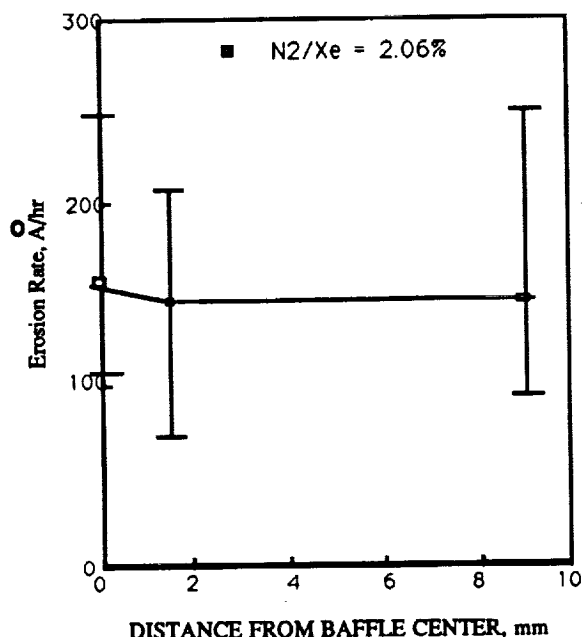


Fig. 5. Plot of the erosion rate of the discharge side of the baffle as a function of distance from the baffle center.

Fig. 6 shows a plot of the erosion rates of the discharge side of the baffle as a function of the percent by mass of nitrogen added to the xenon. The erosion rates at the discharge side of the molybdenum baffle were generally 2-3 times greater than those measured at the screen grid, presumably because of the higher plasma density which exists at this location. The shape of the curve in Fig. 6 is similar to that of the molybdenum screen erosion curve shown in Fig. 4. At a nitrogen addition fraction of 0.5%, the molybdenum erosion rate at this location was reduced by almost a factor of 4 compared to the baseline erosion rate. At a nitrogen fraction of 2%, the erosion rate was reduced by a factor of almost 10.

## BAFFLE EROSION: CATHODE SIDE

The cross-shaped tungsten foils used to mask the molybdenum erosion badges facing the discharge chamber were also used to mask the tantalum erosion badges facing the cathode. The effect of adding small quantities of nitrogen to the xenon is plotted in Fig. 7, which shows the tantalum baffle erosion rates at the baffle center as a function of the percentage by mass of nitrogen added to the

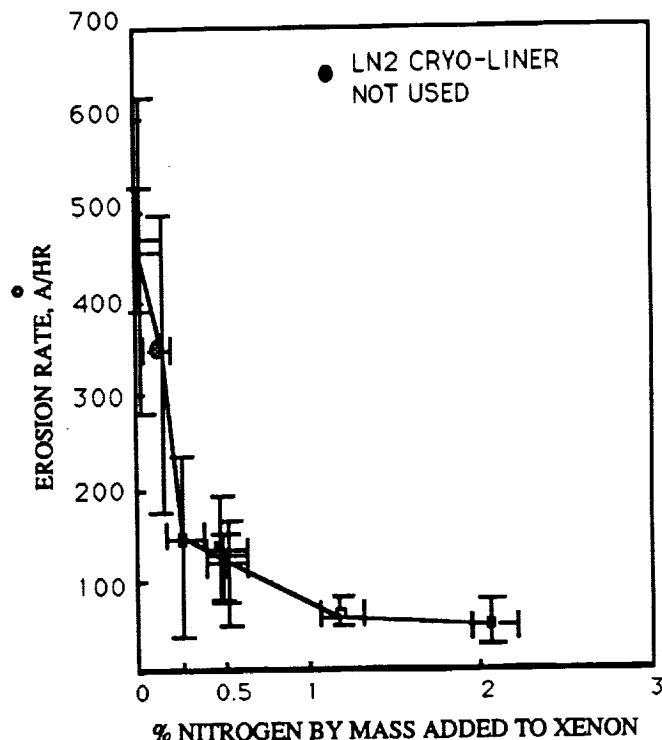


Fig. 6. Plot of the erosion rate of the discharge chamber side of the molybdenum baffle vs the % nitrogen by mass added to the xenon.

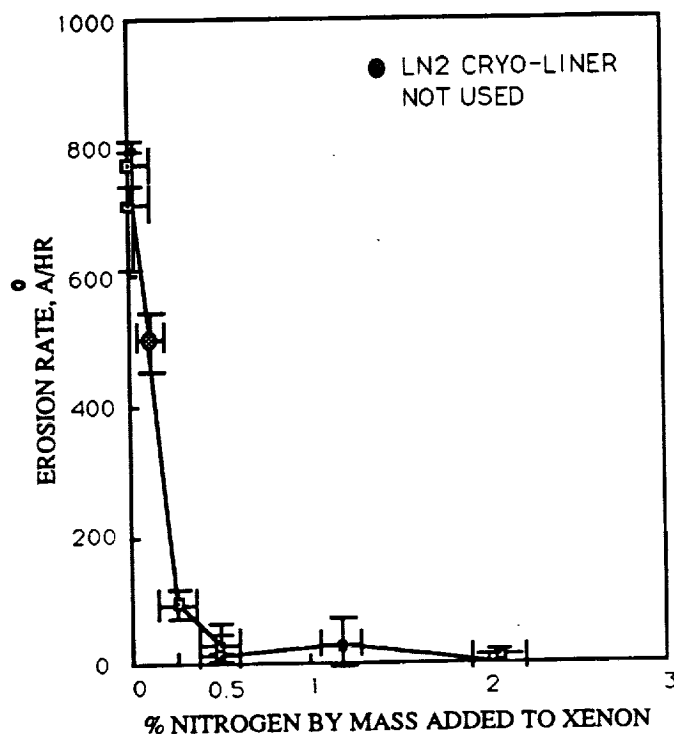


Fig. 7. Plot of the erosion rate of the cathode side of the tantalum baffle vs the % nitrogen by mass added to the xenon.

xenon. As is the case for the molybdenum baffle and screen grid erosion badges, the tantalum baffle erosion

rates fall significantly when a nitrogen mass fraction of 0.5% is added to the xenon, and drop far less sharply thereafter. At a mass fraction of 2.06%, there was at most (including uncertainty) an erosion rate of 12.5 angstroms per hour. This represents a decrease in the baffle center erosion rate of approximately 50, compared to the two baseline erosion rates. It is also a factor of 8 below the cathode side baffle erosion rate measured in the 2.6 kW J-series endurance tests<sup>12</sup>, and implies an engine life (limited by spalling of metal deposits on the keeper isolator shadow shields) of at least 15,000 hours.

In Fig. 8 are plotted the erosion rates of the tantalum baffles from runs #1 and #7; included in this figure are baffle erosion data from a test conducted in 1989<sup>9</sup> in which a cathode having a smaller orifice diameter was used. Data pertinent for comparison are shown in Table V.

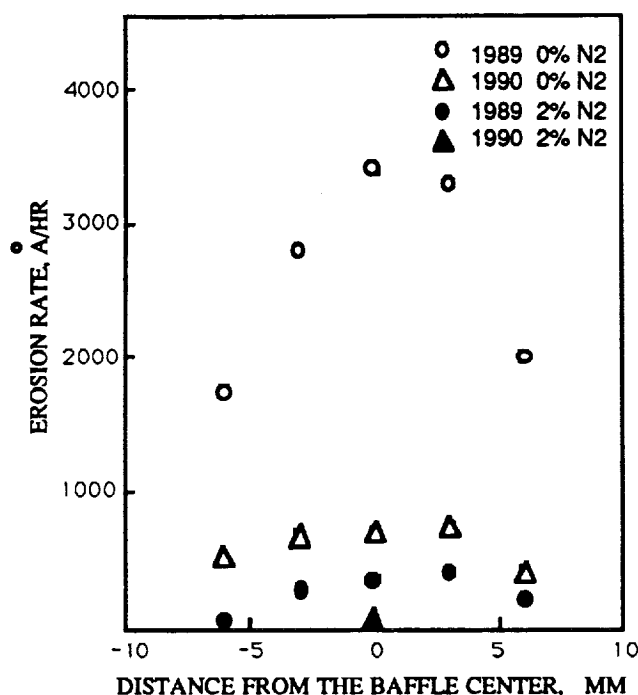


Fig. 8. Plot of the erosion rates of the cathode side of the baffle. Closed and open circles: data from Ref. 9 (cathode orifice dia = 0.76 mm). Closed and open triangles: data from test #7 of this paper (cathode orifice dia = 0.11 cm).

Table V. Erosion Test Data for Two Different Cathode Orifices

TEST	Cath Flow	Cath Orifice Dia	Disch Current	Current Density	Baffle Center Wear Rate
	(sccm)	(cm)	(A)	(A/cm <sup>2</sup> )	(A/hr)
1989 0% N2	2.4	0.07	11.0	2425	3400
1989 2% N2	2.4	0.07	11.0	2425	230
1990 0% N2	2.4	0.11	11.8	301	740
1990 2% N2	2.4	0.11	11.8	301	13

In both sets of experiments the cathode emission currents (discharge current in these cases) were almost identical; the discharge voltage in both was set to 32 volts. However, there are two significant differences in the characteristics of the two sets of data. First, the erosion rates for the test set which used the smaller cathode orifice are greater than for the cathode with the larger orifice. Second, the cathode-side baffle erosion profiles are more peaked for the test set which used the cathode with the smaller orifice.

One possible explanation for the observed behavior is that there is a relationship between the velocities of the ions in the cathode plume and the cathode emission current density. The current density in the cathode orifice of an ion engine hollow cathode is typically hundreds to thousands of amperes/cm<sup>2</sup>. It is possible that as cathode current density is increased, a magnetic body force accelerates the electrons and ions.<sup>12</sup> This phenomenon may have been responsible for anomalously high ion energies in the cathode plume observed in high current hollow cathode testing<sup>9</sup>, as evidenced by the fact that ion energies must have exceeded anode potential to erode the anode faceplate. Until the ion velocity and number density in the cathode plume have been characterized, the mechanism responsible for cathode side baffle erosion will not be understood. However, the data presented in Fig. 8 suggest that very significant reductions in baffle erosion can be obtained by increasing cathode orifice diameter, as well as by adding small quantities of nitrogen to the xenon.

#### TANTALUM POLE PIECE EROSION MONITORS

The tantalum erosion badges placed on the inner diameter of the cylindrical cathode pole piece walls were observed to be affected by nitrogen addition in a way similar to the tantalum baffle, but the magnitude of erosion reduction is less pronounced (Fig. 9). The erosion rates of the tantalum pole piece badges are generally less than the erosion rates at the center of the tantalum baffle, probably due to the fact that the pole piece is eroded predominantly by discharge chamber ions, and the baffle is eroded predominantly by relatively energetic cathode plume ions. When 2.06% nitrogen by mass was added to the xenon, the average erosion rate of the pole piece badge, including uncertainty, was too low to be measured. Because of the reduced erosion rates demonstrated at the pole piece, it may be desirable to fabricate cathode start electrodes from tantalum and add small quantities of nitrogen to the propellant in high power inert gas ion engines.

#### ION ENGINE PERFORMANCE ANALYSIS

The addition of nitrogen to the propellant will degrade thruster performance to some extent. The

performance degradation results from the ionization and acceleration of nitrogen in place of xenon. The nitrogen ion mass (either  $N^+$ , or  $N_2^+$ ) is considerably less than that for xenon; consequently, the nitrogen ion velocities will be much higher than the xenon ion velocity. This ion exhaust velocity difference degrades thruster performance in a way analogous to the degradation caused by multiply charged xenon ions. The most energy efficient way to produce a given thrust and specific impulse is for all of the exhaust particles to have the same exit velocity; any other velocity profile which results in the same thrust and specific impulse will require more power. This is because thruster power varies with the square of the exit velocity, whereas the thrust varies only linearly with velocity.

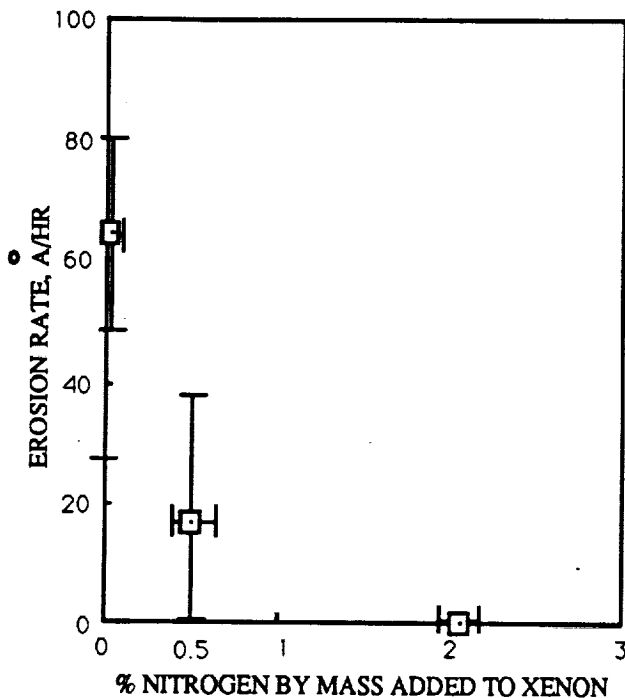


Fig. 9. Plot of the erosion rates of the pole piece badges as a function of the % by mass of nitrogen added to the xenon.

A performance degradation analysis was performed assuming that the fraction of the nitrogen which was ionized and extracted into the exhaust beam (nitrogen propellant efficiency) was the same as the xenon propellant efficiency. In practice, this fraction for nitrogen will be much less than that for xenon since the nitrogen ionization collision cross section is substantially smaller, and the higher nitrogen atom thermal velocity makes the escape of non-ionized nitrogen more likely. The results of this analysis can therefore be characterized as conservative; if an ion engine were operated with a xenon/nitrogen mixture, somewhat better engine performance should be expected than what is predicted from the degradation

analysis. The variation in thrust loss factors and efficiency loss factors, assuming equal nitrogen and xenon propellant efficiencies, are shown as a function of the percentage of nitrogen addition (by mass) to the xenon in Fig. 10.

As can be seen from the data presented in Fig. 10, there is at most only a small degradation in ion engine performance when small quantities of nitrogen (0-2% by mass) are added to the xenon propellant.

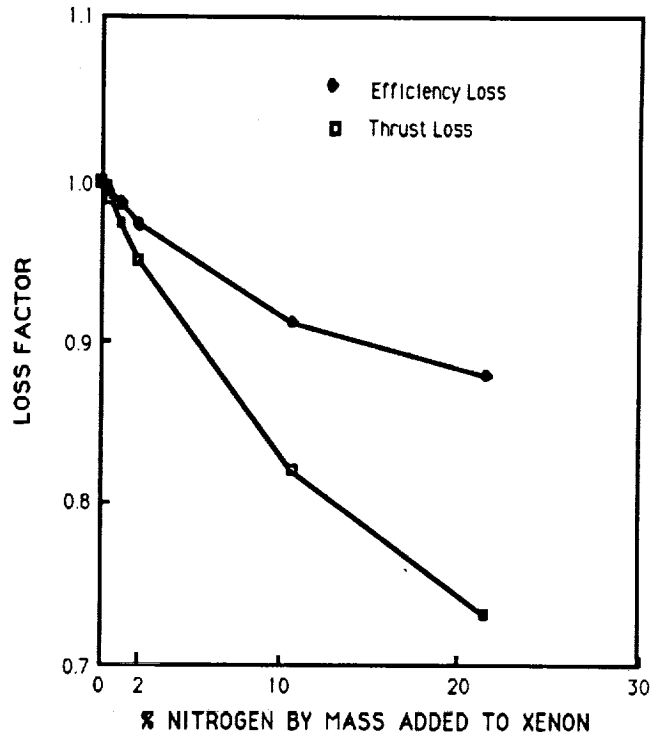


Fig. 10. Thrust and efficiency loss factors as a function of the percentage of nitrogen added to the xenon propellant.

## SURFACE ANALYSES

The mechanism responsible for the reduced discharge chamber component erosion rates may be the formation of surface nitrides that have a lower erosion rate than the pure metal. To verify this hypothesis, various surface analyses were performed on the erosion badges to look for evidence of surface nitrides: Energy Dispersive X-ray analyses (EDX), X-ray Diffraction Analyses (XRD), X-ray Photoelectron Spectroscopy (XPS), and Auger electron bombardment analyses. There was no nitrogen any form (either as nitride or trapped nitrogen) identified in the sample surfaces using EDX; this may be due to the low sensitivity of this analysis technique to nitrogen. The other three techniques used (XPS, Auger, and XRD) did indicate possible existence of surface nitrogen or nitrides.

TABLE VI. Summary of XRD, XPS and Auger analyses.

TEST #	%N2 ADDED TO XENON	SAMPLE MATERIAL	XRD Analyses	XPS Analyses	AUGER Analyses
8	0	Ta Baffle	NP	Ta Ta <sub>2</sub> O <sub>5</sub> BaCO <sub>3</sub> F	Nitrogen Possible
4	0.51	Ta Baffle	NP	Ta Ta <sub>2</sub> O <sub>5</sub> BaCO <sub>3</sub>	Nitrogen Probable
5	0.51	Ta Baffle	NP	Ta Ta <sub>2</sub> O <sub>5</sub> BaCO <sub>3</sub>	NP
2	1.19	Ta Baffle	Ta TaN	Ta Ta <sub>2</sub> O <sub>5</sub> BaCO <sub>3</sub> Ca TaN Probable	Nitrogen
1	0	Mo Baffle	Mo	Mo MoO <sub>3</sub> Graphite	Not Performed
2	1.19	Mo Baffle	NP	Mo MoO <sub>3</sub> Graphite	Not Performed
8	0	Mo Screen	NP	Mo MoO <sub>3</sub> Graphite	Nitrogen Possible
5	0.51	Mo Baffle	NP	Mo MoO <sub>3</sub> Graphite	Nitrogen Probable
7	2.10	Mo Screen	Mo	Mo MoO <sub>3</sub> Graphite	Nitrogen Very Probable

NP = Not Performed

Preliminary data from these last three analyses will be discussed.

Verification of surface nitrides in tantalum and molybdenum is possible using XRD. Chemical compounds and crystalline materials such as tantalum nitride (TaN) are identified by characteristic diffraction lines. XRD analyses of the erosion badges, when compared to the characteristic diffraction lines published by the American Society for Materials Testing (ASMT), provide for determination of the surface composition and is considered highly reliable.

Identification of elements and compounds using XPS is accomplished by determining and analyzing the signal amplitude of various electron states as a function of binding energy. The binding energies for tantalum (21.7 eV for the Ta 4f<sub>7/2</sub>), tantalum oxide (26.2 eV for the Ta<sub>2</sub>O<sub>5</sub> and Ta 4f<sub>7/2</sub>), molybdenum (227.9 eV for Mo 3d<sub>5/2</sub>), and molybdenum oxide (232.4 eV for Mo 3d<sub>3/2</sub> from MoO<sub>3</sub>) are well known.<sup>13,14</sup> Unfortunately, this is not the case for the metal nitrides.<sup>13,14</sup> In principle, however, the presence of a nitride is detectable by chemical shifts of the Mo 3d or Ta 4f signals. Since the binding energy is a measure of the potential at the atomic site of interest, and nitrogen is less electronegative than oxygen, the nitrides would be expected to have binding energies intermediate between the metals and oxide.<sup>13</sup> The presence of nitrides, therefore, can not be measured directly

using XPS but may be inferred. The attenuation depth of this technique is approximately 20 angstroms.

Verification of surface nitrides in tantalum and molybdenum is possible using XRD. Chemical compounds and crystalline materials such as tantalum nitride (TaN) are identified by characteristic diffraction lines. XRD analyses of the erosion badges, when compared to the characteristic diffraction lines published by the American Society for Materials Testing (ASMT), provides for determination of the surface composition which is considered highly reliable.

Identification of elements and compounds using XPS is accomplished by determining and analyzing the signal amplitude of various electron states as a function of binding energy. The binding energies for tantalum (21.7 eV for the Ta 4f<sub>7/2</sub>), tantalum oxide (26.2 eV for the Ta<sub>2</sub>O<sub>5</sub> and Ta 4f<sub>7/2</sub>), molybdenum (227.9 eV for Mo 3d<sub>5/2</sub>), and molybdenum oxide (232.4 eV for Mo 3d<sub>3/2</sub> from MoO<sub>3</sub>) are well known.<sup>13,14</sup> Unfortunately, this is not the case for the metal nitrides.<sup>13,14</sup> In principle, however, the presence of a nitride is detectable by chemical shifts of the Mo 3d or Ta 4f signals. Since the binding energy is a measure of the potential at the atomic site of interest, and nitrogen is less electronegative than oxygen, the nitrides would be expected to have binding energies intermediate between the metals and oxide.<sup>13</sup> The presence of nitrides, therefore, can not be measured directly

using XPS but may be inferred. The attenuation depth of this technique is approximately 20 angstroms.

Direct detection of nitrogen on molybdenum or tantalum using XPS is difficult due to overlap of the nitrogen 1s photoelectron signal with the Mo3p or Ta 4p signals. Therefore an additional technique, Auger spectroscopy, was used to verify the presence of nitrogen in the surface.

Table VI summarizes the results of the XRD, XPS and Auger analyses. The existence of metal nitrides were either determined by comparing the diffraction patterns of the erosion badges to the patterns published by the ASTM, or they were inferred from shifts in the XPS tantalum or molybdenum peaks. The existence of surface nitrogen was verified using Auger spectroscopy.

#### TANTALUM BAFFLE: CATHODE SIDE

XRD analyses were performed on the tantalum baffle used in test # 2. In addition to tantalum, the results of the analyses show clearly the existence of tantalum nitride on the surface. This conclusion is based upon verification of two of the three TaN diffraction pattern lines published in the ASTM. No other materials, such as tantalum oxides, were observed. For future analyses, longer exposure times to the x-rays will be required to observe compounds such as tantalum oxide which were indicated in subsequent XPS analyses.

XPS analyses of these samples were complicated by the existence of a native oxide and a thick surface layer of pure barium carbonate. Barium and calcium are elements included in the low surface work function oxide which is impregnated into ion engine hollow cathode inserts. The barium carbonate layer probably formed when the ion engine was exposed to atmosphere. Great care was taken during these experiments to insure that no oxygen contaminated the ion engine during erosion testing, so it is likely that the tantalum oxide also formed on exposure of the ion engine to atmosphere. Since the attenuation depth of the XPS analyses for these tests was approximately 20 angstroms, and since the nitrogen 4s signal overlaps with the tantalum 4p signal, any nitride layers underneath the oxide and barium carbonate layers would be difficult to detect.

There is no evidence of surface nitrides from analyses of the XPS data for tests 8,4,and 5. However, analysis of the XPS data from test #2, where a high concentration (1.19%) of nitrogen was added to the xenon, indicates there is strong evidence<sup>16</sup> for the existence of a surface nitride. This inference is based on the fact that the low binding energy doublet shifted 1.7 eV relative to the binding energy expected for tantalum.<sup>15</sup>

The Auger analyses indicate that only in test #2 was there clear and conclusive evidence of surface nitrogen on the cathode side of the tantalum baffle. Evidence of surface nitrogen in the other samples are inconclusive due to a weak nitrogen signal and/ or peak overlap. The evidence for surface nitrogen was strongest for cases with the highest concentrations of nitrogen added to the xenon.

#### MOLYBDENUM BAFFLE: DISCHARGE SIDE MOLYBDENUM SCREEN GRID BADGE

There is no evidence of surface nitrides from analyses of the XRD and XPS data for these samples. In all samples studied there was a very thin oxide layer, and evidence suggesting the presence of graphite. The graphite was probably ion-sputter-deposited onto the molybdenum from graphite squares placed near the molybdenum erosion badges.

The Auger spectroscopy, however, has the same characteristics as the tantalum Auger analyses: the higher the concentration of nitrogen added to the xenon, the stronger the evidence for surface nitrogen. Again, the XPS and Auger data are not definitive due to weak signal and peak overlap. For the cases where nitrogen was added to the xenon, there may be a surface nitride layer which is so thin that the XPS signal is weak relative to the metal and oxide signals.

#### XPS AND AUGER AFTER SURFACE CLEANING

To enhance the probability of obtaining clear evidence for surface nitrides and surface nitrogen, the samples listed in Table VII were ion etched for 60-75 seconds to remove surface contaminants and oxides, and subsequently analyzed using XPS and Auger spectroscopy. After ion etching, the molybdenum surface was essentially free of all traces of graphite and oxide; however, the barium carbonate signal was not completely removed from the XPS analyses of the tantalum erosion badge.

Table VII. XPS and Auger spectroscopy after surface cleaning via ion bombardment.

Test #	%N2 Added To Xenon	Sample Material	XPS Analyses	Auger Analyses
8	0	Ta Baffle	Ta Ta <sub>2</sub> O <sub>5</sub> BaCO <sub>3</sub> F	Nitrogen Possible
4	0.51	Ta Baffle	Ta Ta <sub>2</sub> O <sub>5</sub> BaCO <sub>3</sub> F Ca	Nitrogen Probable
5	0.51	Mo Baffle	Mo MoO <sub>3</sub>	Nitrogen Probable

Again, there is no direct evidence of surface nitrides from any of the XPS analyses. Analyses of the Auger spectrometry indicates, however, a correlation between addition of nitrogen to the xenon and the existence of surface nitrogen. The nitrogen peak from the molybdenum sample from test #5 was most evident after ion surface cleaning was performed. The fact that the nitrogen signal increased, while the oxygen and carbon signals (from MoO<sub>3</sub> and graphite) decreased, indicates that the nitrogen is not part of a surface contaminant.<sup>18</sup>

## CONCLUSIONS

Significant reductions in the erosion rates of ion engine discharge chamber components were observed when small quantities (0.5-2.0% by mass) of nitrogen were added to the xenon propellant. The effect is most pronounced for the tantalum baffle facing the cathode, and tantalum erosion badges placed along the ID of the pole piece. A maximum reduction in the erosion rates of tantalum at those locations of a factor of approximately 50 was achieved. Reductions in cathode side baffle erosion were also achieved by reducing the diameter of the cathode orifice. Molybdenum baffle and screen grid erosion rates were reduced by a factor of approximately 8-20 by adding nitrogen to the xenon.

Calculations showed that degradation of ion engine performance of up to only a few percent should be expected at these nitrogen mass fractions. XRD, XPS and Auger analyses indicate that a thick nitride layer forms on the side of the tantalum baffle facing the cathode when nitrogen (1.19% by mass) is added to the xenon. The evidence for surface nitrides in the molybdenum erosion badges and other tantalum badges are less conclusive, perhaps because of surface oxide and contaminant layers which interfere with the nitride signal, or peak overlap. It is also possible that the nitride layer is too thin in some cases to be detected using XRD, XPS and EDX analyses. Auger analyses generally supports a correlation between the percentage by mass of nitrogen added to the xenon and the amount of nitrogen detected in the surfaces of the erosion badges.

The data indicate that significant and useful reductions in discharge chamber component erosion can be achieved using a nitrogen mass fraction of only 0.5 percent. This technique may reduce cathode start-up electrode and screen grid erosion rates in high-power inert gas thrusters. The addition of nitrogen to the propellant in these thrusters may also reduce screen grid erosion from energetic ions in the cathode plume. Additional studies should be conducted to identify possible adverse effects of nitrogen addition on ion engine operation.

## ACKNOWLEDGEMENTS

The authors would like to thank Alison Owens, William Thogmartin, Robert Toomath, Lynn Lowry, and Richard Vasquez for their assistance in completing this work. The work described in this paper was carried out by the Jet Propulsion Laboratory, California Institute of Technology, under a contract with the National Aeronautics and Space Administration. "Approved for public release; distribution unlimited."

## REFERENCES

- (1) Michael Patterson, NASA LeRC, personal communication, (May 1990).
- (2) Brophy, J.R. and Garner, C.E., "Tests of High Current Hollow Cathodes for Ion Engines", AIAA-88-2913, (1988).
- (3) Rawlin, V.K. "Internal Erosion Rates of a 10 kW Xenon Ion Thruster", AIAA-88-2912, (1988).
- (4) Garner, C.E. et al. "The Effects of Gas Mixtures on Ion Engine Erosion and Performance", AIAA-87-1080, (1987).
- (5) Beattie, J.R. "A Model for Predicting the Wearout Life Time of the LeRC/Hughes 30-CM Mercury Ion Thruster", AIAA-79-2079, (1979).
- (6) Rawlins, V.K. and Mantienicks, M.A. "The Effects of Facility Background Gases on Internal Erosion of the 30-CM Mercury Ion Thruster", NASA-TM-73803, (1978).
- (7) Mantienicks, M.A. and Rawlins, V.K. "Sputtering in Mercury Ion Thrusters", NASA-TM-79266, (1979).
- (8) Wilbur, P.J. "A Model for Nitrogen Chemisorption in Ion Thrusters", AIAA-79-2062, (1979).
- (9) Garner, C.E. et al. "Techniques for Reduced Spalling and Increased Operating Life in Xenon Ion Thrusters", AIAA-89-2714, (1989).
- (10) Holman, J.P. "Experimental Methods for Engineers", McGraw-Hill, New York, New York, (1978), pg 65.
- (11) Wilbur, P.J. "Mercury Ion Thruster Research-1977 Annual Report", NASA CR-135317, (Dec. 1977), pgs 142-149.

(12) Bechtel, R.T. et al. "Results of the Mission Profile Life Test", AIAA-82-1905, (1982).

(13) C. D. Wagner, W. M. Riggs, L.E. Davis, J.F. Moulder, and G.E. Muilenberg, Handbook of X-Ray Photoelectron Spectroscopy, Perkin-Elmer, Eden Prairie, MN, (1979).

(14) J.C. Fugle and N. Martensson, J. Electron Spectrosc. Relat. Phenom. 21, 275 (1980).

(15) Personal Communication, Richard Vasquez, Surface Analysis Laboratory, Jet Propulsion Laboratory, Pasadena, Ca, (June 1988).

(16) JPL Internal Document to C. Garner, (July 2-3, 1990).

(17) JPL Internal Document to C. Garner, (June 20, 1990).

(18) JPL Internal Document to C. Garner, (July 3-5, 1990).

**13.2 Appendix B**

**AIAA 90-2756  
Benefits of Electric Propulsion  
for the Space Exploration Initiative**

J. R. Brophy and J. W. Barnett  
Jet Propulsion Laboratory  
Pasadena, CA

## BENEFITS OF ELECTRIC PROPULSION FOR THE SPACE EXPLORATION INITIATIVE

John R. Brophy\* and John W. Barnett\*\*  
Jet Propulsion Laboratory  
California Institute of Technology  
Pasadena, California

### Abstract

An overview of the benefits which may be derived through the use of electric propulsion in support of the Space Exploration Initiative is presented. Lunar cargo, Mars cargo and piloted Mars vehicles using electric propulsion are considered. The high performance of electric propulsion systems is shown to offer substantial benefits for these applications, including: substantially reduced initial masses in low earth orbit, reduced round-trip times for piloted Mars vehicles, availability of large amounts of electrical power in-route and at the destination, less sensitivity to launch dates and windows, reusability, and growth potential for human exploration of the solar system. Hybrid chemical/NEP and NTR/NEP vehicles are discussed for their potential to reduce piloted round trip time to Mars even further. A brief technology assessment of the major electric propulsion system components is also presented.

### Introduction

"When people travel to other planets, what will they have under the hood?" This question, as posed by Ben Bova,<sup>1</sup> is currently the subject of considerable debate as it pertains to the Space Exploration Initiative and human exploration of Mars. The leading propulsion system candidates for piloted and cargo missions to Mars include: chemical O<sub>2</sub>/H<sub>2</sub> with aerobraking, nuclear thermal propulsion, and solar electric and nuclear electric propulsion. This paper highlights the potential benefits which may be realized through the use of solar and nuclear electric propulsion systems in support of the Space Exploration Initiative.

Electric propulsion has been considered for space flight since R. H. Goddard first realized, over eighty years ago, the potential benefits of the very high velocities

which can be imparted to charged particles by devices at relatively low temperatures.<sup>2</sup> Electric thrusters produce exhaust velocities much higher than those possible with chemical engines by decoupling the propellant from the energy source used to accelerate the propellant. While the exhaust velocity is determined by the amount of energy added per unit mass of propellant, the thrust level is determined by the available electric power, and thus electric propulsion systems are referred to as "power limited." The total mass of the required power supply, power conversion and power processing equipment, thrusters, and propellant, for a given power level, always results in a very low thrust-to-mass ratio (i.e. acceleration) for electric propulsion systems. For this reason, electric propulsion systems are also commonly referred to as "low thrust systems."

In a strong gravity field (such as within the Earth's sphere of influence), low thrust, high specific impulse propulsion can result in an order of magnitude savings in propellant mass relative to chemical systems, albeit generally at the expense of increased trip times. Cargo missions, which are not trip time constrained, are ideal candidates for electric propulsion. In the relatively weak gravity field of heliocentric space, electric propulsion vehicles can be significantly faster than chemical rockets since greater energy can be imparted to the vehicle for the same propellant mass.

Electric propulsion encompasses a wide variety of thruster types which cover an impressive range of power levels (ten's of watts to ten's of megawatts) and specific impulse capabilities (a few hundred seconds to greater than ten thousand seconds). This range of capabilities has potential applications to a wide variety of missions as described by Beattie and Penn,<sup>3</sup> and has stimulated numerous research and development programs, as well as a substantial body of flight experience. (There were 77 flight tests of different electric thrusters, conducted by four

---

\*Member Technical Staff, Electric Propulsion and Plasma Technology Group; Member AIAA.

\*\*Supervisor, Electric Propulsion and Plasma Technology Group; Member AIAA.

different countries, between 1962 and 1985.<sup>4</sup> These tests, however, were all performed at power levels substantially less than those required to support the Space Exploration Initiative).

For the Space Exploration Initiative, with projected requirements to move 10's to 100's of metric tons around Earth-Moon space and to and from Mars, electric propulsion systems processing 100's of kilowatts to 10's of megawatts, with specific impulses of greater than 5000 seconds, will be required. This range of power levels and specific impulses narrows the field of candidate thruster concepts for these missions. The two leading candidates are the electrostatic (ion) thruster and the magnetoplasmadynamic (MPD) thruster. Both of these thruster types require development to achieve the performance levels necessary to support the Space Exploration Initiative. However, projected system performance levels for both thrusters are similar enough that selection between thruster concepts at this time is premature. Furthermore, benefits for lunar cargo, Mars cargo and piloted Mars missions are essentially independent of the thruster choice based on their respective projected performance levels.

### Electric Propulsion Systems

All electric propulsion systems have essentially the same generic system architecture, regardless of the details of the particular thruster used. Electric propulsion systems require a power source (typically either photovoltaic solar arrays, or a nuclear reactor), power conversion equipment to generate electric power, power conditioning equipment to transform the raw electric power from the power conversion system into the currents and voltages required by the thruster, a propellant storage and distribution system, thrusters, thermal management systems, and structure. These systems were identified as the principal components of high power electric propulsion systems as early as 1955,<sup>2</sup> and are neatly summarized in Fig. 1 which was taken from a 1967 study on multimewatt nuclear electric propulsion for manned interplanetary missions.<sup>5</sup>

The initial mass of an electric propulsion vehicle may be described by the following expression,

$$M_i = M_L + M_{POW} + M_{PRO} + (1 + f_T) M_P \quad (1)$$

where  $M_i$  is the initial vehicle mass,  $M_L$  is the payload mass,  $M_{POW}$  is the mass of the power source and power conversion equipment,  $M_{PRO}$  is the mass of the propulsion system (which consists primarily of the thrusters and power processing equipment),  $M_P$  is the propellant mass, and  $f_T$  is the tankage fraction. This equation may be

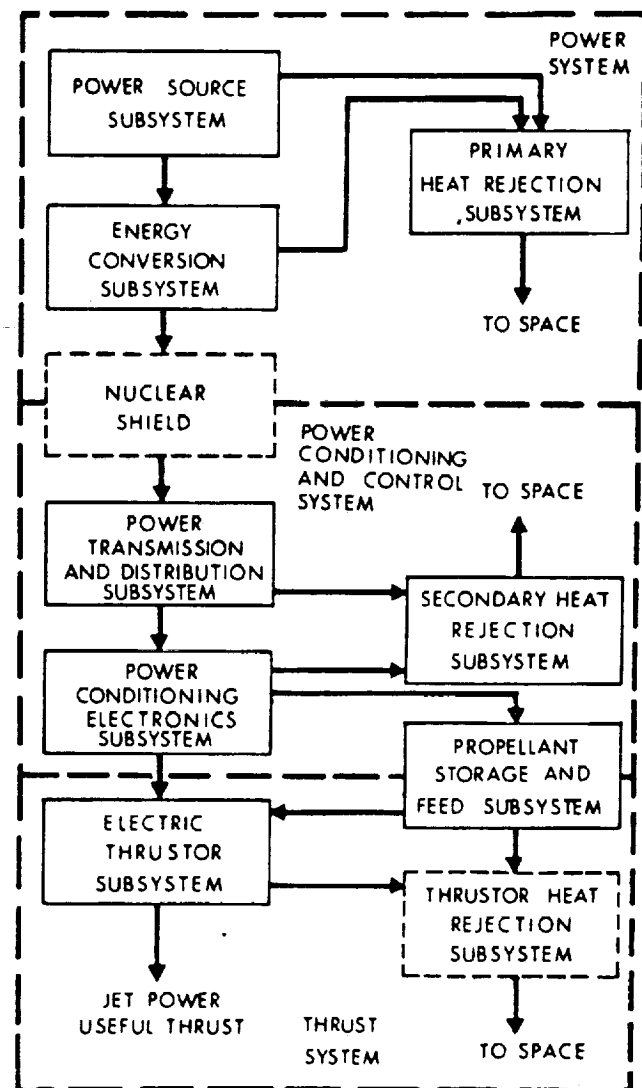


Figure 1 System diagram for nuclear electric propulsion.

rewritten as,

$$M_i = M_L + P(\alpha_{POW} + \alpha_{PRO}) + (1 + f_T) M_P, \quad (2)$$

where,  
 $\alpha_{POW}$  = Power system specific mass, (kg/kW)  
 $\alpha_{PRO}$  = Propulsion system specific mass, (kg/kW).

In this equation,  $P$  is the total electrical power supplied to

the propulsion system. In addition, the power system specific mass includes both the power source and the power conversion masses, and the propulsion system specific mass includes the thrusters and power conditioning masses.

Equation (2) indicates that for a given payload mass, the initial vehicle mass increases with the propulsion system power,  $P$ , as well as with the power and propulsion system specific masses. The trip time, however, decreases with increasing system power, resulting in a tradeoff between trip time and initial vehicle mass. The key performance parameters for electric propulsion systems are: specific impulse, power level, power system specific mass, propulsion system specific mass, and thruster efficiency. The low thrust nature of electric propulsion requires that the propulsion system operate for many thousands of hours to produce the desired spacecraft velocity change. This places a premium on thruster technologies which have long useful life times.

### Mission Benefits

The discussion of mission benefits enabled through the use of high power electric propulsion systems is divided into three mission categories: lunar cargo vehicles, Mars cargo vehicles, and piloted Mars missions. The general benefits provided by low thrust, high specific impulse propulsion for lunar cargo vehicles and piloted Mars missions were eloquently summarized by Earnst Stuhlinger<sup>6</sup> in 1959, and are as true today as they were 31 years ago.

#### Lunar Cargo Vehicles

The establishment and maintenance of a lunar base will require the ability to continuously deliver large masses of material to lunar orbit to supply the base with food, chemical propellants, building material, and equipment (referred to as Operation Moon-lift in Ref. 6). Lunar cargo vehicles using electric propulsion systems have been proposed and analyzed in numerous studies,<sup>2,6-10</sup> and the conclusions of these studies are generally always the same. Electric propulsion systems with power levels ranging from a few hundred kilowatts to a few megawatts can deliver substantial quantities of material to the Moon with significantly reduced initial mass in low earth orbit (IMEO) relative to chemical systems.

For example, a fleet of four 300 kW solar electric propulsion vehicles with an IMEO of 50,000 kg each was shown, in Ref. 7, to be capable of delivering 20 MT of cargo every 100 days to the Moon. In Ref. 8, the IMEO of three different electric propulsion vehicles and a chemical O<sub>2</sub>/H<sub>2</sub> system were compared assuming delivery of a payload mass of 35,000 kg. This comparison is

reproduced here as Fig. 2. The electric propulsion systems in this figure are based on thrusters with an Isp of 5000 s, and are shown to reduce the propellant mass required by approximately 65,000 kg per flight, relative to the 475 s I<sub>sp</sub> chemical system. In this study, the 1 MW propulsion systems were assumed to use a nuclear power system with a specific mass of 10 kg/kW together with a propulsion system specific mass of 1 kg/kW. The 300 kW ion propulsion system was assumed to use a solar array with a 7 kg/kW EOL specific mass coupled to an ion propulsion system with a specific mass of 3.1 kg/kW. Solar array degradation, as a result of spiraling through the Van Allen radiation belts was accounted for in an approximate manner in this analysis.

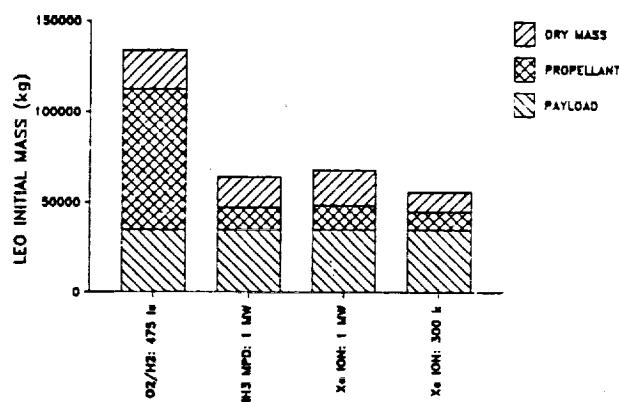
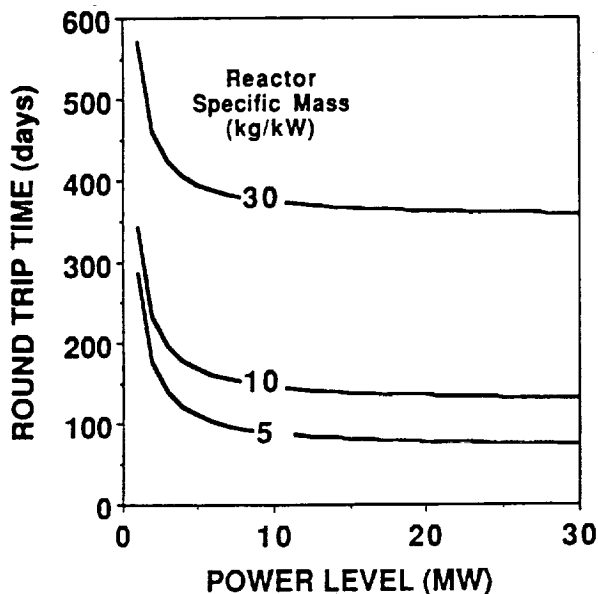


Figure 2 Propulsion system mass comparison for lunar cargo vehicles.

The sensitivity of the round trip time (for a reusable lunar ferry vehicle) to the power system specific mass was investigated by Palaszewski,<sup>9</sup> and is shown in Fig. 3 assuming the use of a 5000 s ammonia MPD thruster system. Clearly, the power system specific mass has a major effect on the vehicle performance. This is characteristic of electric propulsion vehicles and stresses the high desirability for low specific mass power systems. Very recent studies have confirmed the potential for large reductions in IMEO through the use of low thrust, high specific impulse propulsion for lunar cargo vehicles (assuming a power system specific mass of 10 kg/kW).<sup>11</sup>

The large mass savings, and the corresponding reductions in launch costs, however, are not the only benefits of using electric propulsion for lunar cargo vehicles. Palaszewski<sup>9</sup> discusses the benefits of having megawatt power levels available in low lunar orbit for lunar science, including the use of high power radar and other high power instrumentation to select the best initial lunar base location. A high power cargo vehicle could also be used for communications once it is in lunar orbit enabling very high data rates to be relayed to surface rovers that may be very far from the base.<sup>9</sup> Finally, a



**Figure 3** Lunar cargo vehicle round trip time versus power system specific mass.

lunar cargo vehicle using nuclear electric propulsion with a power level of a few megawatts may serve as a technology demonstrator for higher power Mars cargo or piloted Mars missions.<sup>11</sup>

#### Mars Cargo Vehicles

The human exploration of Mars will require the transportation of 100's to 1000's of metric tons of material and equipment to Mars. For example, the study of Mars cargo vehicles in Ref. 12 assumed that a payload mass of 400 MT was to be delivered from a 500 km low Earth orbit to a 6000 km Mars orbit in support of the Phobos gateway mission concept. Performance assessments, in terms of payload mass delivered, IMEO, and one-way and round-trip times have been made for electric cargo vehicles in numerous studies.<sup>12-17</sup> These studies cover a wide range of assumptions concerning the required payload mass to be delivered, system power levels, and power system and electric propulsion system performance levels, but generally find qualitatively the same mass savings benefits.

The trade study performed in Ref. 14 demonstrated that specific impulses of greater than approximately 4000 s are required for NEP cargo vehicles to have a substantial reduction in IMEO relative to 480 s  $I_{sp}$  chemical systems with aerobraking. At specific impulses of 5,000 to 10,000 s, however, the savings in IMEO are enormous. The potential mass savings with NEP are shown in Fig. 4 (reproduced from Ref. 14) as a function of the power

system specific mass. The assumptions used to generate this figure are:

1. A 180,000 kg payload is delivered to a 1,000 km Mars orbit.
2. The chemical propulsion system  $I_{sp}$  is 480 s with aerobraking at Mars.
3. The cargo vehicle does not return to the Earth.
4. The NEP system power level is 4 MW at 10 kg/kW.

The curve in Fig. 4 indicates a mass savings of approximately 300 MT for NEP specific impulses of greater than 5000 s.

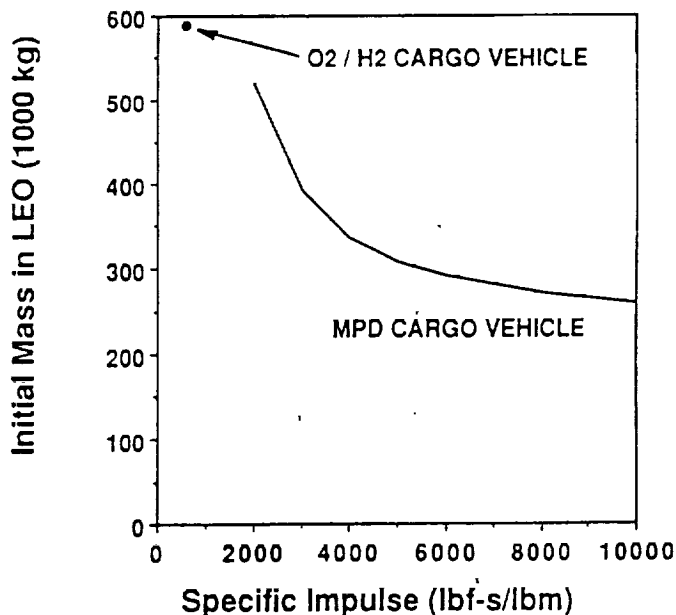


**Figure 4** NEP Mars cargo vehicle initial mass sensitivity to the propulsion system specific impulse.

The effect of power system technology level (as reflected by the value of the power system specific mass) on the IMEO was calculated by LeRC.<sup>11</sup> The results of these calculations are shown in Fig. 5, assuming a payload mass of 400 MT is delivered to Mars aerosynchronous orbit. The IMEO for two chemical propulsion options are also given in this figure for comparison. The relatively long trip times for the NEP systems, shown in this figure, result from the large ratio of payload mass (400 MT) to power level (5 MW) used in the analyses. The use of higher power levels can reduce this trip time substantially.<sup>12</sup> Never the less, Fig. 5 shows that mass savings of many 100's of metric tons can be achieved using an NEP cargo vehicle relative to an advanced chemical/aerobraked system. Significantly, the NEP system is shown to provide these mass savings even over a factor of 3 variation in the power system specific mass (from 10 to 30 kg/kW).

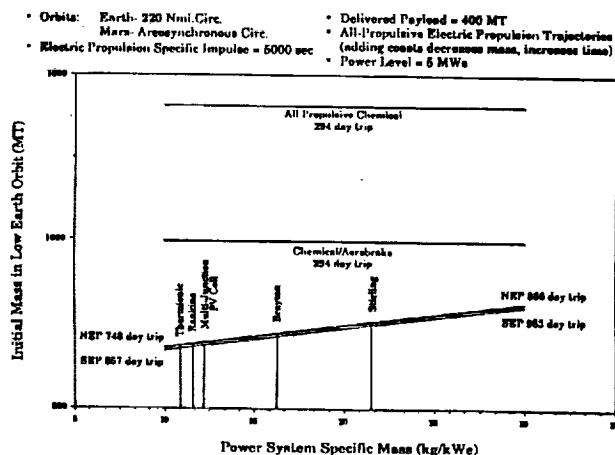


**Figure 5** Sensitivity of NEP Mars cargo vehicle to the power system specific mass and comparison with chemical propulsion systems.

As was the case for lunar cargo vehicles, the use of electric propulsion for Mars cargo vehicles has advantages other than simply the significant reduction in initial mass in low Earth orbit. Chief among these is the availability of megawatts of electric power at Mars. Potential uses of this power are described by Coomes et. al.<sup>18</sup> including the possibility of beamed power transmission to the surface of Mars. A 10 MW nuclear electric power system placed in aerosynchronous orbit above the landing site, together with a microwave power transmission system, could make 5 to 7 MW of electric power available at the Mars surface to support manned and unmanned mission activities, according to Ref. 18. Nuclear electric cargo vehicles could also be used to support in situ propellant production activities at Mars by delivering the necessary hardware<sup>19</sup> and, presumably, by supplying the power required to operate this equipment.

### Piloted Mars Missions

The major propulsion system driver for a piloted mission to Mars is to move, what is of necessity, a massive vehicle to Mars and back as quickly as possible. Faster transfers to Mars require the space vehicle to follow higher energy trajectories. The limited performance of chemical systems for these missions has stimulated studies of a wide variety of higher performance alternatives. Nuclear electric propulsion was seriously proposed for piloted Mars missions as early as 1955.<sup>2</sup> Studies<sup>2,5,6,20,21</sup> of the late 1950's and 1960's showed that nuclear electric propulsion systems could reduce the initial vehicle mass in low earth orbit, as well as the trip time for piloted missions to Mars, relative to advanced chemical systems (which were typically assumed to be  $O_2/H_2$  with an  $I_{sp}$  of 450 s).

Assuming a total power and propulsion system specific mass of 2 kg/kW, Stuhlinger and King<sup>20</sup> showed that a 40 MW nuclear electric propulsion system, with a specific impulse of 14,000 s, could propel a 360 MT piloted spacecraft to Mars and back in 572 days, including a 29 day stay at Mars, and would require approximately 148 MT of propellant. The value of 2 kg/kW for the power and propulsion system specific mass used in this study is optimistic but not unreasonable having been made 28 years ago. A recent study<sup>12</sup> projects ultimate values for this parameter of between 3.0 and 2.1 kg/kW for power levels ranging from 10 MW to 100 MW.

Additional recent studies,<sup>11,22-24</sup> in which power levels of 10's of Megawatts are assumed, have confirmed the general benefits identified in the earlier studies of using electric propulsion for piloted Mars missions; namely, reduced initial mass in low Earth orbit, and reduced round trip times. Furthermore, these studies show that electric propulsion can provide these benefits with power system specific masses on the order of 10 kg/kW. A comparison of initial mass in low Earth orbit for piloted Mars vehicles versus trip time is given in Fig. 6 for several different propulsion systems.<sup>22</sup> This figure indicates that only the speculative, gas core reactor (GCR) system can offer performance superior to the multimegawatt NEP system. Both the NEP and solar electric propulsion (SEP) systems show significant mass and trip time reductions relative to the reference chemical system. Furthermore, the NEP system is shown to have comparable trip times to the NTR system, but with lower initial mass.

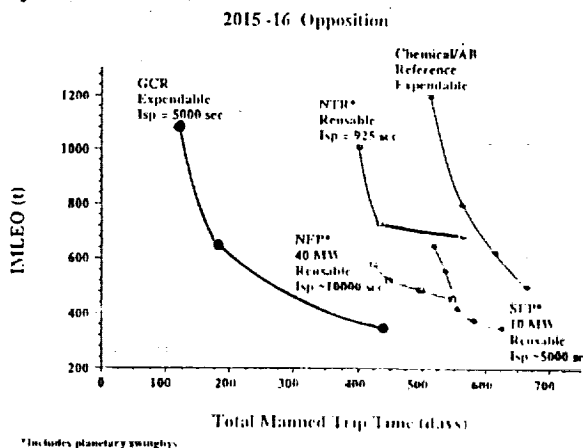


**Figure 6** Comparison of propulsion options for piloted Mars vehicles.

Electric propulsion vehicles for piloted Mars missions tend to be physically large. For NEP systems the vehicle size is determined by the separation distance between the reactor and the crew modules, to minimize crew radiation doses, and by the radiator for the power conversion system. Multimegawatt solar electric vehicles are

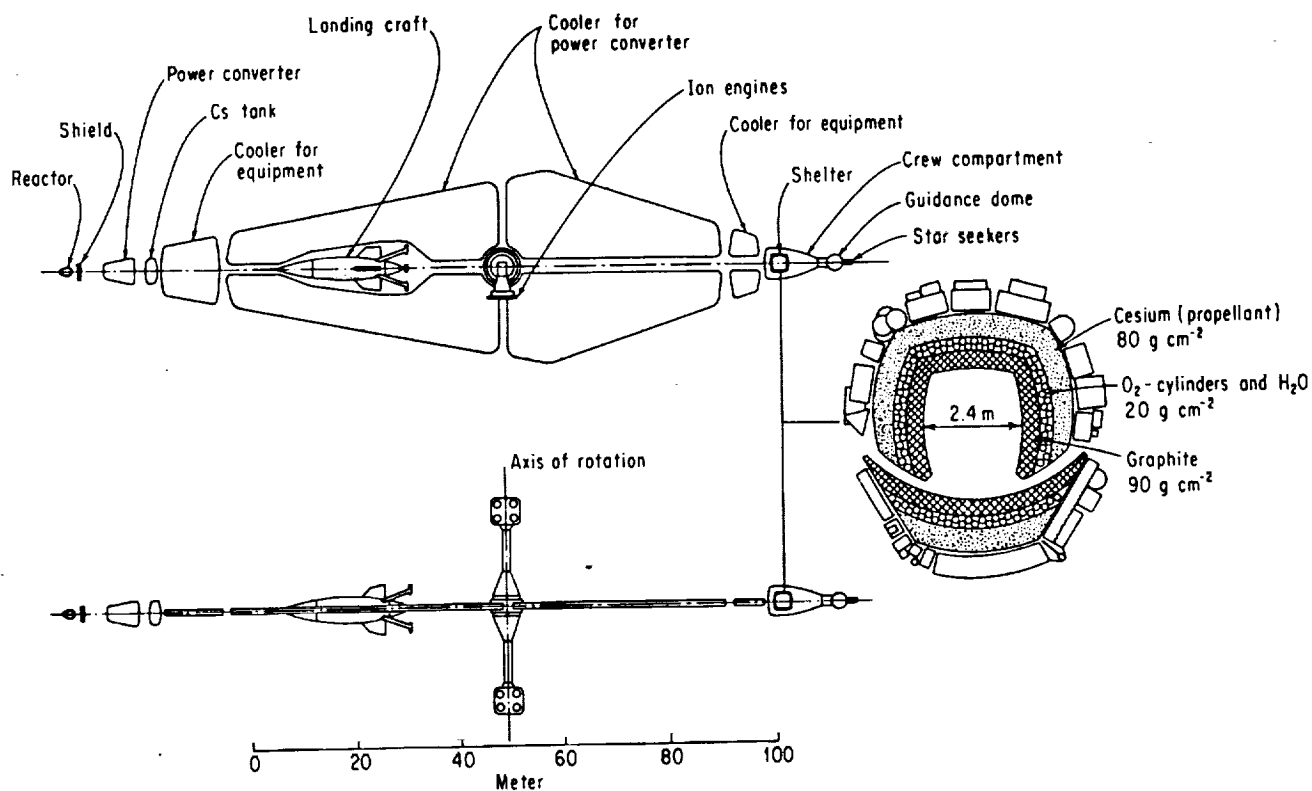


Figure 7A Piloted NEP Mars vehicle concept from 1962.<sup>20</sup>

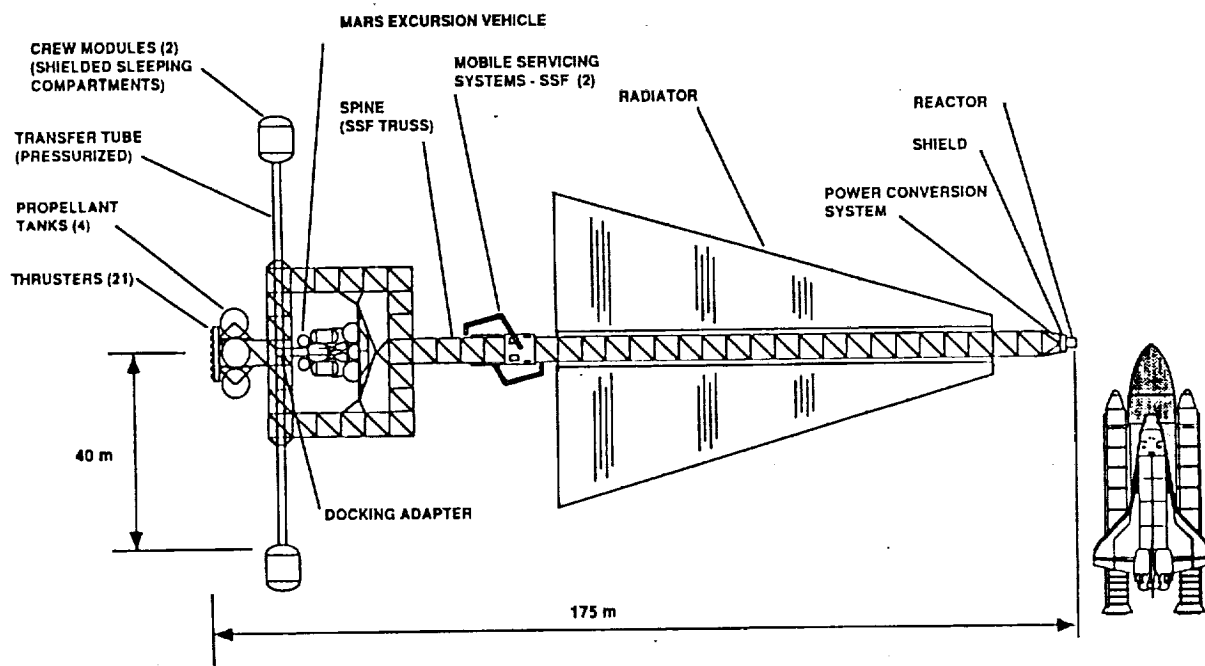


Figure 7B Piloted NEP Mars vehicle concept from 1990.<sup>23</sup>

dominated by the enormous solar array. Sketches of two NEP, piloted Mars vehicle concepts are shown in Fig. 7; one from 1962<sup>20</sup> and the other from 1990.<sup>23</sup> Both vehicles carry a Mars excursion vehicle, provide artificial gravity for the crew, and are of a comparable physical size.

### Hybrid Vehicles

For NEP systems, a significant fraction of the mission time is spent in geocentric space spiraling away from the Earth. The desire to minimize trip times for piloted missions has prompted the study of chemical/NEP and NTR/NEP hybrid vehicles.<sup>2,11,25,26</sup> These hybrid vehicles would use the high thrust system, either chemical or NTR, for earth escape, and then use the NEP system for the rest of the trip to Mars, as well as the return trip. The desirability of hybrid systems was described by Stuhlinger<sup>2</sup> in the following passage.

"The complementary nature of nuclear and electric propulsion systems becomes very obvious when combined chemical-nuclear-electric systems are considered. Preliminary studies show that with a Saturn V as booster, a nuclear engine of the NERVA class as second stage, and an electric system with 4 to 5 MW electric power as third stage, a minimum manned round trip to Mars could be achieved."

Alternatively, hybrid chemical/NEP or NTR/NEP systems can be used to reduce performance requirements on both systems,<sup>11</sup> while retaining most of the performance benefits of all NEP systems operating at higher power levels.

The use of a high-performance electric propulsion system eases constraints on crew accommodations, due to relaxed mass restrictions, and provides ample power for environmental control and life support systems (ECLSS). Power requirements for ECLSS are projected to be on the order of 25 kWe for a piloted Mars vehicle.<sup>27</sup> This is a power level which could easily be provided on a vehicle which has multimegawatts of electrical power capability. The performance of piloted vehicles using electric propulsion is also less sensitive to launch dates and windows,<sup>22</sup> and the vehicles are potentially fully reusable.

Finally, NEP systems have significant growth potential for human exploration of the solar system. Nuclear electric propulsion systems processing on the order of 100 MW at specific impulses of 20,000 s have been proposed with this ultimate goal in mind.<sup>28,29</sup>

### Technology Assessment

There have been 48 electric thruster systems<sup>3</sup> and 22

nuclear power systems<sup>22</sup> launched by the United States as of 1985. Thus, there would seem to be little doubt as to the feasibility of nuclear electric propulsion, the major technological challenge is in scaling these systems up to the power and performance levels required to support the Space Exploration Initiative. The primary emphasis of the technology assessment section of this paper will be on the thrusters, however, it is important to recognize that a large effort which will be required to develop a suitable power supply, power conversion, thermal management system.

### Power Source and Power Conversion

Both photovoltaic solar arrays and nuclear reactors have been proposed for multimegawatt electric propulsion systems. Multimegawatt solar arrays require enormous areas, typically on the order of 1 football field per 2 MW.<sup>22</sup> The feasibility and practicality of such large arrays is an open question. For power levels up to a megawatt, the SP-100 nuclear reactor, or a derived version of this technology, may be appropriate.<sup>16</sup> Above the one megawatt level, there are several candidate reactor concepts. These include evolved SP-100 or NERVA<sup>30</sup> derivative technologies, and other closed cycle systems.

Methods of converting the thermal power of the reactor to electricity include thermodynamic cycles with rotating machinery (Brayton, Sterling, Rankine), thermoelectric conversion, thermionic conversion, and other direct conversion systems. Selection of a power conversion system depends on many mission and system requirements, including the form of power (AC or DC, voltage level, etc.) selected for power distribution, as well as thruster interface requirements.

Finally, the thermal management system, which constitutes a major portion of the NEP system, must be considered. In addition to passive radiators, other candidate technologies include heat pipes and more speculative concepts (such as liquid droplet radiators).

### Thrusters

Two of the leading candidates for high power lunar and Mars electric propulsion systems are ion and MPD thrusters. In addition, numerous other electric thruster concepts, presently at less advanced stages of development than the ion and MPD thrusters, have been proposed.<sup>12</sup> These include quasi-steady pulsed and steady-state devices, utilizing a variety of electromagnetic phenomena, and operating on a wide spectrum of solid, liquid and gaseous propellants.

**Ion:** Ion thrusters convert electrical power to thrust power by electrostatically accelerating positively charged ions. The ions are generated in the discharge chamber of the thruster by electron bombardment of the propellant gas

(which is usually a rare gas such as argon, krypton or xenon; although mercury and cesium have also been used). The chamber in which the ions are created is maintained at a high positive potential, typically on the order of 1,000 volts. The ions and electrons in the discharge chamber form a plasma which assumes a potential approximately equal to the high positive potential applied to the thruster. The high positive plasma potential causes the positive ions to be pushed out of the thruster at very high velocities.

Electrons left behind by the ions which were pushed from the thruster are collected and injected into the ion beam to prevent the spacecraft from becoming negatively charged. A negatively biased grid positioned at the downstream end of the thruster screens the positive high voltage discharge chamber from these electrons while simultaneously permitting the beam ions to pass through and leave the thruster. A second grid is typically positioned a fraction of a millimeter upstream of the negative grid to focus the ions through the apertures of the negative grid. This combination of closely spaced grids is commonly referred to as the ion accelerator system. The thrust density for an ion engine is limited by space charge effects in the accelerator system. In general, higher thrust densities can be achieved by reducing the grid separation. A cutaway view showing the major components of an ion thruster is given in Fig. 8.

The electrostatic acceleration process which produces the high velocity ions is nearly 100 % efficient (actual efficiencies are typically greater than 99.5 %). Consequently, ion thrusters are the most efficient electric propulsion devices, and are potentially capable of processing very large power levels, at very high specific impulses while maintaining relatively low engine component temperatures. Loss mechanisms associated with ionizing the neutral propellant gas serve to lower the overall engine efficiency to 60-85%.

Multimegawatt electric propulsion systems require individual ion thrusters which can process input powers of several 100 to 1,000 kW at specific impulses of 5,000 s to greater than 10,000 s. A 1.5 m diameter mercury ion thruster has been operated at a maximum input power of 130 kW with an overall thruster efficiency of 70 % and a specific impulse of 8150 s.<sup>31</sup> In other work, a mercury ion thruster was operated at specific impulses greater than 20,000 s.<sup>32</sup>

Environmental concerns with mercury, and the limited availability and high cost of xenon and krypton make argon the most likely propellant for high power ion thrusters. A 50 cm diameter thruster has been operated at power levels up to 20 kW at a specific impulse of 4600 s on xenon.<sup>33</sup> If this same thruster were operated on argon, higher input powers and higher specific impulse levels could be achieved. The major technology issue for high

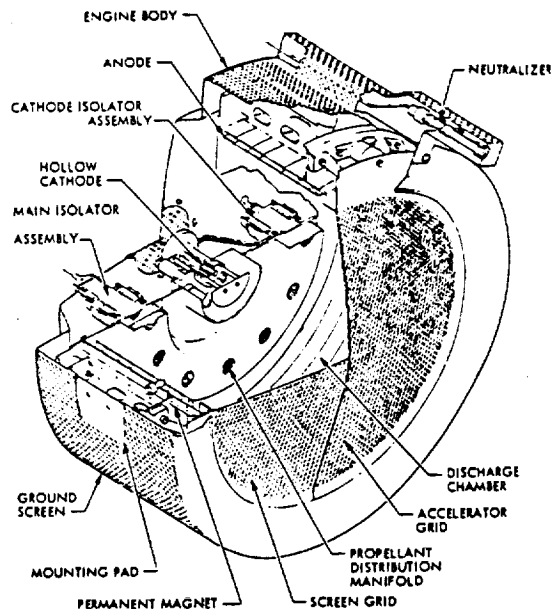


Figure 8 Ion thruster diagram.

power ion propulsion systems is associated with scaling ion engine power levels up one or two orders of magnitude from the present 10's of kW range. Scaling to these power levels will most likely require new engine and accelerator system configurations.

**MPD:** The magnetoplasmadynamic (MPD) thruster produces thrust through the interaction of a multikiloampere arc discharge and a magnetic field, as suggested in Fig. 9. This interaction results in a  $J \times B$  force which expels a relatively dense, fully ionized, plasma from the thruster at high velocities. In "self-field" MPD thrusters, the magnetic field is generated solely by the action of the very large discharge current. "Applied-field" thrusters augment this self-induced field with an externally applied magnetic field. Magnetic flux densities of 0.1 to 1 tesla are typical of both self-field and applied field thrusters.

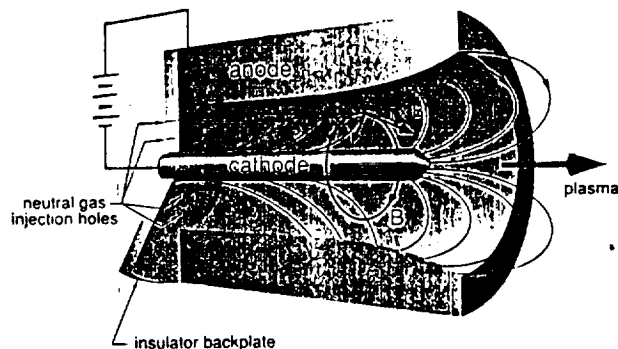


Figure 9 MPD thruster illustration.

Since a neutral plasma is accelerated from the MPD thruster, the thrust density is not limited by space-charge effects as it is in the ion thruster. Thrust densities two orders of magnitude higher than that of the ion thruster may be possible with the MPD thruster at the same specific impulse. Scaling relations developed for the MPD thruster indicate that the most efficient thruster performance will be obtained at megawatt input power levels -- ideal for multimewatt electric propulsion systems.

Steady-state MPD thrusters have been successfully operated at the 100 kW power level at NASA Lewis Research Center.<sup>34</sup> With argon propellant at this power level, the LeRC thruster was 21 % efficient and produced a specific impulse of 1100 s. Improved performance is expected at megawatt power levels. Efficiencies greater than 50 % and specific impulses greater than 5000 s have been reported for pulsed MPD thrusters operating at multimewatt input power levels with hydrogen<sup>35,36</sup> and ammonia<sup>37</sup> propellants. Successful steady-state MPD thruster operation at power levels up to 600 kW, with low electrode erosion, has been demonstrated at the University of Stuttgart, FRG,<sup>38</sup> and steady-state operation up to the megawatt level in the Soviet Union has been reported.<sup>39</sup> A more detailed review of MPD thruster technology may be found in Sovie and Manteniaks.<sup>40</sup> The major technological challenge for MPD propulsion is to simultaneously demonstrate high performance (i.e. greater than 50 % efficiency at specific impulses of 5000 s or higher) with life times of several thousand hours under steady-state operation at megawatts of input power.

### Summary

Electric propulsion systems offer significant benefits for the Space Exploration Initiative provided the component technologies required by these systems can be successfully scaled up to megawatt power levels. Lunar cargo vehicles can provide mass savings of tens to hundreds of metric tons per mission by using electric propulsion systems operating at power levels in the range 300 to 1,000 kW. Mars cargo vehicles will require power levels of 1 to 10 MW to deliver payload masses on the order of 400 MT, but result in reductions in IMEO of several hundred metric tons per mission. Piloted Mars missions using electric propulsion systems with tens of megawatts of power show significant reductions in IMEO and trip time. Minimum round-trip times to Mars may be possible through the use of hybrid chemical/NEP or NTR/NEP systems. Nuclear electric propulsion systems also provide growth potential for expanded human exploration of the solar system.

Finally, it is best to keep in mind that no one propulsion system is ideal for all applications and that human settlement of Mars will no doubt require a variety of advanced propulsion systems. The role of electric propulsion may best be summarized in the following quotation:

"The electric propulsion system will come into life on its own right, not as an all-out competitor, but as another powerful tool for the exploration of space." (Stuhlinger 1959)

### Acknowledgements

The work described in the paper was performed by the Jet Propulsion Laboratory, California Institute of Technology, under contract with the National Aeronautics and Space Administration. "Approved for public release; distribution unlimited."

The authors wish to thank Brad Cothran (Boeing), Jim Gilland (Sverdrup Technology/NASA LeRC), Robert Frisbee (JPL), Paul Sager (General Dynamics, Space System Division), and Joel Sercel (JPL) for providing information about electric propulsion systems for SEI, Marland Stanley (EG&G Idaho) for information about power supplies, and Jay Polk (Princeton) for supplying the updated MPD thruster illustration.

### References

1. Bova, B. "To Mars and Beyond," *Air and Space*, (I SSN, 0886-2257), Vol. 4, Oct.-Nov. 1989, pp. 42-48.
2. Stuhlinger, E., *Ion Propulsion for Space Flight*, McGraw-Hill, New York 1964.
3. Beattie, J. R., and Penn, J. P., "Electric Propulsion -- A National Capability," AIAA Paper No. 89-2490, July 1989.
4. Schreib, R., "Readiness Appraisal: Ion Propulsion for Communications Satellites," AIAA Paper No. 88-0777, March 1988.
5. Tollefson, D. R., "Megawatt Ion-Propulsion Power Conditioning System -- Design Considerations for Manned Interplanetary Missions," AIAA Paper No. 67-52, January 1967.
6. Stuhlinger, E., "How Useful are Low-Thrust Space Vehicles?" ARS 990-59, presented at the ARS 14th Annual Meeting, November 1959.

7. Aston, G. "Advance Electric Propulsion for Interplanetary Missions," AAS-86-259, presented at the 33rd AAS Annual Meeting, October 1986.
8. Palaszewski, B., "Electric Propulsion for Lunar Exploration and Lunar Base Development," Paper No. LBS-88-005, presented at the Lunar Bases & Space Activities in the 21st Century Symposium, April 1988.
9. Palaszewski, B., "Lunar Transfer Vehicle Design Issues with Electric Propulsion," AIAA Paper No. 89-2375, July 1989.
10. Brown, H. and Nicoll, H. E., "Electrical Propulsion Capabilities for Lunar Exploration," ARS 2373-62, presented at the Electric Propulsion Conference, March 1962.
11. Personal Communication with Jim Gilland, NASA Lewis Research Center, July 1990.
12. Frisbee, R. H., Blandino, J. J., and Sercel, J. C., "Advanced Propulsion Options for the Mars Cargo Vehicle," AIAA Paper No. 90-1997.
13. Phillips, P. G., "NEP Freighter -- A Point Design," in: "The Case for Mars III: Strategies for exploration -- Technical," AAS Paper No. 87-255, 1989.
14. Palaszewski, B., Brophy, J., and King, D., "Nuclear-Electric Propulsion -- Manned Propulsion Options," in: "The Case for Mars III: Strategies for exploration -- Technical," AAS Paper No. 87-260, 1989.
15. Galecki, D. L. and Patterson, M. J., "Nuclear Power Mars Cargo Transport Mission Utilizing Advanced Ion Propulsion," NASA TM 100109 (also AIAA Paper No. 87-1903), July 1987.
16. Isenberg, L. and Heller, J. A., "SP-100 Space Reactor as a Power Source for Mars Exploration Missions," in: "The Case for Mars III: Strategies for exploration -- General interest and overview," AAS Paper No. 87-224, 1989.
17. Cassady, R. J., "An MPD Thruster Driven Cargo Ferry for Support of the Manned Mars Mission," AIAA Paper No. 88-2896, July 1988.
18. Coomes, E. P., McCauley, L. A., Christian, J. L., Gomez, M. A., and Wong, W. A., "Unique Mission Options Available with a Megawatt-Class Nuclear Electric Propulsion System," AIAA Paper No. 88-2839, July 1988.
19. Galecki, D. L., "In-Situ Propellant Advantages for Fast Transfer to Mars," AIAA Paper No. 88-2901, July 1988.
20. Stuhlinger, E., and King, J. C., "Concept for a Manned Mars Expedition with Electrically Propelled Vehicles," ARS 2374-62, March 1962.
21. Layton, J. P., "Application of Nuclear Power and Propulsion Technology to Solar System Exploration," AIAA Paper No. 67-512, July 1967.
22. Cothran, B., McGee, J., in presentation to Nuclear Electric Propulsion Workshop, Pasadena, CA., June 1990.
23. Personal communication, Paul Sager, General Dynamics, July 1990.
24. Braun, R. D., and Blersch, D. J., "Propulsion Options for a Manned Mars Transportation System," AIAA Paper No. 89-2950, July 1989.
25. Harris, P. A., and Perry, F. J., "Propulsion System Considerations/Approach for Fast Transfer to Mars," AAS 87-209, in Case for Mars III: Strategies for exploration -- General interest and overview, 1989.
26. Ruffa, G. J., and Cordell, "Performance of Electric/Chemical Combinations for Manned Mars Missions," in, The Case for Mars III: Strategies for exploration, 1989.
27. Valgora, M. E., "Power Considerations for an Early Manned Mars Mission Utilizing the Space Station," AAS Paper No. 87-223, in, The Case for Mars III: Strategies for exploration -- General interest and overview, 1989.
28. Loeb, H. W., "Electric Propulsion for Manned Spaceflights of the Future," AIAA Paper No. 81-0707, April 1981.
29. Sercel, J., "Multimegawatt Nuclear Electric Propulsion, First Order System Design and Performance Evaluation," JPL D-3898, January 1987.
30. Chi, J., Holman, R., and Pierce, B., "Nerva Derivative Reactors for Thermal and Electrical Propulsion," AIAA Paper No. 89-2770, July 1989.
31. Nakanishi, S., and Pawlik, E. V., "Experimental Investigation of a 1.5-m-diam. Kaufman Thruster," *Journal of Spacecraft and Rockets*, Vol. 5, No. 7, July 1968.

32. Byers, D. C., "An Experimental Investigation of a High-Voltage Electron-Bombardment Ion Thruster," NASA TM X-52429, May 1968.
33. Patterson, M. J. and Rawlin, V. K., "Performance of 10-kW Class Xenon Ion Thrusters," AIAA Paper No. 88-2914, July 1988.
34. Sovey, J. S., et al., "Test Facility and Preliminary Performance of a 100 Kw Class MPD Thruster," NASA TM-102021, May 1989.
35. Uematsu, K., Mori, K., Kuninaka, H., and Kuriki, K., "Effect of Electrode Configuration on MPD Arcjet Performance," IEPC 84-31, presented at the 17th International Electric Propulsion Conference, Tokyo, May 1984.
36. Kunii, Y. and Kuriki, K., "Multipole MPD Arcjet," AIAA Paper No. 85-2055, Sept. 1985.
37. Yoshikawa, T., Kagaya, Y., Yokoi, Y. and Tahara, H., "Performance Characteristics of Quasi-Steady MPD Thrusters," IEPC 84-58, presented at the 17th International Electric Propulsion Conference, Tokyo, May 1984.
38. Personal communication, Jay Polk, Princeton University, June 1990.
39. Personal communication, A. S. Koroteev, Director of the Scientific Research Institute for the Study of Thermal Processes; July 1990.
40. Sovey, J. S. and Mantenieks, M. A., "Performance and Lifetime Assessment of MPD Arc Thruster Technology," AIAA Paper No. 88-3211, July 1988.

**13.3 Appendix C**

**AIAA 90-2655  
Simulated Ion Thruster Operation  
Without Beam Extraction**

J. R. Brophy  
Jet Propulsion Laboratory  
Pasadena, CA

# SIMULATED ION THRUSTER OPERATION WITHOUT BEAM EXTRACTION

John R. Brophy\*  
Jet Propulsion Laboratory  
California Institute of Technology  
Pasadena, California

## Abstract

The development of high power (100's of kilowatts) ion engines may be greatly facilitated through the use of a technique which enables optimization of the discharge chamber to be performed without beam extraction. Ion thruster operation without beam extraction results in an experimentally determined decrease in the accelerator system transparency to ions from approximately 0.8 down to 0.22 for the standard J-Series thruster ion optics. This decreased ion transparency translates into a decreased propellant flow rate requirement for operation without beam extraction, enabling testing to be performed in smaller vacuum chambers with lower pumping speeds. Performance curves simulated without beam extraction are shown to agree well with actual performance curves obtained with beam extraction. Screen grid temperatures, however, are shown to be significantly higher without beam extraction due to the decrease in the accelerator system transparency to ions.

## Nomenclature

$A_a$  = Active grid area, ( $m^2$ )  
 $e$  = Electronic charge, (A)  
 $J_a$  = Ion current to accelerator grid, (A)  
 $J_b$  = Ion current leaving the thruster, (A)  
 $J_d$  = Discharge current, (A)  
 $J_s$  = Total grid plane ion current, ( $J_a + J_b + J_d$ ), (A)  
 $J_k$  = Keeper electrode current, (A)  
 $J_s$  = Ion current to screen grid, (A)  
 $\dot{m}$  = Total propellant flow rate, (equivalent amperes)  
 $M_i$  = Ion mass, (kg)  
 $n_i$  = Ion number density, ( $m^{-3}$ )  
 $n_o$  = Neutral atom number density, ( $m^{-3}$ )  
 $Q_o^*$  = Maxwellian electron ionization rate factor, ( $m^3/s$ )  
 $T_e$  = Electron temperature, (eV)  
 $v_b$  = Bohm velocity, (m/s)  
 $V_d$  = Discharge voltage, (V)  
 $V_k$  = Keeper electrode voltage, (V)  
 $v_p$  = Primary electron velocity, (m/s)  
 $V_t$  = Total voltage, (V)  
 $v_o$  = Neutral atom thermal velocity, (m/s)  
 $\bar{V}$  = Ion production volume, ( $m^3$ )

$\epsilon_b$  = Beam ion energy cost, (eV/ion)  
 $\epsilon_p^*$  = Baseline plasma ion energy cost, (eV/plasma ion)  
 $\eta_{ud}$  = Discharge chamber propellant efficiency  
 $\sigma_o'$  = Total inelastic collision cross section at the primary electron energy ( $m^2$ )  
 $\sigma_i'$  = Total ionization cross section at the primary electron energy ( $m^2$ )  
 $\phi_i$  = Accelerator system transparency to ions  
 $\phi_o$  = Accelerator system transparency to neutral atoms

## SuperScripts

$\wedge$  designates without beam extraction

## Introduction

High power ion propulsion systems can substantially benefit the Space Exploration Initiative by greatly reducing the mass of material required to be lifted to low Earth orbit.<sup>1-4</sup> For ion propulsion to fulfill this promise, however, the successful development of ion engines which can process input powers on the order of 100's to 1000's of kilowatts is required. The major technological challenge in this endeavor is in the development of large area, high current density, accelerator systems. However, the development of a light-weight, long-life, discharge chamber which can efficiently supply a uniform flux of ions to this accelerator system over a large area is an essential, and by no means trivial, task.

The development and life testing of large diameter, high power, rare gas, ion engines can be expensive due to the very high pumping speeds ( $10^6$  to  $10^7$  liters/second) that are required to maintain sufficiently low background pressures during beam extraction. Vacuum facilities capable of achieving pumping speeds of this magnitude are expensive to construct and maintain. This paper describes an investigation into the feasibility of a technique to simulate the ion beam extraction operating

\*Member Technical Staff, Electric Propulsion and Plasma Technology Group. Member AIAA

conditions of the discharge chamber without actually extracting a beam. Successful development of such a technique may permit the initial development and optimization of large area, high power, ion engine discharge chambers to be performed in vacuum facilities with more modest pumping capabilities (on the order of  $10^5$  liters/second).

The idea of discharge chamber optimization without beam extraction is not new, and several such investigations are described in the literature.<sup>5-7</sup> Those studies in which the discharge chamber was ultimately tested with beam extraction, however, have typically found that the discharge chamber performs significantly poorer under actual beam extraction tests than was projected based on the tests performed without beam extraction. It is believed that this discrepancy results primarily from a reduction in neutral atom density in the discharge chamber for operation with beam extraction relative to the tests performed without beam extraction at the same propellant flow rate. It has been shown<sup>8</sup> that the discharge chamber performance is strongly dependent on the internal neutral atom density. In fact, the values of all major discharge chamber plasma parameters, including the discharge loss, may be shown to be functions of the neutral atom density and the discharge chamber geometry.<sup>8</sup> The discharge chamber performance is also a function of the ion density distribution.

This suggests that to simulate beam extraction, the most important similarity conditions are to simultaneously match both the neutral atom density and the ion density to the respective values which would be obtained with beam extraction. In this paper the necessary conditions to produce simulated beam extraction are developed analytically. Experimental discharge chamber performance data obtained with and without beam extraction are used to test the validity of the similarity conditions.

### Theory

During normal thruster operation with beam extraction, ions created in the discharge chamber flow essentially collisionlessly toward the discharge chamber boundaries. Some fraction of this ion flux is directed towards the accelerator system. One of the functions of the magnetic field applied to the discharge chamber is to maximize this fraction, thereby increasing the overall engine efficiency by reducing the flux of ions to surfaces other than the accelerator system. Those ions which don't reach the accelerator system recombine with electrons on the walls of the discharge chamber and must be re-ionized before they can be accelerated. Of the ions which reach the accelerator system only a fraction is extracted into the beam; the remaining ions strike the screen grid webbing and recombine with electrons on the grid surface.

The effective accelerator system transparency to ions

is defined as the fraction of the ion flux to the accelerator system which is extracted into the exhaust beam. Focussing effects from the applied grid voltages can result in effective ion transparencies greater than the physical open area fraction of the screen grid. The physical open area fraction of the J-Series screen grid is 67 %, and effective ion transparencies of 80 % have been measured.

With beam extraction, the neutral propellant density in the discharge chamber is typically much greater than the ion density. Yet in an efficient ion engine, greater than 90 % of the propellant leaves the thruster in the form of ions. This is possible because the ions flow toward the accelerator system with a velocity which depends on the electron temperature (i.e. the Bohm velocity), and the electron temperature is generally more than 500 times the neutral atom temperature which governs the escape of neutral atoms from the thruster. In addition, the effective transparency of the accelerator system to ions (67 to 80 percent) is much greater than the effective transparency of the accelerator system to neutral atoms. The neutral atom transparency is governed by the accelerator grid hole size and grid thickness, and is approximately 20 % for the J-Series optics.

Without beam extraction the situation is different. Removal of the high voltages from the grids dramatically reduces the accelerator system transparency to ions. In this case, a large fraction of the ions reaching the accelerator system are focused onto the screen grid and accelerator grid webbings rather than being transmitted through the grid apertures. Ions striking the grids recombine with electrons at the grid surface and leave the surface as neutral atoms. Some fraction of these neutral atoms re-enter the discharge chamber and the others leave the thruster entirely. Since the accelerator system transparency to ions decreases significantly without beam extraction, the fraction of propellant which leaves the discharge chamber as neutral atoms increases. If the propellant flow rate into the discharge chamber is unchanged when the high voltages are removed, then the neutral atom density in the discharge chamber will increase to satisfy continuity. In this case the neutral particle flux through the grids must increase to account for the decrease in ion flux from the engine.

To simulate the beam extraction operating conditions of the discharge chamber without beam extraction, the propellant flow rate into the discharge chamber must be reduced. In addition, it is necessary to match the average ion density in the discharge chamber with and without beam extraction. These ideas are developed more concretely in the following simple analysis. The propellant flow rate into the discharge chamber (in units of equivalent amperes) is given in Eq. (1) for operation with beam extraction.

$$\dot{m} = \frac{1}{4} n_o A_o \phi_o v_o e + 0.6 n_i A_g \phi_i v_b e \quad (1)$$

The first term on the right-hand-side of Eq. (1) represents the flow rate of neutral atoms leaving the discharge chamber through the accelerator system. The second term represents the flow rate of ions extracted into the exhaust beam. Without beam extraction the propellant flow rate is given by,

$$\dot{m} = \frac{1}{4} n_o A_g \phi_o v_o e + 0.6 n_i A_g \phi_i v_b e \quad (2)$$

Writing Eq. (2) in this form recognizes that the electron temperature may not necessarily be the same with and without beam extraction, resulting in a different value of the Bohm velocity. The similarity criteria to match the beam extraction conditions without beam extraction are that the neutral atom and ion densities must be the same in both cases, i.e.,

$$n_o = n_o, \quad n_i = n_i \quad (3)$$

and the electron temperatures must be the same,

$$T_e = T_e \quad (4)$$

Using these conditions, Eq. (2) can be written,

$$\dot{m} = \frac{1}{4} n_o A_g \phi_o v_o e + 0.6 n_i A_g \phi_i v_b e \quad (5)$$

Equation (1) may be rewritten as,

$$1 = \frac{\frac{1}{4} n_o A_g \phi_o v_o e}{\dot{m}} + \eta_{ud} \quad (6)$$

where the discharge chamber propellant efficiency with beam extraction is given by,

$$\eta_{ud} = \frac{0.6 n_i A_g \phi_i v_b e}{\dot{m}} \quad (7)$$

Finally, using Eqs. (6) and (7) in Eq. (5) results in the following relation,

$$\hat{m} = \dot{m} \left[ 1 - \eta_{ud} \left( 1 - \frac{\phi_i}{\phi_o} \right) \right] \quad (8)$$

This equation indicates that the propellant flow rate without beam extraction, required to simulate discharge chamber operation with beam extraction, at a given propellant efficiency and total flow rate, depends only on the ratio of accelerator system transparencies to ions without and with beam extraction, assuming the similarity conditions, Eqs. (3) and (4), have been met. As the

accelerator system ion transparency ratio decreases, so does the required propellant flow rate without beam extraction, according to Eq. (8). If the analysis is extended to include the effect of multiply charged ions, then the form of Eq. (7) is unchanged; however, the discharge chamber propellant efficiency is the value corrected for multiply charged ions.

## Apparatus and Procedure

Experiments to test the theory were performed using a modified J-Series<sup>9</sup>, 30 cm diameter, divergent-field thruster. Modifications to the standard J-Series thruster included removal of the isolator and vaporizer heaters, replacement of the mercury high voltage propellant isolators with isolators designed for improved performance with inert gas propellants<sup>10</sup>, replacement of the perforated ground screen with a solid ground screen, and replacement of all of the teflon coated, kapton wire with ceramic bead insulated wire. In addition, the standard J-Series thruster main cathode was replaced with a 6.35 mm diameter hollow cathode fabricated from a thin walled, molybdenum tube with a 2 % thoriated tungsten orifice plate electron beam welded to one end. A J-Series thruster style porous tungsten insert impregnated with low work function material was used as the emitter inside the molybdenum cathode barrel. The cathode orifice diameter was 1.27 mm, and a Swagelok fitting was used to provide a gas tight seal at the upstream end of the cathode. This fitting also served to mount the cathode to a stainless steel flange which was then bolted to the cathode mounting flange in the J-Series pole piece assembly. A tantalum-sheathed, tantalum swaged heater wire with a 0.51 mm diameter center conductor was used for the cathode tip heater. A 25.4 mm diameter molybdenum baffle was used in place of the J-Series baffle. All tests were performed using the standard J-Series accelerator system.

For some tests the accelerator system was electrically isolated from the thruster body. This was done to enable the ion current to the screen grid to be measured. The accelerator system was electrically isolated by inserting 12.7 mm long ceramic insulators between the thruster body flange and the accelerator system mounting flange. This modification had the side effect of lengthening the discharge chamber by 12.7 mm, which required remaking the ground screen. In addition, a cylindrical section of 0.254 mm thick, non-magnetic stainless steel was spot-welded to the anode pole piece to extend this structure 12.7 mm toward the screen grid. This was done to minimize plasma leakage around the anode pole piece when the accelerator system was displaced downstream by the ceramic insulators.

A simplified power supply circuit diagram for beam extraction operation with the screen grid electrically isolated from the thruster body is given in Fig. 1A. The neutralizer common lead was allowed to float relative to facility ground. The screen grid bias supply is used to bias the screen grid up to 30 volts negative of cathode

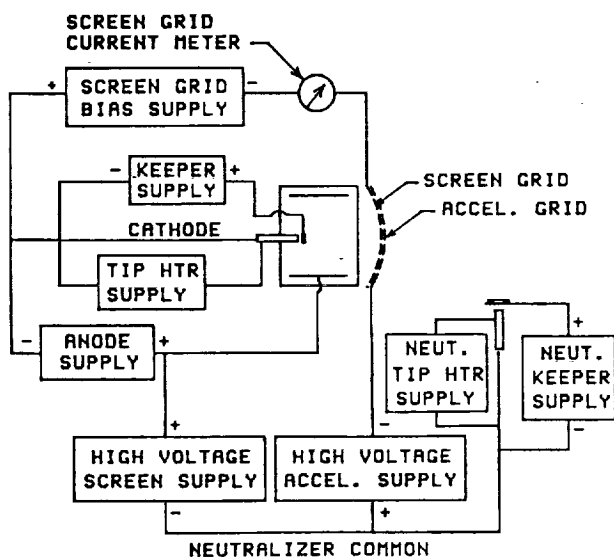


**Figure 1A** Circuit diagram for operation with beam extraction.

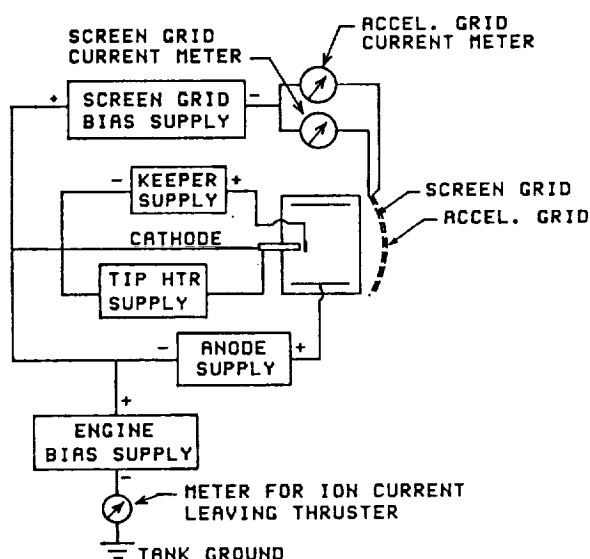


**Figure 1B** Circuit diagram for operation without beam extraction.

potential to prevent electrons from reaching the grid surface. The current through this power supply, under these conditions, represents the current of ions which strike the screen grid. The beam current, on the other hand, is the current of ions which pass through the accelerator system. The sum of the beam current and the ion current reaching the screen grid represents the total flux of ions toward the accelerator system. The ratio of the beam current to this total ion current is the effective transparency of the accelerator system to ions. (The ion current which impinges on the accelerator grid is typically 1 % or less of the beam current, and is neglected.) With this technique, the effective transparency of the

accelerator system to ions was measured at beam currents up to 2.5 A at a total voltage of 1430 V.

For operation without beam extraction, the simplified circuit diagram shown in Fig. 1B is used. The neutralizer common lead is grounded to the vacuum tank walls, and there is no neutralizer cathode. The grid bias supply is used to bias both the screen and accelerator grids up to 30 volts negative of cathode potential, which as before, enables the measurement of the ion current to the grids. The engine bias supply shown in Fig. 1B is used to raise the discharge chamber cathode potential up to 30 volts above facility ground. This is done to prevent electrons in the discharge chamber plasma from leaving the engine, thus enabling the ion current leaving the engine to be measured. In a manner analogous to operation with the high voltage on, the ratio of the ion current leaving the engine to the sum of this current and the ion current striking the grids represents the effective transparency of the grid system to ions. The presence or absence of the high voltage applied to the grids will be shown to have a first order effect on the effective transparency of the accelerator system to ions.

When comparing data obtained from experiments performed with the circuit diagrams in Fig. 1, care must be taken to correctly compute equivalent discharge powers for operation with and without beam extraction. For the circuit in Fig. 1A, the electrons left behind by ions extracted into the beam do not contribute to the discharge current since the screen supply is connected to the positive side of the discharge power supply. Ions which strike the screen grid, however, draw electrons through the discharge supply and, therefore, contribute to the discharge current. Without beam extraction, the ion current striking the grid webbing increases substantially. The end result is that, to compute the discharge power in a physically consistent manner, the beam current obtained with beam extraction must be added to the discharge current, and this sum, multiplied by the discharge voltage, will result in the appropriate discharge power. This added complexity could be eliminated by connecting the high voltage screen power supply to the negative side of the discharge supply for operation with beam extraction (as is often done).

The experiments were conducted by first operating the thruster with beam extraction. The ion current to the screen was measured as a function of the negative bias applied to the screen grid. A typical variation of measured ion current versus bias voltage is given in Fig. 2 for two different beam current levels. These data indicate that the ion current saturates at between 10 and 15 volts negative of cathode potential. To guarantee that measurements were being taken well away from the "knee" of these curves, a constant negative bias of 20 volts was used. Similar tests performed without beam extraction showed the same, well-defined ion current saturation behavior. After completion of the data collection with beam extraction, the high voltage and neutralizer cathode were turned off in preparation for tests performed without beam extraction. It was necessary to

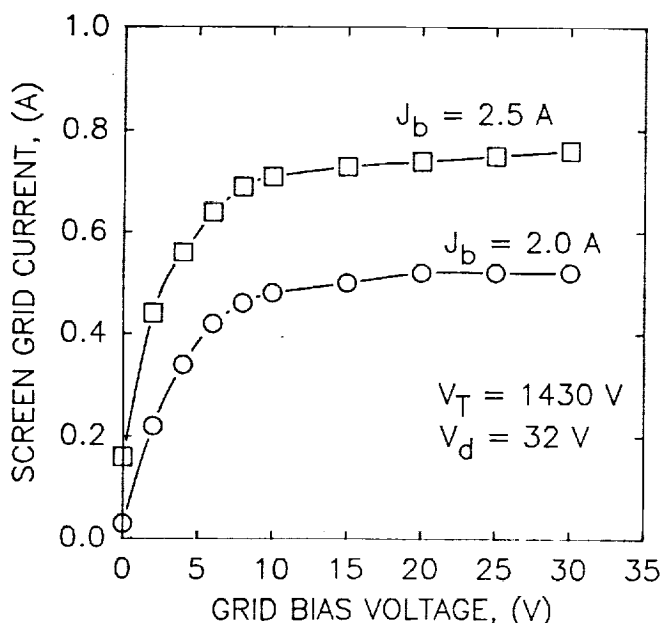


**Figure 2** Effect of negative bias voltage on the measured ion current to the screen grid.

turn the neutralizer off for operation without beam extraction to prevent electron backstreaming to the ion source when the engine bias supply was used to bias the discharge chamber positive of facility ground. Finally, the flow rate through the main cathode was held constant for operation without beam extraction.

Laboratory power supplies were used for all of the power supplies except the discharge, screen and accelerator supplies. These power supplies were comprised of a parallel combination of components from two FMPPU's as described in Ref. 10. All tests were performed using xenon gas for the propellant. Commercial flow controllers and thermal mass flow meters were used to measure and control the xenon propellant flow rates. The flow meters were calibrated using a primary standard, volumetric displacement technique. Repeated checks of the calibrations were performed using a secondary standard volumetric displacement system. Engine operating data were recorded with a computer controlled data acquisition system. For all of the tests describe herein, however, the engine itself was operated under manual control. The ion currents to the screen and accelerator grids, and the ion current leaving the engine without the high voltage on, were measured using digital multimeters.

One series of tests was performed to determine the effect of high voltage operation on the accelerator system temperatures. For these tests, six 36-gauge, Type-J thermocouples were attached to the screen and accelerator grids, three on each grid. The thermocouples were positioned at radial locations of 0, 4.5, and 9.0 cm from the centerline of the grids. The accelerator grid thermocouples were positioned diametrically opposite the

corresponding screen grid thermocouples. Narrow strips of tantalum foil were spot-welded to the upstream side of the screen grid to shield the accelerator grid thermocouple wires from the beam ions when operating with beam extraction. The 36-gauge thermocouples wires were attached to the grids by tightly tying the thermocouple leads around the grid webbing as described in Ref. 11. The thermocouple output voltages were read using components of a data acquisition system which were floated at the appropriate high voltage level (1100 volts for the screen grid and -300 volts for the accelerator grid) and optically coupled to ground. Grid temperature measurements were collected over a range of discharge powers with and without beam extraction.

## Results and Discussion

The effect of the high voltage on the accelerator system transparency to ions is illustrated in Fig. 3. With beam extraction, typically 80 % of the ion flux towards the accelerator system is focused through the grid apertures into the exhaust beam, approximately 20 % strikes the screen grid, and less than 1 % hits the accelerator grid. Without beam extraction, the ions are not focused through the grid apertures, but rather are directed toward the grid webbing. In this case, typically 65 % of the ion flux impinges on the screen grid, 30 % reaches the accelerator grid, and the remaining 5 % leaves the thruster.

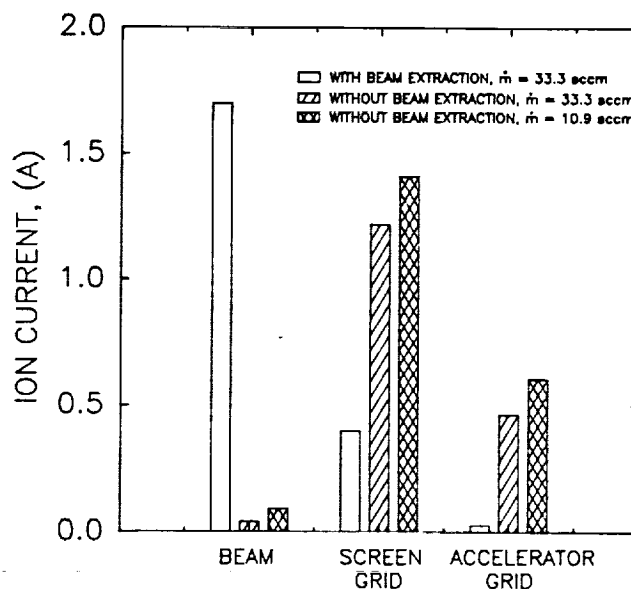


**Figure 3** Ion current distributions with and without beam extraction.

The data in Fig. 3 were obtained at a discharge current and voltage of 10.0 A and 32 volts, and a total flow rate of 33.3 sccm. Careful inspection of this figure indicates that the total ion flux toward the accelerator

system with beam extraction is greater than without beam extraction even though the discharge chamber was operating at the same discharge power and total propellant flow rate. This effect is believed to result from suppression of the Maxwellian electron temperature caused by the high neutral atom density produced by operation without beam extraction. The variation of the ion current to the grid plane with total flow rate is given in Fig. 4 for operation without beam extraction at a constant discharge current of 10.0 A. The maximum ion current to the grid plane occurs over a range of total flow rates from approximately 11 to 14 sccm, and is approximately equal to the ion current measured to the grid plane with beam extraction as indicated by the solid circle in this figure. This suggests that, in this case, the proper flow rate without beam extraction is in the range 11 to 14 sccm.

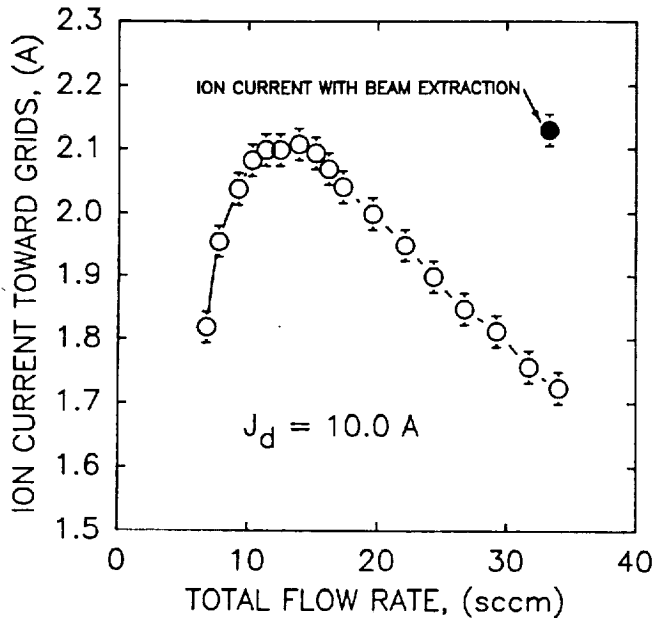


**Figure 4** Variation in total ion current to the grid plane with total propellant flow rate without beam extraction.

The discharge current/voltage characteristic obtained with beam extraction at a total flow rate of 33.3 sccm is compared to that without beam extraction at a flow rate of 10.9 sccm in Fig. 5 (the cathode flow rate was maintained at the same value with and without beam extraction). Operation without beam extraction at flow rates either significantly higher or lower than about 11 sccm resulted in substantially different current voltage characteristics than that shown in Fig. 5. The ratio of the total ion current to the grid plane (which is the sum of the ion currents to the screen grid, accelerator grid, and leaving the thruster) without beam extraction to that with beam extraction is given in Fig. 6 as a function of discharge power. These data indicate that the ion flux to the grid plane is the same with and without beam extraction, provided the total flow rate into the thruster without beam extraction is reduced to the correct level.

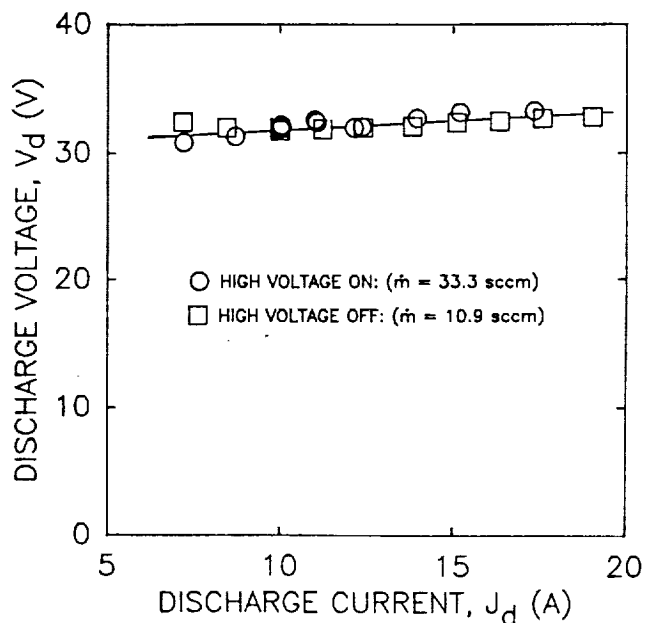


**Figure 5** Comparison of discharge chamber current/voltage characteristics with and without beam extraction.

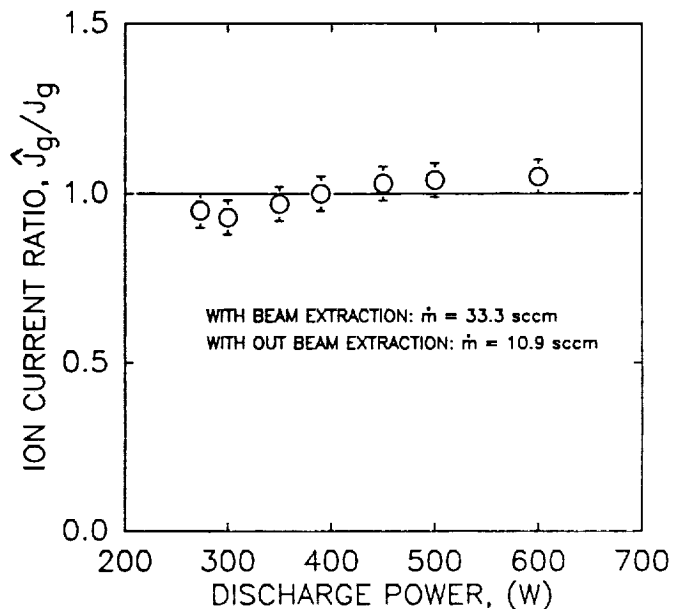


**Figure 6** Ratio of total ion current to grid plane with and without beam extraction.

### Neutral Atom Density

The similarity conditions used to derive Eq. (8) were that the neutral atom density, ion density, and electron temperature without beam extraction must be identical to their respective values with beam extraction. Comparison of calculated neutral atom densities with and without beam extraction is given in Fig. 7. The average neutral density in the discharge chamber with beam extraction

was calculated using the following expression,

$$n_o = \frac{4\dot{m}(1-\eta_{ud})}{A_g\phi_o V_o e} \quad (9)$$

Without beam extraction, the average neutral atom density was calculate from,

$$\hat{n}_o = \frac{4\hat{m}(1-\hat{\eta}_{ud})}{A_g\hat{\phi}_o V_o e} \quad (10)$$

where the propellant efficiency in this case was determined in two different ways corresponding to two different assumptions regarding the behavior of the neutral atoms formed by ion recombination at the accelerator grid. The ions which strike the accelerator grid without beam extraction pick-up electrons at the grid surface and become neutral atoms. These neutral atoms leave the grid surface and either re-enter the discharge chamber or leave the thruster entirely. If it is assumed that all of the ions striking the accelerator grid re-enter the discharge chamber as neutral atoms, then the discharge chamber propellant efficiency without beam extraction is given by,

$$\eta_{ud} = \frac{\mathcal{P}_b}{\dot{m}} \quad (11)$$

which corresponds to the curve labeled "100 %" in Fig. 7. On the other hand, if it is assumed that none of the ions striking the accelerator grid re-enter the discharge chamber, then the propellant efficiency is given by,

$$\eta_{ud} = \frac{\mathcal{P}_b + \mathcal{P}_a}{\dot{m}} \quad (12)$$

corresponding to the "0 %" curve in Fig. 7.

The average neutral atom density without beam extraction calculated using Eqs. (10) - (12) is compared in Fig. 7 to the neutral density with beam extraction calculated from Eq. (9). It is seen that the neutral atom densities with beam extraction fall between the two limiting cases assumed to calculate the neutral density without beam extraction. This indicates that some fraction of the ions which strike the accelerator grid return to the discharge chamber as neutral atoms, but that this fraction is less than one. Reasonably good agreement can be obtained for the neutral atom density variation with discharge power without beam extraction, by assuming that only 45 % of the ions striking the accelerator grid re-enter the discharge chamber as neutral atoms (as indicated in Fig. 8); the other 55 % leave the thruster as neutrals. In making these calculations, an active grid area of  $6.38 \times 10^{-2} \text{ m}^2$ , an accelerator system transparency to neutral atoms of 0.2, and a neutral xenon atom velocity of 311 m/s were used.

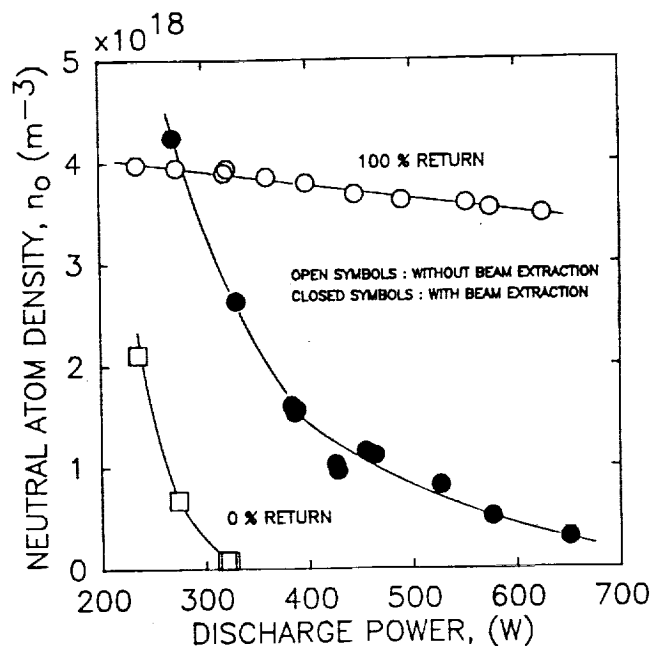


Figure 7 Comparison of calculated neutral atom densities with and without beam extraction. The indicated % return refer to the assumed behavior of the ions striking the accelerator grid.

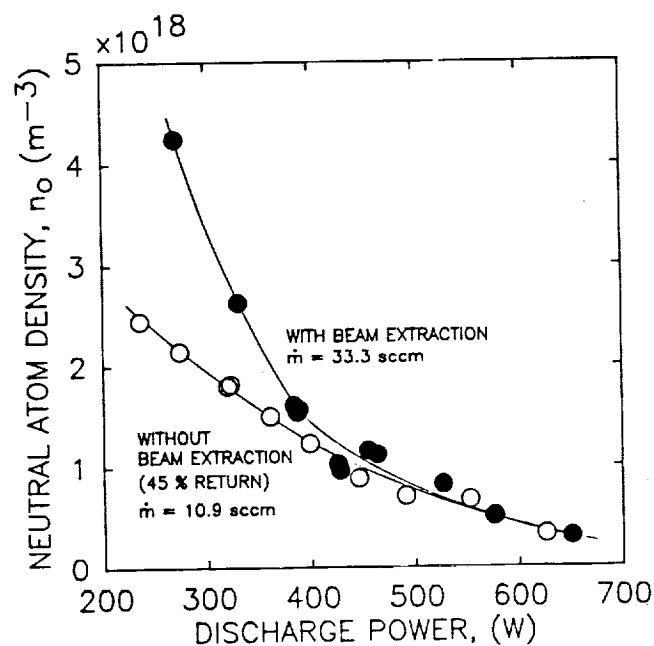


Figure 8 Comparison of calculated neutral atom densities with and without beam extraction assuming 45 % of the ion striking the accelerator grid without beam extraction return to the discharge chamber as neutral atoms.

## Simulated Performance Curve

If 55 % of the ions which strike the accelerator grid, without beam extraction, immediately leave the discharge chamber as neutral atoms, then this effectively increases the accelerator system transparency to ions for the following reason. Ions which strike the accelerator grid when operating without beam extraction, leave the discharge chamber at the Bohm velocity. Those ions which become neutralized at the accelerator grid surface and immediately leave the thruster have essentially left the discharge chamber at the Bohm velocity, not at the neutral atom thermal velocity. Thus, even though they technically did not pass through the accelerator system as ions, for the purposes of computing the average neutral density in the discharge chamber they must be treated as if they did. That is, the effective accelerator system transparency to ions without beam extraction, which is required as an input to Eq. (8), must be computed as

$$\phi_i = \frac{0.55 \mathcal{J}_a + \mathcal{J}_b}{\mathcal{J}_a + \mathcal{J}_a + \mathcal{J}_b} \quad (13)$$

The results using Eq. (13) to calculate the effective ion transparency without beam extraction are given in Fig. 9

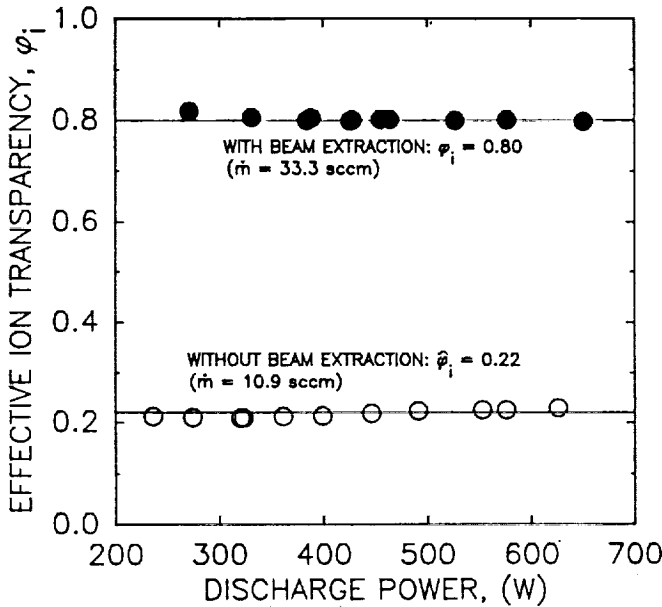


Figure 9 Effective accelerator system transparency to ions with and without beam extraction.

as a function of discharge power, at a total flow rate of 10.9 sccm. For comparison, the effective ion transparency with beam extraction is also given in this figure over the same discharge power range.

Discharge chamber performance data obtained without beam extraction may now be used to determine the discharge chamber performance curve with beam

extraction. To do this it is first assumed that the beam current with beam extraction may be calculated from the total ion current to the grid plane measured without beam extraction, times the ion transparency with beam extraction, i.e.,

$$(\mathcal{J}_b)_{\text{simulated}} = \phi_i \mathcal{J}_g \quad (14)$$

Using Eq. (14), Eq. (8) may be rearranged to yield an expression which enables a simulated propellant efficiency to be calculated based on the propellant flow rate and the total ion flux to the accelerator system measured without beam extraction,

$$(\eta_{ud})_{\text{simulated}} = \frac{\phi_i \mathcal{J}_g}{\dot{m} + \phi_i \mathcal{J}_g \left(1 - \frac{\phi_i}{\phi_i}\right)} \quad (15)$$

where the total flow rate without beam extraction is in units of equivalent amperes. To complete the performance curve, the simulated beam ion energy cost is calculated from

$$(e_B)_{\text{simulated}} = \frac{(\mathcal{J}_a - \phi_i \mathcal{J}_g) \mathcal{V}_d + \mathcal{J}_k \mathcal{V}_k}{\phi_i \mathcal{J}_g} \quad (16)$$

Equations (15) and (16) allow discharge chamber performance data measured without beam extraction to be transformed into a performance curve which simulates the performance of the discharge chamber under beam extraction conditions. To use these equations, a good estimation of the accelerator system transparency to ions with beam extraction is required. Comparison of a real performance curve taken with beam extraction is compared to a simulated performance curve generated using Eqs. (15) and (16) with data obtained without beam extraction in Fig. 10. The performance curve with beam extraction was generated by fixing the main and cathode flow rates while adjusting the discharge current to change the discharge power. Thus, both the discharge voltage and the beam current vary from point to point on this performance curve. Without beam extraction, the cathode flow rate was kept at the same value as for with beam extraction, and the main flow rate was reduced until the total flow rate was 10.9 sccm. These flows were then held constant while the discharge current was varied. The agreement between the real and simulated performance curves is seen to be excellent. In generating the simulated performance curve the grid transparency data from Fig. 9 were used in Eqs. (15) and (16).

## Electron Temperature

In the derivation of Eq. (8), the average electron temperature in the discharge chamber was assumed to be

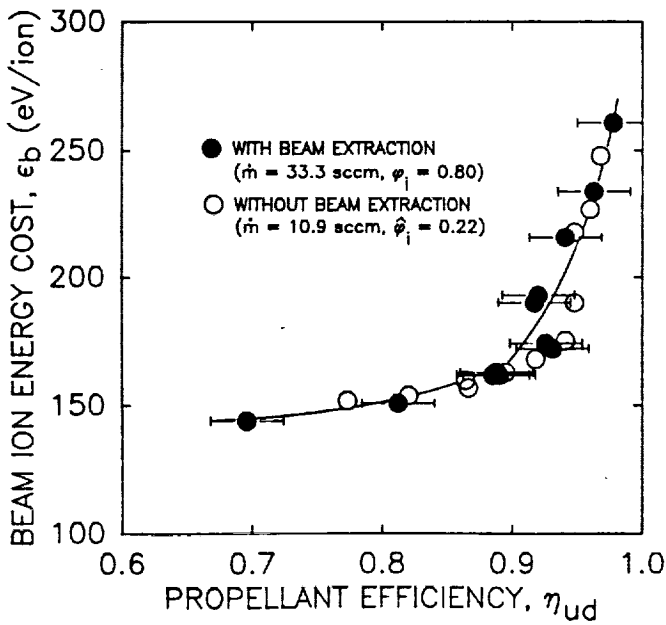


**Figure 10** Comparison of simulated performance curve determined without beam extraction to the actual performance curve obtained with beam extraction.

the same with and without beam extraction. Reference 8 gives an algebraic expression for the average electron temperature expressed in terms of the Maxwellian electron ionization rate factor, and is reproduced here as Eq. (17).

$$Q_o^* = \frac{v_p \sigma_o' \left( \frac{v_p \sigma_o'}{e_p^* \sigma_o'} - 1 \right)}{\left( \frac{v_p v_p \sigma_o' \bar{v}}{0.15 \sigma_e v_p v_p A_p^2 \phi_o \phi_i} \right) \dot{m} (1 - \eta_{ud}) - 1} \quad (17)$$

Substituting appropriate parameter values into this equation, and using Eq. (9) together with the definition of the Bohm velocity, results in the following expression:

$$Q_o^* = \frac{1.08 \times 10^{-13}}{2.08 \times 10^{-17} \frac{n_o}{\phi_i \sqrt{T_e}} - 1} \quad (18)$$

where the total inelastic collision cross section data required in Eq. (17) was obtained from Ref. 12.

The Maxwellian electron rate factor is a function of the electron temperature and the species being ionized. Equation (18) may be used to determine the average electron temperature using the data from Ref. 13 to relate the rate factor to the electron temperature for xenon. Inspection of this equation, however, reveals that if the neutral atom density is held constant, and the grid transparency to ions decreases, then the average electron

temperature must decrease. This indicates that it is impossible to simultaneously match the neutral atom density and the electron temperature with and without beam extraction due to the change in the accelerator system transparency to ions. This is illustrated in Fig. 11, where the calculated electron temperatures with and without beam extraction are given over a range of discharge powers.

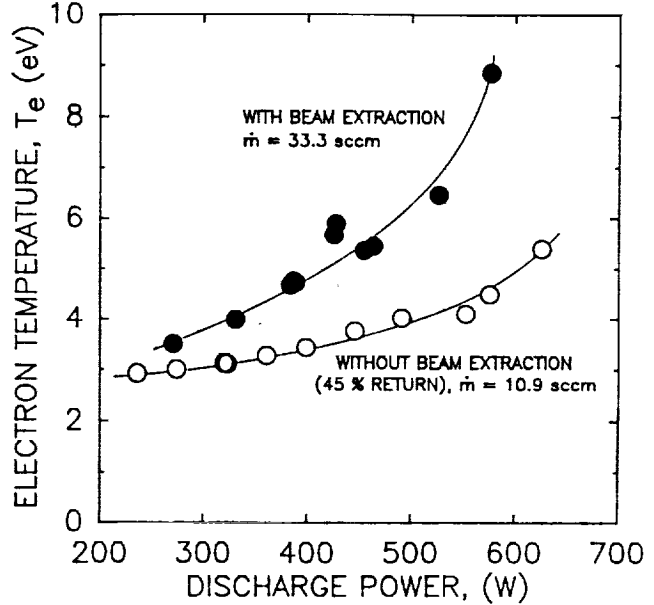


**Figure 11** Comparison of calculated average electron temperatures with and without beam extraction.

The electron temperatures in Fig. 11 were calculated based on the neutral atom density variation with discharge power given in Fig. 8, and the effective accelerator system transparency data in Fig. 9. To calculate the electron temperature, the Maxwellian ionization rate factor versus electron temperature data from Ref. 13 was curve fit over the range 0 to 10 eV, resulting in the following expression,

$$Q_o^* = 10^x \quad (19)$$

where,  $x = A_0 + A_1 T_e + A_2 T_e^2 + A_3 T_e^3 + A_4 T_e^4$

$A_0 = -19.655$  ,  $A_2 = 4.8122 \times 10^{-1}$

$A_1 = 2.6363$  ,  $A_3 = 4.1843 \times 10^{-2}$

$A_4 = -1.3863 \times 10^{-3}$

Equations (18) and (19) were then solved simultaneously for the electron temperature, using the appropriate values of the neutral atom density and the grid ion transparency, to produce the results shown in Fig. 11. These calculations should be used only to indicate that the electron temperature is different with and without beam extraction. The true average electron temperatures will probably be less than those indicated as Ref. 14 showed

that Eq. (17) over-estimates the electron temperature at high discharge powers.

### Ion Density

The total ion current to the grid plane depends on the average ion density and the electron temperature, i.e.,

$$J_g = 0.6 e A_g n_i \sqrt{\frac{e T_e}{M_i}} \quad (20)$$

As shown above, the electron temperature without beam extraction must be less than it is with beam extraction at the same neutral atom density. The data in Fig. 6, however, indicate that the total ion current to the grid plane is the same with and without beam extraction. This can only be possible if the average ion density is higher without beam extraction than it is with beam extraction, so that the product of the ion density and the square root of the electron temperature is constant.

### Revised Similarity Conditions

The similarity conditions assumed in the derivation of Eq. (8), namely Eqs. (3) and (4), have been shown to be impossible to satisfy simultaneously. However, if these similarity conditions are replaced with the following conditions,

$$n_o = n_o, \quad n_i \sqrt{T_e} = n_i \sqrt{T_e}, \quad (21)$$

then Eq. (8) may be re-derived with no changes in the final form of the equation. The validity of the new similarity conditions depends on the experimentally determined observation that the ion current to the grid plane is the same with and without beam extraction, provided the neutral density is the same.

### Screen Grid Temperature

Measurements of screen grid temperatures were made with and without beam extraction as a function of discharge power. The thermocouples attached to the accelerator grid, however, did not withstand the high voltage environment long enough to obtain useful data. The radial temperature profile across the screen grid is given in Fig. 12 for three different operating conditions: with beam extraction at a propellant flow rate of 33.3 sccm, without beam extraction at 29.1 sccm, and without beam extraction at 10.9 sccm. These data were all taken at a discharge power of 450 W, and with the screen grid at cathode potential.

Surprisingly enough, the maximum screen grid temperature does not occur on the centerline of the grids with beam extraction. Without beam extraction the maximum does occur on the centerline. This effect appears to be real, as the data were repeated several

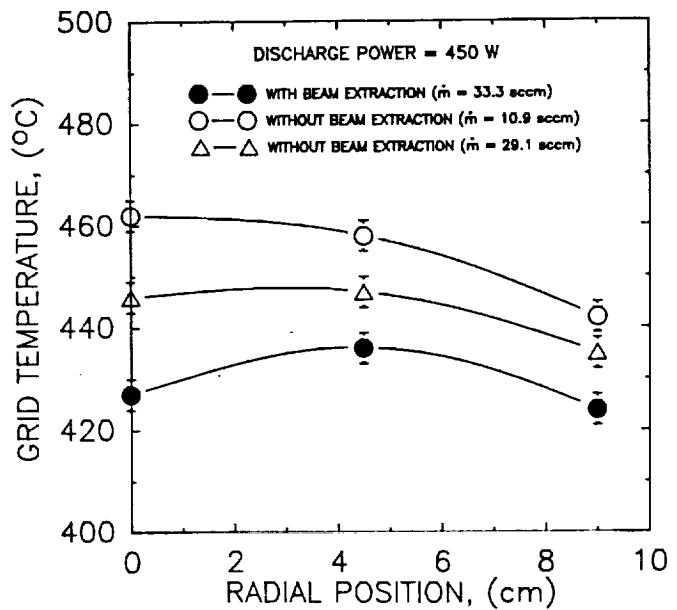


Figure 12 Comparison of screen grid temperature with and without beam extraction at a discharge power of 450 W.

times. In addition, the screen grid temperatures are significantly lower with beam extraction than without. The lower temperatures are most likely a result of the increased screen grid transparency with beam extraction. This increased transparency reduces the energy deposited on the grid by ions from the plasma. The difference in radial temperature profiles with and without beam extraction are substantial enough that it may necessary to account for this difference when modeling the thermal/mechanical behavior of ion accelerator systems.

### Conclusions

A simple model was developed which describes the reduction in propellant flow rate required to simulate beam extraction operating conditions in a ion thruster discharge chamber operating without beam extraction. According to this model, to simulate beam extraction, it is necessary to match the discharge chamber average neutral atom density with and without beam extraction. In addition, the product of the average ion density and the square root of the average electron temperature must be constant. These conditions may be met by merely reducing the total flow rate to the appropriate value to account for the reduced accelerator system transparency to ions without beam extraction.

For the J-Series ion thruster accelerator system, it was experimentally determined that the transparency to ions without beam extraction was 0.22, and that with beam extraction this transparency was 0.80 (for operation at a total voltage of 1430 V, and approximately a 2.0 A beam). The value ion transparency without beam

extraction (0.22) was calculated by first determining that 55 % of the ions recombining on the accelerator grid do not return to the discharge chamber. This determination was made to match calculated neutral atom densities with and without beam extraction. Simulated performance curves obtained from operation without beam extraction agree very well with actual performance curves.

Screen grid temperatures measured with and without beam extraction indicate significantly higher temperatures and a different radial temperature profile without beam extraction. The higher temperatures are believed to result from the added thermal loading due to the increased ion flux to the grid surfaces without beam extraction.

### Acknowledgements

The work described in this paper was carried out by the Jet Propulsion Laboratory, California Institute of Technology, under contract with the National Aeronautics and Space Administration. "Approved for public release; distribution unlimited."

### References

1. Brophy, J. R., and Barnett, J. W., "Benefits of Electric Propulsion for the Space Exploration Initiative," invited paper for the 21st Joint Propulsion Conference, July 1990.
2. Palaszewski, B., Brophy, J. R. and King, D. Q., "Nuclear-Electric Propulsion -- Manned Mars Propulsion Options," AAS Paper 87-260, In the case for Mars III: Strategies for exploration -- Technical, pp 431-451, 1989.
3. Galecki, D. L. and Patterson, M. J., "Nuclear Powered Mars Cargo Transport Mission Utilizing Advanced Ion Propulsion," NASA TM 100109, July 1987.
4. Stuhlinger, E., *Ion Propulsion for Space Flight*, McGraw-Hill, Inc., 1964.
5. Sovey, J. S., "Improved Ion Containment Using a Ring-Cusp Ion Thruster," NASA TM 82990, 1982.
6. Carpenter, R. T., Boardsen, S. A. and Daniels, S. W., "Plasma Characteristics of a 17-cm Diameter Line-Cusp Ion Thruster," AIAA Paper No. 82-1926, November 1982.
7. Aston, G. and Deininger, W. D., "Test Bed Ion Engine Development," NASA CR-174623, March 1984.
8. Brophy, J. R., "Ion Thruster Performance Model," NASA CR-174810, December 1984.
9. Bechtel, R. T., "The 30 cm J-Series Mercury Bombardment Thruster," AIAA Paper No. 81-0714, April 1981.
10. Aston, G., Brophy, J. R., Garner, C. E., Pless, L. C., "A Xenon Ion Propulsion Module for Enhanced Spacecraft Capability," AIAA Paper No. 86-1393, June 1986.
11. Brophy, J. R. and Aston, "Thermal/Mechanical Analyses of Large Diameter Accelerator Systems," AIAA Paper No. 89-2718, July 1989.
12. Hayashi, M., "Determinization of Electron-Xenon Total Excitation Cross Sections, from Threshold to 100 eV, from Experimental Values of Townsend's Alpha," Journal of Physics D: Applied Physics, Vol. 16, pp. 581-589, 1983.
13. Rapp, D. and Englander-Golden, P. "Total Cross Sections for Ionization and Attachment in Gases by Electron Impact. I. Positive Ionization," Journal of Chemical Physics, Vol. 34, No. 5, pp. 1464-1479, 1965.
14. Matossian, J. N. and Beattie, J. R., "Plasma Properties in Electron Bombardment Ion Thrusters," AIAA Paper No. 87-1076, May 1987.

**AIAA 90-2650**  
**An Optical Technique To Measure**  
**Ion Engine Grid Distortion Due To**  
**Thermal Expansion**

V.J. Trava-Airoldi, C. E. Garner,  
T.J. Pivrotto, and J.R. Brophy,  
Jet Propulsion Laboratory,  
Pasadena CA

# AN OPTICAL TECHNIQUE TO MEASURE ION ENGINE GRID DISTORTION DUE TO DIFFERENTIAL THERMAL EXPANSION

V.J. Trava-Airoldi\*, C.E. Garner\*\*, T.J. Pivrotto\*\*, and J. R. Brophy\*\*

*Jet Propulsion Laboratory  
California Institute of Technology  
Pasadena, Ca*

## Abstract

An optical technique to measure small differential grid displacements due to thermal expansion of an ion thruster accelerator system has been developed. Emphasis was placed on an optical technique because of the wide variety of applications, simple operation and easy set-up. There is a great deal of interest in making measurements of small displacements with the purpose of applying them to robotic position-sensing in machine vision systems and also to measure the shape and size of machined parts with a noncontacting sensor. For this work, several techniques were investigated, including interferometric techniques, however, a new, recently developed optical technique based on type II microscope measurement techniques, was selected. Experiments were performed to demonstrate the applicability of this technique for measuring small displacements of ion engine screen and accelerator grids at a distance of several meters. Several different optical components were tested for their ability to discern displacements of a 30-cm diameter, two-grid ion accelerator system which was separated from the thruster body and mounted outside of the vacuum system. Differential thermal expansion of the grids was induced through the use of a 500 W heat lamp placed adjacent to the screen grid. An analysis of these experimental results and a suggestion for future experiments to be performed with the grids inside the vacuum chamber are also presented.

\* Visiting scientist from Instituto de Pesquisas Espaciais, Sao Jose dos Campos, also supported by Conselho de Desenvolvimento Científico e Tecnológico - Brazil.

\*\* Member Technical Staff, Electric Propulsion and Plasma Technology Group. Member AIAA.

## Introduction

The necessity of increasing ion engine diameter in order to increase the engine thrust may aggravate the problem of thermally-induced grid gap changes, degrading accelerator system performance for large diameter thrusters. Measurements of thermally induced grid displacements will facilitate development of accurate modeling of the grid thermal/mechanical behavior. These models may then be used to develop accelerator system designs which avoid undesirable thermal/mechanical behavior. Finite element models of 30 and 50 cm diameter accelerator systems have been performed<sup>1-3</sup>, but there is a distinct lack of experimentally measured grid displacement data taken during actual beam extraction tests with which the validity of these models can be assessed. The most successful grid displacements measurements performed to date are those described in Ref. 3, where the structural and thermal response of a 30 cm diameter ion thruster accelerator system were studied using an intrusive technique without beam extraction. Obtaining grid displacement information during thruster operation with beam extraction may best be performed using optical techniques.

The severe test environment in which the grid displacement measurements must be made, including a bright plasma, rough grid surfaces and small view factor to the inner grid, and the long distances over which the measurement must be made, places difficult requirements on the optical technique which must make the measurements. With these requirements in mind, several optical techniques were studied, including optical interferometry,<sup>4,5</sup> differential confocal optical range,<sup>6</sup> confocal optical microscope techniques (type I and type II),<sup>7</sup> as well as an alternative optical technique described in Ref. 7. These differing techniques were evaluated on both technical and cost considerations, and the availability of

optical components. As a result of these evaluations, the confocal scanning optical microscope type II (CSOM) was selected as the most appropriate technique for a feasibility demonstration.

The type II confocal optical microscope has been the subject of intense recent studies for making film-thickness and profile measurements using its shallow depth of field properties. In addition, this technique has been suggested for robotic applications for determining the quality of machined surfaces,<sup>9</sup> as well as for making small distance and displacement measurements using short focal lengths with sample position scanning, as described in Refs. 5 and 6. Distances of up to 15 cm between the lens plane and the sample have been used.

In this work, the same concept of the type II confocal scanning optical microscope technique is used. For measuring small displacements where there is a substantially greater distance between the lens plane and the sample, instead of scanning the sample, some of the optical components are moved while the sample is kept fixed. In this case, where long distances on the order of a meter or more are required and with the necessity of moving the optical components, alignment is critical.

### Basic Theoretical Concept

The principal objective of this technique is to get information about the geometrical shape of a light spot focused by a precision lens. A mirror is placed in the beam waist region and its position is scanned through the beam waist depth. The light reflected from the mirror passes through a pinhole, which serves as a spatial filter, and is detected by coherent detector, as indicated Fig. 1.

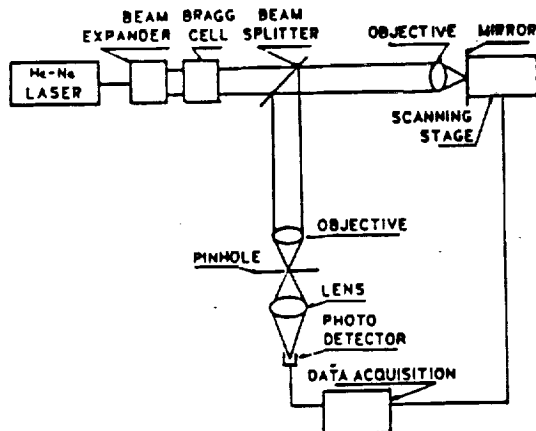


Figure 1. Experimental set-up for the CSOM technique.

In this figure, the beam expander is used to produce a parallel laser beam, the beam splitter is used to separate the incident and reflected light, and the Bragg Cell Chopper is used to provide AC signal detection. The intensity of light reflected from the mirror depends on its position.

The amplitude of reflected light that reaches the detector has been calculated theoretically by K. Liang, et. al.,<sup>10</sup> for an acoustic microscope, and a nonparaxial form of the vector field theory has been derived in Ref. 7. These theories are briefly summarized below.

Assuming a lens with a pupil function  $P(\theta)$ , where  $\theta$  is the angle between a ray from the lens plane to the focal point and the lens axis. The transversal electric field associated with a plane wave focused by the lens depends on the distance ( $z$ ) on the axis, and is given by:

$$E(z) = \int_0^{\theta_0} \frac{(1 + \cos\theta) \sin\theta}{(\cos\theta)^{1/2}} \exp(ikz \cos\theta) P(\theta) d\theta \quad (1)$$

where  $K$  is the wave number, and  $\sin\theta$  is the numerical aperture of the lens. In this equation, the term  $(\cos\theta)^{1/2}$  appears in the denominator as it does in the theory of Richard and Wolf<sup>11</sup> so that power is conserved at the exit plane of the lens. The amplitude and the phase of the plane wave components of the electric field at an angle is exactly the integrand of the Eq. (1). When the light is reflected from the mirror, with reflectivity  $R(\theta)$ , the beam waist image is refocused on the pinhole, and the correspondent field is given by:

$$V(z) = \int_0^{\theta_0} \frac{(1 + \cos\theta) \sin\theta}{(\cos\theta)^{1/2}} \exp(2ikz \cos\theta) P(\theta) R(\theta) d\theta \quad (2)$$

The same simplification used in Ref. 9 is valid in this case, where a large distance between the lens and the sample is used. An approximate form can be given for Eq. (2), so that the observable intensity as outlined in Ref. 10 can be given by:

$$|V(z)|^2 = \left| \frac{\sin Kz(1 - \cos\theta_0)}{Kz(1 - \cos\theta_0)} \right|^2 \quad (3)$$

where it was assumed that  $P(\theta) = 1$  for  $\theta < \theta_0$ , the light is uniformly distributed on the lens surface,  $Ka \gg 1$  (where "a" is the lens ratio), and  $(1 + \cos \theta)/(\cos \theta)^{0.5} = 2$ . Equation (3) provides the shape of a symmetric beam waist with very good accuracy. The depth of the beam waist at the 3-Db point is given by:

$$(\Delta Z)_{3dB} = \frac{0.443}{1 - \cos \theta_0} \quad (4)$$

This equation shows that it is possible to apply this technique using a large lens, and there is no restriction limiting the distance between the lens and the sample, if all the necessary conditions are satisfied. However, in practice, the lens spherical aberrations can increase with the lens diameter, and consequently limit the numerical aperture of the lens. In addition, because of the large lens-sample separation distance, the alignment of the reflected light through the pinhole becomes more critical.

### Experiments

An initial set of experiments was performed using the test set-up indicated in Fig. 2. It should be noted that instead of scanning the mirror through the lens focal plane position, as in Fig. 1, the set of lens and objective-pinhole were moved producing a scanning of the lens focal plane on the fixed mirror position. These experiments were designed to test different optical components, as well as to test the feasibility of this particular configuration. Several kinds of lenses were tested in order to get the best response (i.e. best agreement with the theoretical predictions). Comparison between data obtained using a common plano-convex lens (less aberration), a lens for a high power laser, a camera lens, an achromatic precision lens, and theory is shown in the Fig. 3. It is observed that response for the common lens is more asymmetric than the other lenses and is also

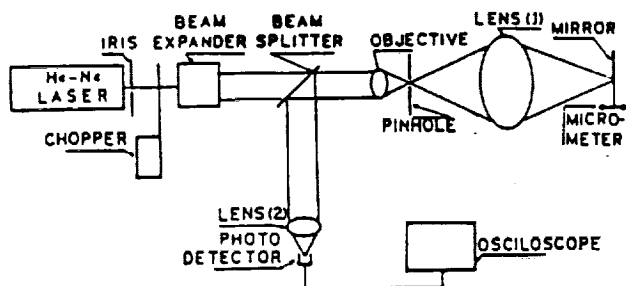


Figure 2. Experimental set-up to test movement of the optical components.

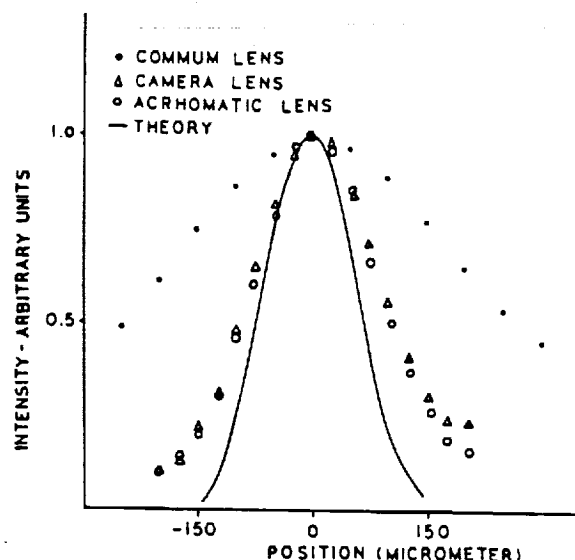


Figure 3. Comparison of the optical response of several kinds of lenses to theoretical predictions.

the widest. This suggests that the beam waist at the focal plane does not have the desired shape; probably as a result of accentuated aberrations. However, for both the camera lens and the achromatic precision lens the response of the beam waist shape is close to the theory. The distance between the lens and the reflective mirror, as well as the laser beam diameter at the lens, was the same for each lens. A lens-mirror separation distance of 302 mm and a laser beam diameter on the lens of 38 mm were used. This provided a lens numerical aperture of 0.0596 in each case.

Using these results, the new experimental set-up shown in Fig. 4 was implemented in order to optically measure the thermally induced grid displacements of a set of 30 cm diameter, 900-series grids. The basic differences between the set-up in Fig. 2 and that in Fig. 4 are the two additional mirrors inserted after the lens, and that the reflective mirror was replaced by the screen and accelerator grids of the ion thruster accelerator system. The two additional mirrors enabled the focused laser beam to be precisely positioned on the grids. In order to get a sufficiently reflective surface, a very small, thin mirror of silicon was attached to the surface of each grid using a ceramic glue. Silicon mirrors were selected based on their tolerance of elevated temperatures and high

reflectivity at these temperatures. The ceramic glue was used to minimize thermal expansion effects.

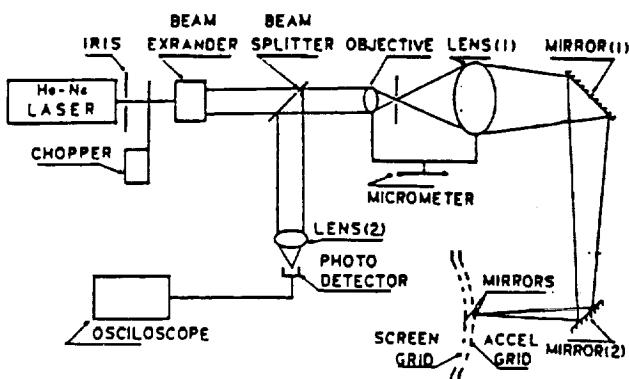


Figure 4. Experimental set-up to measure ion engine grid displacement.

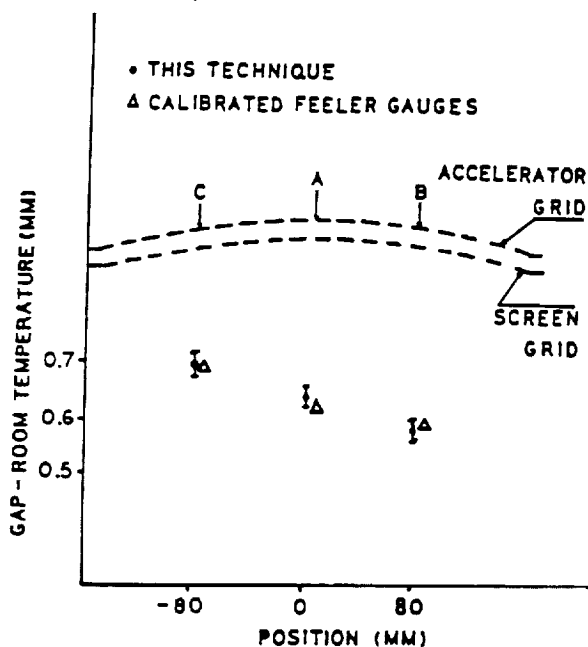


Figure 5. Gap between the screen and accelerator grids at room temperature.

For these experiments, a precision achromatic lens was used, and the results obtained with the grids at room temperature are shown in the Fig. 5. Three different locations were selected at which to measure the

screen-to-accelerator grid separation; one in the center and two others distanced about 80 mm from the center. Measurements of the grid-to-grid separation using this technique agreed well with measurements made using calibrated feeler gauges.

The error bars shown in the Fig. 5 indicate limits on the resolution of this technique, resulting from vibrations of the experimental set-up, as well as uncertainties introduced by the data reduction procedure. In addition, the resolution is limited by the poor shape of the beam waist image on the pinhole. The resolution could be improved by fast position scanning of the set of the lens and pinhole-objective, and by using a differential technique to find the maximum reflected light intensity. In addition, it was noted that the beam alignment is critical. To measure the gap between two grids, the laser beam spot was moved from the accelerator grid to the screen grid surface using only mirror (1). But, because the two silicon mirrors glued to the grid surfaces were not perfectly parallel, it was necessary to readjust the alignment using both mirrors (1) and (2).

An additional set of experiments was performed to determine if this technique can be used to discern thermally induced grid movements and the resulting change in the grid-to-grid separation. For these tests the experimental set-up given in Fig. 4 was used with the addition that a heat gun and a 500 W heat lamp were alternately used to heat the grids. The use of the heat lamp resulted in more azimuthally symmetric heating of the grids than could be obtained with the heat gun and was therefore used for the grid deflection tests. Asymmetric grid heating results in misalignment of the reflected laser light resulting from deflections of grids surfaces, as shown in Fig. 6. The misalignment was smaller for lamp heating.

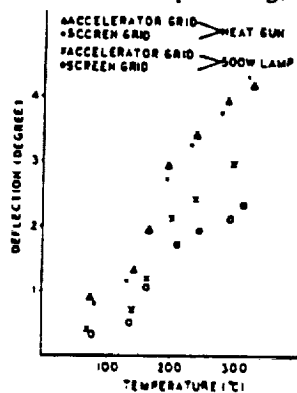


Figure 6. Screen and accelerator grid deflection as a function of grid temperature.

and the use of the lamp did not affect the ability to find the maximum intensity of the reflected laser light. The radial temperature profile on grid surfaces using the high power lamp heating is shown in Fig. 7. The lamp was positioned on the centerline of the accelerator system facing the screen grid. The small size of the lamp resulted in a radial temperature gradient on both grids. In addition, the accelerator grid temperature was significantly lower than the that of the screen grid.

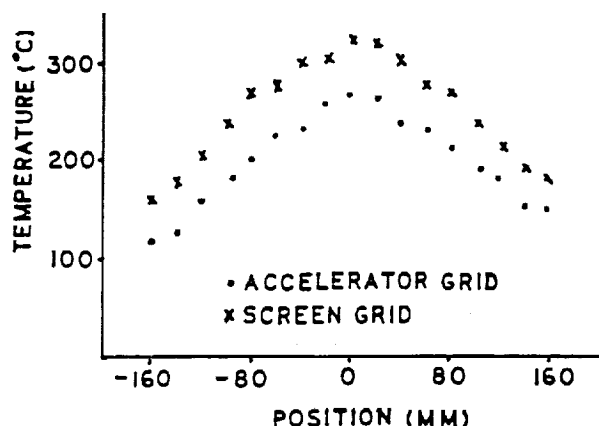


Figure 7. Spatial temperature distribution on the grid surfaces in the equilibrium condition.

Displacement measurements of both grids, and the corresponding grid-to-grid gaps were measured as functions of the grid temperatures. The measured displacements of accelerator and screen grids for the three selected grid locations, and the corresponding grid gaps are given in Fig. 8. Spatially non-uniform displacements versus temperature are clearly evident in these data. In addition, it is noted that after cooling down the grids did not return to their original positions, where a difference of between approximately 20 and 70 microns was observed.

A significant feature of this technique is that it enables the dynamic behavior of the grids to be measured. The time dependence of the displacements for both grids were evaluated, and are given in Fig. 9. The displacement velocity for screen grid is noted to be faster than for accelerator grid, probably because the heating on the screen grid surface is faster than on the accelerator grid surface.

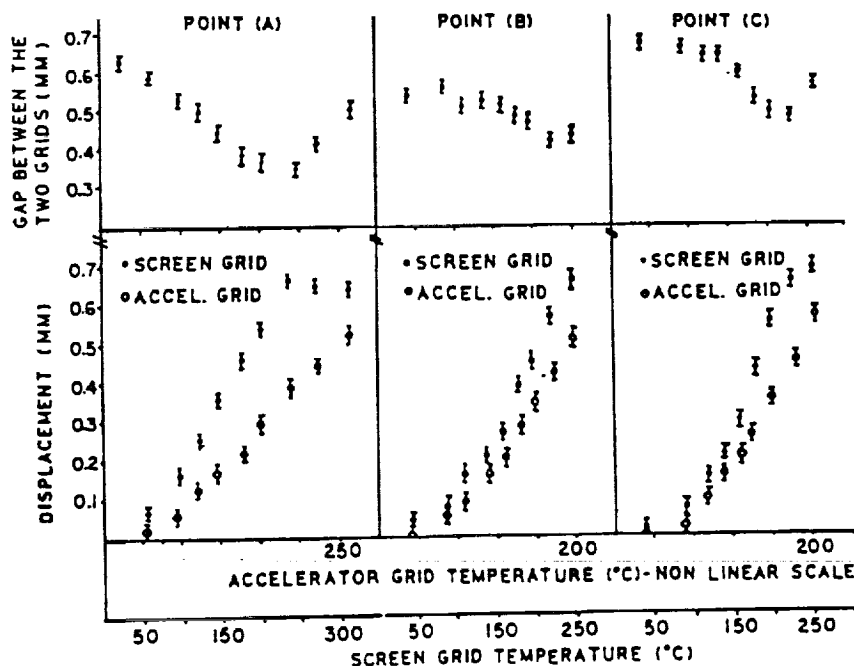


Figure 8. Absolute and relative displacement of the screen and accelerator grids as a function of temperature.

and by Conselho de Desenvolvimento Científico e Tecnológico - Brazil.

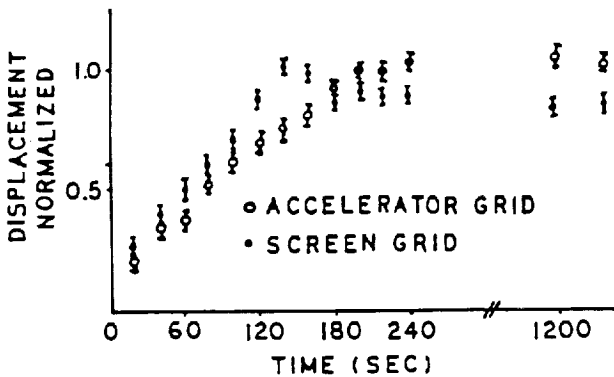


Figure 9. Time dependence of the accelerator and screen grid displacement.

### Conclusions

The feasibility of applying the optical technique described in this paper to measure thermally induced ion thruster grid displacements has been demonstrated in a bench-top simulation. In addition, the dynamic capability of the technique can provide information regarding grid movement resulting from thermal transients such as start-up. The most difficult obstacle to the application of this technique concerns the availability of a precision lens to focus the laser beam on the grids. Application of this technique in a large vacuum chamber where long distances between the lens and the ion engine grids (on the order of meters) are unavoidable, (and assuming a numerical aperture of 0.0596) requires a precision lens with a diameter of 238 mm. In addition, vibrations and asymmetric grid deflections limit the resolution of this technique. To accurately access the effects of vibrations, it is necessary evaluate the technique "in situ." Tests performed to date, however, suggest that this technique can be made to work on an actual ion engine operating with beam extraction.

### Acknowledgements

The work described in this paper was carried out by the Jet Propulsion Laboratory, California Institute of Technology, under contract with the National Aeronautics and Space Administration, and was supported in-part by the Instituto de Pesquisas Espaciais, Sao Jose dos Campos

### References

1. Poeschel, R. L. and Beattie, J. R., "Primary Electric Propulsion Technology Study," NASA CR-159688, November 1979.
2. Brophy, J. R. and Aston, G., "Thermal/Mechanical Analysis of Large Diameter Ion Accelerator Systems," AIAA Paper No. 89-2718, July 1989.
3. MacRae, G., Zavesky, R., and Gooder, S., "Structural and Thermal Response of 30 cm Diameter Ion Thruster Optics," AIAA Paper No. 89-2719 July 1989.
4. Williams, C. C. and Wickramasinghe, H. K., *J. Applied Physics*, Vol. 60(6), pp. 1900 (1986).
5. Rastogi, P. K., Pflug, L. and Delez, R., *Applied Optics*, Vol. 28(7), pp. 1378 (1989).
6. Corle, T. R., Fanton, J. T., and Kino, G. S., *Applied Optics*, Vol. 26(12), pp. 2416 (1987).
7. Corle, T. R., Chou, C. H., and Kino, G. S., *Optics Letters*, Vol. 12(12), pp. 770 (1986).
8. Trava-Airoldi, V. J. and Pivrotto, T. J., to be published.
9. Liang, K. K., Kino, G. S. and Khuri-Yakub, B. T., *IEEE Transaction on Sonics and Ultrasonics*, Vol. SU-32(2), pp. 213 (1985).
10. Cox, I. J., Hamilton, D. K. and Sheppard, C. J. R., *Applied Physics Letters*, Vol. 41, pp. 604 (1981).
11. Richard, B. and Wolf, E., *Proc. R. Soc. London Sr. A256*, pp. 358(1959).

### 13.5 Appendix E: Charge-Exchange Plasma Model

A simple one-dimensional (axial) mathematical model of the charge-exchange plasma in the ion thruster beam is described below. This model has been briefly presented in other references<sup>E1,E2</sup> and is presented in detail here for completeness. The distribution of the charge-exchange ions along the thruster axis is calculated based on the thruster geometry and operating conditions. This distribution is then used as the source of the charge-exchange ions for the propagation model.

The charge-exchange ions are created when a high energy ion from the thruster interacts with a low energy neutral resulting in a high energy neutral and a low energy ion. This low energy ion is referred to as the charge-exchange ion. The local charge exchange generation rate is given by

$$\dot{n}_{CE} = n_o n_i g_{io} \sigma_{CE} . \quad (E1)$$

Since the ion velocity,  $v_i$ , is much larger than the neutral velocity, the relative velocity may be approximated by the ion velocity.

The ion current is assumed to be constant and concentrated on the thruster axis in order to provide a closed form solution. The ion current will actually have a radial distribution. Since the neutral number density is largest on the centerline, this assumption will result in a larger number of charge exchange ions than are actually present. The ion current density,  $J_b$ , is given by

$$J_b = \pi r_b^2 e n_i v_i . \quad (E2)$$

The neutral atoms are considered as a free molecular flow escaping through an orifice with an area equal to the beam area. These neutrals are assumed to have a Maxwellian velocity distribution. The flow rate of the neutrals through the orifice is given by<sup>E3</sup>

$$\dot{N}_o = \frac{1}{4} n_{ref} V_o = \frac{1}{4} n_{ref} \sqrt{\frac{8kT_o}{\pi m_o}} . \quad (E3)$$

Only neutral atoms with velocities capable of reaching the point of interest along the axis are considered for calculating the local number density. That is, only neutrals that may be viewed through the orifice from point P may reach point P, and therefore contribute to the density (see Fig. E1). The density at point P is given by

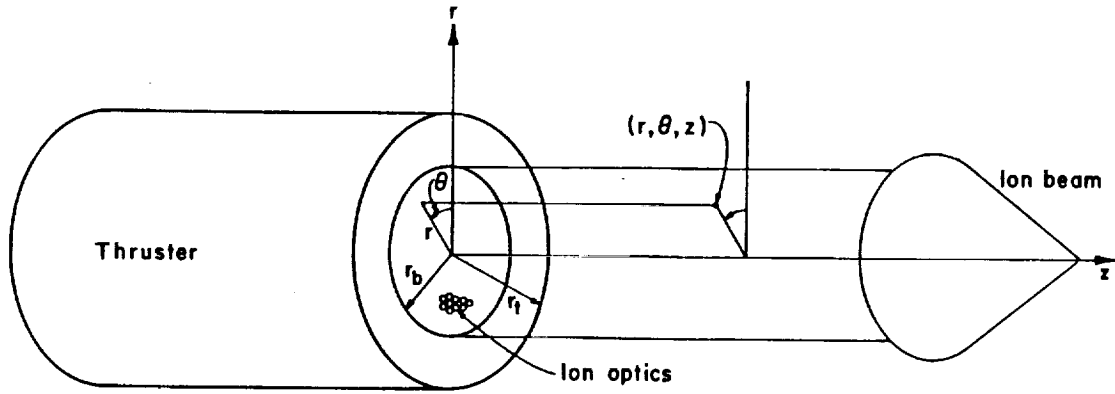


**Figure E1** Model geometry for calculation of neutral atom density (from Ref. 2).

$$n = n_{ref} \int_0^{\infty} f_v dv . \quad (E4)$$

where  $f_v$  is the Maxwell-Boltzmann velocity distribution,

$$f_v = \left( \frac{m_o}{2\pi kT_o} \right)^{3/2} v^2 \exp \left( \frac{-m_o v^2}{2kT_o} \right) . \quad (E5)$$

Integrating over the range of interest, the local number density is determined by

$$n_0 = n_{ref} \int_0^{\infty} \int_0^{\theta_1} \int_0^{2\pi} \left( \frac{m_o}{2\pi kT_o} \right)^{3/2} v^2 \exp \left( \frac{-m_o v^2}{2kT_o} \right) \sin\theta d\phi d\theta dv , \quad (E6)$$

which yields

$$n_0 = \frac{n_{ref}}{2} (1 - \cos\theta_1) , \quad (E7)$$

where

$$\cos\theta_1 = \frac{z}{\sqrt{z^2 + r_b^2}} . \quad (E8)$$

(Note: at the thruster exit the number density equals  $n_{ref}/2$ .)

The propellant utilization is defined as the ratio of the total flux of ions to the total flux of particles from the thruster,

$$\eta_u = \frac{\dot{N}_i}{\dot{N}_{tot}} = \frac{J_b/e}{\dot{N}_{tot}} . \quad (E9)$$

Note that the ratio of the total flux of neutrals to the total flux of particles is given by

$$\frac{\dot{N}_o}{\dot{N}_{tot}} = 1 - \eta_u . \quad (E10)$$

Equation (E1) can be transformed, using Eqs. (E2), (E3), and (E6)-(E10), into

$$\dot{n}_{CE} = \frac{2J_b^2\sigma_{CE}(1 - \eta_u)}{\pi^2 e^2 r_b^4 v_o \eta_u} \left( 1 - \frac{z}{\sqrt{z^2 + r_b^2}} \right) . \quad (E11)$$

The total number of charge-exchange ions created is determined by integrating the local generation rate, Eq. (E11), along the axis as follows:

$$\dot{N}_{CE} = \pi r_b^2 \int_0^\infty \dot{n}_{CE} dz \approx \frac{2J_b^2\sigma_{CE}(1 - \eta_u)}{\pi e^2 r_b v_o \eta_u} . \quad (E12)$$

Since the ion current is assumed to be constant, Eq. (E12) is equivalent to:

$$\dot{N}_{CE} = \frac{J_b\sigma_{CE}}{e} \int_0^\infty n_o(z) dz = \frac{J_b\sigma_{CE} n_{ref} r_b}{2e} . \quad (E13)$$

For the charge-exchange ion propagation model, the z-axis is divided into N number of cells. The path of an ion originating in the center of each cell is traced (see Fig. E1). The distribution is established such that an equal number of charge-exchange ions are contained in each cell ( $n_{CE} = N_{CE} / N$ ). Since the local generation rate of the charge-exchange ions decreases with increasing distance from the thruster, the lengths of the cells

will correspondingly increase. A constant cross-section is assumed. Since the area under consideration is finite, the model assumes that 95 percent of the charge-exchange ions created fall within the model boundaries. Equation (E13) may be transformed into a summation of each of the regions:

$$\frac{1}{2} \sum_{i=0}^{2N} \int_{z_i}^{z_{i+1}} n_o(z) dz = N \int_{z_i}^{z_{i+1}} n_o(z) dz = \frac{0.95 n_{ref} r_b}{2} . \quad (E14)$$

Note that for N ion paths, 2N regions are used, as indicated in Fig. F1. This method is used so that each ion path will have same number of ions on each side. Integrating Eq. (E14) yields

$$\frac{0.95 n_{ref} r_b}{2N} = z_{i+1} - \sqrt{z_{i+1}^2 + r_b^2} - z_i + \sqrt{z_i^2 + r_b^2} . \quad (E15)$$

Starting at the end of the thruster,  $z_0$ , the remaining region boundaries are calculated from Eq. (E15) in the form

$$z_{i+1} = \frac{1}{2} \left[ \frac{0.95 n_{ref} r_b}{2N} + z_i - \sqrt{z_i^2 + r_b^2} - \frac{r_b^2}{\frac{0.95 n_{ref} r_b}{2N} + z_i - \sqrt{z_i^2 + r_b^2}} \right] \quad (E16)$$

The actual ion paths would be the odd number region boundaries.

The number density of the charge-exchange ions is given by

$$n_{CE} = \frac{\dot{N}_{CE}}{N} \frac{1}{2\pi x \Delta d_m v_{CE}} , \quad (E17)$$

where  $v_{CE}$  is the velocity of the charge-exchange ions,

$$v_{CE} = \sqrt{\frac{kT_e}{m_o}} . \quad (E18)$$

Finally, combining Eqs. (E12), (E17) and (E18) yields

$$n_{CE} = \frac{C}{x \Delta d_m \sqrt{T_e}} \quad (E19)$$

where

$$C = \frac{J_b^2 (1 - \eta_u) \sigma_{CE} m_o}{\pi^2 e^2 r_b \eta_u N \sqrt{T_e}} , \quad (E20)$$

which is reproduced as Eq. (8) in this report.

## REFERENCES

- E-1. Robinson, R. S., Deininger, W. D., Winder, D. R., and Kaufman, H. R., "PLASIM: A Computer Code for Simulating Charge Exchange Plasma Propagation," CSU Report 955322 JPL, Jan. 1982.
- E-2. Kaufman, H. R., "Charge Exchange Plasma Generated by an Ion Thruster," NASA CR-1348844, June 1975.
- E-3. Fay, C. E., Samual, A. L., and Shockley, W., "On the Theory of Space Charge Between Parallel Plane Electrodes," Bell System Technical Journal, 17, 1938, p. 76.

### 13.5 Appendix F: Cathode Life Test Software

The computer software for the cathode life test consists of approximately 4350 lines (about 70 pages) of code written in Turbo Pascal V5.5. The computer-controlled data acquisition system is used to monitor the cathode operation, record specified operating data, and shut down the cathode and the vacuum system should an error be detected. This system was designed to enable prolonged unattended operation of the cathode.

The data acquisition system includes an IBM PC XT compatible computer and data acquisition hardware supplied by the Opto 22 corporation. The data acquisition hardware updates the following data once each second:

1. Anode voltage
2. Anode current
3. Starter electrode voltage
4. Xenon flow rate
5. Internal cathode pressure
6. Anode temperature
7. Cathode flange temperature
8. Back plate temperature
9. Anode temperature
10. Vacuum tank pressure
11. Foreline pressure
12. Two cartridge tip heater temperatures
13. Temperatures of both diffusion pumps

The hardware averages "n" successive readings of each input channel together before sending the results to the host computer. The value of "n" is sent to the data acquisition hardware by the host computer and can be changed by the operator without interrupting the life test. Typically a value of  $n = 3$  is used. Averaging the data in this manner minimizes the likelihood that a noise induced error will cause the computer to shut down the test. Since the data acquisition hardware updates each input channel at the rate of approximately once each second, averaging three such readings together implies that new values for all input channels are sent to the computer at the rate of once every three seconds. The host computer polls the data acquisition hardware to determine when the averaging process has been completed for all channels. It then requests that the data be sent and initiates a new averaging cycle.

The host computer computes run-time, amp-hours, and total xenon consumed, and converts the input data from the data acquisition hardware to engineering units. This information is then displayed on the CRT, and is updated approximately once every "n" seconds. In addition, at operator specified time intervals the data is sent to a printer for hard copy data storage, and recorded on the computer's hard disk. In general, a time interval of 5

minutes was selected for the data storage. The system has two printers on-line, but only one printer is used at a time. If the primary printer fails the computer will automatically switch to the other printer. If the backup printer also fails the computer will shut down the experiment and wait for help. The data recorded on the hard disk is stored under a new file name every 24 hours. This prevents a power outage or computer failure from destroying all but the data in the current open file (which at most covers a 24 hour period). It also facilitates copying the data from the hard disk to floppy disks for off-line analysis.

Although the data are recorded on the printer and hard disk every 5 minutes, the computer internally stores the 60 most recent readings from each channel (which are at "n" second intervals). In the event of a cathode shutdown the computer will print out these data, providing a detailed description of the cathode operation leading up to the shutdown.

The computer will shut down the cathode if the anode voltage, tank pressure, or foreline pressure are detected to be outside of their allowed operating bands. In addition, the vacuum system itself will be shut down if the tank pressure or foreline pressure are outside their limits. The computer shuts down the vacuum system by closing the high vacuum valves, turning off the diffusion pump heaters, closing the foreline isolation valves and turning off the mechanical pumps. A hardwired safety feature will shut down the vacuum system if cooling water is lost. The data acquisition hardware monitors the serial communications link between itself and the host computer, and will shut down the cathode in the event that the host computer malfunctions.

The software for the host computer includes modem handling procedures which enable remote monitoring of the life test. The computer will answer incoming phone calls and will output the cathode operating data in real time through the modem. Other software procedures enable the computer to plot on the CRT the most recent 24 hours of data in real time, thus allowing quick evaluation of recent data trends. Finally, the program is run under the DesqView multitasking operating system. This multitasking system allows the data files to be copied from the hard disk for off-line analysis without interrupting the test.